

Struktur - Eigenschaftsbeziehungen
chalkogenidbasierter Schichtmaterialien



Kumulative Dissertation

zur Erlangung des Doktorgrades

der Mathematisch-Naturwissenschaftlichen Fakultät

der Christian-Albrechts-Universität zu Kiel

vorgelegt von

Anna-Lena Hansen, geb. Gritzuhn

Kiel 2017

Referent: Prof. Dr. Wolfgang Bensch

Korreferent: Prof. Dr. Christian Näther

Tag der Prüfung: 07.08.2017

Zum Druck genehmigt: Kiel,
Die Dekanin, Prof. Dr. Natascha Oppelt

·PAX OPTIMA RERUM·

Zusammenfassung

Im Rahmen dieser Arbeit wurden unterschiedliche Materialien basierend auf chalcogenidischen Schichtmaterialien in Bezug auf deren Struktur-Eigenschaftsbeziehungen untersucht. Das Hauptaugenmerk lag auf der Charakterisierung mit Röntgenbeugungsmethoden, da diese Methoden erlauben, die Realstruktur eines Materials auf globaler Ebene zu erfassen. Kombiniert mit lokalen Methoden, wie der Transmissionselektronenmikroskopie und Totalstreuungsmethoden (Pair Distribution Function, PDF), ist es möglich einen detaillierten Einblick in die Struktur auf allen Längenskalen zu erhalten. Im Rahmen der Dissertation konnte nachgewiesen werden, dass es möglich ist in gesputterten $\text{Bi}_2\text{Te}_3/\text{Bi}_{1-x}\text{Sb}_x\text{Te}_3$ Dünnschichten Nanokristallinität mit dem Vorhandensein eines Übergitters strukturell zu kombinieren. Allerdings konnte mit diesen Dünnschichten keine Verbesserung der thermoelektrischen Eigenschaften erreicht werden. Die Charakterisierung epitaktischer $\text{Bi}_2\text{Te}_3/\text{Sb}_2\text{Te}_3$ Übergitter belegt deren außerordentliche strukturelle Qualität. Diese extrem guten Filme ermöglichten erstmals nach über 10 Jahren Forschung, wichtige Fragen in Bezug auf die Temperaturstabilität dieser thermoelektrischen Materialien aufzuklären. Für Materialien wie Thermoelektrika ist die Stabilität bei erhöhten Temperaturen von entscheidender Bedeutung, denn nur so kann eine Langzeitstabilität thermoelektrischer TE Generatoren garantiert werden. Im Rahmen dieser Arbeit konnte jedoch nachgewiesen werden, dass die $\text{Bi}_2\text{Te}_3/\text{Sb}_2\text{Te}_3$ Übergitter bereits ab Temperaturen von 200 °C eine Degradation durch die Interdiffusion der Konstituenten erfahren. Umfassende Untersuchungen an Verbindungen mit der Zusammensetzung $1-x(\text{GeTe})_x(\text{Bi}_2\text{Se}_{0.2}\text{Te}_{2.8})$ belegen eindrücklich, dass Untersuchungen der thermischen Stabilität extrem wichtig sind. Nach wiederholtem thermischen Zyklisieren nimmt der thermoelektrische Gütefaktor ZT von dem rekordverdächtigen Wert von 2.0 auf 1.0 ab. Diese Beobachtung kann mit einer Veränderung der chemischen Zusammensetzung auf strukturelle Veränderungen im Material zurückgeführt werden. Der positive Effekt einer erhöhten Ionenunordnung auf die thermoelektrische Güte von Materialien ist in der Literatur gut dokumentiert. Um die Mobilität und damit die Unordnung von Cu^+ -Ionen in der Pseudo-Schichtverbindung CuCrS_2 zu erhöhen, wurden Cu^+ -Ionen über eine topotaktisch verlaufende Redoxreaktion aus dem Material entfernt. Die strukturelle Charakterisierung ergab die Bildung einer bis heute unbekanntes monoklinen $\text{Cu}_{0.66}\text{CrS}_2$ Phase mit einer Überstruktur. Aufgrund der thermischen Instabilität der Verbindung konnten die thermoelektrischen Kenngrößen nicht bestimmt werden. Diese Beobachtung belegt nochmals, dass bei der Entwicklung neuer Konzepte zur Erhöhung des ZT-Wertes Temperatur-Stabilitätsuntersuchungen unabdingbar sind.

Abstract

Within the scope of this thesis, different materials based on layered chalcogenides were investigated with respect to their structure-property relationships. The focus was on the characterization using X-ray diffraction methods, because these techniques offer the advantage of understanding the real structure of a material on a global scale. Combined with local methods such as transmission electron microscopy and X-ray based total scattering methods, it is possible to obtain a detailed view of the structure on all length scales. For $\text{Bi}_2\text{Te}_3/\text{Bi}_{1-x}\text{Sb}_x\text{Te}_3$ thin films it was demonstrated that nanocrystallinity and superlattices can exist in a thermoelectric material. It is believed that such a combination improves the thermoelectric performance. In contrast to the expectation no improvement of the thermoelectric properties could be achieved. The characterization of epitaxial $\text{Bi}_2\text{Te}_3/\text{Sb}_2\text{Te}_3$ superlattices highlighted their exceptional structural quality. For the first time after more than 10 years of research, important questions regarding the temperature stability of these thermoelectric materials could be clarified. For thermoelectrics, the structural stability and integrity at elevated temperatures is of crucial importance, because thermoelectric generators must exhibit long-term stability. However, experiments performed during this thesis have demonstrated that thermal stability is a pitfall of this class of materials. Noteworthy, investigation of thermal stability is remarkably little addressed in the literature. The $\text{Bi}_2\text{Te}_3/\text{Sb}_2\text{Te}_3$ superlattices already showed a degradation of the superlattice at temperatures of 200 °C by the interdiffusion of the constituents. Studies on the compound $1-x(\text{GeTe})x(\text{Bi}_2\text{Se}_{0.2}\text{Te}_{2.8})$ also evidenced the importance of such stability studies. After repeated thermal cycling, the decrease in the thermoelectric quality factor ZT from above 2.0 to 1.0 at 450 °C was observed. The reasons for this performance degradation were a change in the phase content and structural changes within the material. The positive effect of an increased ion disorder on the thermoelectric quality is known. In order to increase the mobility and therefore the disorder of the Cu^+ ions in the compound CuCrS_2 , Cu^+ was removed from the layers by means of a topotactic redox reaction. The structural characterization showed the formation of a previously unknown monoclinic $\text{Cu}_{0.66}\text{CrS}_2$ phase. However, the thermal instability of the compound prevented its use as a thermoelectric material despite the promising increased disorder of Cu^+ ions. Again, the necessity of rigorous characterization of thermoelectric material is demonstrated including temperature stability studies, which are particularly important when developing new concepts to increase the ZT value.

Inhalt

A Einleitung	1
Thermoelektik.....	3
1. Binäre Chalkogenide	6
1.1 Bi ₂ Te ₃ und Sb ₂ Te ₃	6
1.2 GeTe.....	8
1.3 CrTe ₃	10
2. Ternäre Chromchalkogenide	12
2.1 CuCrS ₂	12
B Untersuchungsmethoden	13
4.1 Röntgendiffraktometrie.....	13
4.2 Totalstreuungsmethoden	15
C Kumulativer Hauptteil.....	17
1. Veröffentlichungen Bi ₂ Te ₃ – Sb ₂ Te ₃	17
1.1 Sputtered n-type Bi ₂ Te ₃ /(Bi,Sb) ₂ Te ₃ superlattice systems.....	17
1.2 Synthesis and Thermal Instability of High-Quality Bi ₂ Te ₃ /Sb ₂ Te ₃ Superlattice Thin Film Thermoelectrics	28
1.3 Nanostructure, thermoelectric properties, and transport theory of V ₂ VI ₃ and V ₂ VI ₃ /IV–VI based superlattices and nanomaterials	34
2. Veröffentlichungen GeTe – Bi ₂ Te ₃ – Sb ₂ Te ₃	45
2.1 Thermoelectric efficiency of (1-x)(GeTe)x(Bi ₂ Se _{0.2} Te _{2.8}) and implementation into highly performing thermoelectric power generators	45
2.2 Enhanced temperature stability and exceptionally high electrical contrast of selenium substituted Ge ₂ Sb ₂ Te ₅ phase change materials	55
3. Veröffentlichung ternäre Chromchalkogenide	65
3.1 Structural properties of the thermoelectric material CuCrS ₂ and of deintercalated Cu _x CrS ₂ on different length scales: X-ray diffraction, pair distribution function and transmission electron microscopy studies.....	65
4. Weitere Veröffentlichungen.....	86
4.1 Elucidation of the Conversion Reaction of CoMnFeO ₄ Nanoparticles in Lithium Ion Battery Anode via Operando Studies.....	86
4.2 CuV ₂ S ₄ : A high rate-capacity and stable anode material for sodium-ion batteries..	100
5. Unveröffentlichte Projekte (<i>to be published</i>).....	110
D Zusammenfassender Ausblick	128
Literaturverzeichnis	130
E Anhang	I
Liste der Veröffentlichungen und Tagungsbeiträge	I
<i>Electronic supporting information</i>	III
Danksagung	XLV
Erklärung	XLVI
Wissenschaftlicher Werdegang.....	XLVII

A Einleitung

Seit Jahrtausenden nutzen Menschen, basierend auf empirischen Erfahrungen, natürlich vorkommende Schichtmaterialien, wie beispielsweise Tone oder Graphit. Mit der Entwicklung der modernen Wissenschaft wurden die Strukturen und auch die damit einhergehenden physikalischen Eigenschaften immer weiter aufgeklärt und verstanden. Zu den Schichtmaterialien zählt eine Vielzahl von Verbindungen, allerdings ist dieser Begriff nicht besonders scharf definiert. Zahlreiche Verbindungen lassen sich als solche beschreiben, sogar beispielsweise Diamant oder Halit (Abbildung 1). Doch während es in Ausnahmefällen sinnvoll sein kann, diese Strukturen als Schichten zu betrachten, beispielsweise um Stapelfehler zu beschreiben, würde niemand so weit gehen und NaCl zu den Schichtstrukturen zählen.

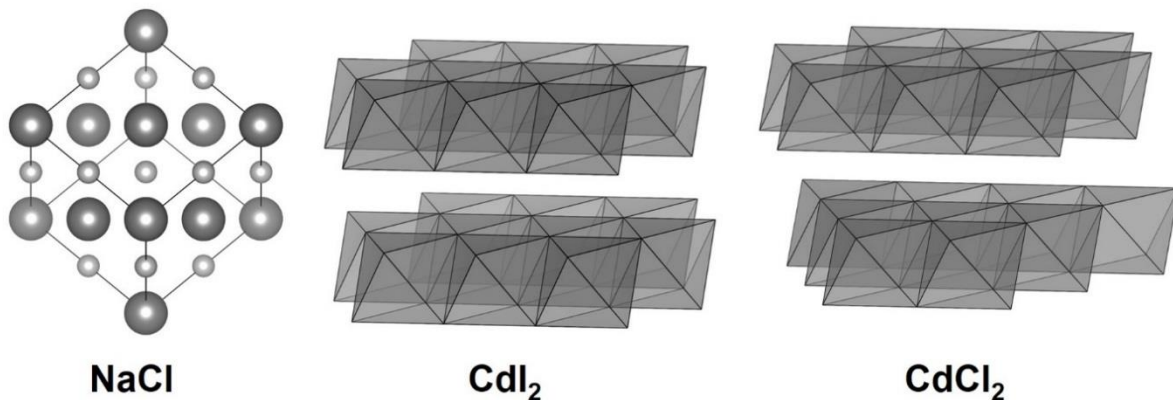


Abbildung 1: Vergleich der Kristallstrukturen der Strukturtypen NaCl^[1], CdI₂^[2] und CdCl₂^[3].

Denn bei einem Vergleich mit den Hauptstrukturtypen der am besten untersuchten klassischen Schichtmaterialien, den Dichalkogeniden (MX_2), mit NaCl in Abbildung 1 fällt auf, dass nicht nur eine alternierende Abfolge der Atome ausschlaggebend ist, sondern vielmehr die Anisotropie der Bindungen als das wesentliche Charakteristikum für Schichtstrukturen

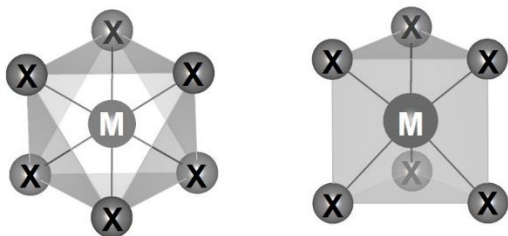


Abbildung 2: Schematische Darstellung der Koordination der Metallkationen in chalcogenidischen Schichtstrukturen. Links: oktaedrische Koordination des Zentralkations, rechts: trigonal-prismatische Koordination. X: Chalkogenid-Anion, M: Metall-Kation.

anzusehen ist. Während in den Schichten starke kovalente Bindungen dominieren, liegen zwischen den Schichten nur schwache van-der-Waals Wechselwirkungen vor.^[4] Dichalkogenide unterscheiden sich strukturell einerseits durch die Koordination der Kationen (oktaedrisch/trigonal-prismatisch, Abbildung 2) und andererseits durch das Arrangement der Schichten zueinander. Letzteres wird als Stapelung der

Schichten beschrieben. Der wichtigste Vertreter, in dem die Metallkationen trigonal-prismatisch von den Anionen koordiniert sind, stellt MoS_2 dar. Auf Grund der Vielzahl an möglichen Stapelungsvarianten und Koordination der Metallkationen kommt es zur Ausbildung zahlreicher Polymorphe oder auch Polytype, wie beispielsweise dem hexagonalen 2H- MoS_2 und rhomboedrischen 3R- MoS_2 .^[5,6] Allgemein lässt sich das Strukturmotiv der Schichtmaterialien demnach als van-der-Waals verbrückte 2D Schichten zusammenfassen. Die Entdeckung des Graphens und die Erkenntnis, dass sich die physikalischen Eigenschaften von MoS_2 mit der Anzahl der Schichten signifikant verändern lassen, führte zu einem enormen Interesse an Schichtverbindungen.^[7-9] Die Idee, dass sich Materialien gezielt designen lassen, beflügelte Wissenschaftler auf der ganzen Welt und führte zur Entwicklung neuer Konzepte,

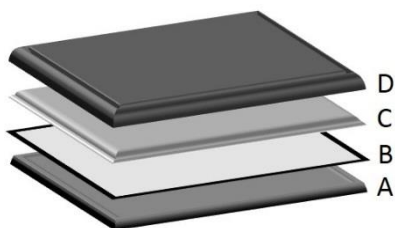


Abbildung 3: Schematische Darstellung einer 2D Heterostruktur aus den Materialien A – D.

wie etwa der Van-der-Waals-Heterostrukturen. Hierbei werden, wie in Abbildung 3 schematisch dargestellt, 2D Schichten kombiniert und somit künstliche Schichtmaterialien erzeugt.^[10] Auf diese Weise lassen sich die physikalischen Eigenschaften der Einzellagen gezielt kombinieren, was zu völlig neuartigen physikalischen Phänomenen führen kann.^[10-14] Dieses Konzept (Modulated Element Reactants, MER) ermöglicht die nahezu unendliche

Kombination von Schichten. Jedoch ist es für eine Realisierung und das gezielte Design solcher Materialien nötig, die eingesetzten Verbindungen hinsichtlich ihrer Struktur-Eigenschaftsbeziehungen genau zu charakterisieren und zu verstehen. Wie bereits erwähnt gibt es eine weite Bandbreite an Schichtmaterialien angefangen vom Paradebeispiel, dem Graphit und Graphen und seinem strukturellen Analogon, dem hexagonalen Bornitrid (hBN), oft ‚weißes Graphen‘ genannt,^[7,15] Metalloxide und Hydroxide wie beispielsweise MnO_2 , MnO_3 oder $\text{MgAl}_6(\text{OH})_{16}$,^[16-20] Schichtsilikate^[21-23] und schließlich die bereits erwähnten Metaldichalkogenide und deren isostrukturellen Dihalogenide. Die Chalkogenide lassen sich in die binären Mono- (MX ; M = Metallkationen, $X = \text{S, Se, Te}$)^[24], Di- (MX_2) und Trichalkogenide (MX_3 und M_2X_3), sowie die ternären Chalkogenide (AMX_2 , A = meist Alkalimetalle und Übergangsmetalle wie Cu und Ag) unterteilen.^[25-28] Letztere weisen zusätzliche Metallkationen (A) zwischen den van-der-Waals verbrückten Schichtstapeln auf. Diese sind je nach ihrem Ionenradius tetraedrisch, oktaedrisch oder trigonal-prismatisch koordiniert. Die mit Abstand am besten untersuchte Gruppe stellen die mit ~40 Verbindungen binären Übergangsmetaldichalkogenide (transition metal dichalcogenides, TMDC) dar.^[29] Innerhalb dieser Gruppe ist MoS_2 mit fast 10000 Publikationen seit der bahnbrechenden Arbeit von Heinz *et al.* im Jahre 2010 das am besten erforschte TMDC.^[8,30,31] Die strukturell komplexere Gruppe der Chalkogenide umfasst die Übergangsmetalltrichalkogenide (TMT), wie beispielsweise TiX_3 und ZrX_3 , die in kettenartigen (nahezu 1D) Strukturen kristallisieren,^[32]

sowie die Hauptgruppenelement-trichalkogenide mit Verbindungen wie Bi_2Te_3 und Sb_2Te_3 (die unter 1.1.1 näher vorgestellt werden). Allen gemein ist, dass die Verbindungen ein Höchstmaß an struktureller Anisotropie aufweisen. Daraus resultieren nicht nur Eigenschaften wie eine gute mechanische Spaltbarkeit, welche für die Exfoliation ein bedeutendes Kriterium darstellt.^[33] Auch viele physikalische Eigenschaften spiegeln den zweidimensionalen Charakter wieder. Dass das von Vorteil sein kann, soll im Folgenden am Beispiel der Thermoelektrik verdeutlicht werden.

Thermoelektik

Thermoelektrika sind Materialien, die Wärme in nutzbare elektrische Energie umwandeln können. Auf Grund dieser Eigenschaft könnten sie in der Zukunft einen entscheidenden Beitrag zur viel diskutierten Energiewende leisten, denn thermisch ineffiziente Prozesse (Energiedissipation) werden nie gänzlich vermieden werden können. Erste grundlegende Arbeiten zu Beginn des 19. Jahrhunderts gehen auf Seebeck, Thompson und Peltier zurück. Die Güte thermoelektrischer Materialien wird mit einem dimensionslosen Faktor angegeben, dem ZT Wert:

$$ZT = \frac{\sigma \cdot S^2}{\kappa} T \quad (1)$$

Wobei σ die elektrische Leitfähigkeit, S den Seebeck- Koeffizienten ($\sigma \cdot S^2$ wird auch als der Powerfaktor bezeichnet), T die absolute Temperatur und κ die thermische Leitfähigkeit

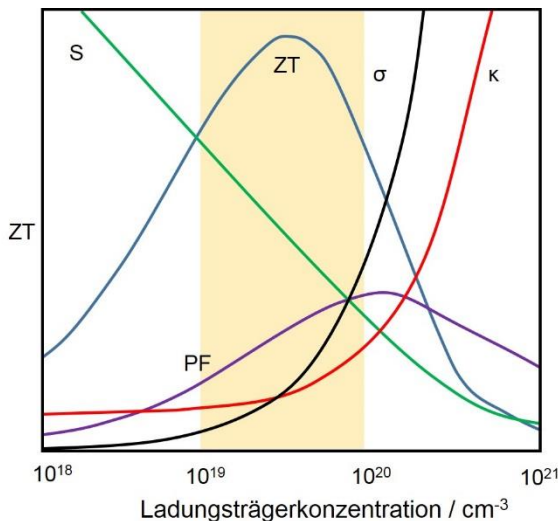


Abbildung 4: Schematische Darstellung des Zusammenhangs zwischen den thermoelektrischen Kennzahlen, dem Gütefaktor ZT und der Ladungsträgerkonzentration. Vereinfacht nach ^[34]

darstellt, welche der Summe von Ladungsträger- (κ_e) und Phononenanteil (κ_{ph}) zur Leitfähigkeit entspricht. Hauptproblem bei der Optimierung des ZT Wertes liegt in der in Abbildung 4 schematisch dargestellten wechselseitigen Abhängigkeit der einzelnen Größen, so dass eine große thermoelektrische Effizienz immer einen Kompromiss darstellen muss aus großem Powerfaktor und geringer thermischer Leitfähigkeit.^[34] Die elektrische Leitfähigkeit ist folgendermaßen definiert:

$$\sigma = n \cdot e \cdot \mu \quad (2)$$

n ist die Ladungsträgerdichte, e die Elementarladung und μ die Ladungsträgermobilität. Eine erhöhte Ladungsträgerdichte führt gleichzeitig zu einer Erniedrigung des Seebeck-Koeffizienten (Pisarenko-Relation^[35]). Die thermische Leitfähigkeit von Metallen ist

proportional zu ihrer elektrischen Leitfähigkeit (Wiedemann-Franz-Gesetz), so dass eine Erhöhung der elektrischen Leitfähigkeit eine gleichzeitig größere thermische Leitfähigkeit bedingt. Ihr Verhältnis, die sogenannte Lorenz-Zahl, ist jedoch eine Funktion der Bandstruktur, weshalb für große Gütefaktoren extrinsische Halbleiter mit Ladungsträgerkonzentrationen im Bereich von $10^{19} - 10^{20} \text{ cm}^{-3}$ (in Abbildung 4 orange hinterlegt) den idealen Kompromiss darstellen. Die übrigen Größen für anwendungstechnisch relevante Thermoelektrika liegen typischerweise um $\sigma \sim 1000 \text{ S/cm}$, $S \sim 200 \text{ } \mu\text{V/K}$ (wobei positive Vorzeichen einen p-Typ Halbleiter und negative Vorzeichen einen n-Typ Halbleiter kennzeichnen), einem resultierenden Powerfaktor von ca. $40 \text{ } \mu\text{W/cmK}^2$ und einer Wärmeleitfähigkeit κ von ca. 1 W/mK . Mit einem Wert für ZT von ca. 1 zeigten Bi_2Te_3 und $\text{Sb}_2\text{Te}_3/\text{Bi}_2\text{Te}_3$ Verbindungen über Jahrzehnte die höchsten ZT -Werte bei Raumtemperatur und stellten daher das obere Limit dar.^[36] Anhand der Gleichung für den maximalen Gütefaktor soll verdeutlicht werden, warum anisotrope Materialien eine für thermoelektrische Anwendungen attraktive Materialklasse darstellen:

$$Z_{max} \propto \gamma \frac{T^{3/2} \tau_z \sqrt{\frac{m_x m_y}{m_z}}}{\kappa_{ph}} e^{(r+1/2)} \quad (3)$$

γ stellt die Entartung der Extrema der Bänder, T die Temperatur, τ_z die Relaxationszeit der Ladungsträger, m die effektive Masse der Ladungsträger in der jeweiligen Richtung x, y, z , r den Beugungsparameter und κ_{ph} den phononischen Anteil an der thermischen Leitfähigkeit dar. Ohne näher auf die Bedeutung der einzelnen Parameter einzugehen, soll hiermit verdeutlicht werden, dass eine verringerte effektive Masse m_z bei gleichzeitig erhöhten m_x und m_y , wie dies in stark anisotropen Kristallstrukturen der Fall ist, zu einem größeren Wert für Z führt. Dies gilt wenn der Transport der Ladungsträger in z Richtung erfolgt.^[37] Gleichzeitig weisen Schichtverbindungen meistens eine niedrigere Wärmeleitfähigkeit parallel zu ihrem Stapelvektor auf. Bereits 1968 konnte an Si-Ge Verbindungen gezeigt werden, dass es möglich ist durch das gezielte Einbringen von Störstellen, an denen niederfrequente Phononen gestreut werden, die thermische Leitfähigkeit zu reduzieren.^[38,39] Jedoch muss auch hier ein Kompromiss gefunden werden, denn durch den Einbau von Defekten wird gleichzeitig die Ladungsträgerdichte reduziert.^[40] Im Jahr 1993 folgten theoretische Arbeiten von Hicks und Dresselhaus, die zur Entwicklung einer neuen Generation thermoelektrischer Materialien führte. Die Ergebnisse der Berechnungen wiesen darauf hin, dass es möglich sein sollte durch *Quanten Confinement Effekte* in nanostrukturierten niederdimensionalen Systemen (2D, 1D), einen wesentlich größeren Seebeck Koeffizient zu erreichen.^{[41],[42]} Auch wenn diese theoretischen Konzepte praktisch nicht verifiziert werden konnten, wurde dennoch durch die Nanostrukturierung eine erhöhte Streuung der Phononen erreicht, welches zu einer drastischen Reduktion von κ_{ph} und damit einhergehend einem größeren ZT -Wert führte. Mitte der 1990er Jahre wurde schließlich das *Phononen-Glas-Elektronen-Kristall (PGEK)* Konzept

entwickelt. Dieses Konzept postuliert, dass Phononen als Hauptträger der thermischen Energie in einem idealen thermoelektrischen Material gestreut werden sollten wie in einem Glas, wohingegen die Elektronen frei beweglich sein sollten wie in einem perfekten Kristall^[43] In mehreren Arbeiten konnte demonstriert werden, dass durch Verdampfungsverfahren Dünnschichten mit *künstlichen* Schichtstrukturen (Übergitter/*superlattices*) herstellbar sind, welche eine sehr geringe thermische Leitfähigkeiten aufweisen.^[44–46] Für fehlgeordnete WSe_2 Dünnschichten konnte sogar das Minimum der Wärmeleitfähigkeit für amorphe Materialien unterschritten werden.^[47] Diese Systeme stellen daher nahezu ideale *PGEK* Materialien dar. Neuere synthetische Ansätze versuchen alle diese Erkenntnisse, Einbau von Defekten, Nanostrukturierung, Fehlordnung, Anisotropie, etc. in einem Material zu verwirklichen. Erreicht werden kann dies durch komplex nanostrukturierte Kompositmaterialien, sogenannte hierarchische Strukturen. Bei diesen werden gezielt Nanoausscheidungen erzeugt, möglichst auf verschiedenen Längenskalen, um hoch- und niederfrequente Phononen zu streuen.^[48–51] Der Grundgedanke bei diesen Arbeiten bleibt stets die Entkoppelung der einzelnen thermoelektrischen Kenngrößen (Gleichung 1). Während immer komplexere Materialien konzipiert und synthetisiert werden, wirft dies gleichzeitig die Frage nach ihrer exakten und umfassenden Charakterisierung sowie der Reproduzierbarkeit dieser komplexen Materialien auf. Dies soll im Rahmen dieser Arbeit demonstriert werden. Bei den experimentellen Arbeiten hat sich herausgestellt, dass zwar die Kristallstrukturen vieler der hier untersuchten Materialien sehr gut untersucht sind, aber zum einen ist der Zusammenhang zwischen Realstruktur und Eigenschaften und zum anderen die Veränderungen dieser Materialien während des Einsatzes als Thermoelektrikum meistens nur ungenügend erforscht. Der Überbegriff Realstruktur umfasst beispielsweise die Kristallitgröße und deren Größenverteilung, Verzerrungen des Kristallgitters (*strain*), das Vorhandensein von Fremdphasen, Defekten, die die Eigenschaften eines Materials empfindlich beeinflussen können. Im Rahmen der vorliegenden Arbeit wurden ausgewählte Schichtmaterialien, die im folgenden Kapitel vorgestellt werden, in Bezug auf deren Realstruktur mittels Röntgendiffraktions- und Totalstreuungsmethoden (*total scattering*) untersucht, um Einblicke in das komplexe Zusammenspiel zwischen Realstruktur und Eigenschaften zu generieren.

1. Binäre Chalkogenide

1.1 Bi₂Te₃ und Sb₂Te₃

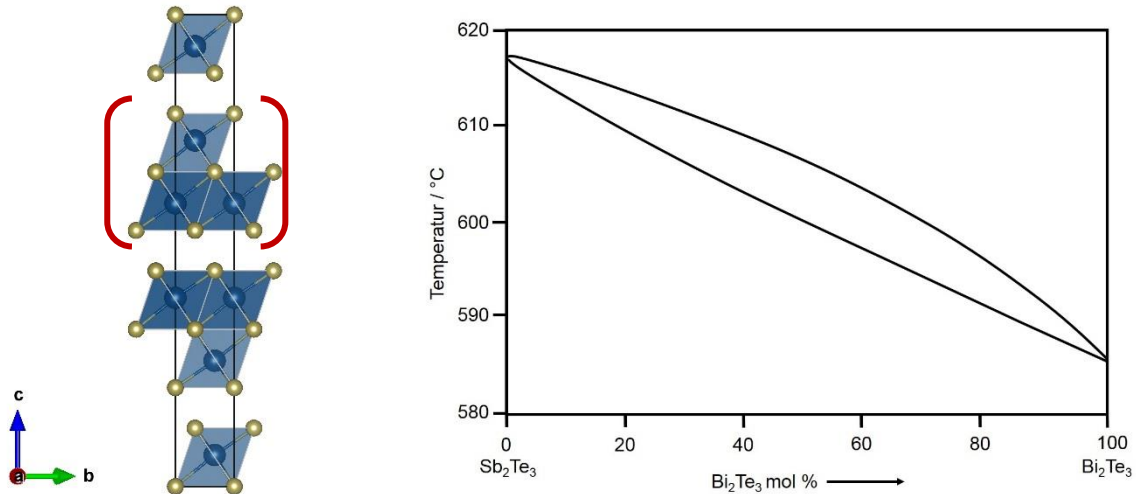


Abbildung 5: links: Kristallstruktur des Bi₂Te₃. Bi Oktaeder sind blau, Telluranionen sind gold dargestellt. Ein Schichtstapel ist rot markiert. Rechts: Pseudobinäres Phasendiagramm.^[52,53]

Die Verbindung Bi₂Te₃ und das isostrukturelle Sb₂Te₃ kristallisieren in der Raumgruppe $R\bar{3}m$, und leiten sich im weitesten Sinne von der CdCl₂-Struktur ab (Abbildung 5). Beide Verbindungen sind lückenlos miteinander mischbar und unterscheiden sich nur geringfügig bei den Zellparametern (Bi₂Te₃: $a_{\text{hex}} = 4.38 \text{ \AA}$, $c_{\text{hex}} = 30.5 \text{ \AA}$; Sb₂Te₃: $a_{\text{hex}} = 4.27 \text{ \AA}$, $c_{\text{hex}} = 30.45 \text{ \AA}$).^[53–55] Die Metallkationen sind oktaedrisch von Te²⁻ koordiniert und anders als im CdCl₂-Strukturtyp werden so genannte Quintupel als Schichtpakete beobachtet (Atomabfolge: Te – Bi – Te – Bi – Te; rot markiert in Abbildung 5). Die Bi – Te-Bindungen in den Schichtpaketen sind ionisch–kovalenter Natur, während zwischen Te²⁻-Anionen nur schwache van der Waals Wechselwirkungen vorhanden sind. Die van der Waals Lücken werden auch als intrinsische planare Defektschichten (*vacancy layer*) bezeichnet.^[56] Die ausgeprägte Anisotropie der Struktur spiegelt sich deutlich in den Transporteigenschaften wieder.^[40] Dass sich eine solche Anisotropie günstig auf die Güte eines (thermoelektrischen) Materials auswirken kann, wurde bereits Mitte des letzten Jahrhunderts erkannt.^[57–59] Darüber hinaus ist der Diffusionskoeffizient von Ionen wie beispielsweise Se²⁻ um Größenordnungen geringer senkrecht zur Stapelungsrichtung ($\parallel c$), als parallel zu den Schichten ($\parallel a$).^[60,61] Wie wichtig das Kenntnis der Realstruktur von Materialien ist, lässt sich eindrücklich an Bi₂Te₃/Sb₂Te₃ deutlich machen, da die Transporteigenschaften durch die Defektchemie dieser Verbindungen dominiert sind. Besonders wichtig sind Substitutionsdefekte (*antisite defects*), also die Besetzung von Anionenplätzen durch Kationen und umgekehrt (Bi_{Te}/Te_{Bi}), sowie

Leerstellendefekte ($V_{\text{Bi}}/V_{\text{Te}}$).^[62,63] Durch diese Defekte werden Elektronen- bzw. Löcherleitung generiert. Bei Bi_2Te_3 und Bi reichen Mischphasen überwiegt die Elektronenleitung (n-typ Halbleiter), während bei Sb_2Te_3 die gegenteilige Beobachtung gemacht wird und ein p-typ Halbleiter vorliegt.^[64] Seit der erstmaligen Erwähnung als thermoelektrisches Material Mitte der 1950er Jahre gilt Bi_2Te_3 bis heute als eines der effizientesten thermoelektrischen Materialien bei Raumtemperatur.^[40,65,66] Es ist damit *das* klassische Thermoelektrikum. In kommerziell erhältlichen Modulen wird typischerweise $(\text{Bi}, \text{Sb})_2\text{Te}_3$ als p-Leiter und Selen substituiertes Bi_2Te_3 als n-leitendes Gegenstück verwendet. Die Güte dieser Materialien konnte, wie in der Einleitung bereits angedeutet, durch Nanostrukturierung weiter gesteigert werden. ZT Werte von 1.2 - 1.4 konnten für hierarchisch aufgebaute Volumenmaterialien erreicht werden $(\text{Bi},\text{Sb})_2\text{Te}_3$.^[67] Die Frage der Langzeitstabilität solcher Materialien, insbesondere in Bezug auf die Kristallitgrößenentwicklung der Nanoausscheidungen bei wiederholtem Aufheizen und Abkühlen bleibt jedoch offen.

1.2 GeTe

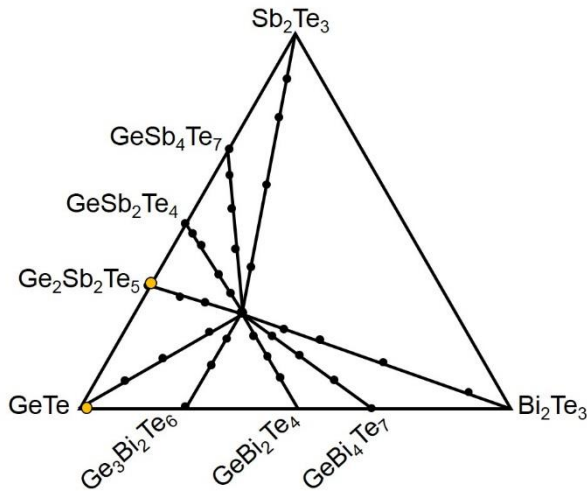


Abbildung 6: Phasendiagramm des quasiternären Systems GeTe – Bi₂Te₃ – Sb₂Te₃. Die im Rahmen dieser Arbeit behandelten Phasen sind orange markiert.^[71]

GeTe kristallisiert in 2 Polymorphen, einer kubischen β -Phase mit NaCl-Struktur ($Fm\bar{3}m$) und einer rhomboedrisch verzerrten Raumtemperaturphase (α -GeTe, $R3m$).^[54,68] Je nach Stöchiometrie findet diese Umwandlung bei 390 – 460 °C statt.^[69,70] Wie in Abbildung 6 dargestellt, bildet GeTe ein quasiternäres System mit Bi₂Te₃ und Sb₂Te₃.^[71] Charakteristisch für die mit schwarzen Punkten gekennzeichneten Verbindungen ist eine unterschiedliche Stapelabfolge der Schichten und eine spezifische Verteilung von intrinsischen Leerstellen.^[56,72–74] Die im Rahmen dieser

Arbeit näher untersuchten Verbindungen (orange markiert in Abbildung 6) sollen im Folgenden kurz vorgestellt werden

Die Verbindung $(1-x)(\text{GeTe}) x(\text{Bi}_2\text{Se}_{0.2}\text{Te}_{2.8})$; $x = 0.038, 0.063$

Abrikosov *et al.* beschreibt die Löslichkeit von Bi₂Te₃ in GeTe mit einem Maximalwert von 8 %, einhergehend mit einer Reduzierung der Phasenumwandlungstemperatur auf bis zu 325 °C. Gleichzeitig kommt es zur vermehrten, für Bi₂Te₃ charakteristischen, Ausbildung planarer Defekte (*vacancy layer*).^[54]

Die Verbindung Ge₂Sb₂Te₅

Mit zunehmender Konzentration x werden im pseudobinären System $(1-x)(\text{GeTe}) x(\text{Sb}_2\text{Te}_3)$ Kationenleerstellen ($\frac{x}{1-2x}$) generiert, um Ladungsneutralität zu erhalten.^[75] Dies führt gleichzeitig dazu, dass die kubische und die von ihr abgeleitete rhomboedrisch verzerrte Phase von GeTe bei Raumtemperatur metastabil werden und sich die Phasenumwandlungstemperatur zu niedrigeren Temperaturen verschiebt.^[76] Die thermodynamisch stabile Modifikation kristallisiert in der trigonalen Raumgruppe $P\bar{3}m1$ und ist charakterisiert durch eine Ausordnung der Kationenleerstellen.

Neben der möglichen Anwendung als Thermoelektrika^[74,77–79] werden GeTe basierte Verbindungen als Phasenwechselmaterialien (*phase change materials*, PCM) untersucht und bereits industriell eingesetzt. Das Grundprinzip beruht auf der Schaltbarkeit durch thermische

Energie (z.B. Laserpulse). Unter Schaltbarkeit versteht man in diesem Zusammenhang die reversible Änderung der Kristallstruktur (Phase). In den hier vorgestellten Verbindungen findet der Schaltvorgang zwischen einer amorphen und einer metastabilen kristallinen Phase statt. Je nachdem ob zwischen diesen Phasen ein ausgeprägter optischer (Reflexionsvermögen) oder elektrischer Kontrast (Widerstand) vorliegt, finden sie Anwendung als optische oder elektrische Speichermedien (DVD/BluRay oder PC-RAM).^[80-84]

1.3 CrTe₃

Die Verbindung CrTe₃ kristallisiert in einer komplexen Kristallstruktur (Raumgruppe P^{2_1}/C , $a = 7.88 \text{ \AA}$, $b = 11.22 \text{ \AA}$, $c = 11.56 \text{ \AA}$ und $\beta = 118.41^\circ$), die in Anlehnung an die Dichalkogenide als Chrom defizitäres Derivat der CrTe₂-Struktur (CdI₂ Strukturtyp, vgl. Abbildung 1) mit der Formel Cr_{2/3}Te₂ beschrieben werden kann. In der Struktur (Abbildung 7) sind die Schichten aus ecken- und kantenverknüpften CrTe₆-Oktaedern nur zu 2/3 besetzt und die Schichten werden über van der Waals Wechselwirkungen zusammen gehalten. Die kantenverknüpften Oktaeder bilden ihrerseits Cr₄Te₁₆ Rauten (*Quadrupel*).

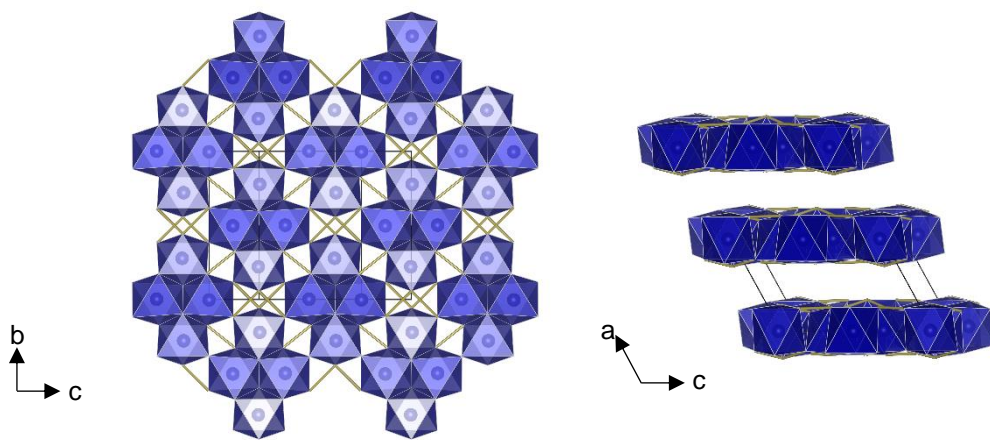


Abbildung 7: CrTe₃ Kristallstruktur. CrTe₆ Oktaeder sind in blau dargestellt. Te – Te Bindungen in gold. Links: Projektion auf die (100) Ebene. Rechts: Projektion auf die (010) Ebene.^[85]

Anders als bei den meisten Schichtchalkogeniden ist der Stapelvektor die kristallographische *a* Achse. Magnetische Suszeptibilitätsmessungen ergeben für Chrom die Oxidationsstufe +III, und Ladungsneutralität wird durch ein polyanionisches Te Netzwerk erreicht, so dass die Verbindung mit der Formel $[\text{Cr}^{3+}]_2[\text{Te}]^2[\text{Te}_2]^2[\text{Te}_3]^2$ beschrieben werden kann.^[85–87] CrTe₃ ist bis 753 K stabil und oberhalb dieser Temperatur tritt peritektische Zersetzung in Cr₅Te₈ und eine Te reiche Schmelze ein. Der in Abbildung 8 dargestellte Ausschnitt des binären Cr–Te Phasendiagramms beruht auf Ergebnissen von Differentialthermoanalyseuntersuchungen (DTA) und Röntgenbeugungsuntersuchungen. Ipsier *et al.* beobachtete ein zusätzliches thermisches Signal während des Aufheizens in Verbindungen mit 64 – 74 at. % Te Gehalt. Diese Beobachtung wurde als peritektischer Zerfall von CrTe₃ in ein unbekanntes Polychalkogenid interpretiert. Während des Abkühlens wurde

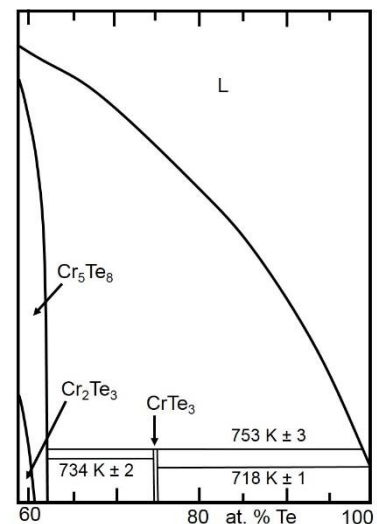


Abbildung 8: Ausschnitt des binären Cr – Te Phasendiagramms. Vereinfacht nach Ipsier, 1983.

dieses Signal nicht detektiert. Die Struktur und damit verbundenen Eigenschaften dieser unbekanntes CrTe_x Verbindung wurden in der Literatur nicht weiter verfolgt. Des Weiteren wurde für Zusammensetzungen $>74.9\%$ das Vorhandensein eines degenerierten Eutektikums bei 718 K identifiziert. Zusätzlich konnte auch nach monatelangem Tempern kein CrTe_3 ohne geringe Verunreinigungen von Te erhalten werden.^[88] Letzteres deutet auf ein komplexes Zusammenspiel zwischen Te und CrTe_3 hin, welches bisher nicht vollständig verstanden ist. Im Gegensatz zu den anderen Chromtelluriden, mit Ausnahme von CrTe_2 , ist CrTe_3 ein Halbleiter mit einer geringen Bandlücke von ~ 0.3 eV.^[85,89] Bisher sind noch keine technischen Anwendungen für dieses Material bekannt, was sich jedoch durch deren vielversprechenden Eigenschaften ändern könnte. Auf Grund der perfekten Spaltbarkeit und der Möglichkeit CrTe_3 , neben der Hochtemperaturfestkörpersynthese, mittels Multilagensynthese (*modulated elemental reactants*) als ausgeprägt (*h00*)-orientierte Dünnschichten zu synthetisieren^[90,91], könnte CrTe_3 als halbleitender Baustein in 2D Heterostrukturen Anwendung finden. Eine weitere Anwendung ist im Bereich der Spintronik denkbar, wobei dafür umfassende Untersuchungen der magnetischen Eigenschaften, insbesondere der Einzellschichten, unabdingbar sind. Erste Untersuchungen deuten auf eine antiferromagnetische Ordnung in dem Material hin.^[89]

2. Ternäre Chromchalkogenide

2.1 CuCrS₂

Das ternäre Chromchalkogenid CuCrS₂ kristallisiert in einer von der CdCl₂ Struktur abgeleiteten Pseudo-Schichtstruktur. Die Cu⁺-Kationen besetzen in jedem zweiten

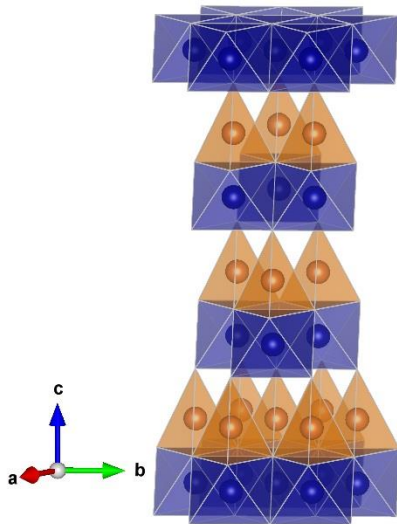


Abbildung 9: Kristallstruktur des CuCrS₂. CrS₆-Oktaeder sind in blau und CuS₄-Tetraeder in orange dargestellt.

Schichtstapel die Hälfte der Tetraederpositionen (Raumgruppe $R\bar{3}m$, $a = 3.4 \text{ \AA}$, $c = 18.7 \text{ \AA}$; Abbildung 9).

[25,92,93] Bei Temperaturen oberhalb von $\sim 400 \text{ }^\circ\text{C}$ ist CuCrS₂ ein Ionenleiter. Das hochmobile Cu⁺-Ion ist statistisch über beide Tetraederplätze verteilt.^[93–95] Diese

Mobilität wird als Grund für die sehr niedrige Wärmeleitfähigkeit bei erhöhten Temperaturen diskutiert ($\sim 0.3 \text{ W/mK}$ bei $650 \text{ }^\circ\text{C}$).^[95,96] CuCrS₂ ist ein p-Typ Halbleiter mit einer indirekten Bandlücke von 0.58 eV .^[97]

Die Ladungsträgerdichte beträgt $10^{19}\text{-}10^{20} \text{ cm}^{-3}$ und der Seebeck-Koeffizient ca. $400 \text{ } \mu\text{V}\cdot\text{K}^{-1}$.^[97] Theoretische

Berechnungen weisen darauf hin, dass neben der dynamischen Cu⁺-Fehlordnung auch die Ordnung der Cr³⁺-Ionen einen großen Einfluss auf die thermoelektrischen Eigenschaften ausübt. Bei einer zunehmend ungeordneten Besetzung der Chromplätze wurde ein Übergang von halbleitendem zu metallischem Verhalten postuliert, bei allerdings für Metalle relativ großem Seebeck-Koeffizienten.^[97] Diese theoretischen Ergebnisse werden durch die Beobachtung unterstützt, dass Cr-Leerstellen durch Sintern bei höheren Temperaturen generiert werden können. Die resultierende Eigendotierung mit Ladungsträgern führt zu einer erhöhten Leitfähigkeit des Materials. Je nach Dotierungsgrad ergeben sich Seebeck-Koeffizienten zwischen 150 und $450 \text{ } \mu\text{V/K}$.^[98] Je nach Literaturstelle werden ZT Werte von $0.01 - 2$ berichtet.^[96,98–101] Die weite Bandbreite dieser Ergebnisse spiegelt erneut die Wichtigkeit der Untersuchung der Realstruktur eines Materials wider. Jedoch ist eine umfassende Charakterisierung, einschließlich eines Bezugs auf die resultierenden Eigenschaften, noch immer selten in der Literatur zu finden.

B Untersuchungsmethoden

Hauptfokus der vorliegenden Arbeit ist die Charakterisierung der Realstruktur von Schichtmaterialien mittels Röntgenstromethoden. Im Folgenden wird dargestellt, wie sich die verschiedenen Komponenten der Realstruktur auf das Beugungsbild einer Verbindung auswirken und ermittelt werden können. Die Grundlagen der Röntgenbeugung sind in der Literatur dokumentiert.^[102,103] Nähere Angaben zu Geräten und Programmen finden sich im kumulativen Hauptteil in den Veröffentlichungen.

4.1 Röntgendiffraktometrie

Die Röntgendiffraktion oder –beugung beruht auf der Wechselwirkung zwischen Röntgenstrahlen und den Elektronen von Atomen. Das resultierende Beugungsbild enthält eine Vielzahl an Information, einerseits über die Kristallstruktur, andererseits über die Realstruktur (Abbildung 10). Der Überbegriff Realstruktur umfasst die Domänengröße und deren Größenverteilung, Mikroverzerrungen des Gitters, das Vorhandensein von Fremdphasen und Defekten, wie beispielsweise Stapelfehler.

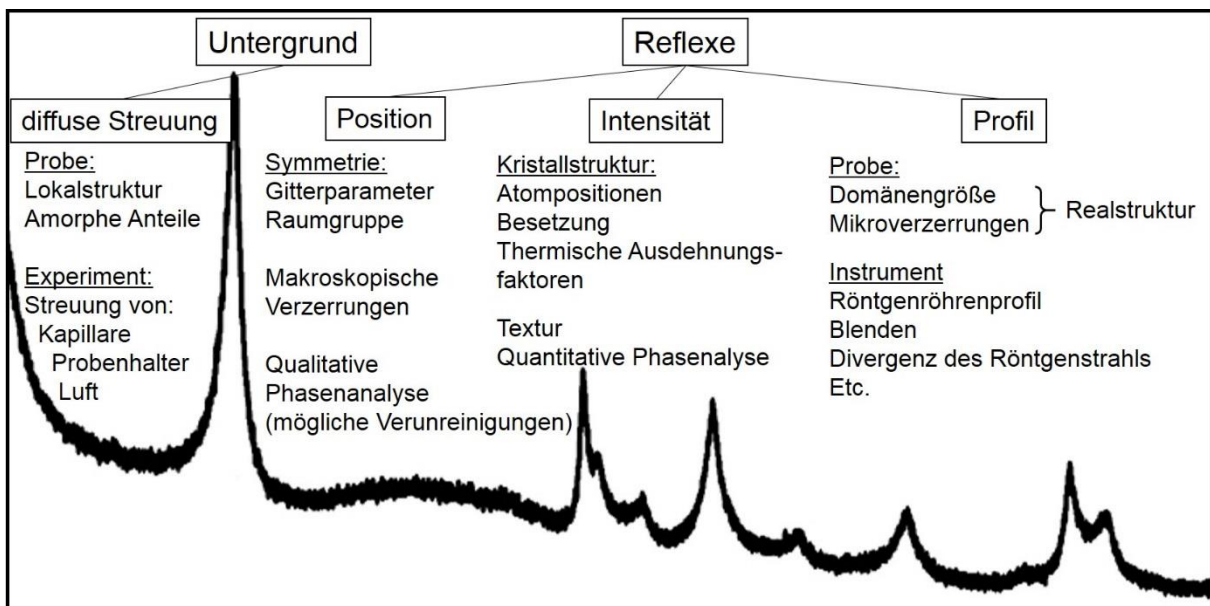


Abbildung 10: Informationen in einem Pulverdiffraktogramm. Nach Mittemeijer *et al.* am Beispiel eines 2H-MoS₂ Diffraktogramms^[103]

Um die Informationen aus dem gemessenen Diffraktogramm zu extrahieren, entwickelte Rietveld vor 50 Jahren die nach ihm benannte Methode.^[104] Ziel der Methode ist, das gesamte Beugungsbild zu modellieren und mittels least squares Verfeinerung (Methode der kleinsten Fehlerquadrate) an das gemessene Diffraktogramm anzupassen.^[105–107] Besonderes Augenmerk für die Analyse der Realstruktur liegt in der Charakterisierung des Reflexprofils. Das gemessene Profil ergibt sich aus der Faltung des durch die Realstruktur der Probe

erzeugten Profils und der Instrumentenfunktion. Die Instrumentenfunktion enthält den Beitrag der Röntgenquelle (Emissionsprofil) und der verwendeten Blenden und Optiken. Das Instrumentenprofil kann einerseits durch die so genannten Fundamentalparameter oder durch das Reflexprofil eines Standardmaterials (z.B. LaB₆), das keinen mikrostrukturellen Beitrag zum Reflexprofil erzeugt, bei der Verfeinerung von Pulverdiffraktogrammen berücksichtigt werden.^[108,109] Sowohl die Größe der kohärent streuenden Domänen (im Weiteren als Kristallitgröße bezeichnet), als auch mikroskopische Verzerrungen des Gitters (im Folgenden als strain bezeichnet) verursachen eine Verbreiterung des Reflexprofils. Jedoch zeigen Kristallitgröße und strain eine andere Abhängigkeit vom Beugungswinkel, was bereits 1949 als Methode zur Separation von Kristallitgröße und strain vorgeschlagen wurde.^[110,111]

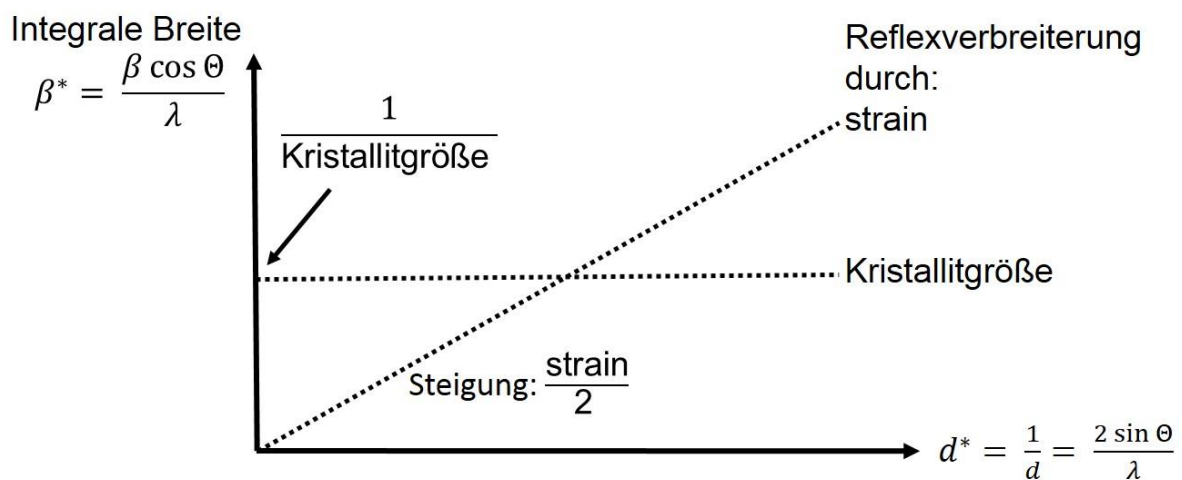


Abbildung 11: Schematische Darstellung des Williamson-Hall Plots. β^* ist die integrale Breite des Reflexes, d^* gibt den reziproken Netzebenenabstand wieder.

Wird die integrale Breite β^* eines Reflexes gegen den reziproken Netzebenenabstand d^* aufgetragen, wird der so genannte Williamson-Hall Plot erhalten (Abbildung 11). Mit Hilfe dieser Auftragung lässt sich die Hauptursache der Reflexverbreiterung und näherungsweise quantitativ die Kristallitgröße (<100 nm) sowie der strain abschätzen. Näherungsweise deshalb, da diese Art der Analyse auf der vereinfachten Annahme beruht, dass sowohl Kristallitgröße als auch strain zu einer Lorentz-Verbreiterung der Reflexe führen. Seit der Entwicklung dieser Analysemethoden wurden weitere Methoden entwickelt, um möglichst quantitative und realistische Aussagen über die Mikrostruktur eines Materials auf globaler Ebene und deren Verteilung zu treffen, im Gegensatz zu lokalen Methoden wie der Transmissionselektronenmikroskopie (TEM), die nur Aussagen über Probenbereiche von ein paar Nanometern zulässt. Eine Weiterentwicklung basierend auf Fourier-Analysen, wie der Warren-Averbach-Analyse, stellt das Whole Powder Pattern Modelling (WPPM) dar.^[112-116] Das WPPM beruht ausschließlich auf der quantitativen Modellierung physikalischer Effekte, die zur Profilverbreiterung beitragen. Scardi *et al.* haben mikrostrukturelle Phänomene wie Stapelfehler und die Verteilung der Kristallitgrößen (im Gegensatz zum bisherigen Ansatz

eines gemittelten Wertes) in die Modellierung der Diffraktogramme einbezogen. Dieser Ansatz wurde kürzlich in gängige Software zur (Rietveld-) Verfeinerung wie TOPAS implementiert.^[117,118]

4.2 Totalstreumethoden

In der Röntgendiffraktometrie werden die Bragg-Reflexe analysiert, um ein möglichst detailliertes Verständnis über die kristalline Struktur eines Materials zu erlangen. Diese Struktur stellt eine global gemittelte ideale Kristallstruktur dar. Die im Untergrund eines Pulverdiffraktogramms auftretende diffuse Streuung (Abbildung 10), spiegelt die lokale Struktur und damit die Abweichung von der perfekten gemittelten Kristallstruktur wider. Um Informationen über die lokale Struktur (nicht nur von kristallinen Verbindungen) zu erhalten, wurden Totalstreumethoden entwickelt, aus denen eine radiale Paarverteilungsfunktion ermittelt werden kann (pair distribution function, PDF).^[119] Die Experimente sind den klassischen Röntgenbeugungsexperimenten sehr ähnlich. Allerdings ist es nötig, bis zu sehr hohen Q Werten ($= \frac{4\pi \sin\theta}{\lambda}$) zu messen, um eine hohe Auflösung im direkten Raum zu ermöglichen. Dazu ist es nötig, Diffraktogramme mit hochenergetischer Strahlung

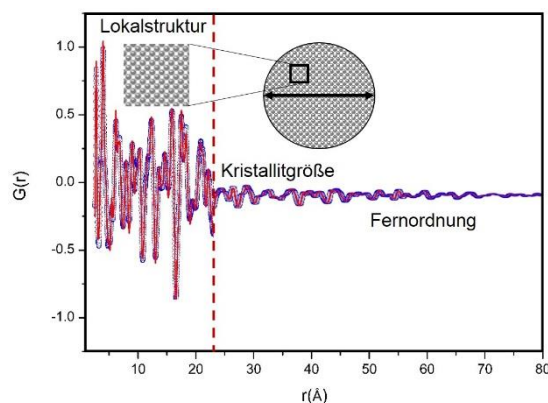


Abbildung 12: Schematische Darstellung einer radialen Paarverteilungsfunktion eines Nanokristallits.

(Synchrotronstrahlung) oder Neutronen zu messen. Die gesamten Streudaten (Bragg plus diffuse Streuung) beinhalten auch die Streu-Information des Probenträgers (z.B. Kapillare), welche von den Gesamtdaten subtrahiert werden muss. Die nach Reduzierung und Normalisierung erhaltene Totalstreu-Strukturfunktion $S(Q)$ wird anschließend fouriertransformiert:

$$G(r) = \frac{2}{\pi} \int_0^{\infty} Q[S(Q) - 1] \sin Q(r) dQ \quad (4)$$

Q ist der Betrag des Streuvektors. Die dadurch erhaltene PDF, $G(r)$, stellt die Wahrscheinlichkeit dar, im direkten Raum (im Gegensatz zum reziproken Fourier Raum der klassischen Beugungsmethoden) ein anderes Atom im Abstand r zu finden. Die Position der Peaks wird durch die Atom-Atom-Abstände bestimmt, während der Abfall der Funktion, $Q(r)$, die kristalline Korrelationslänge (Kristallitgröße) und die Instrumentenfunktion enthält. Letztere kann durch Messen eines kristallinen Standardmaterials bestimmt werden. Eine Paarverteilungsfunktion ist in Abbildung 12 exemplarisch für ein nanokristallines Material dargestellt. Ursprünglich wurde PDF bei der Untersuchung von Flüssigkeiten und amorphen Materialien eingesetzt.^[120] In der Literatur ist sehr gut dokumentiert, dass die lokale Struktur

eines Materials und damit die Abweichung von der ‚perfekten‘ Kristallinität die Eigenschaften entscheidend beeinflusst.^[121–126]

C Kumulativer Hauptteil

1. Veröffentlichungen Bi_2Te_3 – Sb_2Te_3

1.1 Sputtered n-type $\text{Bi}_2\text{Te}_3/(\text{Bi,Sb})_2\text{Te}_3$ superlattice systems

Mit dem Nanoalloying-Verfahren wurden gesputterte $\text{Bi}_2\text{Te}_3/(\text{Bi}_{0.9}\text{Sb}_{0.1})\text{Te}_3$ Übergitter mit Schichtdicken von jeweils 25 nm synthetisiert. Beim Nanoalloying werden wenige Nanometer dicke elementare Schichten auf Substraten (z.B. Si/SiO_2) abgeschieden (Abbildung 13). Im anschließenden Heizschritt interdiffundieren die Elemente und bilden kristalline Verbindungen.

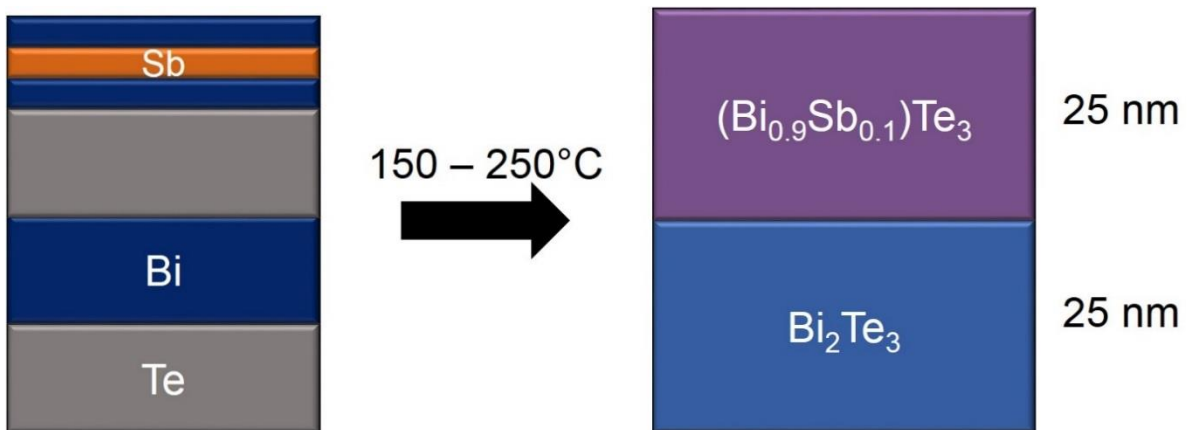


Abbildung 13: Schematisch dargestelltes Prinzip des Nanoalloyings.

Die Dünnschichten wurden in Abhängigkeit vom Antimon-Gehalt auf ihre thermoelektrischen Eigenschaften untersucht. Da ein erhöhter Sb-Gehalt eine p-Leitung generiert, wurden geringe Anteile (0.05, 0.1, 0.2) gewählt. Bereits 20% Antimon führten zu signifikant erniedrigter Ladungsträgerkonzentration, was auf eine Kompensation der Elektronen durch beginnende „Löcherbildung“ zurückzuführen ist. Für den Gehalt von 10% Sb konnte der optimale Powerfaktor erhalten werden. Der Einfluss der Temperatur (150 – 250°C) auf die Struktur und Transporteigenschaften wurde ebenfalls untersucht. Nur bei der Probe, die bei 150°C getempert wurde, konnte das Übergitter im Rasterelektronenmikroskop (REM) erkannt werden, d.h. bei höheren Temperaturen findet zunehmende Interdiffusion der Konstituenten statt und das Übergitter verschwindet. Die Röntgendiffraktogramme der polykristallinen Filme zeigten eine deutliche (00 l) Textur. Rietveld Verfeinerung ergab nicht nur eine Zunahme der Kristallitgröße mit der Temperatur, sondern die Rauigkeit der Filme nahm ebenfalls stetig zu. Diese Rauigkeit ist typisch für Bi reiche $(\text{Bi}_{1-x}\text{Sb}_x)_2\text{Te}_3$ Dünnschichten. Der Powerfaktor betrug (je nach Dauer des Temperns) 20 – 22 $\mu\text{W}/\text{cmK}^2$, was zu den besten Werten für n-typ Bi_2Te_3 gehört. Die Untersuchung der thermischen Leitfähigkeit ergab zwar eine deutliche Verringerung im Vergleich zum Volumenmaterial, jedoch lag diese im Rahmen für homogene nanokristalline Systeme (0.53 – 0.79 W/mK). Dies zeigt, dass es zu keiner direkten Kumulation von Phononenstreuungseffekten (Nanokristallinität + Übergitter) in diesem System kommt.

Dennoch weisen die gesputterten $\text{Bi}_2\text{Te}_3/(\text{Bi}_{0.9}\text{Sb}_{0.1})\text{Te}_3$ Übergitter sehr gute thermoelektrische Eigenschaften auf, die mit Selen substituierten Bi_2Te_3 basierten Dünnschichten konkurrieren können. Die Se-haltigen Filme sind jedoch deutlich aufwändiger herzustellen.

Reprinted with permission from M. Winkler, X. Liu, A.-L. Hansen, J. D. König, W. Bensch, L. Kienle, H. Böttner, K. Bartholomé, *Nanothermoelectrics* **2013**, 1, 1–9. Copyright 2013 De Gruyter.

Sputtered n-type $\text{Bi}_2\text{Te}_3 / (\text{Bi,Sb})_2\text{Te}_3$ superlattice systems

Abstract

In this work, we report on n-type nanostructured layers of Bi_2Te_3 , $(\text{Bi}_{1-x}\text{Sb}_x)_2\text{Te}_3$ and layered $\text{Bi}_2\text{Te}_3/(\text{Bi}_{1-x}\text{Sb}_x)_2\text{Te}_3$ superlattices fabricated by nanoalloying. Our approach is based on the sequential sputtering of nanoscale layers of the elements and subsequent annealing in order to induce a solid state reaction. While conventionally $\text{Bi}_2(\text{Se}_x\text{Te}_{1-x})_3$ compounds are used as n-type V_2VI_3 material system, the deposition of Se proves to be problematic especially for sputtering deposition and is therefore replaced by $(\text{Bi}_{1-x}\text{Sb}_x)_2\text{Te}_3$. A superlattice consisting of 25 nm $\text{Bi}_2\text{Te}_3/25$ nm $(\text{Bi}_{0.9}\text{Sb}_{0.1})_2\text{Te}_3$ – ML (periodicity of 50 nm) was synthesized and annealed at temperatures of 150, 200, 225, and 250°C. The layers are slightly rough and polycrystalline, and the grain sizes increase with increasing annealing temperature. The XRD analysis shows a pronounced (00l) texture of the sputtered layers. SIMS depth profiles reveal that the chemical separation into layers is present, yet smeared out to some degree after annealing at 200°C.

High Seebeck coefficients of up to ~ -190 $\mu\text{V/K}$ were achieved. A high maximum power factor of 22 $\mu\text{W/cmK}^2$ can be attained after annealing at 250 °C for 12 h. The superlattice system $\text{Bi}_2\text{Te}_3 / (\text{Bi}_{1-x}\text{Sb}_x)_2\text{Te}_3$ can compete with $\text{Bi}_2\text{Te}_3 / \text{Bi}_2(\text{Se}_x\text{Te}_{1-x})_3$ in terms of electrical properties while representing a good practical alternative for the sputter deposition due to the substitution of problematic Se with Sb. Cross-plane thermal conductivities are in the range of 0.55 to 0.6 W/mK. The thermal conductivity is generally reduced due to the nanocrystallinity of the material, however, there seems to be no measurable reduction of the thermal conductivity by the superlattice-type 2D nanostructuring.

Keywords

PACS:

© 2013 M. Winkler et al., licensee Versita Sp. z o. o.
This work is licensed under the Creative Commons Attribution-NonCommercial-NoDerivs license (<http://creativecommons.org/licenses/by-nc-nd/3.0/>), which means that the text may be used for non-commercial purposes, provided credit is given to the author.

M. Winkler¹, X. Liu², A.-L. Hansen², J. D. König¹,
W. Bensch², L. Kienle³, H. Böttner¹, K. Bartholomé¹

¹ Fraunhofer Institute for Physical Measurement Techniques (IPM),
Heidenhofstr. 8, D-79110 Freiburg, Germany

² Institute of Inorganic Chemistry, Christian-Albrechts-University
Kiel, Max-Eyth-Str. 2, D-24118 Kiel, Germany

³ Institute for Materials Science, Christian-Albrechts-University Kiel,
Kaiserstr. 2, D-24143 Kiel, Germany

Received 20 June 2013

Accepted 17 August 2013

1. Introduction

Already known for several decades, the material system $(\text{Bi/Sb})_2(\text{Se/Te})_3$ still remains unrivalled in terms of thermoelectric efficiency around room temperature. Sputtering this V-VI material on non lattice-matched substrates (Si/SiO_2 wafers) has been proven as a suitable [1] and less costly deposition method compared to other methods such as Metal-Organic Chemical Vapor Deposition (MOCVD). It is well known from theory that thermoelectric device performance can be enhanced significantly by

nanostructuring [2]. The state of the art in fabrication, characterization, and theoretical modelling of nanolayered and superlattice $(\text{Bi/Sb})_2(\text{Se/Te})_3$ – based thin films was recently reviewed in [3]. Among the most prominent experimental results are the outstanding ZT values of ~ 2.4 and ~ 1.7 that were reported for p/n-type V_2VI_3 -superlattices (SL) created by MOCVD [4]. Compared to bulk materials, the enhanced ZT values were achieved by reducing the thermal conductivity without significantly impairing the electrical properties. Therefore, a sputter process to cre-

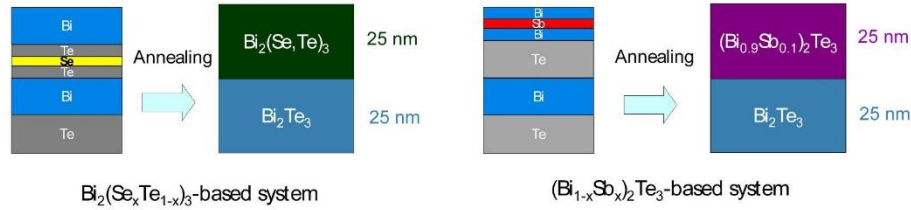


Fig 1. Left: $\text{Bi}_2(\text{Te}_{1-x}\text{Se}_x)_3$ – based SL system examined in [5]. Right: n-type $(\text{Bi}_{1-x}\text{Sb}_x)_2\text{Te}_3$ – based system examined in this work. The pattern was repeated 30 times to give a total thin film thickness of $\sim 1.5 \mu\text{m}$.

ate similar SLs for the cost-effective mass production of miniaturized thermoelectric devices would be very useful. One way to create SLs and nanostructured layers in general, is a process called nanoalloying, i.e. sequential deposition of element layers with thicknesses in the nm range on a cold substrate. The thicknesses of the adjacent layers can be adjusted to the desired stoichiometric ratio (here, 40 at% Bi/Sb, 60 at% Te). Subsequently the material is subjected to a low-temperature (typically $\sim 150 - 300^\circ\text{C}$) annealing process, in which the compound formation takes place in a solid state reaction [15, 18]. Böttner et al. have shown that the nanoalloying process can be applied to create n-type $\text{Bi}_2\text{Te}_3/\text{Bi}_2(\text{Se}_x\text{Te}_{1-x})_3$ – SLs by sputtering [5]. The thin films were strongly oriented along the *c*-axis and showed power factors of around $20 \mu\text{W}/\text{cmK}^2$. However, sputtering of Se can cause several practical problems due to its low melting point, low thermal / electrical conductivity and very high vapour pressure. Se deposition is also known to be problematic in thermal evaporation methods since Se forms Se_x ($x \geq 2$) molecules during evaporation with poor chemical reactivity, necessitating the use of a cost-intensive cracker cell [6].

For these reasons, an alternative n-type SL system has been developed where the $\text{Bi}_2(\text{Se}_x\text{Te}_{1-x})_3$ layer was replaced with n-type $(\text{Bi}_{1-x}\text{Sb}_x)_2\text{Te}_3$. Figure 1 shows the two layer systems in comparison.

There are hardly any reports on Bi-rich n-type $(\text{Bi}_{1-x}\text{Sb}_x)_2\text{Te}_3$ solid solutions since better figures of merit have been achieved by alloying Bi_2Te_3 with small amounts of Bi_2Se_3 , leading to the establishment of $\text{Bi}_2(\text{Te}_{1-x}\text{Se}_x)_3$ solutions as standard n-type material for thermoelectric applications. However, it was stated by Scherrer et al. that under certain conditions the use of $(\text{Bi}_{1-x}\text{Sb}_x)_2\text{Te}_3$ instead of $\text{Bi}_2(\text{Te}_{1-x}\text{Se}_x)_3$ based solutions may be advantageous due to various problems with accurately adjusting small Se concentrations and achieving homogeneity [7]. In the corresponding work, $(\text{Bi}_{1-x}\text{Sb}_x)_2\text{Te}_3$ with varying *x* was fabricated by mechanical alloying and it was found that the alloys were n-conducting if the Sb_2Te_3 content was below 50 wt%. Carrier concentrations in the favor-

able range of 10^{19}cm^{-3} were observed for the n-type materials, demonstrating their potential for thermoelectric applications. Furthermore, the maximum ZT of 0.69 reported by Champness et al. for $(\text{Bi}_{0.875}\text{Sb}_{0.125})_2\text{Te}_3$ [8] is not much smaller than that of the best Se-based materials $\text{Bi}_2(\text{Te}_{0.975}\text{Se}_{0.025})_3$ and $\text{Bi}_2(\text{Te}_{0.95}\text{Se}_{0.05})_3$ with a ZT of 0.87 [9].

2. Experimental Procedures

For the SLs, the deposition sequence depicted in Fig. 1 for the $(\text{Bi}_{1-x}\text{Sb}_x)_2\text{Te}_3$ – based system was used, forming a 25 nm $\text{Bi}_2\text{Te}_3/25 \text{nm } (\text{Bi}_{0.9}\text{Sb}_{0.1})_2\text{Te}_3$ stack after annealing. 30 periods of this pattern with 50 nm period length were deposited, giving a nominal, total thin film thickness of $1.5 \mu\text{m}$. During annealing, an interdiffusion between Bi and Sb is unavoidable, and thus a “softening” of the $\text{Bi}_2\text{Te}_3/(\text{Bi}_{1-x}\text{Sb}_x)_2\text{Te}_3$ boundaries occurs, giving the thin films the characteristics of “soft superlattices”. Additionally, Bi_2Te_3 and $(\text{Bi}_{0.9}\text{Sb}_{0.1})_2\text{Te}_3$ were each deposited according to the lower and upper half of the deposition pattern shown in Fig. 1 (right) and examined separately. All element layers were sputtered using the system MS150x4 from “FHR Anlagenbau”, Germany. The layers were deposited from Bi, Te, and Sb targets with a purity of 99.99 at% (metal basis). 4” Si/SiO₂-wafers (thermal oxide thickness of 100 nm) were used as substrates. The thermal treatment was conducted in a self-developed annealing system. During the annealing, the samples were kept in a closed quartz ampoule under vacuum with additional Te as source material in order to yield a Te-rich atmosphere in the ampoule, thus avoiding Te evaporation from the samples.

The electrical characterization was carried out in-plane at room temperature. The electrical conductivity, charge carrier mobility and charge carrier concentration were measured by Hall-effect measurements using the Van-der-Pauw method with a measurement uncertainty for the conductivity of $\sim 5 \%$ and $\sim 10 \%$ for charge carrier mobility and concentration. The Seebeck coefficient was measured

via a self-constructed calibrated setup (Ni reference) with a measurement uncertainty of $\sim 5\%$. The cross-plane thermal conductivity at room temperature was measured with a Time Domain Thermal Reflectance (TDTR) measurement system [10] calibrated with a Si/SiO_2 standard. The total measurement uncertainty is typically around 10 % for smooth samples and higher for rough samples such as examined in this work, i.e. 11 – 20 % depending on sample roughness. The total incident laser power was 26 mW while the modulation frequency of the pump beam was 10.7 MHz. Three measurements were carried out for each sample and averaged.

The cross-sectional SEM images on cleaved samples were recorded with a S4700 and SU70 SEM from Hitachi, mixing secondary electron (SE) and backscattered electron (BSE) signals if not indicated otherwise. For imaging the cross-section of the as-grown film, an additional ring-shaped, high-Z sensitive BSE detector was used. The film thickness was determined on the cross sections acquired using fast-scan mode with an uncertainty of $\sim 5\%$. The element concentrations were determined by an EDAX EDX (energy dispersive X-ray) system. The measurement was carried out on at least three points on the sample. The X-ray diffraction (XRD) patterns were collected at room temperature on a Bragg-Brentano geometry diffractometer (Stoe Stadi-P Diffractometer) equipped with a Cu sealed tube and a curved $\text{Ce}(111)$ monochromator providing $\text{CuK}\alpha_1$ radiation and a 1 mm slit before the detector. The measurements were performed in the 2θ range of $5 - 140^\circ$ with a step width of 0.03° in $\theta/2\theta$ scans. Rietveld analysis was carried out using the program TOPAS-Academics [11]. All data could be fitted to a rhombohedral unit cell with the space group R-3m [12]. The March Dollase Model [13] has been used to refine the strongly preferred orientation (*c*-texture). The effect of the surface roughness has been corrected using an approach by Suortti [14].

The secondary ion mass spectrometry (SIMS) depth profiles were recorded using 5 keV Cs^+ primary ions at an impinging angle of 45° and detecting secondary ions of MCs^+ (with $M = \text{Bi, Sb, Te}$).

3. Results and Discussion

3.1. Optimizing the Sb-content in $(\text{Bi,Sb})_2\text{Te}_3$

The optimal Sb-content in $(\text{Bi}_{1-x}\text{Sb}_x)_2\text{Te}_3$ for the SL films had to be determined. According to work on bulk materials, the reduction of thermal conductivity is expected to be more pronounced for higher Sb-contents. On the other hand, $(\text{Bi}_{1-x}\text{Sb}_x)_2\text{Te}_3$ bulk samples tend towards p-type conduction for higher Sb contents x . However, it had previously been found that the defect chemistry and transport

properties of $(\text{Bi}_{1-x}\text{Sb}_x)_2\text{Te}_3$ thin films differ remarkably from that of bulk materials [15], so that previous results from bulk materials could not be transferred to thin films. To determine the optimum Sb content, we restricted our synthesis and characterization to three nanoalloyed homogeneous films of $(\text{Bi}_{1-x}\text{Sb}_x)_2\text{Te}_3$ with $x = 0.05, 0.1, 0.2$. The electrical transport properties, Seebeck coefficient S , carrier mobility μ and carrier concentration n in dependence on Sb content x are given in Fig. 2. The measurement of the element concentrations by EDX proved to be problematic since there is a strong overlap of the Sb and Te peaks in the spectrum and no element calibration standard was available for low Sb concentrations. Therefore, the Sb fraction was extrapolated from experiments with EDX concentration measurements with solid solutions of Sb+Bi. The determined Te content of the films ranged between 59.4 and 60 at%.

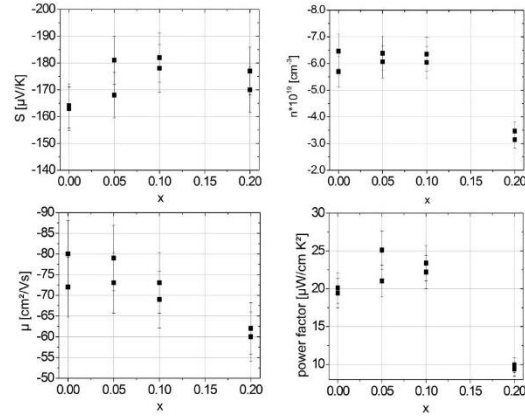


Fig 2. Electrical properties of $(\text{Bi}_{1-x}\text{Sb}_x)_2\text{Te}_3$ in dependence on Sb content x after annealing for 2 hours at 250°C . To verify reproducibility and consistency of the results, two samples from each growth run were analyzed.

Compared to the bulk material, the carrier mobility for the examined material compositions close to Bi_2Te_3 is significantly lower. The inferiority of μ compared to bulk material was already observed for binary nanoalloyed Bi_2Te_3 films grown with an MBE setup [15]. Compared to these, the Bi_2Te_3 films shown here display similar μ . The decrease in charge carrier mobility with increasing Sb content can be explained by alloy scattering of the charge carriers. The decrease of mobility does not exactly follow the linear trend reported for bulk materials [16]. Interestingly, for $x = 0.05$ and 0.10 , the Seebeck coefficient increases slightly (in conformance with [8]) while the charge carrier concentration remains constant, yielding an increased PF. For $x = 0.2$, there is a sharp drop in n while S remains constant which may be explained by the intro-

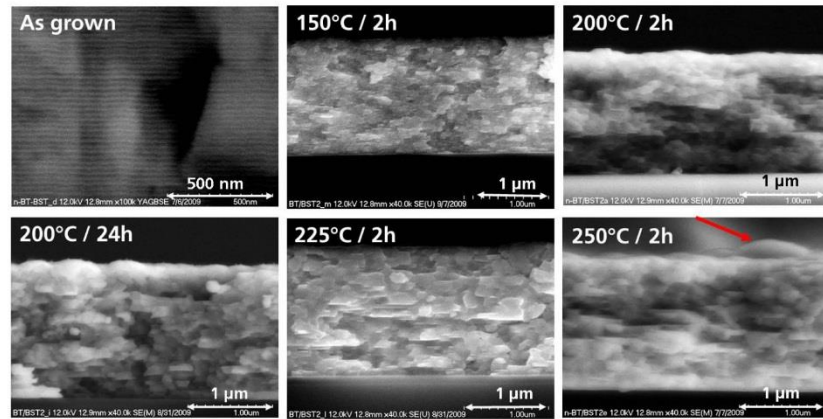


Fig 3. SEM cross-sections of $\text{Bi}_2\text{Te}_3/(\text{Bi}_{1-x}\text{Sb}_x)_2\text{Te}_3$ SLs in as-grown and annealed state. The ss grown image is a back scattered electron image. Images for 150°C and 225°C are shown as secondary electron image for a better resolution of the individual grains and for demonstration of grain growth. The grain size increases with annealing temperature and starting at 250°C, the film roughness increases significantly, i.e. additional flat and large hill-like structures appear (red arrow).

duction of first holes as charge carriers with larger Sb contents that compensate with the electrons. As a consequence of the lower charge carrier concentration, the power factor drops significantly.

Obviously, a Sb content of $x = 0.1$ offers the best compromise between sufficiently high element contrast and good electrical properties. Thus, $(\text{Bi}_{0.9}\text{Sb}_{0.1})_2\text{Te}_3$ was used in the SL systems.

3.2. $\text{Bi}_2\text{Te}_3/(\text{Bi}_{1-x}\text{Sb}_x)_2\text{Te}_3$ – SL systems

3.2.1. Structural characterization

The $\text{Bi}_2\text{Te}_3 / (\text{Bi}_{0.9}\text{Sb}_{0.1})_2\text{Te}_3$ SLs were annealed at 150, 200, 225, and 250°C for 2 hours. The determined Te contents of the annealed films ranged from $\sim 59.1 - 60.3$ at%. This measurement is not completely reliable due to Sb and Te peak overlap in EDX and the absence of an appropriate calibration standard with similar matrix properties. Lateral homogeneity was verified by the small difference of measured Te contents. In most cases, the maximum deviation for different points on the samples was below 0.6 at% (corresponding to the measurement uncertainty of the EDX setup) and reached ~ 1 at% in a few exceptional cases, which could be attributed to sample roughness effects. SEM cross-sections of the as-grown and annealed films are shown in Fig. 3. The thin films become slightly rough during sputtering, covered with spherical bumps with a diameter of ~ 500 nm and a height of ~ 100 nm. These bumps gradually appear in Bi-rich layer systems after the total thin film thickness exceeds ca. 800 nm. The appearance of the bumps is due to the roughness of sputtered Bi as also observed by other authors [17]. Dur-

ing deposition, the roughness caused by Bi gradually adds up and leads to a roughening of the total layer system. In the as-grown state, BSE imaging clearly reveals the multilayered structure with a spacing of 25 nm for the Bi-rich areas and a period length of 50 nm as intended (Fig. 3, top left). After annealing, platelet-like grains appeared which are preferably aligned parallel to each other. Such morphology was found as a characteristic feature on similar p-type nanoalloyed films [18] demonstrating a strong *c*-axis orientation of the films. The grain sizes increase with annealing temperature. At an annealing temperature of several 100 °C, additional hill-like structures with a height of several 100 nm begin to appear that mark the onset of recrystallization processes due to increasing bulk diffusion. A further increase of annealing temperature would lead to very rough thin films with holes, unsuitable for device fabrication. This degradation of thin film morphology was observed in a homogenous thin film of $(\text{Bi}_{0.9}\text{Sb}_{0.1})_2\text{Te}_3$ that was annealed at 300°C (not shown here).

Figure 4 shows XRD patterns for the as-grown and three annealed samples of this study. Already for the as-grown sample broad reflections of the compound phase can be observed. Additional broad reflections arise from amorphous or not fully crystallized material. For the annealed samples, pronounced reflections of the (00*l*) type beside weak (*hkl*) reflections are detected. This result indicates the formation of thin films with highly *c*-oriented crystallites. The sharpening and increasing intensity of the (00*l*) reflections with increasing annealing temperature indicates larger grain sizes in agreement with the SEM images.

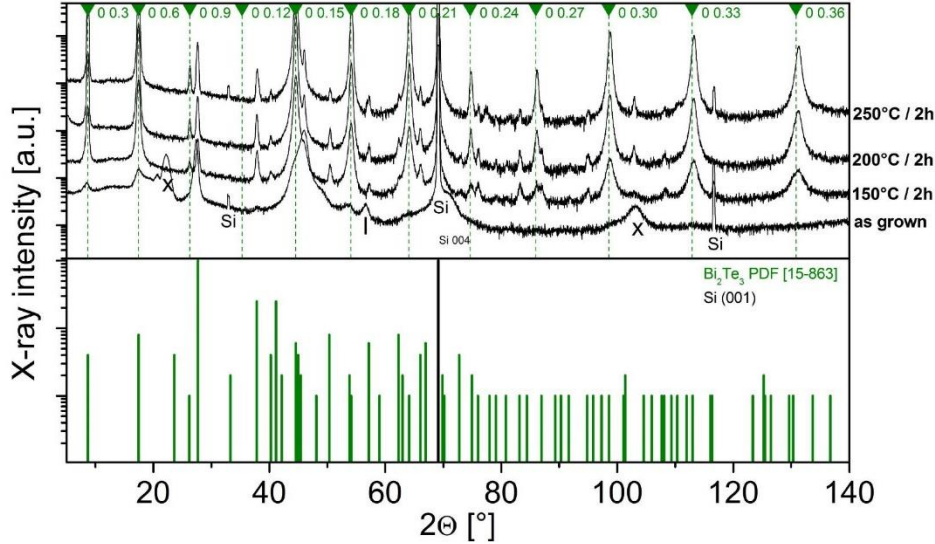


Fig 4. $\theta - 2\theta$ scan of $\text{Bi}_2\text{Te}_3/(\text{Bi}_{1-x}\text{Sb}_x)_2\text{Te}_3$ – SLs annealed for 2 h at different temperatures, logarithmic intensity scaling. From top to bottom: 250, 200, 150°C, and as grown. (00l) – reflections of Bi_2Te_3 are indicated by dashed lines. For comparison, a powder diffractogram (JCPDS database) is shown as vertical bars below the experimental patterns.

Rietveld analysis was carried out on the XRD patterns recorded for the samples annealed at 150, 200, and 250°C. The results are given in Fig. 4.

Table 1. Structural parameters obtained from Rietveld analysis on the XRD shown in Figure 4.

annealing temperature	lattice parameters		average crystallite size L [nm]
	a, b (Å)	c (Å)	
150°C	4.3718 (18)	30.4809 (10)	38
200°C	4.3842 (31)	30.4789 (10)	86
250°C	4.3890 (83)	30.4646 (10)	124

The characterization of the nanostructuring via SIMS depth profiling proved to be difficult since the thin films exhibited considerable roughness as mentioned above and consequently, the mass spectrometer signals for the different ions were noisy. For the SIMS analysis, a modified layer system was deposited where the sequence of the metal/chalcogen layers was inverted so that the thin film growth started with Bi instead of Te. The films deposited with the inverted deposition pattern exhibited less roughness, allowing a better evaluation of the nanostructuring. However, XRD patterns showed that there was a much

less defined c -axis orientation than for the original sequence, so the SIMS profiles (Sb ion signals), shown in Tab. 1, give only a lower limit for the thermal stability of the nanostructure. After annealing at 250°C, there is no clear proof that a nanostructure is still present. At 200°C, the thin film definitely shows a chemical segregation of Sb, and therefore the stability of the SLs is considered to be stable up to that temperature.

Overall, the chemical segregation appears significantly less defined than for similarly grown, nanoalloyed sputtered p-type $\text{Sb}_2\text{Te}_3/(\text{Bi}_{0.2}\text{Sb}_{0.8})_2\text{Te}_3$ SL films [18] and was not observed throughout the whole film. SEM images of the SIMS crater support this assumption as shown in Fig. 5. At 150 °C annealing temperatures, only a very faint indication of the SL structure was observed, while the SL was clearly observed in the p-type films annealed at 250°C. We assume that this is predominantly a consequence of the lower degree of c -texture compared to the p-type samples since diffusion coefficients in Bi_2Te_3 -related materials parallel to the c -axis are orders of magnitude lower than perpendicular to it [19]. It is also possible that the diffusion coefficient of Sb in Bi_2Te_3 is higher than that of Bi in Sb_2Te_3 , however due to a lack of literature data on this subject this cannot be verified.

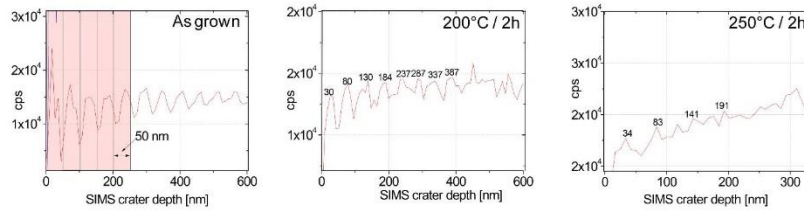


Fig 5. SIMS depth profiles of $\text{Bi}_2\text{Te}_3/(\text{Bi}_{1-x}\text{Sb}_x)_2\text{Te}_3$ - SLs with modified stacking sequence annealed for 2 h at different temperatures. The Sb ion signal is plotted versus the crater depth. Numbers indicate the peak positions. The spacing between the peaks corresponds to a SL period length of 50 nm.

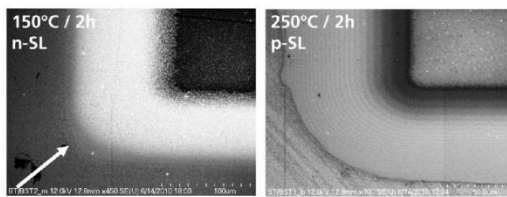


Fig 6. SEM images of SIMS craters of n-type $\text{Bi}_2\text{Te}_3/(\text{Bi}_{0.95}\text{Sb}_{0.05})_2\text{Te}_3$ and p-type $\text{Sb}_2\text{Te}_3/(\text{Bi}_{0.2}\text{Sb}_{0.8})_2\text{Te}_3$ SLs [18]. In spite of the lower annealing temperature, the nanostructure in the n-type SL (only traces visible, see white arrow) appears only weakly expressed in comparison to the p-type SL.

3.3. Transport properties

In Fig. 6, the electrical properties of the SLs are shown and compared to the results of the mentioned $\text{Bi}_2\text{Te}_3/\text{Bi}_2(\text{Se},\text{Te})_3$ - SLs [5]. The dependence on annealing temperature is analogous to these films and also the p-type nanoalloyed SL [18]. The as-grown film displays metallic characteristics (low S and μ , high n) due to the presence of pure Bi layers (see XRD patterns). With increasing grain size, μ improves for higher annealing temperatures and S follows a parabolic trend. The charge carrier concentration and Seebeck coefficient remain at similar values for the thin films shown in this work. A high maximum Seebeck of $\sim -190 \mu\text{V}/\text{K}$ was achieved.

3.4. Power factor and thermal conductivity

Generally, a longer annealing time leads to a higher power factor as seen in Fig. 7. With an annealing time of 2 h, power factors of $\sim 20 \mu\text{W}/\text{cmK}^2$ can be attained. Increasing the annealing time to 12 h leads to another small increase in the power factor up to $22 \mu\text{W}/\text{cmK}^2$. This is among the highest values reported for n-conducting Bi_2Te_3 -based sputtered thin films (see e.g. [17, 20]); however, the texture of the deposited material also has to be taken into account when comparing different values.

Another important point is that the SL system $\text{Bi}_2\text{Te}_3/(\text{Bi}_{1-x}\text{Sb}_x)_2\text{Te}_3$ can compete with similarly textured $\text{Bi}_2\text{Te}_3/\text{Bi}_2(\text{Se},\text{Te})_3$ SLs in terms of electrical properties while being significantly easier to sputter due to the substitution of problematic Se by Sb.

The cross-plane thermal conductivity at room temperature was determined with the TDTR method in dependence of the annealing temperature, Fig. 7. The lattice thermal conductivity λ_l was estimated from the total thermal conductivity λ by subtracting the electronic part of thermal conductivity. This was done by 1) using the Lorentz number from a numerical calculation based on Boltzmann transport theory for parabolic single bands, one-band conduction, and acoustic scattering (scattering parameter = $-1/2$) as given in Ref. [21] with an effective density of states mass of $0.58 \cdot \text{electron mass}$ [22] and 2) estimating the electrical cross-plane conductivity σ_{cross} from the in-plane conductivity σ by assuming a conductivity anisotropy factor $\sigma_{\text{cross}}/\sigma$ of 0.2 (value of bulk Bi_2Te_3 [9]). The homogenous films whose data is shown in Fig. 7 were prepared with the Bi_2Te_3 and $(\text{Bi}_{1-x}\text{Sb}_x)_2\text{Te}_3$ partial pattern from the SL deposition pattern.

Single crystalline bulk Bi_2Te_3 with similar composition exhibits a thermal conductivity of about $1 \text{ W}/\text{mK}$ along the c -axis [9]. Noteworthy, the cross-plane thermal conductivity of the strongly c -axis oriented homogenous thin film of Bi_2Te_3 is significantly lower. This reduction is due to the polycrystalline nature of the material. In previous works, a smaller grain size also was found to correlate with a lower value for the thermal conductivity [23, 24] λ of $0.55 - 0.75 \text{ W}/\text{mK}$ for polycrystalline Bi_2Te_3 with a grain size from $30 - 100 \text{ nm}$ were reported in agreement with the value for Bi_2Te_3 measured here.

As can be seen in Fig. 7, λ and λ_l of the SL across all annealing temperatures are not lower than the average thermal conductivities of comparable homogenous compounds Bi_2Te_3 and $(\text{Bi}_{0.95}\text{Sb}_{0.05})_2\text{Te}_3$. Remarkably, there is also no minimum in λ and λ_l at $150 \text{ }^\circ\text{C}$ where the SL is still relatively well preserved. The lattice thermal conductivities

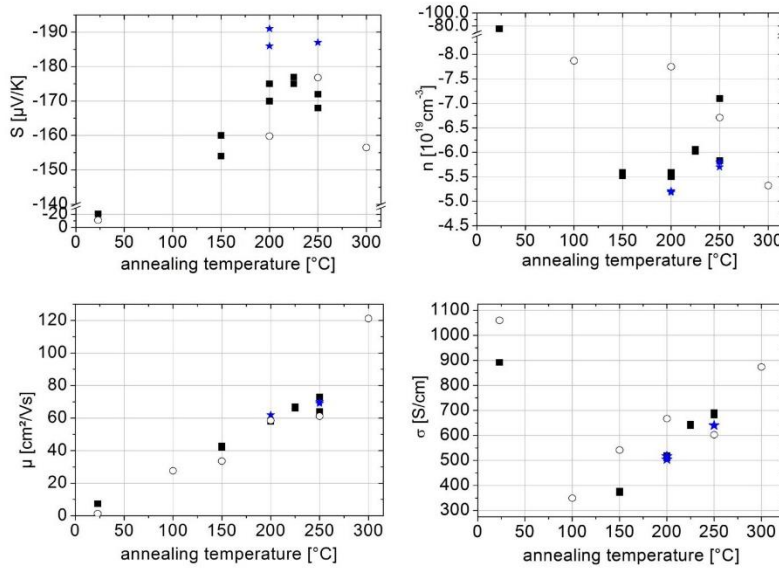


Fig 7. Electrical transport properties of $\text{Bi}_2\text{Te}_3/(\text{Bi}_{1-x}\text{Sb}_x)_2\text{Te}_3$ – SLs annealed at different temperatures. Full squares: Thin films from this work, annealed for 2 h. Blue stars: Thin films from this work, annealed for 12 h (250 °C) and 24 h (200 °C). Black empty circles: Data for comparison, $\text{Bi}_2\text{Te}_3/\text{Bi}_2(\text{Se,Te})_3$ – SLs [5] with a similar period length of 45 nm, annealed for 2 h. Note the broken axis in the top graphs. Error bars omitted for clarity.

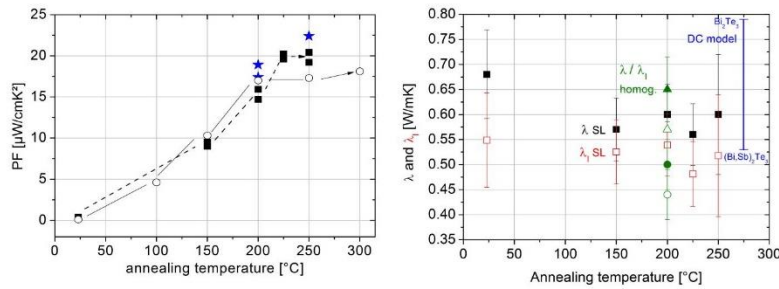


Fig 8. Left: PF of $\text{Bi}_2\text{Te}_3/(\text{Bi}_{0.9}\text{Sb}_{0.1})_2\text{Te}_3$ – SLs versus annealing temperature. Symbols analogous to Fig. 6. Right: Cross-plane total and lattice thermal conductivity λ and λ_l as function of annealing temperature. Black full squares: SL, 2 h annealing. Black star: SL, 24 h annealing (at 200°C, not visible since value is identical to the one after 2 h annealing). Green circle: Homogenous film of $(\text{Bi}_{0.95}\text{Sb}_{0.05})_2\text{Te}_3$. Green triangle: Homogenous film of Bi_2Te_3 . Blue bar: Range of λ_l as predicted by Debye-Callaway model [24] (see text). In all data sets all hollow data points indicate corresponding lattice thermal conductivities.

are also compared to values given by a Debye-Callaway model for homogenous films shown in [24] for Bi_2Te_3 and $(\text{Bi,Sb})_2\text{Te}_3$. For the application of the model, the grain sizes L of the films in this work were estimated from the Rietveld refinement (values given in Fig. 4). From the model, a lower boundary for λ_l of 0.53 W/mK is obtained for $(\text{Bi/Sb})_2\text{Te}_3$ with $L = 38$ nm and an upper boundary of 0.79 W/mK is obtained for Bi_2Te_3 with $L = 124$ nm. The $\text{Bi}_2\text{Te}_3/(\text{Bi}_{0.9}\text{Sb}_{0.1})_2\text{Te}_3$ – SLs are “weakly alloyed”

with low contents of Sb and fall between a binary and the modelled alloy. Thus, it is sensible to compare them according to the range given by each of these two λ_l . Evidently, the measured λ_l of the SL films are only slightly below this range, meaning that they are compatible to model predictions for homogenous films. A lower λ_l than anticipated from the model was also observed for homogenous $(\text{Bi/Sb})_2\text{Te}_3$ films in the reference.

In conclusion, the SL structure appears to have no measurable effect on the thermal conductivity, judging by the fact that 1) λ and λ_l of the SL at any annealing temperature are not lower than the average thermal conductivities of comparable homogenous compounds, 2) no minimum in the (lattice) thermal conductivity is apparent for the lowest annealing temperature and 3.) the data compares to the predictions of the Debye-Callaway model. This may seem puzzling at first glance since very pronounced effects on (lattice) thermal conductivity were previously reported for epitaxial $\text{Bi}_2\text{Te}_3/\text{Sb}_2\text{Te}_3$ SLs [25]. However, the situation is clearly different in the case of nanoalloyed, nanocrystalline SLs. As can be explained qualitatively, e.g. by Matthiessen's rule, multiple scattering effects are not directly cumulative and adding a weak multilayer-induced phonon scattering to significantly pronounced grain-boundary scattering (as is the case here) should not significantly influence the total relaxation time. A deeper analysis requires considering the particular effects of nanostructures on the phonon spectrum. A nanocrystalline structure (i.e. pronounced boundary scattering) leads to a cutoff of the low-frequency range of the phonon spectrum while the SL structure is believed to affect the low-frequency range, too [25, 26]. Thus, it can be concluded that qualitatively, the cutoff-effect on phonon frequencies, i.e. the reducing effect on thermal conductivity by adding a SL structure to an already nanocrystalline material, should not be very strong. If additionally the layered structure is "softened out" as demonstrated here, its cutoff-effect should be reduced even further. In contrast, a stronger reduction of λ was evidently possible for related p-type sputtered SLs where, in contrast to the n-type SLs, a low thermal conductivity was evident at 150°C that could likely be attributed to the more sharply defined SLs ([18], more details to be published).

4. Conclusion

In this work, sputtered n-type nanostructured layers of Bi_2Te_3 and $(\text{Bi}_{1-x}\text{Sb}_x)_2\text{Te}_3$ and layered $\text{Bi}_2\text{Te}_3/(\text{Bi}_{1-x}\text{Sb}_x)_2\text{Te}_3$ superlattices were fabricated by the nanoalloying method, i.e. nanoscale layers of the constituting elements were sequentially sputtered and subsequently annealed in order to induce a solid state reaction. It was found that $(\text{Bi}_{1-x}\text{Sb}_x)_2\text{Te}_3$ solid solutions proved to be good n-type thermoelectric materials for $x = 0.05$ and 0.1 and could possibly replace the commonly used $\text{Bi}_2(\text{Te}_{1-x}\text{Se}_x)_3$ compounds in cases where the deposition of Se is too costly or technically challenging. $\text{Bi}_2\text{Te}_3/(\text{Bi}_{1-x}\text{Sb}_x)_2\text{Te}_3$ SLs displayed high power factors and low thermal conductivities. However, the thermal conductivity reduction towards bulk materials can most likely be attributed to the polycrystalline

nature of the material and not to the artificial 2D layered nanostructuring.

Acknowledgements

The authors would like to thank T. Fuchs and M. Grimm (Fraunhofer IAF) for the SIMS depth profiles. Special thanks goes to D.G. Cahill, University of Illinois, for assembling the TDTR system and helping in interpreting and analyzing the TDTR data and advising in operating the TDTR measurement system. The authors thank the Deutsche Forschungsgesellschaft (DFG) for funding this work via SPP 1386 "Nanothermoelectrics". The authors thank the Bundesministerium für Bildung und Forschung for funding this work via the program frame "Werkstoffinnovationen für Industrie und Gesellschaft—WING" within the funding program "Nanochance", grant-number 03X4506B. All responsibilities for this publication lie with the authors.

References

- [1] H. Böttner, J. Nurnus, A. Gavrikov, G. Kühner, M. Jäggle, C. Künzel, D. Eberhard, G. Plescher, A. Schubert, K.-H. Schlereth, *J. Microelectromech. S.* 13, 2004, 414
- [2] M.S. Dresselhaus, G. Chen, M.Y. Tang, R. Yang, H. Lee, D. Wang, Z. Ren, J.-P. Fleurial, P. Gogna, *Adv. Mater.* 19, 2007, 1043
- [3] M. Winkler, X. Liu, U. Schürmann, J.D. König, L. Kienle, W. Bensch, H. Böttner, *Z. Anorg. Allg. Chem.* 638, 2012, 2441
- [4] R. Venkatasubramanian, E. Siivola, T. Colpitts, B. O'Quinn, *Nature* 413, 2001, 597
- [5] H. Böttner, A. Schubert, H. Kölbl, A. Gavrikov, A. Mahlke, J. Nurnus, *Proceedings 23rd International Conference on Thermoelectrics (2004, Adelaide, Australia)*, 114
- [6] L. Zhang, R. Hammond, M. Dolev, M. Liu, A. Palevski, A. Kapitulnik, *Appl. Phys. Lett.* 101, 2012, 153105
- [7] R. Martin-Lopez, H. Scherrer, *Solid State Commun.* 108, 1998, 285
- [8] C.H. Champness, P.T. Chiang, P. Parker, *Can. J. Phys.* 43, 1965, 653
- [9] H. Scherrer, S. Scherrer, *Bismuth Telluride, Antimony Telluride, and Their Solid Solutions*, In: *CRC Handbook of Thermoelectrics*, ed. D.M. Rowe, CRC press, Boca Raton, FL, 1995
- [10] D.G. Cahill, *Rev. Sci. Instr.* 75, 5119 (2004)
- [11] A. Coelho, *TOPAS-Academic, version 5 (Computer Software)*, Coelho Software, Brisbane, 2007
- [12] N.H. Abrikosov, V.F. Bankina, L.V. Poretzkaya, L.E.

- Shelimova, E.V. Skudnova, *Semiconducting II-VI, IV-VI, and V-VI Compounds*, Plenum Press, New York, 1969
- [13] W.A. Dollase, *J. Appl. Cryst.* 19, 1986, 267
- [14] P.J. Suortti, *Appl. Cryst.* 5, 1972, 325
- [15] M. Winkler, X. Liu, J. D. König, S. Buller, U. Schürmann, L. Kienle, W. Bensch, H. Böttner, *J. Mater. Chem.* 22, 2012, 11323
- [16] A.F. Joffe, L.S. Stil'bans, *Rep. Prog. Phys.* 22, 1959, 167
- [17] C.N. Liao, S.W. Kuo, *J. Vac. Sci. Technol. A* 23, 2005, 559
- [18] M. Winkler, X. Liu, J. D. König, L. Kirste, H. Böttner, W. Bensch, and L. Kienle, *J. Electron. Mater.* 41, 2012, 1322
- [19] H. Böttner, G. Chen, R. Venkatasubramanian, *MRS Bulletin* 31, 211 (2006)
- [20] H. Böttner, J. Nurnus, A. Gavrikov, G. Kühner, M. Jägle, C. Künzel, D. Eberhard, G. Plescher, A. Schubert, K.-H. Schlereth, *J. Microelectromech. S.* 13, 2004, 414
- [21] H. J. Goldsmid, *Thermoelectric refrigeration*, Plenum Press, New York, 1964, p.46
- [22] G.S. Nolas, J. Sharp, H.J. Goldsmid, *Thermoelectrics – Basic Principles and New Materials Developments*, Springer-Verlag, Berlin-Heidelberg, 200, p.118
- [23] M. Takashiri, S. Tanaka, K. Miyazaki, H. Tsukamoto, *J. Alloy Compd.* 490, 2010, 44
- [24] C. Chiritescu, C. Mortensen, D. G. Cahill, D. Johnson, and P. Zschack, *J. Appl. Phys.* 106, 2009, 073503
- [25] R. Venkatasubramanian, *Phys. Rev. B* 61, 2000, 3091
- [26] V. Narayanamurti, H.L. Störmer, M.A. Chin, A.C. Gosard, W. Wiegmann, *Phys. Rev. Lett.* 43, 1979, 2012

1.2 Synthesis and Thermal Instability of High-Quality Bi₂Te₃/Sb₂Te₃ Superlattice Thin Film Thermoelectrics

Durch Co-Evaporation wurden Bi₂Te₃/Sb₂Te₃ Übergitter epitaktisch auf BaF₂-Substraten abgeschieden. Die Wiederholeinheiten betragen 1 nm Bi₂Te₃ und 5 nm Sb₂Te₃. Mit dieser Art Übergitter wurden 2001 ZT Werte von 2.4 für n-typ und ~ 1.5 für p-typ Bi₂Te₃/(Bi_{1-x}Sb_x)Te₃ bei Raumtemperatur erreicht. Diese Werte konnten jedoch von keiner Arbeitsgruppe reproduziert werden. Zusätzlich war es auf Grund fehlender qualitativ hochwertiger Proben nicht möglich aufzuklären, wie sich diese nanostrukturierten Materialien bei erhöhten Temperaturen verhalten. Die Temperaturstabilität ist jedoch ein wesentlicher Aspekt, um die Langzeitstabilität von Thermoelektrika zu beurteilen. (111) orientierte BaF₂ Einkristalle haben einen geringen Gittermismatch mit Bi₂Te₃/Sb₂Te₃ und ermöglichten erstmals die Herstellung von Übergittern von außerordentlich guter Qualität. Röntgen- (XRD) sowie Elektronenbeugungsuntersuchungen im Transmissionselektronenmikroskop (TEM) konnten das Vorhandensein von Übergitterreflexen belegen. Gleichzeitig wurden nanoskalige Versetzungen der Schichten im TEM detektiert (Abbildung 14). Bei *in situ* Heizexperimenten stellte sich heraus, dass diese Versetzungen als Diffusionspfade dienen, welche die Durchmischung der Verbindungen parallel zu den Schichten erlauben. Bereits ab ~200°C nimmt die Intensität der Übergitterreflexe ab und es kristallisiert Sb_{1.66}Bi_{0.33}Te₃.

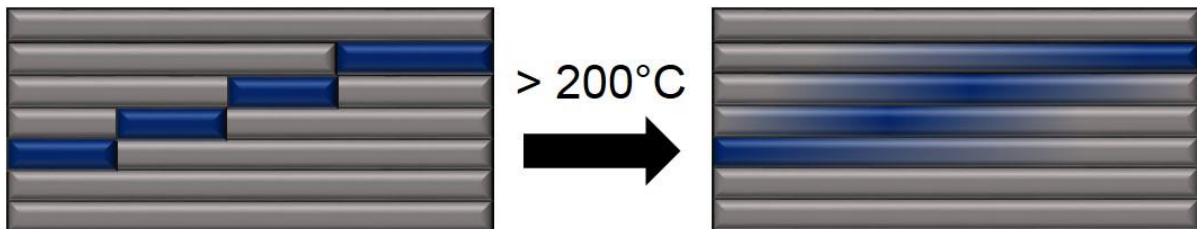


Abbildung 14: Schematische Darstellung der Interdiffusion von Bi₂Te₃ (blau) in die Sb₂Te₃ (grau) an Versetzungen des Übergitters oberhalb von 200°C.

Reprinted with permission from A.-L. Hansen, T. Dankwort, M. Winkler, J. Ditto, D. C. Johnson, J. D. König, K. Bartholomé, L. Kienle, W. Bensch, *Chem. Mater.* **2014**, 26, 6518–6522. Copyright 2014 American Chemical Society

Synthesis and Thermal Instability of High-Quality Bi₂Te₃/Sb₂Te₃ Superlattice Thin Film Thermoelectrics

Anna-Lena Hansen,^{†,‡} Torben Dankwort,^{‡,‡} Markus Winkler,[§] Jeffrey Ditto,^{||} Dave C. Johnson,^{||} Jan D. Koenig,[§] Kilian Bartholomé,[§] Lorenz Kienle,^{*,‡} and Wolfgang Bensch^{*,†}

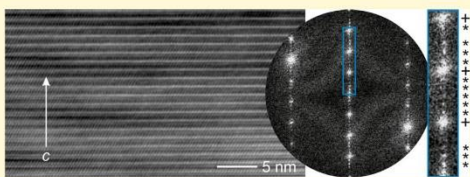
[†]Institute for Inorganic Chemistry, University of Kiel, Max-Eyth-Strasse 2, 24118 Kiel, Germany

[‡]Institute for Materials Science, University of Kiel, Kaiserstrasse 2, 24143 Kiel, Germany

[§]Fraunhofer Institute for Physical Measurement Techniques IPM, Heidenhofstrasse 8, 79110 Freiburg, Germany

^{||}Department of Chemistry and Materials Science Institute, University of Oregon, 373 Klamath Hall, Eugene, Oregon 97403, United States

ABSTRACT: The quality and temperature stability of 1 nm Bi₂Te₃/5 nm Sb₂Te₃ superlattices prepared by molecular beam epitaxy for the first time was investigated by in situ and ex situ X-ray diffraction and transmission electron microscopy. Upon heating, the superlattice structures are not stable against interdiffusion of the components, with micro- and nanostructural changes occurring at temperatures as low as 200 °C. The interdiffusion preferably starts next to superlattice defects. At 300 °C the Bi₂Te₃ and Sb₂Te₃ layers were mostly interdiffused, forming the thermodynamically stable Sb_{1.66}Bi_{0.33}Te₃ alloy. The data suggests that structural integrity of Bi₂Te₃/Sb₂Te₃ superlattices will not be stable for extended times above 200 °C, thus inhibiting application of such superlattices over a wide temperature range.



INTRODUCTION

The potential of thermoelectricity for power applications and thermoelectric materials for cooling applications is enhanced by the lack of moving parts and hence long-term reliability. The longevity of thermoelectric devices offsets the relatively low efficiencies, as demonstrated by modules built from bulk Bi₂Te₃/Sb₂Te₃ alloys launched 30 years ago and still working in space. The performance of a thermoelectric device depends on the dimensionless figure of merit (*ZT*) of the material. *ZT* is defined as

$$ZT = \frac{\sigma S^2 T}{\kappa} \quad (1)$$

where σ is the electrical conductivity, S the Seebeck coefficient, κ thermal conductivity, and T absolute temperature. σS^2 is referred to as the power factor. The higher the *ZT* value, the more efficient the thermoelectric material. For decades, bulk Bi₂Te₃ and Bi₂Te₃/Sb₂Te₃ alloys were known as the materials with the highest *ZT* (~1) at room temperature.¹ In 1968 and later, it was proposed and also demonstrated for Si–Ge-based alloys that the lattice thermal conductivity can be significantly reduced by scattering of low-frequency phonons at grain boundaries.^{2–4} In 1993, Hicks and Dresselhaus proposed that the power factor of thermoelectric materials could be significantly enhanced by nanostructuring due to the formation of sharp features in the density of states as dimensionality was reduced, resulting in enhanced Seebeck coefficients.⁵ Soon after, in 1995, Slack suggested that the ideal thermoelectric

material would behave as a glass with respect to phonons but as a crystal with respect to charge carriers, known as the “phonon glass–electron crystal” concept.⁶ This concept may also be a suitable approach for superlattices (SLs), as phonons are scattered at the interfaces in the multilayers, whereas electrons could pass these interfaces without significant hindrance.

These two concepts spurred considerable experimental efforts leading to exceptional *ZT* values, with the enhanced efficiency attributed to nanoscale features reducing thermal conductivity rather than enhancing the power factor. High *ZT* values and low thermal conductivities have been reported and confirmed for skutterudites and a variety of bulk as well as thin film materials containing nano-inclusions, nanosized precipitations, or structural disorder.^{7–25} In 2001, *ZT* values of 2.4 for p-type and ~1.5 for n-type Bi₂Te₃/(Bi,Sb)₂Te₃ SLs were reported, which remain benchmarks up to now.²⁶ Extended research has been performed to reproduce the reported efficiencies using a variety of approaches including modulated elemental reactants synthesis,²⁷ sputtering techniques,^{28,29} and molecular beam epitaxy (MBE)^{30,31} as summarized in 2012 by Winkler et al.³² Despite these efforts, information about the detailed structure and stability of Bi₂Te₃/Sb₂Te₃ SL structures remains sparse or does not exist in part because of the lack of high-quality samples. The quality of superlattice samples

Received: August 27, 2014

Revised: October 17, 2014

Published: October 22, 2014

depends on many factors. Although Bi_2Te_3 and Sb_2Te_3 mainly grow layer by layer via MBE under ideal conditions (Frank van der Merwe growth) providing theoretically perfectly layered films, the lattice mismatch between substrate and Sb_2Te_3 and between Bi_2Te_3 and Sb_2Te_3 of 2.8% leads to the formation of threading dislocations.³⁴ Depending on the substrate, this mismatch can be huge (22% for GaAs) or small (2.7% for BaF_2), leading to superlattices with varying amounts of dislocations. Coonley et al. investigated the stability of the electrical properties of such SLs up to 150 °C,³⁵ but no structural information or thermal stability information above 150 °C was presented. More generally, it is surprising that the essential question of whether nanostructures can withstand the conditions found in an operative thermoelectric device—elevated temperatures and a temperature gradient—has not been more thoroughly investigated. This work presents X-ray diffraction (XRD) and transmission electron microscopy (TEM) structural data as a function of temperature, which indicate that MBE-grown $\text{Bi}_2\text{Te}_3/\text{Sb}_2\text{Te}_3$ SL thin films are not kinetically stable at temperatures above 200 °C. The characterization by both in situ and ex situ approaches sheds light on the interdiffusion mechanisms of the components at the nanoscale.

EXPERIMENTAL SECTION

The samples were prepared via MBE^{34,35} at a substrate temperature of 350 °C. We note that the challenge in finding an appropriate growth temperature was to select a temperature that (i) is high enough to provide sufficient thermal energy to form single-crystalline $\text{Bi}_2\text{Te}_3/\text{Sb}_2\text{Te}_3$ SLs out of the coevaporated elements and (ii) is low enough not to supply further energy to trigger interdiffusion globally. Both conditions were apparently satisfied by this growth temperature, that is, (i) it was found that the single compounds Bi_2Te_3 and Sb_2Te_3 grown at 350 °C proved to be single crystalline with high carrier mobilities (Sb_2Te_3 —500 $\text{cm}^2/(\text{V s})$, details will be published in a later work) while (ii) the sharpness of the SL stacking of these compounds was demonstrated as shown below. We note that the growth temperature is high enough that this study suggests that some interdiffusion occurs during growth. The compounds Bi_2Te_3 and Sb_2Te_3 were deposited by coevaporation of the elements from different standard thermal effusion cells. Beam equivalent pressures of 3.5×10^{-7} , 2.5×10^{-7} , and 2.0×10^{-7} Torr were set for Te, Sb, and Bi, respectively. The background pressure was in the low 10^{-9} Torr range during growth. The growth rates of Bi_2Te_3 and Sb_2Te_3 were 0.18 and 0.17 nm/min in all of the SL samples. The 166 1 nm $\text{Bi}_2\text{Te}_3/5$ nm Sb_2Te_3 bilayers with a total thickness of ca. 1 μm were deposited. As substrates, single-crystalline (111)-oriented BaF_2 platelets with a thickness of around 700–1000 μm were used. The platelets were hand-cleaved before growth from $10 \times 10 \times 25$ mm³ bars supplied by Crystec GmbH, Berlin. The composition of the films was verified by energy-dispersive X-ray (EDX) analysis. XRD data of the SL films were collected at temperatures from room temperature to 400 °C on a Philips X'Pert Pro X-ray diffractometer (Cu $K\alpha$ radiation, $\lambda_1 = 1.54056$ Å and $\lambda_2 = 1.54439$ Å), which is equipped with a PIXCel detector. High-angle XRD data were collected in a flat plate θ/θ geometry from 5° to 126° 2θ in steps of 0.033° with an effective scan time of 15 s per step. Low angle XRD measurements were performed from 0.05° to 5° θ in steps of 0.005° with an effective scan time of 15 s/step. In situ heating experiments were performed in an Anton-Paar HTK 1200 high-temperature chamber, with a heating rate of 5 °C/min under He

atmosphere. During every scan (2 h) the temperature was kept constant at the given temperature. To investigate the change of the SL structure at the nanoscale with respect to the heat treatment, ex situ and in situ heating TEM experiments were performed using a Tecnai F30 G²ST and a Titan 80-300 equipped with an image corrector. For TEM sample preparation, cross sections were cut by focus ion beam (FIB) milling using a Helios 2 Dual Beam system. For the ex situ experiments cross sections were prepared in the as-deposited state and from the same sample after subsequent heating on a hot plate for 1 h at 250, 300, and 350 °C under nitrogen atmosphere. Further, for the in situ heating experiment a heating rate of 7 °C/min was chosen. At 150, 200, 215, 250, 300, 360, and 400 °C, the temperature was kept constant until minimal drift was obtained and images were recorded. This procedure took about 20 min for every temperature step.

RESULTS AND DISCUSSION

Figure 1 contains a specular high-angle diffraction pattern of a representative 5 nm $\text{Sb}_2\text{Te}_3/1$ nm Bi_2Te_3 SL before annealing

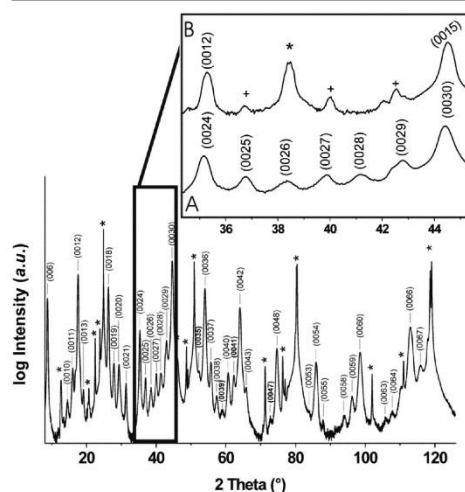


Figure 1. XRD pattern of the as-deposited $\text{Bi}_2\text{Te}_3/\text{Sb}_2\text{Te}_3$ sample showing (00 l) reflections of the SL. The enlarged inset displays sections of patterns recorded on the sample at room temperature before (A) and after (B) annealing to 400 °C. Reflections from the BaF_2 substrate are marked by an asterisk and the peaks with a cross are caused by polychromatic radiation (Cu $K\beta$ and W $L\alpha$), which become more intense after heating the sample and formation of the intermixed alloy. Additionally, the substrate recrystallizes and an extra substrate reflection occurs ($\sim 38.2^\circ$ 2θ) after annealing.

and the inset displays sections of patterns taken before and after annealing. Before annealing, the pattern clearly evidences the c -orientation of the SL by the restriction to many orders of (00 l) reflections. The narrow profiles of the reflections prove the structural integrity of the SL structure within wide areas of the sample. The SL reflections (00 l with $l \neq 6n$) could be indexed assuming the SL c -axis lattice parameter of ca. 6.1 nm. After annealing the sample at 400 °C, all SL reflections were extinct and only (00 l) intensities from the $\text{Sb}_{1.66}\text{Bi}_{0.33}\text{Te}_3$ alloy could be

observed. Indexing the pattern after annealing yields a *c*-axis lattice parameter of 3.51 nm, close to that reported for alloys at this composition.³⁶

Figure 2 shows a representative collection of the low-angle diffraction patterns collected while the sample temperature was

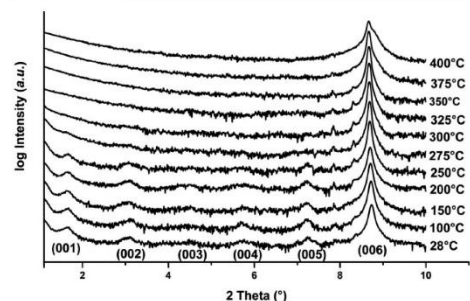


Figure 2. Scans collected during in situ low-angle XRD measurements on a SL sample. The temperature was increased to the indicated temperatures shown on the right of each data set.

systematically increased. In the as-deposited state, the first five low-angle SL reflections are all clearly visible and at the angles expected from the SL unit cell. There is little change in the patterns as the temperature is raised until a slight decrease in intensity is observed at 250 °C. The SL reflections are no longer detectable in the scan collected after annealing for 60 min at 300 °C. These results indicate that the constituents of the SL start interdiffusing at around 250 °C.

Figure 3 shows the normalized change in intensity as a function of temperature for a number of different (00*l*) SL

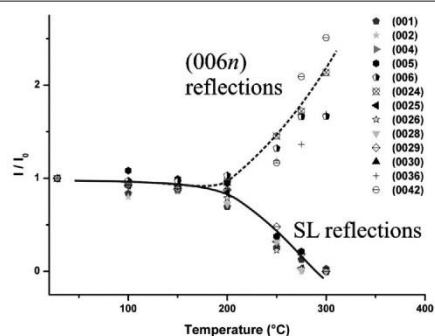


Figure 3. Change in normalized intensity of 13 low- and high-angle 00*l* reflections as a function of temperature. The intensity of each 00*l* reflection was divided by the corresponding intensity of that reflection measured in the initial scan to normalize the intensity change in this plot. The lines drawn are only a guide to the eye.

reflections, $I_{00l}(T)/I_{00l}(\text{as-deposited})$, that are not coinciding with reflections of the substrate. Below 150 °C the intensities do not change within the time spent at each temperature, agreeing with the results of electrical stability presented by Coonley et al.³³ At 200 °C, the intensities start to change and two different groups of reflections can be identified.

The intensity of reflections 00*l* with $l \neq 6n$ decreases as annealing temperature is increased, reflecting the interdiffusion of the constituting Bi_2Te_3 and Sb_2Te_3 layers. The intensity of reflections 00*l* with $l = 6n$ increases as annealing temperature is increased, being in accordance with the formation of the $\text{Sb}_{1.66}\text{Bi}_{0.33}\text{Te}_3$ alloy. The intensities of all reflections 00*l* with $l \neq 6n$ are no longer observable above 275 °C, suggesting that above this temperature the fully intermixed solid solution has formed. The thermodynamic instability of $\text{Bi}_2\text{Te}_3/\text{Sb}_2\text{Te}_3$ SLs was known from the phase diagram of the pseudo binary system at constant pressure determined by Caillat et al. that shows a complete miscibility over the entire compositional range.³⁷ Surprisingly, the onset of interdiffusion around 200 °C is remarkably low, considering the melting temperatures of Sb_2Te_3 and Bi_2Te_3 of about 585 °C. In the case of bulk samples it is assumed that diffusion is very slow below two-thirds of the melting temperature; however, for the present SL the impact of nanostructure and defects must be taken into account.

Electron microscopy was applied to provide insights into the structure of the as-grown SL and its thermally induced changes by interdiffusion of the Bi_2Te_3 and Sb_2Te_3 layers. In the as-grown sample, HRTEM micrographs and the corresponding Fourier transform (cf. Figure 4a) prove the periodicity (ca. 6

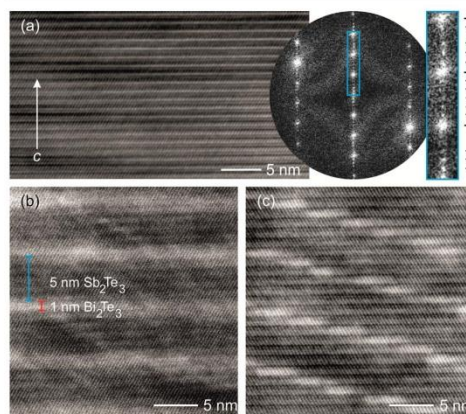


Figure 4. (a) HRTEM micrograph recorded on the SL structure and corresponding Fourier transform ([110] zone axis). The (003), (006), and (009) reflections are marked by crosses. Asterisks mark SL reflections. (b) and (c) HAADF-STEM micrographs of the as-grown sample. The micrographs display the 5 nm Sb_2Te_3 and 1 nm Bi_2Te_3 (dark and bright contrast, respectively) of a straight (b) and bowed (c) SL structure, respectively. The bowed SL contains an arrangement of steplike Bi_2Te_3 stripes.

nm) of the SL structure. The Fourier transform shows commensurate SL reflections along the [00*l*] direction. However, localized Fourier transform revealed areas with incommensurate SL reflections, too. The sequence of one layer of Bi_2Te_3 and five layers of Sb_2Te_3 is clearly visible in the atomic-number-dependent (*Z*) contrast of high-angle annular dark-field (HAADF) scanning transmission electron microscopy (STEM) images taken across the entire observation field; see Figure 4b. When parts (b) and (c) of Figure 4 are compared, there are two distinct types of intergrowth structures that account for most of the sample. The first one contains

straight Bi_2Te_3 (ca. 1 nm) and Sb_2Te_3 layers (ca. 5 nm), which are parallel to the substrate. For the second type the SL tends to be bowed, forming a steplike structure made of coherently intergrown Bi_2Te_3 stripes preserving the crystallographic superstructure within each of the steps. As for the straight SL, the average distance between the centers of consecutive Bi_2Te_3 stripes is ca. 6 nm, demonstrating that the overall chemical composition is approximated also for the bowed SL. There are also areas close to threading dislocations where the SL structure is not observed. Peranio et al. reported that areas with no SL correspond to regions with an increased defect density.³¹ While the overall structure of the film is consistent with the XRD results presented above, the presence of a significant portion of the film with the step structure was a surprise.

To obtain information on the interdiffusion of the layers by ex situ observation, cross-section samples were prepared after different annealing steps and HAADF-STEM micrographs were collected. Compared with STEM images of the cross section recorded on the as-deposited sample (Figure 5a), STEM

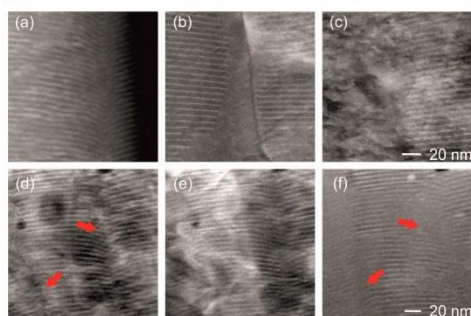


Figure 5. (a)–(c) HAADF-STEM micrographs (same scales) for ex situ heating experiments. (a) As-deposited state where strongly bowed SL structures are frequently observed. (b) Sample heated for 1 h at 250 °C. The absence of strongly bowed SL structures is evident. (c) Further heat treatment for 1 h at 300 °C led to a strong fading of the SL structure. Most of the sample showed no SL structure at all. (d–f) HAADF-STEM micrographs (same scales) for in situ heating experiments. (d) $T = 215$ °C, (e) $T = 300$ °C, and (f) $T = 360$ °C, arrows are marking positions with strongly bowed SL in as-deposited state.

images taken from a sample annealed for 1 h at 250 °C (Figure 5b) contain larger areas without any indications for a SL structure. Such alloyed areas preferably coexist with regions containing the straight SL structure (Figure 5b), suggesting that the bowed SL shows an enhanced diffusivity of the constituents. Further heating of the sample for 1 h at 300 °C leads to an almost complete vanishing of the SL structure (Figure 5c). Heating the sample for 1 h at 350 °C results in a complete loss of the SL structure and formation of the well-crystalline alloy structure. Thus, the ex situ STEM investigation confirms the XRD results. These results were also verified by in situ heating experiments, cf. Figures 5d–f. At $T = 215$ °C (Figure 5d) the bowed SL was still observed. Further heating to $T = 300$ and 360 °C (parts (e) and (f), respectively, of Figure 5) led to fading of the characteristic Z-contrast, particularly, next to strongly bowed SL structures (cf. arrows in Figure 5d,f). As for

the ex situ observations, it can be concluded that the diffusion of the constituents is faster next to defects of the SL structure, for example, within areas containing strongly bowed SL.

Figure 6 displays a sketch of the proposed mechanism for enhanced diffusion found in the bowed regions of the sample.

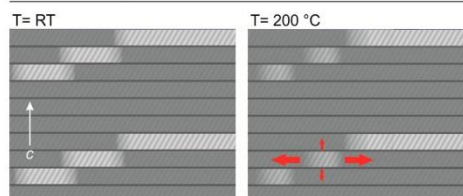


Figure 6. Schematic drawing of the diffusion mechanism for the bowed SL. Bright contrast represents Bi_2Te_3 layers similar to HAADF-STEM micrographs. Red arrows mark diffusion directions. The bold arrows indicate the higher diffusion rate. It is assumed that the diffusion rate within bowed SL structures is increased due to the facile diffusion paths in a - and b -directions at 200 °C.

The enhanced diffusion might be a result of defects, for example, threading dislocations that act as high-diffusivity paths. Moreover, the diffusion is enhanced as a result of the stepped structure in the bowed SL, leading to the mixing of bismuth and antimony along the a - and b -directions, rather than diffusion along the c -direction. This would be consistent with the strongly anisotropic nature of diffusivity, for example, in Bi_2Te_3 , with diffusion along the c -axis being significantly lower compared to diffusivity along a - and b -directions.^{38–40} In this picture, the higher kinetic stability of the nonbowed regions is a consequence of the slower diffusion rates along the c -axis.

CONCLUSION

The data presented indicates that 1 nm Bi_2Te_3 /5 nm Sb_2Te_3 SLs are not kinetically stable above 200 °C, and that in-plane diffusion occurs at a higher rate than cross-plane diffusion. Consequently, extended regions with straight SL are more kinetically stable than regions with bowed structure and small lateral domain sizes. The surprisingly low temperature for interdiffusion strongly suggests that the properties of nanostructured thermoelectric materials should be tested through several temperature cycles and also as a function of annealing time and temperature to determine the long-term stability of these kinetically stable structures.

AUTHOR INFORMATION

Corresponding Authors

*E-mail: wbensch@ac.uni-kiel.de.

*E-mail: lk@tf.uni-kiel.de.

Author Contributions

[†]A.-L. Hansen and T. Dankwort contributed equally to this work. The manuscript was written through contributions of all authors. All authors have given approval to the final version of the manuscript.

Notes

The authors declare no competing financial interest.

ACKNOWLEDGMENTS

The authors acknowledge funding via the German Research Foundation (DFG) within the frame of priority program

"Nanostructured Thermoelectric Materials: Theory, Model Systems and Controlled Synthesis" (SPP 1386). Co-authors J.D. and D.C.J. acknowledge support from the National Science Foundation through Grant DMR-1266217.

REFERENCES

- (1) Rowe, D. M. *Handbook of thermoelectrics*; CRC Press: Boca Raton, FL, 1995.
- (2) Savvides, N.; Goldsmid, H. J. *J. Phys. C: Solid State Phys.* **1980**, *13*, 4657.
- (3) Savvides, N.; Goldsmid, H. J. *J. Phys. C: Solid State Phys.* **1980**, *13*, 4671.
- (4) Goldschmid, H. J.; Penn, A. W. *Phys. Lett.* **1968**, *A 27*, 523.
- (5) Hicks, L. D.; Dresselhaus, M. S. *Phys. Rev. B* **1993**, *47*, 16631–16634.
- (6) Slack, G. In *Handbook of thermoelectrics*; Rowe, D. M., Ed.; CRC Press: Boca Raton, FL, 1995; p 407.
- (7) Ikeda, T.; Collins, L. A.; Ravi, V. A.; Gascoin, F. S.; Haile, S. M.; Snyder, G. F. *Chem. Mater.* **2007**, *19*, 763–767.
- (8) Snyder, G. J.; Toberer, E. S. *Nat. Mater.* **2008**, *7*, 105–114.
- (9) Vining, C. B. *Nat. Mater.* **2008**, *7*, 756–766.
- (10) Rao, A. M.; Ji, X.; Tritt, T. M. *MRS Bull.* **2006**, *31*, 218–223.
- (11) Böttner, H.; Venkatasubramanian, R. R. *MRS Bull.* **2006**, *31*, 199–205.
- (12) Thiagarajan, S. J.; Jovic, V.; Heremans, J. P. *Phys. Status Solidi (RRL)* **2007**, *1*, 256–258.
- (13) Ebling, D. G.; Jacquot, A.; Jäggle, M.; Böttner, H.; Kühn, U.; Kirste, L. *Phys. Status Solidi (RRL)* **2007**, *1*, 238–240.
- (14) Arachchige, I. U.; Wu, J.; Dravid, V. P.; Kanatzidis, M. G. *Adv. Mater.* **2008**, *20*, 3638–3642.
- (15) Chiritescu, C.; Cahill, D. G.; Nguyen, N.; Johnson, D. C.; Bodapati, A.; Koblinski, P.; Zschack, P. *Science* **2007**, *315*, 351–353.
- (16) Poudel, B.; Hao, Q.; Ma, Y.; Lan, Y.; Minnich, A.; Yu, B.; Yan, X.; Wang, D.; Muto, A.; Vashaee, D.; Chen, X.; Liu, J.; Dresselhaus, M. S.; Chen, G.; Ren, Z. *Science* **2008**, *320*, 634–638.
- (17) Bux, S. K.; Fleurial, J.-P.; Kaner, R. B. *Chem. Commun.* **2010**, *46*, 8311–8324.
- (18) Lin, Q.; Smeller, M.; Heideman, C. L.; Zschack, P.; Koyano, M.; Anderson, M. D.; Kykyneshi, R.; Keszler, D. A.; Anderson, I. M.; Johnson, D. C. *Chem. Mater.* **2010**, *22*, 1002–1009.
- (19) Zahid, F.; Lake, R. *Appl. Phys. Lett.* **2010**, *97*, 212102.
- (20) Ganguly, S.; Brock, S. L. *J. Mater. Chem.* **2011**, *21*, 8800–8806.
- (21) Nielsch, K.; Bachmann, J.; Kimling, J.; Böttner, H. *Adv. Energy Mater.* **2011**, *1*, 713–731.
- (22) Rosenthal, T.; Schneider, M. N.; Stiewe, C.; Döblinger, M.; Oeckler, O. *Chem. Mater.* **2011**, *23*, 4349–4356.
- (23) Ma, Y.; Ahlberg, E.; Sun, Y.; Iversen, B. B.; Palmqvist, A. E. C. *J. Electrochem. Soc.* **2012**, *159*, D50–D58.
- (24) Heremans, J. P.; Dresselhaus, M. S.; Bell, L. E.; Morelli, D. T. *Nat. Nanotechnol.* **2013**, *8*, 471–473.
- (25) Nolas, G. S.; Sharp, J. W.; Goldsmid, H. J. *Principles of Thermoelectrics: Basics and New Materials Developments*; Springer-Verlag: Heidelberg, 2001.
- (26) Venkatasubramanian, R. R.; Siivola, E.; Colpitts, T.; O'Quinn, B. *Nature* **2001**, *413*, 597.
- (27) Mortensen, C.; Rostek, R.; Schmid, B.; Johnson, D. C. *Int. Conf. Thermoelectr.* **2005**, 270–272.
- (28) Winkler, M.; Liu, X.; Hansen, A.-L.; König, J. D.; Bensch, W.; Kienle, L.; Böttner, H.; Bartholomé, K. *Nanothermoelectrics* **2013**, *1*, 1–9.
- (29) Winkler, M.; Liu, X.; König, J. D.; Kirste, L.; Böttner, H.; Bensch, W.; Kienle, L. *J. Electron. Mater.* **2012**, *41*, 1322.
- (30) Winkler, M.; Liu, X.; König, J. D.; Buller, S.; Schürmann, U.; Kienle, L.; Bensch, W.; Böttner, H. *J. Mater. Chem.* **2012**, *22*, 11323.
- (31) Peranio, N.; Eibl, O.; Nurnus, J. *J. Appl. Phys.* **2006**, *100*, 114306.
- (32) Winkler, M.; Liu, X.; Schürmann, U.; König, J.; Kienle, L.; Bensch, W.; Böttner, H. *Z. Anorg. Allg. Chem.* **2012**, *15*, 2441–2454.
- (33) Coonley, K. D.; O'Quinn, C. B.; Caylor, J. C.; Venkatasubramanian, R. R. *Mater. Res. Soc. Symp. Proc.* **2004**, *793*, 67–72.
- (34) Nurnus, J. Ph.D. Thesis, University of Freiburg, Freiburg, Germany, 2001.
- (35) Nurnus, J.; Böttner, H.; Lambrecht, A. In *CRC Handbook of Thermoelectrics*; Rowe, D. M., Ed.; CRC Press: Boca Raton, FL, 2006.
- (36) Smith, M. J.; Knight, R. J.; Spencer, C. W. *J. Appl. Phys.* **1962**, *33*, 2186.
- (37) Caillat, T.; Carle, M.; Perrin, D.; Scherrer, H.; Scherrer, S. *J. Phys. Chem. Solids* **1992**, *2*, 227.
- (38) Chitroub, M.; Scherrer, S.; Scherrer, H. *J. Phys. Chem. Solids* **2000**, *61*, 1693–1701.
- (39) Keys, J. D.; Dutton, H. M. *Phys. Chem. Solids* **1963**, *24*, 563–571.
- (40) Carlson, R. O. *J. Phys. Chem. Solids* **1960**, *13*, 65–70.

1.3 Nanostructure, thermoelectric properties, and transport theory of V_2VI_3 and $V_2VI_3/IV-VI$ based superlattices and nanomaterials

In diesem Artikel werden die Ergebnisse des Projektes „Break and Beyond“ des Schwerpunktprogramms (SPP 1386) „Nanostrukturierte Thermoelektrika“ der Deutschen Forschungsgemeinschaft zusammengefasst. Der Hauptfokus des Projektes lag in der Aufklärung des unerreicht hohen ZT Wertes, der 2001 mit Bi_2Te_3/Sb_2Te_3 Übergittern erreicht wurde. Diese Ergebnisse führten im Anschluss zu einem erheblichen Interesse an nanostrukturierten thermoelektrischen Materialien. Die ungewöhnlich geringe Anisotropie der elektrischen Leitfähigkeit konnte nicht reproduziert werden. Zusätzlich konnten theoretische Berechnungen die Reduktion der Anisotropie durch Quanten Confinement Effekte nicht erklären. Auch die hohe Ladungsträgerkonzentration und der große Seebeck-Koeffizient konnten nicht reproduziert werden, da es zwischen p-typ Sb_2Te_3 und n-typ Bi_2Te_3 Schichten zwangsläufig zu Kompensationseffekten kommen muss. Dies legt die Vermutung nahe, dass es sich bei den Dünnschichten in der Arbeit von 2001 entweder um ein homogenes $(Bi_{1-x}Sb_x)Te_3$ handelte oder dass es während des Abscheidungsprozesses mit Metallorganischer Gasphasenepitaxie (MOCVD) zur Fremddotierung gekommen ist. Die Reduktion der thermischen Leitfähigkeit konnte jedoch verifiziert werden. Allerdings ist die thermische Stabilität dieser nanostrukturierten Materialien sehr gering, da bereits bei Temperaturen von ca. 200°C Interdiffusion von Sb_2Te_3 und Bi_2Te_3 erfolgt.

T. Dankwort, A.-L. Hansen, M. Winkler, U. Schürmann, J. D. König, D. C. Johnson, N. F. Hinsche, P. Zahn, I. Mertig, W. Bensch, L. Kienle, *Phys. Status Solidi A* **2016**, 213, 662–671.

Copyright Wiley-VCH Verlag GmbH & Co. KGaA. Reproduced with permission

Nanostructure, thermoelectric properties, and transport theory of V_2VI_3 and $V_2VI_3/IV-VI$ based superlattices and nanomaterials

Torben Dankwort¹, Anna-Lena Hansen², Markus Winkler³, Ulrich Schürmann¹, Jan D. Koenig³, David C. Johnson⁴, Nicki F. Hinsche⁵, Peter Zahn⁶, Ingrid Mertig^{5,7}, Wolfgang Bensch², and Lorenz Kienle^{*1}

¹Institute for Materials Science, Christian Albrechts University Kiel, Kaiserstr. 2, 24143 Kiel, Germany

²Institute for Inorganic Chemistry, Christian Albrechts University Kiel, Max-Eyth-Str. 2, 24118 Kiel, Germany

³Fraunhofer Institute for Physical Measurement Techniques IPM, Heidenhofstr. 8, 79110 Freiburg, Germany

⁴Department of Chemistry and Materials Science Institute, University of Oregon, Eugene, OR 97403, USA

⁵Institute of Physics, Martin Luther University Halle-Wittenberg, 06099 Halle/Saale, Germany

⁶Helmholtz-Zentrum Dresden-Rossendorf e.V., Bautzner Landstr. 400, 01328 Dresden, Germany

⁷Max Planck Institute of Microstructure Physics, Weinberg 2, 06120 Halle, Germany

Received 1 July 2015, revised 11 December 2015, accepted 11 December 2015

Published online 12 January 2016

Keywords Bi_2Te_3 , electron microscopy, nanoalloying, Sb_2Te_3 , superlattices, thermoelectrics, thin films

*Corresponding author: e-mail lk@tf.uni-kiel.de, Phone: +49 431 880 6196, Fax: +49 431 880 6178

The scope of this work is to review the thermoelectric properties, the microstructures, and their correlation with theoretical calculations and predictions for recent chalcogenide based materials. The main focus is put on thin multilayered Bi_2Te_3 , Sb_2Te_3 films, and bulk $V_2VI_3/IV-VI$ mixed systems. For all films a systematic characterization of the thermoelectric properties as well as the micro- and nanostructure was performed. The degree of crystallinity of the multilayered films varied from epitaxial systems to polycrystalline films. Other multilayered thin films revealed promising thermoelectric properties. $(SnSe)_{1,2}TiSe_2$ thin films with rotational disorder

yielded the highest Seebeck coefficient published to date for analogous materials. For bulk $V_2VI_3/IV-VI$ mixed systems insides are given into a complete “material to module” process resulting in a high performance thermoelectric generator using $(1-x)(GeTe)_x(Bi_2Se_{0.7}Te_{2.8})$ ($x=0.038$). Cyclic heating of this system with $x=0.063$ resulted in a drastic change of the micro- and nanostructure observed by *ex situ* and *in situ* X-ray diffraction (XRD) and transmission electron microscopy (TEM). Consequently a degradation of ZT at $450^\circ C$ from ~ 2.0 to ~ 1.0 was observed, while samples with $x=0.038$ showed a stable ZT of 1.5.

© 2016 WILEY-VCH Verlag GmbH & Co. KGaA, Weinheim

1 Introduction Thermoelectric materials are used in power generators to convert thermal gradient into electrical power. The efficiency of the thermoelectric generator correlates with the figure of merit ZT which is a dimensionless number defined as

$$ZT = \frac{S^2 \sigma}{\lambda} T. \quad (1)$$

S , σ , and λ represent the Seebeck coefficient (also referred to as the thermopower), the electrical, and the thermal

conductivity, respectively. Hence, low thermal and high electrical conductivity as well as a high Seebeck coefficient are desirable.

Typically, good thermoelectric materials are heavily doped semiconductors showing electrical conductivity σ , thermal conductivity λ , Seebeck coefficient S , and power factor $S^2 \sigma$ in the range of $\sim 1000 \text{ S cm}^{-1}$, $\sim 1 \text{ W m}^{-1} \text{ K}^{-1}$, $\sim 200 \mu\text{V K}^{-1}$, and $\sim 40 \mu\text{W cm}^{-1} \text{ K}^{-2}$, respectively. The resulting ZT around room temperature is ~ 1 . Such characteristics are usually fulfilled by extrinsic semiconductors like Bi_2Te_3 and Sb_2Te_3 (doped with Bi_2Se_3)

© 2016 WILEY-VCH Verlag GmbH & Co. KGaA, Weinheim

Wiley Online Library

which are all V_2VI_3 compounds. Consequently, these materials show the highest ZT values at room temperature since decades.

In the 1990s, Hicks and Dresselhaus [1] proposed that nanostructuring should lead to enhanced power factors due



Torben Dankwort is currently a Ph.D. candidate in the group “Synthesis and Real Structure” at the Christian Albrechts University Kiel (CAU), Germany, where he also accomplished his Bachelor and Master degree. During his studies, he was employed at the Fraunhofer Institute for Silicone Technology, working in the field of piezoelectric materials for microelectromechanical systems. His current research interests focus on the characterization of nanomaterials by TEM.



Markus Winkler is a member of the Department “Functional Materials” at the Fraunhofer Institute for Physical Measurement Techniques (IPM). He received his Ph.D. degree in 2015 for his research on Bi_2Te_3/Sb_2Te_3 -based superlattice systems fabricated by MBE and sputtering. Furthermore, he has been working on and managing several projects with a focus on the synthesis and characterization of (nanostructured) V_2VI_3 based thin-film materials for thermoelectric applications. His work was awarded the Nachwuchspreis (young talent award) by the German Thermoelectric Society in 2015. His work (of which parts are shown in this paper) was funded by the SPP1386 initiated by the Deutsche Forschungsgemeinschaft and the program frame “Werkstoffinnovationen für Industrie und Gesellschaft,” funding program “Nanochance,” 03X4506B initiated by the Bundesministerium für Bildung und Forschung. Currently, Dr. Winkler is also active in the field of electrocalorics.



Wolfgang Bensch studied Chemistry at the Ludwig-Maximilians-University of Munich (Germany) and received his Dr. rer. nat. with Prof. Eberhard Amberger in 1983. He was a postdoctoral fellow in the group of Prof. Han-Rudolf Oswald at the University of Zurich (Switzerland) and in 1986 he joined Siemens Company (Munich). He finished his habilitation in 1993 at the Johann Wolfgang Goethe University Frankfurt (Germany). In 1997, he was appointed as full professor for Inorganic Solid State Chemistry at the Christian-Albrechts-University Kiel (Germany).

to quantum confinement effects in materials with reduced dimensionality. This report was a major driving force for the investigation of nanostructured systems and new types of thermoelectric materials.

Soon after, the “phonon-glass/electron-crystal concept” (PGEC) was developed. Accordingly, an ideal thermoelectric material should scatter phonons like a glass while simultaneously allow charge carrier conduction like a single crystal [2]. Superlattices (SLs) and multilayer structures (MLs) are in good accordance with this concept, as phonons are scattered at the interfaces of the multilayers while electrons should move unimpeded. Transferring this concept of nanostructuring to bulk materials led to the idea of hierarchical structures. It was shown that polycrystalline PbTe samples including nanoprecipitates of SrTe exhibit a higher thermoelectric performance ($ZT = 2.2$) than conventional bulk materials or nanostructured PbTe [3]. Even materials like $(AgSbTe_2)_{0.15}(GeTe)_{0.85}$ (TAGS) and $(AgSbTe_2)_x(PbTe)_{1-x}$ (LAST), which are well known thermoelectrics since the 1950s, are actually hierarchically structured, possessing nanoprecipitates and twin boundaries [4–6].

However, after decades of research one work still remains unchallenged in terms of efficiency. In 2001, ZT values of 2.4 at room temperature were reported for Bi_2Te_3/Sb_2Te_3 SLs prepared by metalorganic chemical vapor deposition (MOCVD) [7]. The cross-plane lattice thermal conductivity was decreased significantly by a factor of 4–7. Lowest thermal conductivity was measured for SLs of 1 nm Bi_2Te_3 and 5 nm Sb_2Te_3 . Simultaneously, very high values for the Seebeck coefficient (about $200\text{--}270\ \mu\text{V K}^{-1}$) and cross-plane electrical conductivity were maintained due to an extremely low anisotropy factor. However, several questions remained unanswered including a systematic characterization of structural and thermoelectric properties and the low-anisotropy ratio for the electrical conductivity. Furthermore, the thermal stability of the obtained SLs was not addressed [8].

Consequently, efforts of several groups to reproduce these results using different deposition techniques, e.g.,



Lorenz Kienle is full time professor and head of the group “Synthesis and Real Structure” at the Christian Albrechts University Kiel (CAU), Germany. After the habilitation, he was awarded for the Heisenberg grant in 2006, followed by a Heisenberg professorship at CAU in 2008. In 2010, he was appointed as head of the electron microscopy facilities at the Institute for Material Science. Since 2011, he is the vice executive director of the Institute for Material Science at CAU. His main research interests focus on the synthesis of new bulk and nanomaterials and their characterization via HRTEM and other techniques.

MOCVD [9–15], molecular beam epitaxy (MBE) [16–19], sputter deposition [20–23], electrochemistry [24–26], and pulsed laser deposition (PLD) [27] failed. A critical discussion on the current state of $\text{Bi}_2\text{Te}_3/\text{Sb}_2\text{Te}_3$ SLs and a detailed review can be found elsewhere [28].

Considering high Seebeck coefficient and high electrical conductivity, other layered compounds showed promising results as well [29–32]. Especially layered compounds with turbostratic disorder exhibited low-thermal conductivities which makes them highly interesting for thermoelectric applications [33, 34].

This work is intended to give an overview of the progress in chalcogenide-based thin film and bulk thermoelectric materials mainly achieved during the funding period of the priority program I386 of the German research foundation (DFG). The first part of this article focuses on $\text{Bi}_2\text{Te}_3/\text{Sb}_2\text{Te}_3$ -based thin film SLs. Besides different approaches to synthesize SLs, also theoretical calculations are presented to clarify the origin of the unusually high ZT value of $\text{Bi}_2\text{Te}_3/\text{Sb}_2\text{Te}_3$ SLs.

The second part deals with recently obtained turbostratically disordered multilayered materials like $(\text{SnSe})_{1.2}\text{TiSe}_2$ as promising candidates for advanced thin film thermoelectric materials.

In the third part, a measurement tool for the cross-plane electrical conductivity is presented. One reason for the variety of results in thin film thermoelectrics, especially for SLs, is the lack of appropriate characterization tools for cross-plane measurements.

In Section 4, thermoelectric generators based on bulk GeTe doped with $\text{Bi}_2(\text{Se},\text{Te})_3$ are presented.

Most of the results have been published in several peer reviewed journals [8, 28, 35–46] and in a Ph.D. thesis [47].

2 Thin films based on Bi_2Te_3 , Sb_2Te_3 and $\text{Bi}_2\text{Te}_3/\text{Sb}_2\text{Te}_3$ superlattices

2.1 Theoretical investigations on electrical anisotropy in $\text{Bi}_2\text{Te}_3/\text{Sb}_2\text{Te}_3$ superlattices Compared to bulk materials, $\text{Bi}_2\text{Te}_3/\text{Sb}_2\text{Te}_3$ SLs were reported to show decreasing anisotropy of the charge carrier mobility, and consequently a low-anisotropy factor for the electrical conductivity. It was assumed that this reduction was a result of weak-confinement and near-zero band-offset [7]. However, theoretical calculations discussing the transport properties of $\text{Bi}_2\text{Te}_3/\text{Sb}_2\text{Te}_3$ SLs were rarely performed [48].

Therefore, theoretical investigations were implemented to clarify the origin of the unusual decrease of the electrical conductivity anisotropy. To this end, density functional theory and semi-classical transport calculations were performed on Bi_2Te_3 and Sb_2Te_3 multilayers taking into account epitaxial in-plane strain.

No significant change in electrical conductivity anisotropy of the multilayers with respect to bulk material could be found. Furthermore, strain effects as possible explanation for the anisotropy reduction could be excluded.

The theoretical investigations were extended to SLs with 3 nm periodicity and varying layer thicknesses

including calculations of the band structures and band gaps for the different SL periodicities. Furthermore, quantum confinement effects and band structure effects were included for the calculation of the electrical anisotropy and the cross-plane ZT [49].

All these calculations could not reveal the reason for the change of electrical anisotropy reported in Ref. [7]. The obtained theoretical results showed an approximately linear relation between the anisotropy values of the electrical conductivity and different individual layer thicknesses for p-type multilayers. In addition, calculations of the cross-plane ZT yielded values of 0.9 at room temperature and 1.3 at elevated temperatures, which correlate well to the experimental findings described below. Even more noteworthy are the results taking into account n-type doping of the multilayer and quantum-confinement effects which would lead to a severe increase of the anisotropy factor. Such a film would show a drastic decrease of the cross-plane ZT value.

It can be concluded that detailed *ab initio* calculations could not clarify the increase of in-plane electrical conductivity and the strong reduction of electrical conductivity anisotropy and hence the very high ZT values reported in Ref. [7].

A detailed discussion of these results can be found in Refs. [44, 45, 47, 49].

2.2 Molecular beam epitaxy (MBE)

2.2.1 Nanoalloyed Bi_2Te_3 and Sb_2Te_3 and $\text{Sb}_2\text{Te}_3/\text{Bi}_2\text{Te}_3$ multilayered thin films The high-performance p-type SLs described by Venkatasubramanian et al. [7] are formed by alternating layers of Bi_2Te_3 and Sb_2Te_3 . Consequently, a comprehensive study of nanoalloyed binary compounds was carried out.

Nanoalloying is an alternative method compared to epitaxial growth and has been proven to be an appropriate substitute [35, 36, 47] for thin-film production. This method is based on a “two-step” process as it is schematically shown in Fig. 1. First elemental thin films are deposited in the desired stoichiometry by changing the thickness of the respective element layers. Hence, the individual elemental layer thicknesses range from Ångstrom to nanometer scale

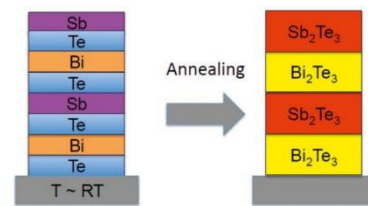


Figure 1 Schematic representation of the nanoalloying process for $\text{Bi}_2\text{Te}_3/\text{Sb}_2\text{Te}_3$ based SLs. In a first step elemental layers of Bi, Te, and Sb are deposited followed by a post-annealing step leading to formation of the compounds in a solid state reaction [47].

and the total film thickness is proportional to the number of repeating layers deposited, resulting in total film thicknesses that can be in the range of microns. After deposition, the thin films are annealed and compound formation takes place by a solid state reaction. Nanoalloying is closely related to the modulated elemental reactants method (MER) [50, 51]. The nanoalloying method is advantageous compared to dedicated MBE because films are easier to produce due to the absence of internal heating systems during the deposition process. Therefore, less re-evaporation occurs allowing a better and easier control of the stoichiometry. Furthermore, highly textured films can be deposited without the use of epitaxially compatible substrates. Also film deposition rates are higher and films can be deposited by using standard MBE or sputtering. Consequently, nanoalloying is much less cost intensive, however, multilayer films prepared by nanoalloying often show a polycrystalline structure inside the compound layers.

To obtain Bi_2Te_3 and Sb_2Te_3 , sequences of thin layers of Te and Bi or Te and Sb were deposited. The individual thicknesses of the elemental layers were varied which allows to modify (i) the degree of texture and (ii) the Te content and hence the electrical properties.

Prior to the growth of SLs as shown in Fig. 1, binary homogeneous films of Bi_2Te_3 and Sb_2Te_3 were grown by the nanoalloying method and examined. For both films, the formation temperature of binary compounds is around 100°C which was experimentally determined by *in situ* XRD measurements. Temperature-dependent measurements of the Seebeck coefficient and electrical conductivity showed an abrupt change due to compound formation at this temperature; see Fig. 2 for Bi_2Te_3 films.

For Bi_2Te_3 , polycrystalline films with preferred (001)-orientation could be obtained. The films showed only n-type conduction, even with a large excess of Bi. This is a major difference compared to bulk materials where Bi excess leads to p-type conducting Bi_2Te_3 . This finding might be interrelated with the low annealing temperature for thin films in comparison to bulk materials. Low temperatures lead to a low density of Bi_{Te} antisite defects and hence a low number of holes are generated. Moreover, other defects like the formation of BiTe and other strongly n-conducting phases are proposed to dominate the electrical behavior of these samples.

Room temperature measurements of electrical properties clearly evidenced a maximum close to stoichiometric binary Bi_2Te_3 with values of $\sim 200 \mu\text{V K}^{-1}$ for the Seebeck coefficient and a power factor of $14 \mu\text{W cm}^{-1} \text{K}^{-2}$. Minimum thermal conductivities were measured to be $\sim 0.4 \text{ W m}^{-1} \text{K}^{-1}$ for some of these samples.

The above described dependence of annealing temperature and electrical conductivity led to the development of a two-zone high temperature annealing procedure. By adding a controlled Te flux, this method can also be used to control the stoichiometry. Using this approach, it was possible to produce films close to the ideal stoichiometry. Temperature dependent measurements of the Seebeck coefficient showed

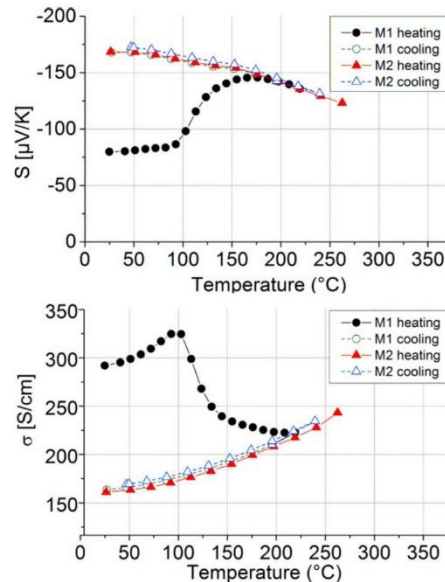


Figure 2 Temperature-dependent measurements of the Seebeck coefficient (upper graph) and the electrical conductivity (lower graph) for Bi_2Te_3 films during the nanoalloying procedure. Graphs M1 and M2 represent first and second heating/cooling cycle, respectively. An abrupt change of the Seebeck coefficient and the electrical conductivity is observed at 100°C , which can be attributed to the compound formation process [46]. Reproduced with permission of The Royal Society of Chemistry.

that annealing at elevated temperatures ($450\text{--}500^\circ\text{C}$) results in the formation of p-conducting Bi_2Te_3 . These results highlight the proposed importance of antisite defects.

Growth of polycrystalline Sb_2Te_3 films with preferred orientation perpendicular to the *c*-axis could also be achieved. For Te contents $>60\text{ at.}\%$, elemental Te could be identified by XRD measurements as minor impurity. Seebeck coefficients approached a maximum of $140 \mu\text{V K}^{-1}$ at $60\text{ at.}\%$ Te and remained constant when further increasing the Te content.

The electrical conductivity ranged from ~ 1300 to $\sim 2000 \text{ S cm}^{-1}$ and no dependence on the Te concentration could be detected. Further, a high power factor of $30 \mu\text{W cm}^{-1} \text{K}^{-2}$ and a thermal conductivity of $1.6 \text{ W m}^{-1} \text{K}^{-1}$ were obtained.

To calculate the cross-plane *ZT* values, in-plane electrical properties and cross-plane thermal conductivities were introduced. As an approximation it was assumed that the Seebeck coefficient is isotropic while the electrical conductivity is anisotropic. Accordingly, the anisotropy ratio (in-plane vs. cross-plane) is 1 for perfect isotropic films (e.g., polycrystalline films) and 4 for perfectly *c*-oriented materials. This procedure allows estimating an upper and

lower value for ZT , namely $ZT \sim 0.7\text{--}0.17$ and $\sim 0.6\text{--}0.14$ for Bi_2Te_3 and Sb_2Te_3 , respectively.

In summary, the nanoalloying method yields Bi_2Te_3 and Sb_2Te_3 thin films with good thermoelectric properties and stoichiometry control as fully discussed in Refs. [22, 35, 41, 42, 46, 47, 52, 53].

Based on the promising results of the binary thin films the next step was to fabricate multilayers with different Sb_2Te_3 to Bi_2Te_3 ratios (1:1 to 7:1) and period lengths. The nominal layer thickness of Bi_2Te_3 layers was 3 nm for all stacking ratios, except for the stacking ratio 1:1 where a nominal thickness of 9 nm was chosen.

Annealing the samples at 150 or 250 °C for 2 h resulted in formation of polycrystalline $\text{Bi}_2\text{Te}_3/\text{Sb}_2\text{Te}_3$ films with a less pronounced c -axis texture. *In* and *ex situ* (S)TEM and HRTEM revealed a high roughness of the as-deposited films. During compound formation, temperature-induced interdiffusion of Sb and Bi occurred, leading to grains with a multilayer core surrounded by intermixed $(\text{Sb,Bi})_2\text{Te}_3$ rims at the grain boundaries (Fig. 3). Interdiffusion and hence the integrity of the SL and the crystallinity strongly influence the transport properties. An efficient reduction of thermal conductivity by the SL structure was not achieved. A possible explanation might be the ineffective scattering of the weakly defined SL structure. As expected, due to the stacking of n-type conducting Bi_2Te_3 and p-type conducting Sb_2Te_3 strong compensation effects occurred. The best performance was achieved choosing a high Sb_2Te_3 to Bi_2Te_3 ratio and an annealing temperature of 250 °C,

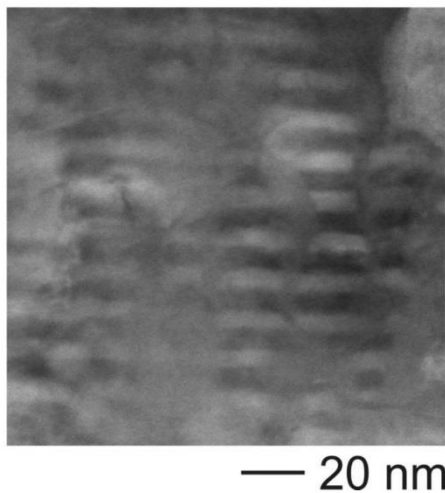


Figure 3 Z-contrast micrograph of an in situ heated nanoalloyed polycrystalline SL deposited by an MBE system and annealed at 250 °C. Bright and dark stripes represent Bi_2Te_3 and Sb_2Te_3 , respectively. The SL is only weakly defined next to grain boundaries. Reprinted (adapted) by permission of Wiley & Sons [28].

resulting in high power factors of $\sim 30\text{--}40 \mu\text{W cm}^{-1} \text{K}^{-2}$. ZT values of 0.3–0.9 were estimated for the SLs. A detailed discussion can be found in Refs. [22, 47, 35].

2.2.2 Epitaxial superlattices As described above, the nanoalloyed SL films lack of thermal stability due to their polycrystalline nature. Consequently, MBE was used to grow Bi_2Te_3 , Sb_2Te_3 , and $\text{Bi}_2\text{Te}_3/\text{Sb}_2\text{Te}_3$ SLs epitaxially on (111)- BaF_2 substrates. Electron diffraction, HRTEM, and Z-contrast sensitive STEM micrographs confirmed the growth of epitaxial high quality SLs, however, TEM investigations also showed the presence of step-like defects which locally deform the parallel and straight multilayers. Figure 4 shows a XRD pattern of a 1 nm Bi_2Te_3 and 5 nm Sb_2Te_3 SL. Besides the formation of the main structure reflections ($006n$) many SL reflections are observed, as a result of additional periodicity introduced by the sharply defined SL structure. Clear SL reflections were never reported by Venkatasubramanian et al. indicating that our present samples should show a higher degree of ordering. Annealing the sample for 1 h at 400 °C resulted in a complete intermixing of the SL components and consequently no SL reflections were observed in XRD patterns after heating (Fig. 4, inset).

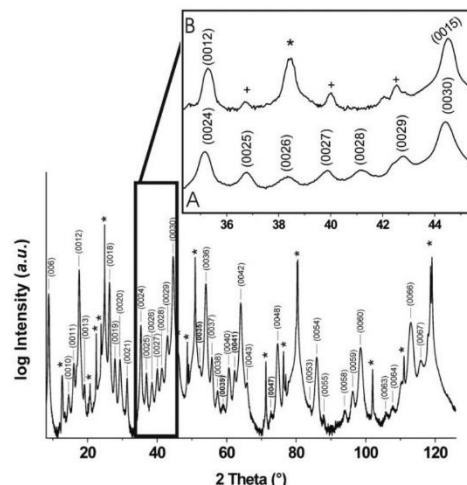


Figure 4 XRD pattern (θ - θ geometry) of an epitaxially deposited SL consisting of 1 nm Bi_2Te_3 and 5 nm Sb_2Te_3 . Besides the main structure reflections ($006n$) also SL reflections are observed. Reflections from the BaF_2 substrate are marked by an asterisk while crosses mark reflections by polychromatic radiation (Cu K_β and W L_α). The inset shows an enlarged section before (A) and after (B) heating the sample at 400 °C for 1 h. Consequently the intensity of the SL reflections decreases upon heating. Reprinted with permission from Ref. [8]. Copyright 2014, American Chemical Society.

Further, *ex* and *in situ* TEM heating experiments demonstrated that the step-like defects represent areas with enhanced diffusivity compared to perfectly ordered SLs [8].

The thermal lattice conductivities of films with different thicknesses of the individual Bi_2Te_3 and Sb_2Te_3 layers were determined [47]. The results indicate that SLs can reduce the thermal lattice conductivity. Further, the SL consisting of 1 nm Bi_2Te_3 and 5 nm Sb_2Te_3 showed the most significant reduction of the thermal lattice conductivity confirming the results in Ref. [7]. Compared to the nanoalloyed films, where thermal conductivity reduction is the result of nanocrystallinity, the epitaxial films exhibited a decreased thermal conductivity solely due to the SL structure.

However, the electrical properties for the MBE SL samples significantly deviate from the results reported in Ref. [7]. Seebeck coefficients and carrier mobilities were significantly lower and consequently the high ZT of 2.4 at room temperature could not be reproduced. It is assumed that the significantly worse electrical properties are the result of charge carrier compensation effects due to the stacking of p-type Sb_2Te_3 and n-type Bi_2Te_3 layers.

2.3 Sputtering techniques Further experiments on the deposition of nanoalloyed SLs were carried out by sputtering. Sputtering is advantageous due to its high and stable deposition rates being achieved for long deposition times. Furthermore, it is a well-established method in semiconductor industries and allows mass and cost-efficient production. To eliminate the carrier compensation effects which limited the thermoelectric performance of epitaxially grown SLs as described above, the deposited constituents need to be either solely n- or p-type semiconductors.

Thin film p-type SLs with period lengths of 12.5, 25, and 50 nm could be obtained by the nanoalloying method for $\text{Sb}_2\text{Te}_3/(\text{Bi,Sb})_2\text{Te}_3$. In this case, both single layers were p-type semiconductors.

The annealing temperature was varied ranging from 150 to 350 °C for 2 h. In addition, one sample was annealed for 24 h at 250 °C.

All films exhibited a pronounced *c*-axis texture. SLs with a period length of 12.5 nm revealed the growth of exclusively *c*-oriented grains highlighting the high quality of the film (Fig. 5), and only minor roughness was observed. Annealing temperatures above 300 °C led to an increased porosity and roughness. Below this temperature the SL structure was well developed within the polycrystalline films. Electrical properties comparable to single crystalline bulk materials were achieved with thermal conductivity between ~ 0.45 and $0.65 \text{ W m}^{-1} \text{ K}^{-1}$ and very high power factors $> 40 \mu\text{W cm}^{-1} \text{ K}^{-2}$. Furthermore, very low thermal conductivities of $\sim 0.4 \text{ W m}^{-1} \text{ K}^{-1}$ (thermal lattice conductivity $0.26 \text{ W m}^{-1} \text{ K}^{-1}$) were determined for a stacking sequence of 12.5 nm $\text{Sb}_2\text{Te}_3/12.5 \text{ nm } (\text{Bi}_{0.2}\text{Sb}_{0.8})_2\text{Te}_3$ (period length: 25 nm).

For samples annealed at 300 °C, a ZT was estimated between 1.0 and 1.9 under conservative and optimistic assumptions, respectively. Intriguingly, all data implied that

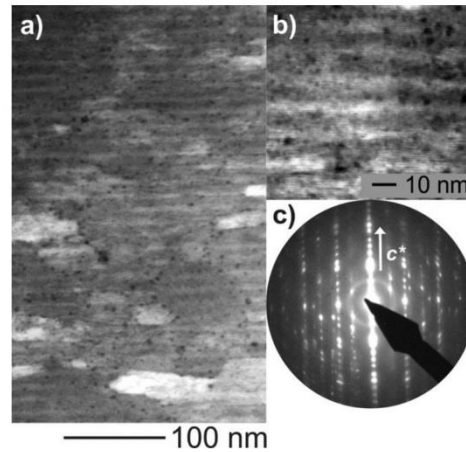


Figure 5 Panels (a) and (b) depict an overview and an enlarged STEM micrograph of a sputtered $\text{Sb}_2\text{Te}_3/(\text{Bi,Sb})_2\text{Te}_3$ sample clearly showing smooth multilayers by dark and bright contrast. Electron diffraction (panel c) verifies the high degree of *c*-texturing [47].

the SL structure has only small impact on the thermal conductivity compared to the effects of nanocrystallinity. Upscaling the film thickness to $\sim 18 \mu\text{m}$ did not alter the electrical and thermal properties. More details about syntheses and characterization were reported in Refs. [36, 47].

With the same approach it was possible to grow n-type $\text{Bi}_2\text{Te}_3/\text{Bi}_2(\text{Se,Te})_3$ SLs with high power factors [54]. The sputtering of Se may cause several problems due to the low-melting point and corresponding high vapor pressure leading to re-evaporation. In addition, it was observed for bulk materials that Se tends to segregate at grain boundaries thus leading to formation of inhomogeneities [55]. Therefore, reduction of the Se content is of practical importance. Another approach to obtain n-type, Se free films is to use n-type $(\text{Bi}_{1-x}\text{Sb}_x)_2\text{Te}_3$ to substitute $\text{Bi}_2(\text{Se,Te})_3$. The thickness of each layer of Bi_2Te_3 and $(\text{Bi}_{0.9}\text{Sb}_{0.1})_2\text{Te}_3$ was fixed at 25 nm. The samples were annealed for 2 h at varying temperatures ranging from 150 to 250 °C.

The resulting polycrystalline films showed a high degree of *c*-axis orientation. Annealing at temperatures above 250 °C led to the formation of an alloy without SL structure. For lower annealing temperatures, the SL was significantly less developed compared to the sputtered p-type $\text{Sb}_2\text{Te}_3/(\text{Bi,Sb})_2\text{Te}_3$ multilayer system discussed above.

Nevertheless, power factors of $\sim 20 \mu\text{W cm}^{-1} \text{ K}^{-2}$ were obtained. Heating the sample for 12 h at 250 °C, an increase of the power factor to $22 \mu\text{W cm}^{-1} \text{ K}^{-2}$ was obtained, and the thermal conductivity ranged from 0.55 to $0.60 \text{ W m}^{-1} \text{ K}^{-1}$. A comparison with the literature values suggests that the reduced thermal conductivity is solely attributed to the

nanocrystallinity of the films, and the SL structure had no measurable influence on the thermal conductivity. In Refs. [37, 47], more details about the materials are presented.

3 (SnSe)₂TiSe₂ turbostratically disordered compounds According to the results described above, the potential of the SL approach for enhancing the ZT value is limited. Thus, alternative structural motifs, like disordering of layered chalcogenides must be analyzed for their impact on the thermoelectric efficiency. Recently, we selected turbostratically disordered compounds which are similar to so called misfit layered compounds and show promising thermoelectric properties [56]. The general chemical formula can be described as $[(MCh)_{1+\delta}]_m (TCh_2)_n$ ($M = Sn, Pb, Sb, Bi$, rare earth metal; $T = Ti, V, Cr, Nb, Ta$; $Ch = S, Se$, δ accounts for the difference of in-plane atomic density of the respective subsystems) [57]. In comparison to misfit layered compounds, the turbostratically disordered compounds show an additional arbitrary rotation with respect to their adjoining MCh and TCh_2 layers. It was found that these structures show a significant reduction of thermal conductivity and can exhibit higher carrier concentrations and Seebeck coefficients compared to the solely misfit layered compounds [58]. Turbostratically disordered compounds are prepared by the modulated elemental reactants method (MER) where thin elemental layers with the desired stoichiometry of the subsystem are alternately deposited on a substrate. The resulting amorphous precursors self-assemble upon heating. Exemplarily, $(SnSe)_{1.2}TiSe_2$ was fabricated using a custom built high vacuum chamber ($p < 5 \times 10^{-7}$ mbar). Sn and Ti were deposited using electron beam guns. For the evaporation of Se an effusion cell was applied. $(SnSe)_{1.2}TiSe_2$ was found to form a turbostratically disordered film with Sn–Se and Ti–Se building blocks over a wide range of layer thicknesses and compositions. In accordance with the former results, the film revealed to have carrier concentrations in the range of $\sim 2 \times 10^{21} \text{ cm}^{-3}$ and the highest Seebeck coefficient measured for $TiCh_2$ ($Ch = Se, Te$) containing misfit layered compounds to date ($-77 \text{ W m}^{-1} \text{ K}^{-2}$). For $(SnSe)_{1.2}TiSe_2$, this effect is most likely caused by electron transfer from SnSe to $TiSe_2$, indicated by a negative Hall and Seebeck coefficient. For a more detailed elaboration the reader is referred to Ref. [40].

4 Cross-plane measurement techniques for thin films A major obstacle in the discussion of thin film SLs and their thermoelectric properties is the lack of measurement tools for determining the cross-plane electrical conductivity to determine the degree of anisotropy. Hence, a measurement setup for cross-plane electrical conductivity was developed. The electrical data are acquired using a Keithley SCS 4200 semiconductor characterization system in combination with a 4-point probe setup.

A major point besides the measurement setup was the development of an appropriate sample structuring routine. Demands on sample structuring were high as it was

necessary to fabricate microscale structures with high accuracy. For identification of the best set up, different structures were examined. A surprising result was yielded during an examination of the modified Transmission Line Measurement (TLM) method proposed in Refs. [7, 59]. In this method, TLM structures are produced by etching trenches with different depths between the contact pads. By measuring the resistance for different etching depths the cross-plane electrical resistance could be determined. According to our theoretical investigations, the method apparently does *not* yield correct results because it relies on assumptions that are too simple (i.e., a constant transfer length was assumed which apparently does not hold for the examined cases).

With a combined experimental and simulation approach, improved measurement structures were investigated. In previous literature reports, the role of the contacts (equipotentiality, parasitic resistances) is mostly neglected. Special attention was paid to establish equipotential electrical contacts to yield a uniform current injection, allowing calculation of the electrical resistivity from the injected current, measured voltage, and structure diameter. Finally, a novel and very accurate measurement procedure based on electrical measurements on contacted film “pillars” with different thicknesses was established (Fig. 6). The cross-plane resistivity was obtained by a linear regression of the measured resistances versus pillar heights. Thus, the contact resistance can be excluded because it only influences

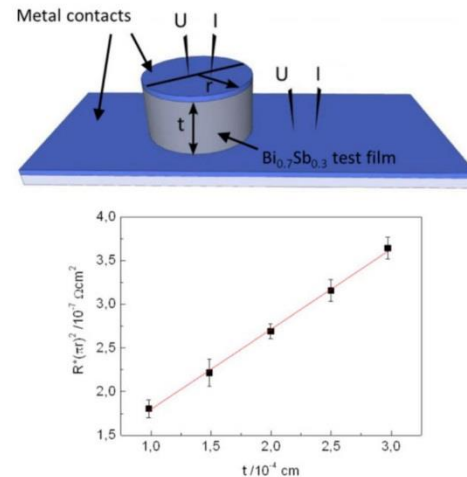


Figure 6 Top: Schematic representation of electrical cross-plane measurements on film pillars. Currents I are injected into “film pillars” with a height of t and voltages U are measured to determine the cross-plane resistances R . Bottom: The resistances R (multiplied with the pillar footprint $\pi \times r^2$) are plotted versus the pillar heights to yield the cross-plane resistivity by linear regression.

the x -intercept of the regression line. For the validation of the method, an appropriate isotropic test material ($\text{Bi}_{0.7}\text{Sb}_{0.3}$) was used in order to be able to compare the cross-plane resistivity values obtained with the setup to in-plane reference values determined with the van-der-Pauw method. The measurement yielded in average cross-plane values that differed from the reference values by less than 3%, demonstrating the excellent accuracy of the method.

5 Systems consisting of V_2VI_3 and IV-VI materials Besides layered films also bulk materials of mixed $\text{V}_2\text{VI}_3/\text{IV-VI}$ were investigated. Such systems like $\text{Bi}_2\text{Te}_3/\text{GeTe}$ offer interesting real structure property relationships with high ZT . $\text{V}_2\text{VI}_3/\text{IV-VI}$ mixed compounds exhibit a layer like structure with vacancy layers (VL) as reported for many Ge-Sb-Te and Ge-Bi-Te phases [60, 61]. The formation of VL is strongly dependent on chemical composition and thermal treatment [62] and consequently corresponding changes of thermoelectric performance are expected.

Polycrystalline powders have been synthesized in quartz ampoules at elevated temperatures by alloying GeTe and $\text{Bi}_2\text{Se}_{0.2}\text{Te}_{2.8}$. The materials were reground after cooling to room temperature and compacted by spark plasma sintering (SPS).

Sintered powders with compositions of $(1-x)(\text{GeTe})x(\text{Bi}_2\text{Se}_{0.2}\text{Te}_{2.8})$ with $x=0.038$ and 0.063 were thoroughly characterized by *in* and *ex situ* XRD and TEM experiments with focus on changes of the micro- and nanostructure during operation and processing of the materials. These heating experiments yielded a detailed picture of the alterations occurring during heat treatment. To obtain temperature dependent ZT values, the thermal conductivities and the electrical properties (Seebeck coefficient and electrical conductivity) have to be performed in two different setups by independent measurements. A detailed description of the process to determine the temperature dependent ZT can be found in Ref. [39].

For $x=0.038$, the microstructure of the as-prepared sample (no formation of VL) remained unchanged, and consequently, excellent and stable thermoelectric performance with a ZT value of 1.5 at $\sim 400^\circ\text{C}$ was obtained.

For the material with $x=0.063$, very high ZT values of about 2.0 at 450°C were measured. Similar values were also reported by other groups explaining the high ZT by a band convergence effect [63]. However, after several heating cycles ZT dropped to moderate values of about 1.0 at 400°C . XRD and TEM investigations revealed the formation of a high temperature phase and strain phenomena resulting in contrast modulation in the HRTEM micrographs. After several heating cycles, the strain was released by the formation of VL (Fig. 7).

Thermoelectric modules were also assembled with $(1-x)(\text{GeTe})x(\text{Bi}_2\text{Se}_{0.2}\text{Te}_{2.8})$ ($x=0.038$). Thermoelectric characterization was carried out for several heating and cooling cycles, exceeding the typical characterization procedures for thermoelectric materials. Very low contact resistances were

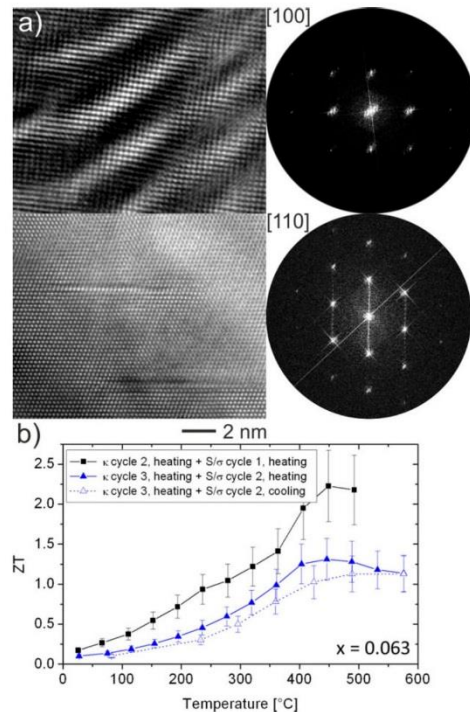


Figure 7 (a) HRTEM micrographs and corresponding FFT representing the contrast modulation due to strain (upper image) and the formation of VL after several heating cycles (lower image); (b) measured ZT values for $(1-x)(\text{GeTe})x(\text{Bi}_2\text{Se}_{0.2}\text{Te}_{2.8})$ ($x=0.063$) before (black line) and after heat cycling (blue line) [39]. Reproduced by permission of The Royal Society of Chemistry.

obtained and thermoelectric modules serving as TEG (thermoelectric generator) with a high power density of $\sim 1\text{ W cm}^{-2}$ were successfully assembled. The properties obtained from material and contact characterization were double checked for the first time by a comparison of maximum power output data with simulations taking into account the material and contact data. An excellent match between experiment and simulation was evident and confirmed the very good material and contact properties. These results highlight the importance of material integration and stability after several heating cycles as presented in detail in Ref. [39].

6 Summary Nanostructuring, like superlattices, turbostratic disorder, as well as vacancy ordering are procedures to improve thermoelectric properties of thin film and bulk materials.

Various SLs with varying degrees of ordering can be produced by methods like nanoalloying and MBE.

However, regarding the reproduction of the results presented in Ref. [7] several discrepancies still remain.

First, the unusual low anisotropy of the electrical conductivity could not be reproduced nor could theoretical calculations show that the quantum confinement leads to a decrease of the electrical anisotropy. However, precise measurements of the cross-plane electrical conductivity are necessary and newer measurement techniques as described above might lead to a significant progress in comparability.

Secondly, the reported high carrier mobility, high Seebeck coefficient, and consequently the high power factor in Ref. [7] could not be reproduced. There are strong indications that compensation effects between the majority charge carriers of n-type Bi_2Te_3 and p-type Sb_2Te_3 are responsible for the poor electrical properties. One explanation for the previously reported excellent electrical properties is that due to interdiffusion, a p-type layer of $(\text{Bi}_{1-x}\text{Sb}_x)_2\text{Te}_3$ with $x > 0.5$ layer has formed eliminating compensation effects. Another approach that might have played a role in the previous work is the use of external dopants that could lead to p-type Bi_2Te_3 layer. However, it was not reported that dopants were used.

The reduction of thermal lattice conductivity with lowest thermal conductivity for SLs of 1 nm Bi_2Te_3 and 5 nm Sb_2Te_3 could be verified.

Other promising layered materials are turbostratically disordered compounds. These compounds show an additional arbitrary rotation with respect to their adjoining layers. Hence, a further reduction of the lattice thermal conductivity was observed. Additionally, an increase of the Seebeck coefficient was found compared to the related misfit layered compounds.

However, nanostructures are often metastable and prone to degradation upon heat treatment. As it was shown for the $(\text{BiSb})_2\text{Te}_3$ SLs, step-like defects and grain boundaries can even further accelerate the decay of the SL structure. The investigation of mixed $\text{V}_2\text{VI}_3/\text{IV-VI}$ bulk materials revealed that several heat treatments lead to an alteration of the nanostructure by vacancy ordering. Consequently, the stability of nanostructures, thermoelectric properties, and hence the stability of devices are still major challenges.

Acknowledgements Financial support by the Deutsche Forschungsgemeinschaft (DFG), Priority Program 1386 (SPP 1386), is gratefully acknowledged. DCJ acknowledges support from the National Science Foundation under grant DMR-1266217. Original data of Figs. 2 and 7 can be found in Journal of Materials Chemistry and Dalton Transactions, respectively. Furthermore, the reprint permissions by Wiley and Sons, the American Chemical Society and Royal Society of Chemistry is gratefully acknowledged. TD likes to thank Niklas Wolff for additional proof reading.

References

- [1] L. D. Hicks and M. S. Dresselhaus, *Phys. Rev. B* **47**, 12727 (1993).
- [2] G. A. Slack, *CRC Handbook of Thermoelectrics* (CRC Press, Boca Raton, 1995).
- [3] K. Biswas, J. He, I. D. Blum, C.-I. Wu, T. P. Hogan, D. N. Seidman, V. P. Dravid, and M. G. Kanatzidis, *Nature* **489**, 414 (2012).
- [4] B. A. Cook, M. J. Kramer, X. Wei, J. L. Harringa, and E. M. Levin, *J. Appl. Phys.* **101**, 053715 (2007).
- [5] N. Chen, F. Gascoin, G. J. Snyder, E. Müller, G. Karpinski, and C. Stiewe, *Appl. Phys. Lett.* **87**, 171903 (2005).
- [6] G. J. Snyder and E. S. Toberer, *Nature Mater.* **7**, 105 (2008).
- [7] R. Venkatasubramanian, E. Siivola, T. Colpitts, and B. O'Quinn, *Nature* **413**, 597 (2001).
- [8] A.-L. Hansen, T. Dankwort, M. Winkler, J. Ditto, D. C. Johnson, J. D. Koenig, K. Bartholomé, L. Kienle, and W. Bensch, *Chem. Mater.* **26**, 6518 (2014).
- [9] D. Teweldebrhan, V. Goyal, and A. A. Balandin, *Nano Lett.* **10**, 1209 (2010).
- [10] K. D. Coonley, B. C. O'Quinn, J. C. Caylor, and R. Venkatasubramanian, *Mater. Res. Soc. Symp. Proc* **793**, S2.5.1 (2004).
- [11] S. Nakajima, *J. Phys. Chem. Solids* **24**, 479 (1963).
- [12] H. Cui, I. Bhat, B. C. O'Quinn, and R. Venkatasubramanian, *J. Electron. Mater.* **30**, 1376 (2001).
- [13] G. Wang, L. Endicott, and C. Uher, *Sci. Adv. Mater.* **3**, 539 (2011).
- [14] H. You, S.-H. Bae, J. Kim, J.-S. Kim and C. Park, *J. Electron. Mater.* **40**, 635 (2011).
- [15] M. N. Touzelbaev, P. Zhou, R. Venkatasubramanian, and K. E. Goodson, *J. Appl. Phys.* **90**, 763 (2001).
- [16] Y. Iwata, H. Kobayashi, S. Kikuchi, E. Hatta, and K. Mukasa, *J. Cryst. Growth* **203**, 125 (1999).
- [17] N. Peranio, O. Eibl, and J. Nurnus, *J. Appl. Phys.* **100**, 114306 (2006).
- [18] Z. Aabdin, N. Peranio, and O. Eibl, *Adv. Mater.* **24**, 4589 (2012).
- [19] J. Nurnus, H. Böttner, and A. Lambrecht, in: *Thermoelectrics Handbook: Macro to Nano*, edited by D. M. Rowe (CRC Press, Boca Raton, 2006), pp. 48–17.
- [20] B. Zheng, Z. Xiao, B. Chhay, R. L. Zimmerman, M. E. Edwards, and D. Ila, *Surf. Coat. Technol.* **203**, 2682 (2009).
- [21] Z. Xiao, K. Hedgemen, M. Harris, and E. DiMasi, *J. Vac. Sci. Technol. A* **28**, 679 (2010).
- [22] M. Winkler, J.D. König, S. Buller, U. Schürmann, L. Kienle, W. Bensch, and H. Böttner, 8th European Conference on Thermoelectrics, Como, Italy, p. 19 (2010).
- [23] C. H. Champness, P. T. Chiang, and P. Parker, *Can. J. Phys.* **43**, 653 (1965).
- [24] M.A. Ryan, J.A. Herman, and J.-P. Fleuriel, 206th Meeting of The Electrochemical Society, Inc., Abs. 238 (2004).
- [25] F. Takahashi, Y. Hamada, T. Mori, and I. Hatta, *Jpn. J. Appl. Phys.* **43**, 8325 (2004).
- [26] D. Banga, J. L. Lensch-Falk, D. L. Medlin, V. Stavila, N. Y. C. Yang, D. B. Robinson, and P. A. Sharma, *Cryst. Growth Des.* **12**, 1347 (2012).
- [27] I. Yamasaki, R. Yamanaka, M. Mikami, H. Sonobe, Y. Mori, and T. Sasaki, 17th International Conference on Thermoelectrics, Nagoya, Japan, p. 210 (1998).
- [28] M. Winkler, X. Liu, U. Schürmann, J. D. König, L. Kienle, W. Bensch, and H. Böttner, *Z. Anorg. Allg. Chem.* **638**, 2441 (2012).
- [29] R. Funahashi, I. Matsubara, H. Ikuta, T. Takeuchi, U. Mizutani, and S. Sodeoka, *Jpn. J. Appl. Phys.* **39**, L1127 (2000).
- [30] C. Wan, Y. Wang, N. Wang, and K. Koumoto, *Materials* **3**, 2606 (2010).

- [31] E. Guilmeau, Y. Bréard, and A. Maignan, *Appl. Phys. Lett.* **99**, 052107 (2011).
- [32] I. Terasaki, Y. Sasago, and K. Uchinokura, *Phys. Rev. B* **56**, 75397 (1997).
- [33] C. Chiritescu, D. G. Cahill, N. Nguyen, D. Johnson, A. Bodapati, P. Koblinski, and P. Zschack, *Science* **315**, 351 (2007).
- [34] C. Chiritescu, C. Mortensen, D. G. Cahill, D. Johnson, and P. Zschack, *J. Appl. Phys.* **106**, 073503 (2009).
- [35] J. D. König, M. Winkler, S. Buller, W. Bensch, U. Schürmann, L. Kienle, and H. Böttner, *J. Electron. Mater.* **40**, 1266 (2011).
- [36] M. Winkler, X. Liu, J. D. König, L. Kirste, H. Böttner, W. Bensch, and L. Kienle, *J. Electron. Mater.* **41**, 1322 (2012).
- [37] M. Winkler, X. Liu, A.-L. Hansen, J. D. König, W. Bensch, L. Kienle, H. Böttner, and K. Bartholomé, *Nanothermoelectrics* **1**, 1 (2013).
- [38] U. Schürmann, M. Winkler, J. D. König, X. Liu, V. Duppel, W. Bensch, H. Böttner, and L. Kienle, *Adv. Eng. Mater.* **14**, 139 (2012).
- [39] J. D. König, M. Winkler, T. Dankwort, A.-L. Hansen, H.-F. Pernau, V. Duppel, M. Jaegle, K. Bartholomé, L. Kienle, and W. Bensch, *Dalton Trans.* **44**, 2835 (2015).
- [40] D. R. Merrill, D. B. Moore, J. Ditto, D. R. Sutherland, M. Falmbigl, M. Winkler, H.-F. Pernau, and D. C. Johnson, *Eur. J. Inorg. Chem.* **83**, 83–91 (2015).
- [41] N. Peranio, M. Winkler, D. Bessas, Z. Aabdin, J. D. König, H. Böttner, R. P. Hermann, and O. Eibl, *J. Alloys Compd.* **521**, 163 (2012).
- [42] Z. Aabdin, N. Peranio, O. Eibl, W. Töllner, K. Nielsch, D. Bessas, R. P. Hermann, M. Winkler, J. D. König, H. Böttner, V. Pacheco, J. Schmidt, A. Hashibon, and C. Elsässer, *J. Electron. Mater.* **41**, 1792 (2012).
- [43] N. Peranio, M. Winkler, M. Dürrschnabel, J. D. König, and O. Eibl, *Adv. Funct. Mater.* **23**, 4969 (2013).
- [44] N. F. Hinsche, B. Y. Yavorsky, M. Gradhand, M. Czerner, M. Winkler, J. König, H. Böttner, I. Mertig, and P. Zahn, *Phys. Rev. B* **86**, 085323 (2012).
- [45] B. Y. Yavorsky, N. F. Hinsche, I. Mertig, and P. Zahn, *Phys. Rev. B* **84**, 165208 (2011).
- [46] M. Winkler, X. Liu, J. D. König, S. Buller, U. Schürmann, L. Kienle, W. Bensch, and H. Böttner, *J. Mater. Chem.* **22**, 11323 (2012).
- [47] M. Winkler, Nanostructured thermoelectrics: Bi₂Te₃/Sb₂Te₃ based superlattice systems fabricated by MBE and sputtering, Dissertation der Mathematisch-Naturwissenschaftlichen Fakultät der Eberhard Karls Universität Tübingen, 2015.
- [48] H. Li, D. Bilc, and S. D. Mahanti, *Mater. Res. Soc. Symp. Proc.* **793**, 837 (2004).
- [49] N. F. Hinsche, B. Y. Yavorsky, I. Mertig, and P. Zahn, *Phys. Rev. B* **84**, 165214 (2011).
- [50] D. C. Johnson, *Curr. Opin. Solid State Mater.* **3**, 159 (1998).
- [51] L. Fister, X. M. Le, J. McConnell, T. Novet, and D. C. Johnson, *J. Vac. Sci. Technol.* **A11**, 3014 (1993).
- [52] N. Peranio, M. Winkler, Z. Aabdin, J. König, H. Böttner, and O. Eibl, *Phys. Status Solidi A* **289**, 289 (2012).
- [53] Z. Aabdin, N. Peranio, M. Winkler, D. Bessas, J. König, R. P. Hermann, H. Böttner, and O. Eibl, *J. Electron. Mater.* **41**, 1493 (2012).
- [54] H. Böttner, A. Schubert, H. Kölbl, A. Gavrikov, A. Mahlke, and J. Nurnus, in: *Proc. ICT04: 23rd International Conference on Thermoelectrics*, Adelaide, Australia, p. 114 (2004).
- [55] R. Martin-Lopez, B. Lenoir, A. Dauscher, H. Scherrer, and S. Scherrer, *Solid State Commun.* **108**, 285 (1998).
- [56] D. R. Merrill, D. B. Moore, S. R. Bauers, M. Falmbigl, and D. C. Johnson, *Materials* **8**, 2000 (2015).
- [57] J. Rouxel, A. Meerschaut, and G. A. Wiegers, *J. Alloys Compd.* **229**, 144 (1995).
- [58] D. B. Moore, M. Beekman, S. Disch, P. Zschack, I. Häusler, W. Neumann, and D. C. Johnson, *Chem. Mater.* **25**, 2404 (2013).
- [59] R. Venkatasubramanian, in: *Recent Trends in Thermoelectric Materials Research III*, edited by T. M. Tritt, *Semiconductors and Semimetals*, Vol. 71 (Academic, San Diego, 2001), chap. 4.
- [60] O. G. Karpinsky, L. E. Shelimova, M. A. Kretova, and J.-P. Fleurial, *J. Alloys Compd.* **268**, 112 (1998).
- [61] U. Schürmann, V. Duppel, S. Buller, W. Bensch, and L. Kienle, *Cryst. Res. Technol.* **46**, 561 (2011).
- [62] T. Rosenthal, M. N. Schneider, C. Stiewe, M. Döblinger, and O. Oeckler, *Chem. Mater.* **23**, 4349 (2011).
- [63] D. Wu, L.-D. Zhao, S. Hao, Q. Jiang, F. Zheng, J. W. Doak, H. Wu, H. Chi, Y. Gelbstein, C. Uher, C. Wolverton, M. G. Kanatzidis, and J. He, *J. Am. Chem. Soc.* **136**, 11412 (2014).

2. Veröffentlichungen GeTe – Bi₂Te₃ – Sb₂Te₃

2.1 Thermoelectric efficiency of (1-x)(GeTe)x(Bi₂Se_{0.2}Te_{2.8}) and implementation into highly performing thermoelectric power generators

Mittels Spark-Plasma (SPS) verdichtete Verbindungen aus der Kombination eines klassischen Phasenwechselmaterials mit einem klassischen Thermoelektrikum (1-x)(GeTe)x(Bi₂Se_{0.2}Te_{2.8}) wurden in Abhängigkeit von der Zusammensetzung x auf die thermoelektrischen Eigenschaften untersucht. Die besten Verbindungen (x = 0.038, 0.063) wurden mit *in situ* XRD und TEM strukturell charakterisiert. Besonderes Augenmerk lag auf der Veränderung der Realstruktur durch mehrmaliges Aufheizen und Abkühlen. Während sich die Realstruktur und dementsprechend die Transporteigenschaften der Probe x = 0.038 nicht signifikant durch das Zyklisieren veränderten, konnte eine ausgeprägte Degradation des ZT-Wertes von über 2.0 auf 1.0 bei 450 °C für die Verbindung 0.937(GeTe)0.063(Bi₂Se_{0.2}Te_{2.8}) beobachtet werden. Nach dem Sinterprozess wies die Probe eine schlechte Kristallinität auf und sowohl im Röntgendiffraktogramm als auch im TEM konnten Hinweise auf das Vorhandensein einer nanokristallinen kubischen β-GeTe Hochtemperaturphase gefunden werden. Durch mehrmaliges Aufheizen der Probe auf 500 °C verbesserte sich die Kristallinität und die β-Phase verschwand. Gleichzeitig bildeten sich planare Defekte (vacancy layer) aus. Rietveld-Verfeinerungen der Diffraktogramme vor und nach dem Zyklisieren der Probe ergab einen um den Faktor 2.5 verringerten strain nach dem Heizen. Auch nach mehreren Heizzyklen der Probe mit x = 0.038 konnten keine planaren Defekte gefunden werden, was an einer zu geringen Defektdichte liegen kann. Um die thermoelektrische Effizienz zu testen, wurde ein thermoelektrischer Generator mit Bi dotiertem PbTe als n-typ Halbleiter und dem temperaturstabilen 0.962(GeTe)0.038(Bi₂Se_{0.2}Te_{2.8}) konstruiert. Dabei lag die maximale elektrische Leistung bei einer Temperaturdifferenz von 525 °C bei 0.35 W (0.97 W/cm²), was bisher nur durch wenige Materialien übertroffen wurde.

Reprinted with permission from J. König, M. Winkler, T. Dankwort, A.-L. Hansen, H.-F. Pernau, V. Duppel, M. Jaegle, K. Bartholomé, L. Kienle, W. Bensch, *Dalton Trans* **2015**, 44, 2835–2843. Copyright 2015 Royal Society of Chemistry.

Cite this: *Dalton Trans.*, 2015, **44**,
2835

Thermoelectric efficiency of (1 - x)(GeTe) x(Bi₂Se_{0.2}Te_{2.8}) and implementation into highly performing thermoelectric power generators†

J. Koenig,^a M. Winkler,^a T. Dankwort,^b A.-L. Hansen,^c H.-F. Pernau,^a V. Duppel,^d
M. Jaegle,^a K. Bartholomé,^a L. Kienle*^b and W. Bensch*^c

Here we report for the first time on a complete simulation assisted “material to module” development of a high performance thermoelectric generator (TEG) based on the combination of a phase change material and established thermoelectrics yielding the compositions (1 - x)(GeTe) x(Bi₂Se_{0.2}Te_{2.8}). For the generator design our approach for benchmarking thermoelectric materials is demonstrated which is not restricted to the determination of the intrinsically imprecise *ZT* value but includes the implementation of the material into a TEG. This approach is enabling a much more reliable benchmarking of thermoelectric materials for TEG application. Furthermore we analyzed the microstructure and performance close to in-operandi conditions for two different compositions in order to demonstrate the sensitivity of the material against processing and thermal cycling. For *x* = 0.038 the microstructure of the as-prepared material remains unchanged, consequently, excellent and stable thermoelectric performance as prerequisites for TEG production was obtained. For *x* = 0.063 we observed strain phenomena for the pristine state which are released by the formation of planar defects after thermal cycling. Consequently the thermoelectric performance degrades significantly. These findings highlight a complication for deriving the correlation of microstructure and properties of thermoelectric materials in general.

Received 7th November 2014,
Accepted 17th December 2014

DOI: 10.1039/c4dt03425b

www.rsc.org/dalton

1. Introduction

Thermoelectric generators (TEG) are used in radioisotopic power systems as energy sources for space exploration since the early 1960s.^{1,2} As a pure solid state device TEGs can convert a heat flux partially into an electrical current using the Seebeck effect. TEG consists of several n- and p-type conducting elements (so called legs) which are electrically connected in series while the heat flow from the electrical hot side contacts through the thermoelectric material to the electrical cold side contacts. The module is covered on the hot and cold side by insulating (ceramic) plates as thermal contacts and in order to obtain a better handling. The critical point for wide terrestrial application

is the low conversion efficiency of the thermoelectric material and the commercial unavailability of TEGs for high temperature applications up to ~500 °C. The conversion efficiency is directly related to the material-specific figure of merit *Z* at an absolute temperature *T* which can be calculated according to

$$ZT = \frac{\sigma \cdot S^2 \cdot T}{\kappa} \quad (1)$$

All physical transport parameters in eqn (1) (*S*: Seebeck coefficient, σ : electrical conductivity, κ : thermal conductivity) are temperature dependent. In recent years, great efforts were undertaken to improve the *ZT* value of various classes of thermoelectric materials, mainly degenerated semiconductors, applying different concepts. The main efforts are devoted to a reduction of the thermal conductivity and the improvement of the electrical properties which can be achieved using solid solutions, improving the nanostructuring, introducing nano-inclusions in bulk materials, increasing the disorder in thin film based materials, or by band structure engineering.^{3–20} Generally, it is difficult to evaluate the suitability of different materials since there is a measurement uncertainty (estimated values given below) for each of the values *S*, σ , and κ contributing to the figure of merit *ZT*, adding up to a total uncertainty

^aFraunhofer Institute for Physical Measurement Techniques IPM, Thermoelectric Systems, Heidenhofstraße 8, 79110 Freiburg, Germany

^bInstitute for Materials Science, Synthesis and Real Structure, Christian-Albrechts-University, Kaiserstr. 2, 24143 Kiel, Germany. E-mail: lk@tf.uni-kiel.de

^cInstitute of Inorganic Chemistry, Christian-Albrechts-University, Max-Eyth Str. 2, 24118 Kiel, Germany. E-mail: wbensch@ac.uni-kiel.de

^dMax Planck Institute for Solid State Research, Heisenbergstrasse 1, 70569 Stuttgart, Germany

† Electronic supplementary information (ESI) available: Including Fig. S1–S10. See DOI: 10.1039/c4dt03425b

on ZT as large as 20 to 50%, depending on whether Gaussian or linear error propagation is assumed. In this context we note that until today there is a lack of standardized test procedures and reference materials for thermoelectric transport property measurement particularly at high temperature.²¹ Only recently, a low-temperature standard reference material for the Seebeck coefficient from 10 K to 390 K became available by the National Institute of Standards and Technology (NIST).²²

Evidently, a more solid experimental proof of a high ZT material is highly desirable and can be achieved by the implementation of the material in a TEG and the comparison of the output power with simulated results. In this context, besides a high ZT value a low contact resistance between the thermoelectric material and electrical contact structure is another, yet frequently overlooked prerequisite for any application in terms of high power generation efficiency.

Here we report on the development of a TEG with a new stable high ZT material and low resistant contacts for space applications together with an experimental proof of high power performance. The high ZT material is chosen from the range of phase change materials (PCMs) combined with the classical thermoelectric alloys $\text{Bi}_2\text{Te}_3/\text{Bi}_2\text{Se}_3$. PCMs are mainly Ge-Sb based tellurides which play *e.g.* an important role in several types of data storage media.^{23–30} Bi_2Te_3 based thermoelectric materials are intensively studied for a long time and such materials are prepared as films, in form of superlattices, as bulk or nanostructured material.^{31–46}

Similar to classic thermoelectric materials, many PCMs are small-band gap semiconductors with low thermal conductivity. For this reason, PCMs have become interesting as thermoelectric materials, particularly since they are known to exhibit lamellar and unusual nanostructures^{47–49} which have the potential to further reduce thermal conductivity and thus increase ZT .⁵⁰ For example, $(\text{GeTe})_{1-x}\text{Sb}_x\text{Te}_3$ located on the pseudobinary section of the classic IV–VI and V–VI thermoelectric materials GeTe and Sb_2Te_3 was shown to have a ZT of 1.3 at 450 °C.⁵¹ Similar research was carried out on some members of the $(\text{GeTe})_n(\text{Bi}_2\text{Te}_3)_m$ series yielding lower ZT values in the range of 0.5 to 1.2.^{52–55}

However, to the author's best knowledge no attempts have been published to actually use any PCM and thermoelectric materials to fabricate and characterize a working and efficient thermoelectric module including, among other technical challenges, the necessary development of low-resistance electrical contacts.

2. Material and methods

2.1. Synthesis

In a first step raw materials were produced. Ingots of Bi-doped PbTe, GeTe and $\text{Bi}_2\text{Se}_{0.2}\text{Te}_{2.8}$ were prepared *via* high-temperature solid state reactions from the elements. Ge (Alfa Aesar, 99.999%), Te (Chempur, 99.999% low oxygen), Bi (Chempur, 99.9999%), Se (Chempur, 99.999%) and Pb (Mateck, 99.999%) with an element mole ratio corresponding to the stoichiometric composition were sealed into freshly cleaned quartz ampoules under vacuum. The ampoules were then heated up by a H_2 -flame (samples with $x < 0.108$ and Bi:PbTe) above the melting point or to 800 °C in a rocking furnace (other samples) for two hours and then cooled down in air at room temperature. Thereafter, the ingots of GeTe and $\text{Bi}_2\text{Se}_{0.2}\text{Te}_{2.8}$ were re-ground in a glovebox. Afterwards, the two obtained powders were mixed, again molten and cooled to yield p-type ingots of $(1-x)(\text{GeTe})_x(\text{Bi}_2\text{Se}_{0.2}\text{Te}_{2.8})$ with weight proportions $x = 0.038, 0.063, 0.087, 0.108$ and 0.128 (corresponding mole proportions are given in Table 2). Next, these ingots and those of Bi:PbTe were milled and separately compacted using the Spark-Plasma Sintering (SPS) technique⁵⁶ in order to obtain a dense and mechanically robust sinter bodies ($T = 550$ °C and 500 °C for $(1-x)(\text{GeTe})_x(\text{Bi}_2\text{Se}_{0.2}\text{Te}_{2.8})$ and Bi:PbTe, heating rate of 50 K min^{-1}). A pressure of 4kN corresponding to a uniaxial pressure of 50 MPa was applied while the samples were held at the respective temperature for 10 min.

EDX analyses prove the presence of Bi by significant intensity of the Bi M-line, however no significant Se content could be identified. (*cf.* Fig. S1†).

Characterization was carried out for three sample conditions: 1. The so called "pristine" state referring to the ingots grown in quartz ampoules, 2. The SPS-compacted samples prepared from the pristine sample and 3. The SPS-compacted samples after thermal cycling in the two thermoelectric characterization setups described below.

2.2. Structure analysis

X-ray powder diffraction data for $0.937(\text{GeTe})_0.063(\text{Bi}_2\text{Se}_{0.2}\text{Te}_{2.8})$ were collected within the temperature range of 20 °C and 500 °C on a Philips X'Pert Pro X-ray diffractometer (Ni filtered Cu K α radiation, $\lambda_1 = 1.54056$ Å and $\lambda_2 = 1.54439$ Å, PIXCel detector). Data were collected in a flat plate θ/θ geometry from 20 to 90° in steps of 0.039° with an effective scan time of 800 s per step. *In situ* heating experiments were performed in an Anton-Paar HTK 1200 high temperature chamber. The temperature protocol was adjusted in order to simulate the thermal cycling procedure described for the thermoelectric characterization.

Structural refinements were carried out by Rietveld analysis using the program TOPAS Academic.⁵⁷ To obtain information about the structural reason of the line broadening (stress and strain within the structure), the instrumental contribution has been taken into account using the fundamental parameter approach.⁵⁸ A trigonal model (space group $R\bar{3}m$) and a cubic model (space group $Fm\bar{3}m$) were employed according to the low (α) and high temperature (β) phases of GeTe, respectively. In case of the α -GeTe-type the rhombohedral setting ($a \approx 4.29$ Å) is applied. Bi/Ge and Se/Te are placed on the Wyckoff position 1a (x, x, x) with $x \approx 0.53$ and $x = 0$, respectively. For the cubic β -GeTe-type the lattice parameter is $a \approx 6.0$ Å with Bi and Ge atoms located on 4a (0, 0, 0) and Te and Se sharing the 4b site (0.5, 0.5, 0.5).

SAED (selected area electron diffraction) patterns and high resolution images of the specimens were recorded with a Phillips CM30/ST microscope (operated at 300 kV, LaB₆

cathode) using a GATAN slow scan CCD camera. For elemental analyses by EDX performed in the TEM a nanoprobe mode was adjusted (Si/Li detector, system Noran NSF 7). Moreover, TEM investigations were performed in a Teana F30 G²-STwin microscope at 300 kV with a field emission gun cathode and Si/Li detector (EDAX System) for EDX analysis. For TEM preparation, grinded specimens were suspended in n-butanol and the dispersion was placed onto holey-carbon copper grid.

2.3. Thermoelectric property characterization

The electrical characterization (Tables 1 and 2) at room temperature was carried out on 1 mm thick samples as follows: The electrical conductivity, charge carrier mobility and charge carrier concentration of the samples were determined in-plane at room temperature by Hall-effect measurements using the Van-der-Pauw method (samples contacted with gold-coated pins) with an uncertainty of *ca.* 5% for the conductivity and *ca.* 10% for the charge carrier mobility and concentration. The Seebeck coefficient *S* was measured in-plane at room temperature *via* a homebuilt setup calibrated with a Ni reference (measurement uncertainty *ca.* ~5%).

For the temperature dependent electrical measurements of *S* (measurement uncertainty *ca.* 7%) and σ (uncertainty *ca.* 10%) on the SPS-compacted samples the setup SRX developed by Fraunhofer IPM was used.⁵⁸ The sample chamber was evacuated and then kept under a nitrogen pressure of 100 mbar. The thermal conductivity was determined as the product of thermal diffusivity, density and heat capacity with a total measurement uncertainty of *ca.* 10%. These properties were measured using a Netzsch LFA 457 (an apparatus based on the laser flash method which determines thermal diffusivity and heat capacity) and a balance/micrometer screw (density). The value for *ZT* calculated from the electrical properties and thermal conductivities is presented assuming Gaussian error propagation.

For the thermal cycling two different setups had to be used subsequently. Therefore, a standard procedure for such measurements was developed: First, a so-called κ -cycle was performed by measuring the thermal conductivity within a temperature cycle until κ stabilized. Afterwards, the samples were cycled in the Seebeck/conductivity setup (so-called *S*/ σ -cycle) in order to receive data for *ZT* calculation. This “benchmarking” procedure, *i.e.* the collection of transport data in multiple heating/cooling cycles particularly serves for probing the reproducibility of the data and to characterize the fatigue resistance of the material under thermal influence. We also note that such procedure exceeds the usually applied temperature-dependent characterization of thermoelectric materials, since it is common to only heat up the sample once while the transport properties are recorded.

The values for the contact resistances were determined with a homebuilt setup based on a 4-wire method (current: of 30 mA) by measuring the voltage drop between the front electrical contact and a voltage probe needle which was scanned from back contact to front contact across the whole length of the thermoelectric leg including the contact material layers. Dividing the measured voltage drop by the applied current flowing through the leg yields a resistance value for each distance between front contact and probe needle. The contact resistance between leg and contact can readily be determined from a plot of resistance *versus* distance by measuring the sharp resistance drop when scanning over the leg to contact interface.

The assembled module was characterized using a homebuilt system under nitrogen atmosphere.⁵⁹

The module performance is characterized by the maximum power P_{Max} under resistance-matched conditions which is given by $P_{\text{Max}} = U_{\text{O}}/4R_{\text{i}}$ with U_{O} as module open-circuit voltage and R_{i} as internal module resistance. The cold side temperature was maintained at typically 15–20 °C by a cooler.

Table 1 Transport properties of Bi-doped PbTe, GeTe and Bi₂Se_{0.2}Te_{2.8} at room temperature. For all compounds, two samples from different synthesis runs were analyzed, demonstrating a very good reproducibility of the process

Composition (a = after SPS, i = pristine)	Seebeck coefficient [$\mu\text{V K}^{-1}$]	Electrical conductivity [S cm^{-1}]	Carrier concentration [cm^{-3}]	Carrier mobility [$\text{cm}^2 \text{V}^{-1} \text{s}^{-1}$]
Bi : PbTe (a)	-80 ± 4	2750 ± 140	$2.0 \times 10^{19} \pm 0.2 \times 10^{19}$	-840 ± 80
Bi : PbTe (i)	-87 ± 4	2530 ± 130	$1.9 \times 10^{19} \pm 0.19 \times 10^{19}$	-850 ± 90
Bi ₂ Se _{0.2} Te _{2.8} (i)	-212 ± 11	333 ± 17	$1.5 \times 10^{19} \pm 0.15 \times 10^{19}$	-141 ± 14
Bi ₂ Se _{0.2} Te _{2.8} (a)	-202 ± 10			
GeTe (i)	35 ± 2	5200 ± 300	$5.0 \times 10^{21} \pm 0.5 \times 10^{21}$	56 ± 6
GeTe (a)	36 ± 2	5100 ± 300		

Table 2 Thermoelectric properties of p-type (1 - x)(GeTe) x(Bi₂Se_{0.2}Te_{2.8}) sinter bodies at room temperature with x as weight/atomic proportion

Proportion x [wt./at.]	Seebeck coefficient [$\mu\text{V K}^{-1}$]	Electrical conductivity [S cm^{-1}]	Carrier concentration [cm^{-3}]	Carrier mobility [$\text{cm}^2 \text{V}^{-1} \text{s}^{-1}$]	Thermal conductivity [$\text{W m}^{-1} \text{K}^{-1}$]
0.038/0.0098	34 ± 2	6400 ± 300	$1.2 \times 10^{21} \pm 0.12 \times 10^{21}$	34 ± 3	6.1 ± 0.6
0.063/0.0168	42 ± 2	4800 ± 200	$9.2 \times 10^{20} \pm 0.9 \times 10^{20}$	33 ± 3	4.8 ± 0.5
0.087/0.0236	56 ± 3	3680 ± 180	$5.8 \times 10^{20} \pm 0.6 \times 10^{20}$	40 ± 4	3.8 ± 0.4
0.108/0.0298	58 ± 3	2540 ± 130	$6.0 \times 10^{20} \pm 0.6 \times 10^{20}$	27 ± 3	2.8 ± 0.3
0.128/0.0360	61 ± 3	3330 ± 170	$5.6 \times 10^{20} \pm 0.6 \times 10^{20}$	37 ± 4	3.3 ± 0.3

The uncertainty for the maximum power measurement was estimated to ca. 3–5%. Note that the uncertainty of P_{Max} is significantly lower than the one of ZT , thus enabling a much more reliable benchmarking of thermoelectric materials for TEG application.

“Multiphysics” finite element modeling was employed for the simulation of module properties. A description of the used thermoelectric coupled field equations is given in the ref. 60 and 61. The temperature dependence of the transport properties as well as the thermal radiation were included in the model.

3. Results and discussion

3.1. Transport properties of constituent materials at room temperature

The transport properties of GeTe and $\text{Bi}_2\text{Se}_{0.2}\text{Te}_{2.8}$ that serve as “raw materials” for the synthesis of p-type $(1-x)(\text{GeTe})x(\text{Bi}_2\text{Se}_{0.2}\text{Te}_{2.8})$ are summarized in Table 1. Additionally, the properties of the complementary Bi-doped n-type material PbTe are listed. High Seebeck coefficients and/or carrier mobilities indicate that PbTe and $\text{Bi}_2\text{Se}_{0.2}\text{Te}_{2.8}$ are stoichiometric. Consistent with reference data, substituting pure p-type Bi_2Te_3 with Bi_2Se_3 yields the ternary n-type $\text{Bi}_2\text{Se}_{0.2}\text{Te}_{2.8}$ with low charge carrier concentration,⁶² cf. Table 1.

The application of pure GeTe for TEG is known to be complicated by the formation of Ge vacancies (Te content ca. 50.4–51.5 at%) and the corresponding high carrier concentration (up to $2.2 \times 10^{21} \text{ cm}^{-3}$).^{54,63} These vacancies can be eliminated by adding small amounts of Bi_2Te_3 . Thus, the thermoelectric properties are enhanced due to the reduction of the carrier concentration and improvement of the Seebeck coefficient.⁶³ In addition alloying also reduces the thermal conductivity due to enhanced point defect scattering. Thus, alloying of GeTe with $\text{Bi}_2\text{Se}_{0.2}\text{Te}_{2.8}$ to form $(1-x)(\text{GeTe})x(\text{Bi}_2\text{Se}_{0.2}\text{Te}_{2.8})$ should further improve the thermoelectric properties compared to $(1-x)(\text{GeTe})x(\text{Bi}_2\text{Te}_3)$. As can be seen from the data compiled in Table 2, alloying GeTe with $\text{Bi}_2\text{Se}_{0.2}\text{Te}_{2.8}$ in different ratios greatly affects the carrier concentration analogous to Bi_2Te_3 , i.e. a reduction by almost a factor of 10 from $5 \times 10^{21} \text{ cm}^{-3}$ down to $6 \times 10^{20} \text{ cm}^{-3}$. On the other hand, the decrease of the carrier concentration is accompanied by a reduction of the electrical conductivity by a factor of two, while the Seebeck coefficient is increased by almost the same factor. As expected, increasing the $\text{Bi}_2\text{Se}_{0.2}\text{Te}_{2.8}$ content is also accompanied by a reduction of thermal conductivity. All these changes have a beneficial effect on the thermoelectric performance of the materials, which is expressed in an increase of the value for ZT by a factor of 4 according to eqn (1).

3.2. Transport properties in dependence of temperature and thermal cycling

In order to evaluate the properties and the stability of the material for high temperature application, two compacted samples by spark plasma sintered (SPS) $(1-x)(\text{GeTe})x(\text{Bi}_2\text{Se}_{0.2}\text{Te}_{2.8})$ with

$x = 0.038$ and 0.063 were subjected to the benchmarking procedure described in the Experimental section.

3.2.1. $0.962(\text{GeTe})0.038(\text{Bi}_2\text{Se}_{0.2}\text{Te}_{2.8})$. First, the thermal conductivity (κ) was characterized. Two x -cycles need to be performed until stabilization of the thermal conductivity was observed (Fig. 1a). Afterwards, one full S/σ -cycle was introduced (Fig. 1b and c). The electrical conductivity at room temperature is very high, and as expected for a non-compensated semiconductor, the Seebeck coefficient (S) increases with temperature and the electrical conductivity (σ) decreases. While a certain reduction of σ may be evident at room temperature after completing one heating and cooling cycle, it appears that the transport properties have not degraded significantly, indicating that the material properties are relatively stable under thermal influence. Such stability represents a very important material's demand for possible applications, particularly in the field of TEG.⁶⁴ Besides stability, the thermoelectric performance is excellent, reaching ZT values of 1.5 at $\sim 530 \text{ }^\circ\text{C}$ (Fig. 2) which is comparable to state of the art p-type material TAGS (Tellurium–Silver–Germanium–Antimony).^{65–67}

At a temperature of 300–400 $^\circ\text{C}$, a change in slope of the electrical conductivity vs. temperature is evident. We note that this effect is likely to stem from a band convergence effect which was reported very recently for GeTe doped with PbTe

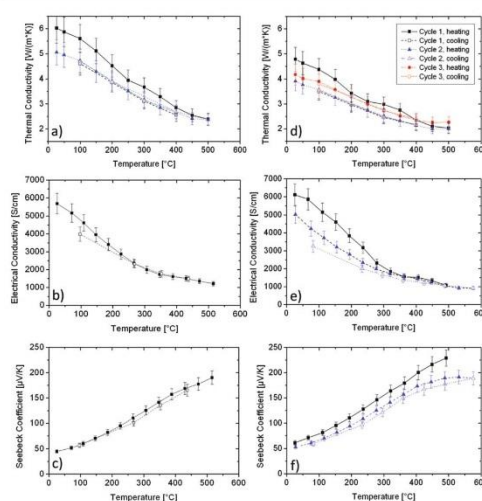


Fig. 1 Left: Transport data of SPS-compacted $0.962(\text{GeTe})0.038(\text{Bi}_2\text{Se}_{0.2}\text{Te}_{2.8})$ in dependence on temperature. (a) Thermal conductivity, acquired for two heating/cooling cycles. The data acquired for heating and cooling in cycle two are nearly identical. (b) Electrical conductivity and (c) Seebeck coefficient, both acquired for one cycle. Full data points: heating, empty points: cooling. Right: transport data of SPS-compacted $0.937(\text{GeTe})0.063(\text{Bi}_2\text{Se}_{0.2}\text{Te}_{2.8})$ in dependence on temperature. (d) Thermal conductivity, acquired for three heating/cooling cycles. (e) Electrical conductivity and (f) Seebeck coefficient, both acquired for two cycles. Full data points: heating, empty points: cooling.

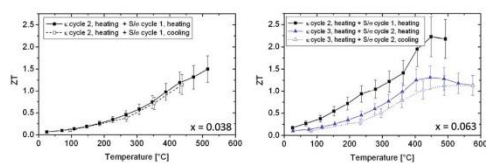


Fig. 2 Figure of merit ZT of SPS-compacted $(1-x)(\text{GeTe})x(\text{Bi}_2\text{Se}_{0.2}\text{Te}_{2.8})$ in dependence on temperature for $x = 0.038$ (left) and $x = 0.063$ (right). The thermoelectric properties of $0.937(\text{GeTe})0.063(\text{Bi}_2\text{Se}_{0.2}\text{Te}_{2.8})$ are apparently not stable under heat treatment. The transport property data used to calculate ZT is indicated in the caption. For temperatures above $500\text{ }^\circ\text{C}$, the thermal conductivity data was extrapolated to values at temperatures corresponding to the S/σ measurements.

and Bi_2Te_3 .⁶⁸ In the mentioned work, it was concluded that at these temperatures the Hall coefficient decreases and contributions of the second heavy valence band become significant.

3.2.2. $0.937(\text{GeTe})0.063(\text{Bi}_2\text{Se}_{0.2}\text{Te}_{2.8})$. Measurements were performed in two sequences. First, two full κ cycles and one half S/σ -cycle was carried out in order to calculate ZT values serving as reference for degradation processes. Second, a further full S/σ cycle was carried out, followed by a third κ cycle to determine κ values that corresponded as closely as possible to the last S/σ -values for calculation of ZT . While an outstanding maximum ZT value larger than 2 was observed after the first sequence which is even higher than for $0.962(\text{GeTe})0.038(\text{Bi}_2\text{Se}_{0.2}\text{Te}_{2.8})$, unlike with this material the electrical properties of $0.937(\text{GeTe})0.063(\text{Bi}_2\text{Se}_{0.2}\text{Te}_{2.8})$ degraded significantly during further heating/cooling cycles (Fig. 1e), finally leading to a significantly lower ZT value (Fig. 2). The decay in ZT is particularly evident at higher temperatures, we note that this is due to a decrease of S and simultaneous increase of κ . The results demonstrate that repeated thermal cycling could be of great importance to determine whether the thermoelectric properties exhibit long-term stability. However, it is very common in literature to present the data just for one heating cycle, possibly the first one yielding the best ZT values. As a consequence, one may assume that the large spread of ZT values reported by different groups for the same or very similar materials is due to missing information about thermal pre-treatments of the materials.

3.3. Structural analysis of $0.937(\text{GeTe})0.063(\text{Bi}_2\text{Se}_{0.2}\text{Te}_{2.8})$

All three processing stages (*cf.* Experimental section) of $0.937(\text{GeTe})0.063(\text{Bi}_2\text{Se}_{0.2}\text{Te}_{2.8})$ were investigated *via* X-ray powder diffraction *ex situ* and by TEM. Moreover, *in situ* XRD measurements were performed to investigate the structural changes that occur during the temperature cycling by heating up a SPS compacted sample up to $500\text{ }^\circ\text{C}$ and cooling down to room temperature.

Polymorphism is well known in the GeTe system.⁶⁹ GeTe crystallizes in the low temperature α -phase (space group $R\bar{3}m$) which can be described as a distorted NaCl-type structure and transforms into the parent structure type (β -phase, space

group $Fm\bar{3}m$) in the temperature range from 390 to $460\text{ }^\circ\text{C}$ depending on the actual composition.^{70,71} Abrikosov *et al.* reported the solubility of Bi_2Te_3 in GeTe to be about 5% .⁷²

For the low temperature phase vacancies lead to the formation of planar defects which have been frequently observed and were attributed to vacancy layers. From this it is also known that the doping concentration and the heat treatment significantly influence the formation of planar defects indicating that their formation is associated with diffusion processes.^{49,73}

The X-ray powder diffraction data show that $0.937(\text{GeTe})0.063(\text{Bi}_2\text{Se}_{0.2}\text{Te}_{2.8})$ crystallizes in single α -phase for the pristine state and after thermal cycling (Fig. 3a and c). Rietveld refinements evidence the presence of the low temperature α -GeTe-type structure, *cf.* Fig. S2[†] and the refined crystallographic parameters summarized in Table 3. For the pristine sample, planar defects like vacancy layers were only very rarely noticed by TEM, but HRTEM micrographs display micron-sized twin domains (see Fig. S3[†]) and additionally broad contrast fringes on a much smaller scale. The fringe spacing is around $3\text{--}5\text{ nm}$. To the authors best knowledge such fringes were not described before for doped GeTe. Fourier analysis of these

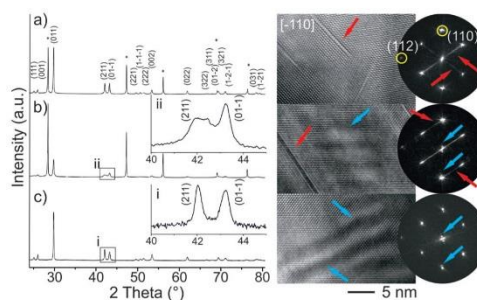


Fig. 3 Powder diffraction pattern and high resolution micrographs including corresponding FFTs of $0.937(\text{GeTe})0.063(\text{Bi}_2\text{Se}_{0.2}\text{Te}_{2.8})$ of the three different processing stages. Figure a, b and c represent XRD and TEM data of the sample after heat cycling, after SPS and in pristine stage, respectively. The reflections in the powder diffraction pattern (* mark the reflections of the internal Si standard) and the FFTs were indexed according to the rhombohedral setting of the space group $R\bar{3}m$. The insets i and ii represent enlarged sections of the (111) and (001) reflections of the powder diffraction pattern in b and c, respectively. Red and blue arrows in the HRTEM micrographs and the FFTs mark planar defects with corresponding diffuse intensities and the fringes with corresponding additional reflections in the FFTs, respectively.

Table 3 Refined parameters for the samples of $0.937(\text{GeTe})0.063(\text{Bi}_2\text{Se}_{0.2}\text{Te}_{2.8})$ at room temperature

x	Pristine	After SPS	Cubic metastable phase	After thermal cycling
Lattice parameters	$a = 4.2905(2)\text{ \AA}$ $\alpha = 58.264(3)^\circ$	$a = 4.2979(5)\text{ \AA}$ $\alpha = 58.24(1)^\circ$	$a = 6.008(1)\text{ \AA}$	$a = 4.2946(1)\text{ \AA}$ $\alpha = 58.346(3)^\circ$
R_{Bragg}	0.0530	0.0399	0.0408	0.0197

areas show satellites next to fundamental peaks assigned to the α -GeTe-type structure. As demonstrated by Fourier filtering the fringe contrast correlates with the satellite intensities, cf. Fig. S4.† In case of the $\langle -110 \rangle$ zone axis, streaks made of several satellite reflections are mostly aligned parallel to $\langle 110 \rangle$. However, depending on the fringe orientation in HRTEM micrographs the alignment of the satellite reflections could vary. One possible explanation for the fringes is based on areas where vacancies start to agglomerate thus domains with differently pronounced deviations from cubic metrics may coexist. Consequently, the fringes can be rationalized by a superposition of the α -phase and the β -phase structures with rhombohedral angles of 58.4° and 60° (primitive pseudocubic representation), respectively (see Fig. S5†). Due to the absence of planar defects one might speculate that the fringes represent preliminary stages of vacancy aggregation and thus initial stages of the vacancy layer formation.

As can be seen in Fig. 3b, the diffraction pattern after the SPS process shows less intense and broader reflections, which indicate a distorted structure and a loss of long range order. This finding is confirmed by electron diffraction (not shown) and HRTEM. Additional overlapping reflections occur, which could be assigned to the β -phase being metastable at room temperature. During the thermal cycling these additional reflections disappear cf. XRD pattern in Fig. 3a.

The peak broadening and the existence of β -phase can be explained by considering that during SPS the structure was heated above the phase transition temperature. Subsequent cooling is performed rapidly, thus, metastable cubic domains remained in the material. The broadening of the reflections refers to an increase of strain. HRTEM micrographs show frequently spatially confined planar defects and less pronounced contrast fringes. The spatially confined defects are indicated by dark and bright line contrast in HRTEM micrographs and corresponding diffuse scattering in the FFTs along the $\langle 111 \rangle$ and $\langle 001 \rangle$ directions, cf. Fig. 3 (right column).

Rietveld refinements performed on samples before and after thermal cycling indicate a strain release by a factor 2.5. Since the reflections of the metastable β -phase and the α -phase overlap in the diffraction pattern the absolute values of the strain analysis are not unambiguous hence the ratio is specified above.⁷⁴

After performing several heating cycles neither planar defects nor fringes were observed for the sample $0.962(\text{GeTe})\ 0.038(\text{Bi}_2\text{Se}_{0.2}\text{Te}_{2.8})$. It can be assumed that the concentration of vacancies is too low to form aggregates as can be seen in Fig. S6,† where a representative comparison of both samples after thermal cycling is depicted.

In order to investigate the structural changes during the thermal cycling, *in situ* XRD measurements have been performed. As can be seen in Fig. 4 the reflections become sharper after every heat cycle, due to an increase of the crystallinity and the relaxation of the formerly strained structure. Moreover, the disappearance of the metastable cubic phase is evident from the diffractograms recorded after the first and second cycle. The third cycle doesn't reveal changes compared

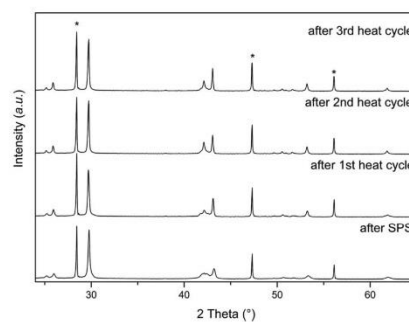


Fig. 4 Powder diffraction patterns of $0.937(\text{GeTe})\ 0.063(\text{Bi}_2\text{Se}_{0.2}\text{Te}_{2.8})$ recorded on thermally cycled samples (measured at 100°C , asterisks mark the reflections of the internal Si standard).

to the second cycle. Thus, it can be concluded that one heating cycle is not enough to fully relax the strained structure.

3.4. Module fabrication

The most critical challenges regarding module fabrication deal with the electrical contacts between the n- and p-type thermoelectric material and the metallic interconnects. The contacts should be mechanically and chemically stable up to temperatures beyond the working temperature; they should provide low ohmic contact resistance and should not poison the thermoelectric material. Moreover, matching thermal expansion coefficients between the thermoelectric material and the contacts are required in order to reduce mechanical stress during thermal cycling.

3.4.1. Complementary n-type material Bi:PbTe. For assembling a thermoelectric module with the p-type $0.962(\text{GeTe})\ 0.038(\text{Bi}_2\text{Se}_{0.2}\text{Te}_{2.8})$, n-type Bi-doped PbTe was chosen as complementary material. Room temperature transport data are given in Table 1, while the corresponding transport properties and ZT values as function of temperature are shown in Fig. S7 and S8.† A figure of merit of *ca.* $ZT = 0.9$ is obtained at 350°C , which is comparable to the best values published for n-type PbTe ($ZT \sim 1$).⁷⁵

3.4.2. Formation of low-resistance electrical contacts. For $(1-x)(\text{GeTe})\ x(\text{Bi}_2\text{Se}_{0.2}\text{Te}_{2.8})$ the heavily degenerate p-type semiconductor SnTe with a metal-like carrier concentration⁷⁶ in the range of 10^{20} – $10^{21}\ \text{cm}^{-3}$ was used to form a contact to the Ni back electrode that connects the thermoelectric legs. The front- and back side SnTe contacts with a thickness around 1 μm were introduced by SPS-compacting them with the thermoelectric material in one step. Homogenous thickness of the contact layers was adjusted by a stepwise filling of the powders into the graphite die followed by pre-compacting of each layer.

Contact resistances were determined as described in the Experimental section. As shown in Fig. S9,† the resistance drop upon scanning over the leg to contact interface is very small, yielding a very low electrical contact resistance with the

average value of $(3.2 \pm 0.8) \times 10^{-10} \Omega \text{ m}^2$ being lower than typical values reported for thermoelectric modules. We note that such values are rarely given in literature and were not found for the material system considered here. The values given for metal contacts to skutterudite materials by Caillat *et al.*⁷⁷ and Zhao *et al.*⁷⁸ of $<5 \times 10^{-10} \Omega \text{ m}^2$ and $20\text{--}30 \times 10^{-10} \Omega \text{ m}^2$, respectively, can serve as a reference.

For n-type PbTe, Ni was found to join well to this material using SPS. The low-resistance in the range of $0.75\text{--}1.9 \times 10^{-9} \Omega \text{ m}^2$ and temperature-stability of the contact material could be confirmed.⁷⁸ For all contacts optical and SEM inspection proved that they are mechanically stable and free of cracks at the contact-material interface.

3.4.3. Module assembly. Thermoelectric modules with 8 p/n leg pairs were fabricated from stable $0.962(\text{GeTe})_0.038(\text{Bi}_2\text{Se}_{0.2}\text{Te}_{2.8})$ and Bi : PbTe with the presented low-ohmic contacts. As interconnect material, a Ni foil of 200 μm thickness was used. Legs with a relatively small cross-section area (1.5 mm \times 1.5 mm), a height of 6.2 mm and a distance of 3 mm between each leg were used, resulting in a small fill factor and a high efficiency. The small cross-section was chosen to minimize stability problems due to the mismatch of the thermal expansion coefficients of Bi : PbTe and SnTe to Ni. In units of 10^{-6} K^{-1} these are 19.8, 21.3 and 13.4 for PbTe, SnTe and Ni, respectively.⁷⁹ In a first step, the legs were connected to the contact material. Afterwards, ceramic plates (AlN, 500 μm thickness) were glued on top and bottom of the contact to increase the stability of the module and to simplify handling. A schematic drawing of the complete module is shown in Fig. S10.†

The module was analyzed with the module characterization system developed at Fraunhofer IPM by heating the upper side and cooling the cold side to 25 °C. The module proved to be stable during heat treatment and did not develop any cracks in the investigated temperature range up to a temperature difference ΔT of 550 K. The maximum power output obtained under resistance-matched operation in dependence of ΔT is plotted in Fig. 5.

The maximum electrical power output with a heater temperature of 550 °C and a cold side temperature of 25 °C was

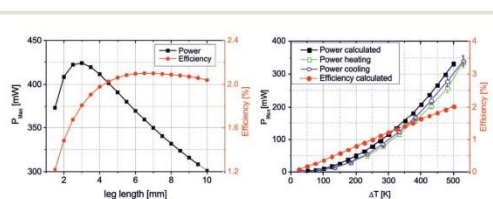


Fig. 5 Left: Calculated module power output P_{Max} and efficiency in dependence on leg length. Right: Experimental and calculated module power output P_{Max} for leg length of 6.2 mm in dependence ΔT between hot and cold side (cold side temperature kept at 25 °C). The calculated efficiency is also shown. Experimental data is given for the heating and cooling part of the thermal cycle the module was exposed to.

measured to be 0.35 W, thus, the maximum power output per area of thermoelectric material cross sectional area (36 mm²) resulted in an output power of 0.97 W cm⁻², which is very high and among the best reported values for thermoelectric modules. Only very recently, this value has been exceeded significantly by our group⁸⁰ and Joshi *et al.*⁸¹ both using half-Heusler compounds.

3.4.4. Validation of measured transport properties. The high figures of merit determined for the thermoelectric materials are afflicted with a high measurement uncertainty as mentioned above. To confirm and validate these data as well as the remarkably low contact resistances, simulations as described in the Experimental section were carried out taking into account the material parameters, *i.e.* the given transport properties and contact resistances. Module maximum output power P_{Max} under resistance-matched conditions and module efficiency were calculated. The thermal radiation was modelled with an assumed emissivity of 0.5 and an environment temperature of 20 °C. Simulated and experimental data was fitted by varying the heat transfer coefficient between the hot and cold side and their surroundings, *i.e.* the heat source at the hot side and the cooler at the cold side. Realistic values of 500 W m⁻² K for the hot side and 250 W m⁻² K for the cold side were found. For the contact resistance, low values as determined by measurement were assumed. The calculated module output power is shown in dependence of leg length in Fig. 5. Hot side and cold side temperature were assumed to be 550 °C and 25 °C, respectively. For the whole module, the simulation yielded a P_{Max} of 366 mW, *i.e.* a power density of 1.02 W cm⁻². This is in very good agreement with the measurement data, impressively confirming the very good material properties and low contact resistances. The calculated dependence of the maximum output power in dependence on ΔT also indicated in Fig. 5 shows a good agreement with Experimental data.

4. Conclusions

In conclusion, PCMs with very good thermoelectric properties were fabricated by high-temperature synthesis and subsequent re-compaction with SPS. The material was thoroughly characterized using a variety of measurement techniques. Thermoelectric characterization was carried out for several heating and cooling cycles, exceeding the typical characterization procedure for thermoelectric materials. Special attention was given to the stability and defect structure of the materials. Very low contact resistances were obtained and thermoelectric modules serving as TEG with a high power density of $\sim 1 \text{ W cm}^{-2}$ were successfully assembled. The properties obtained from material and contact characterization were double-checked for the first time by a comparison of maximum power output data with simulations taking into account the material and contact data. An excellent match between experiment and simulation was evident and confirmed the very good material and contact properties.

Acknowledgements

Financial support by the German Research Foundation within priority program SPP1386, "Nanostructured Thermoelectric Materials: Theory, Model Systems and Controlled Synthesis", is gratefully acknowledged.

Notes and references

- 1 R. G. Lange and W. P. Carroll, *Energ. Convers. Manage.*, 2008, **49**, 393.
- 2 L. Summerer and K. Stephenson, *Proc. Inst. Mech. Eng., IMechE Conf.*, 2011, **225**, Part G: J. Aerospace Engineering.
- 3 J. R. Sootsman, D. Y. Chung and M. G. Kanatzidis, *Angew. Chem., Int. Ed.*, 2009, **48**, 8616.
- 4 T. Ikeda, L. A. Collins, V. A. Ravi, F. S. Gascoin, S. M. Haile and G. F. Snyder, *Chem. Mater.*, 2007, **19**, 763.
- 5 G. J. Snyder and E. S. Toberer, *Nat. Mater.*, 2008, **7**, 105.
- 6 C. B. Vining, *Nat. Mater.*, 2008, **7**, 765.
- 7 A. M. Rao, X. Ji and T. M. Tritt, *MRS Bull.*, 2006, **31**, 218.
- 8 H. Böttner, G. Chen and R. R. Venkatasubramanian, *MRS Bull.*, 2006, **31**, 199.
- 9 S. J. Thiagarajan, V. Jovic and J. P. Heremans, *Phys. Status Solidi RRL*, 2007, **1**, 256.
- 10 D. G. Ebling, A. Jacquot, M. Jäggle, H. Böttner, U. Kühn and L. Kirste, *Phys. Status Solidi RRL*, 2007, **1**, 238.
- 11 I. U. Arachchige, J. Wu, V. P. Dravid and M. G. Kanatzidis, *Adv. Mater.*, 2008, **20**, 3638.
- 12 C. Chiritescu, D. G. Cahill, N. Nguyen, D. C. Johnson, A. Bodapati, P. Keblinski and P. Zschack, *Science*, 2007, **315**, 351.
- 13 B. Poudel, Q. Hao, Y. Ma, Y. Lan, A. Minnich, B. Yu, X. Yan, D. Wang, A. Muto, D. Vashaee, X. Chen, J. Liu, M. S. Dresselhaus, G. Chen and Z. Ren, *Science*, 2008, **320**, 634.
- 14 S. K. Bux, J.-P. Fleurial and R. B. Kaner, *Chem. Commun.*, 2010, **46**, 8311.
- 15 Q. Lin, M. Smeller, C. L. Heideman, P. Zschack, M. Koyano, M. D. Anderson, R. Kykyneshi, D. A. Keszler, I. M. Anderson and D. C. Johnson, *Chem. Mater.*, 2010, **22**, 1002.
- 16 F. Zahid and R. Lake, *Appl. Phys. Lett.*, 2010, **97**, 212102; S. Ganguly and S. L. Brock, *J. Mater. Chem.*, 2011, **21**, 8800.
- 17 K. Nielsch, J. Bachmann, J. Kimling and H. Böttner, *Adv. Energy Mater.*, 2011, **1**, 713.
- 18 T. Rosenthal, M. N. Schneider, C. Stiewe, M. Döblinger and O. Oeckler, *Chem. Mater.*, 2011, **23**, 4349.
- 19 Y. Ma, E. Ahlberg, Y. Sun, B. B. Iversen and A. E. C. Palmqvist, *J. Electrochem. Soc.*, 2012, **159**, D50.
- 20 J. P. Heremans, M. S. Dresselhaus, L. E. Bell and D. T. Morelli, *Nat. Nanotechnol.*, 2013, **8**, 471.
- 21 H. Wang, W. D. Porter, H. Böttner, J. König, L. Chen, S. Bai, T. M. Tritt, A. Mayolet, J. Senawiratne, C. Smith, F. Harris, P. Gilbert, J. W. Sharp, J. Lo, H. Kleinke and L. Kiss, *J. Electron. Mater.*, 2013, **42**, 654.
- 22 N. Lowhorn, W. K. Wong-Ng, W. Zhang, J. Lu, M. Otani, E. L. Thomas, M. L. Green and T. Tran, *Appl. Phys. A: Mater. Sci. Process.*, 2009, **94**, 231.
- 23 M. Wuttig and N. Yamada, *Nat. Mater.*, 2007, **6**, 824.
- 24 W. Welnic and M. Wuttig, *Mater. Today*, 2008, **11**, 20.
- 25 M. N. Schneider, T. Rosenthal, C. Stiewe and O. Oeckler, *Z. Kristallogr.*, 2010, **255**, 463.
- 26 W. Bensch and M. Wuttig, *Chem. unserer Zeit*, 2010, **44**, 92.
- 27 M. Wuttig and C. Steimer, *Appl. Phys. A*, 2007, **87**, 411.
- 28 T. Matsunaga and N. Yamada, *Phys. Rev.*, 2004, **B69**, 104111.
- 29 E. R. Sittner, K. S. Siegert, P. Jost, C. Schlockermann, F. R. L. Lange and M. Wuttig, *Phys. Status Solidi A*, 2013, **210**, 147.
- 30 M. Wuttig and S. Raoux, *Z. Anorg. Allg. Chem.*, 2012, **638**, 2455.
- 31 C. B. Satterthwaite and R. W. Ure Jr., *Phys. Rev.*, 1957, **108**, 1164.
- 32 H. Böttner, D. G. Ebling, A. Jacquot, J. König, L. Kirste and J. Schmidt, *Phys. Status Solidi RRL*, 2007, **1**, 235.
- 33 R. Venkatasubramanian, *Phys. Rev. B: Condens. Matter*, 2000, **61**, 3091.
- 34 N. M. Abdullayev, S. I. Mekhtiyeva, N. R. Memmedov, M. A. Ramazanov and A. M. Kerimova, *Semiconductors*, 2010, **44**, 824.
- 35 F. Zahid and R. Lake, *Appl. Phys. Lett.*, 2010, **97**, 212102.
- 36 M. Saleemi, M. S. Toprak, S. Li, M. Johnsson and M. Muhammed, *J. Mater. Chem.*, 2012, **22**, 725.
- 37 S. Sumithra, N. J. Takas, D. K. Misra, W. M. Nolting, P. F. P. Poudeu and K. L. Stokes, *Adv. Energy Mater.*, 2011, **1**, 1141.
- 38 A. Soni, Z. Yanyuan, Y. Ligen, M. Khor, K. Aik, M. S. Dresselhaus and Q. Xiong, *Nano Lett.*, 2012, **12**, 1203.
- 39 G. Wang, L. Endicott and C. Uher, *Sci. Adv. Mater.*, 2011, **3**, 539.
- 40 Z. Su, J. He, X. Ji, N. Gothard and T. M. Tritt, *Sci. Adv. Mater.*, 2011, **3**, 596.
- 41 Y. Ma, E. Ahlberg, Y. Sun, B. B. Iversen and A. E. C. Palmqvist, *J. Electrochem. Soc.*, 2012, **159**, D50.
- 42 D. Bourgault, B. Schaechner, C. Giroud Garampon, T. Crozes, N. Caillault and L. Carbone, *J. Alloys Compd.*, 2014, **598**, 79.
- 43 R. Venkatasubramanian, E. Siivola, T. Colpitts and B. O'Quinn, *Nature*, 2001, **413**, 597.
- 44 I. Chowdhury, R. Prasher, K. Lofgreen, G. Chrysler, S. Narasimhan, R. Mahajan, D. Koester, R. Alley and R. Venkatasubramanian, *Nat. Nanotechnol.*, 2009, **4**, 235.
- 45 M. Scheele, N. Oeschler, K. Meier, A. Kornowski, C. Klinker and H. Weller, *Adv. Funct. Mater.*, 2009, **19**, 3467.
- 46 C. Bae, T. Bohnert, J. Gooth, S. Lim, S. Lee, H. Kim, S. Heimann, S. Schulz, H. Shin and K. Nielsch, *Semicond. Sci. Technol.*, 2014, **29**, 064003.
- 47 J. Tomforde, W. Bensch, L. Kienle, V. Duppel, P. Merkelbach and M. Wuttig, *Chem. Mater.*, 2011, **23**, 3871.
- 48 M. N. Schneider and O. Oeckler, *Z. Anorg. Allg. Chem.*, 2008, **634**, 2557.

- 49 T. Rosenthal, M. N. Schneider, C. Stiewe, M. Döbbling and O. Oeckler, *Chem. Mater.*, 2011, **23**, 4349.
- 50 T. Schröder, M. N. Schneider, T. Rosenthal, A. Eisele, C. Gold, E.-W. Scheidt, W. Scherer, R. Berthold and O. Oeckler, *Phys. Rev. B: Condens. Matter*, 2011, **84**, 184104.
- 51 M. N. Schneider, T. Rosenthal, C. Stiewe and O. Oeckler, *Z. Kristallogr.*, 2010, **255**, 463.
- 52 E. Shelimova, P. P. Konstantinov, O. G. Karpinskii, E. S. Avilov, M. A. Kretova and V. S. Zemskov, *J. Alloys Compd.*, 2001, **329**, 50.
- 53 T. Schröder, M. N. Schneider, T. Rosenthal, A. Eisele, C. Gold, E.-W. Scheidt, W. Scherer, R. Berthold and O. Oeckler, *Phys. Rev. B: Condens. Matter*, 2011, **84**, 184104.
- 54 G. C. Christakudis, S. K. Plachkova, L. E. Shelimova and E. S. Avilov, *Phys. Status Solidi A*, 1991, **128**, 465.
- 55 T. Rosenthal, S. Welzmler and O. Oeckler, *Solid State Sci.*, 2013, **25**, 118.
- 56 Z. A. Munir, U. Anselmi-Tamburini and M. Ohyanagi, *J. Mater. Sci.*, 2006, **41**, 763.
- 57 A. A. Coelho, *TOPAS-Academic, version 5 (Computer Software)*. Coelho Software, Brisbane.
- 58 O. Boffoué, A. Jacquot, A. Dauscher, B. Lenoir and M. Stölzer, *Rev. Sci. Instrum.*, 2005, **76**, 053907.
- 59 J. D. Koenig, U. Nussel, M. Bartel and U. Vetter, *MRS Online Proc. Libr.*, 2009, **1218**, 1218-Z04-10, DOI: 10.1557/PROC-1218-Z04-10.
- 60 D. Ebling, M. Jäggle, M. Bartel, A. Jacquot and H. Böttner, *J. Electron. Mater.*, 2009, **38**, 1456.
- 61 M. Jäggle, M. Bartel, D. Ebling, A. Jacquot and H. Böttner, *Proceedings ECT 08: 6th European Conference on Thermoelectrics*, Paris, France, 2008, O-27-1.
- 62 H. Scherrer and S. Scherrer, in *CRC Handbook of Thermoelectrics*, ed. D. M. Rowe, CRC Press, Boca Raton, FL, 1995, ch. 19.
- 63 T. A. Christakudi, S. K. Plachkova and G. C. Christakudis, *Phys. Status Solidi A*, 1995, **147**, 211.
- 64 R. R. Furlong and E. J. Wahlquist, *Nuclear News April*, 1999, 26.
- 65 E. A. Skrabek and D. S. Trimmer, in *CRC Handbook of Thermoelectrics*, ed. D. M. Rowe, CRC Press, Boca Raton, FL, 1995, ch. 22.
- 66 J. R. Salvador, J. Yang, X. Shi, H. Wang and A. A. Wereszczak, *J. Solid State Chem.*, 2009, **182**, 2088.
- 67 Z. Sun, S. Kyrsta, D. Music, R. Ahuja and J. M. Schneider, *Solid State Commun.*, 2007, **143**, 240.
- 68 D. Wu, L.-D. Zhao, S. Hao, Q. Jiang, F. Zheng, J. W. Doak, H. Wu, H. Chi, Y. Gelbstein, C. Uher, C. Wolverton, M. Kanatzidis and J. He, *J. Am. Chem. Soc.*, 2014, **136**(32).
- 69 T. Chattopadhyay, J. X. Boucherle and H. G. von Schnering, *J. Phys. C: Solid State Phys.*, 1987, **20**, 1431.
- 70 K. Schubert and H. Fricke, *Z. Naturforsch.*, 1951, **a6**, 781.
- 71 K. Schubert and H. Fricke, *Z. Metallkd.*, 1953, **44**, 457.
- 72 N. H. Abrikosov, V. F. Bankina, L. V. Poretskaya, L. E. Shelimova and E. V. Skudnova, *Semiconducting II-VI, IV-VI, and V-VI Compounds*, Plenum Press, New York, 1969, 165.
- 73 U. Schürmann, V. Duppel, S. Buller, W. Bensch and L. Kienle, *Cryst. Res. Technol.*, 2011, **46**, 561.
- 74 N. C. Popa and D. Balzar, *J. Appl. Crystallogr.*, 2002, **35**, 338.
- 75 V. Fano, in *CRC Handbook of Thermoelectrics*, ed. D. M. Rowe, CRC Press, Boca Raton, FL, 1995, ch. 21.
- 76 N. H. Abrikosov, V. F. Bankina, L. V. Poretskaya, L. E. Shelimova and E. V. Skudnova, *Semiconducting II-VI, IV-VI, and V-VI Compounds*, Plenum Press, New York, 1969, 165.
- 77 T. Caillat, J.-P. Fleurial, G. J. Snyder and A. Borshchevsky, *Proceedings ICT 01: 20th International Conference on Thermoelectrics*, Beijing, China, 2001, 282.
- 78 D. Zhao, X. Li, Y. Cai, W. Jiang and L. Chen, *Mater. Sci. Forum*, 2010, **631–632**, 313.
- 79 M. Orihashi, Y. Noda, L. Chen, Y. Kang, A. Moro and T. Hirai, *Proceedings ICT 98: 17th International Conference on Thermoelectrics*, Nagoya, Japan, 1998, **543**.
- 80 K. Bartholomé, B. Balke, D. Zuckermann, M. Köhne, M. Müller, K. Tarantik and J. König, *J. Electron. Mater.*, 2014, **43**, 1775.
- 81 G. Joshi, R. He, M. Engber, G. Samsonidze, T. Pantha, E. Dahal, K. Dahal, J. Yang, Y. Lan, B. Kozinsky and Z. Ren, *Energy Environ. Sci.*, 2014, **7**, 4070–4076.

2.2 Enhanced temperature stability and exceptionally high electrical contrast of selenium substituted $\text{Ge}_2\text{Sb}_2\text{Te}_5$ phase change materials

Das klassische Phasenwechselmaterial $\text{Ge}_2\text{Sb}_2\text{Te}_5$ wurde mit Selen substituiert und die resultierenden strukturellen Änderungen mit *in situ* XRD und TEM Untersuchungen charakterisiert. Gegenüber dem reinen Tellurid zeigten die amorphen Phasen von $\text{Ge}_2\text{Sb}_2\text{Te}_4\text{Se}$ und $\text{Ge}_2\text{Sb}_2\text{Te}_2\text{Se}_3$ Dünnschichten eine erhöhte Temperaturstabilität. Der Einbau von Se in die Struktur der metastabilen kubischen Phase verursacht Verzerrungen des Gitters, was zu einer Reduktion der Symmetrie führt ($Fm\bar{3}m \rightarrow R\bar{3}m$). Elektrische Schichtwiderstandsmessungen belegen einen außergewöhnlich großen elektrischen Kontrast zwischen den amorphen und kristallinen Phasen, die im Vergleich zu etablierten Phasenwechselmaterialien um den Faktor 100 größer ist. Der optische Kontrast nimmt mit zunehmendem Selengehalt auf Grund größerer struktureller Verzerrungen in den selenreichen kristallinen Phasen und einer damit einhergehenden Abnahme der Resonanzbindung ab. Die Ergebnisse deuten darauf hin, dass die Grenze für erfolgreiche optische Datenspeichermaterialien bei großer Ionizität und Hybridisierung der chemischen Bindungen erreicht wird.

Reprinted with permission from C. Koch, A.-L. Hansen, T. Dankwort, G. Schienke, M. Paulsen, D. Meyer, M. Wimmer, M. Wuttig, L. Kienle, W. Bensch, *RSC Adv.* **2017**, 7, 17164–17172. Copyright 2017 Royal Society of Chemistry.

Cite this: *RSC Adv.*, 2017, 7, 17164

Enhanced temperature stability and exceptionally high electrical contrast of selenium substituted $\text{Ge}_2\text{Sb}_2\text{Te}_5$ phase change materials†

Christine Koch,^a Anna-Lena Hansen,^a Torben Dankwort,^b Gerrit Schienke,^a Melf Paulsen,^a Dominik Meyer,^c Martin Wimmer,^c Matthias Wuttig,^c Lorenz Kienle^b and Wolfgang Bensch^{*a}

$\text{Ge}_2\text{Sb}_2\text{Te}_4\text{Se}$ (I) and $\text{Ge}_2\text{Sb}_2\text{Te}_2\text{Se}_3$ (II) thin films were synthesized and compared to the pure telluride $\text{Ge}_2\text{Sb}_2\text{Te}_5$. *In situ* X-ray diffraction (XRD) and *in situ* transmission electron microscopy (TEM) investigations revealed a remarkably increased stability of the as-deposited amorphous phase. The transition temperature (beginning transition) determined with *in situ* XRD increases from 135 °C for the pure telluride to 165 °C for (I) and to 225 °C for (II). An identical trend for the transition temperatures (transition complete) was observed by sheet resistance measurements with values of 153, 190 and 243 °C, respectively. Optical properties determined with Fourier-transform-infrared (FTIR) spectroscopy and variable incident angle spectroscopic ellipsometry (VASE) exhibit a significant energy-dependent behavior of the dielectric functions. Major changes of the maxima and intensities of the extinction coefficients and the indices of refraction are observed with increasing Se content. These results are in agreement with the results obtained by Rietveld refinement and TEM. The incorporation of Se into the structure of the metastable cubic phase causes small distortions, leading to a phase transition. Electrical sheet resistance measurements reveal an exceptionally large electrical contrast between the amorphous and crystalline phases, which is increased by a factor of 100 for compound (II) compared to established phase change materials.

Received 25th January 2017
Accepted 3rd March 2017

DOI: 10.1039/c7ra01140g

rsc.li/rsc-advances

Introduction

Today, data storage is of particular technological importance. For the last few thousands of years information was stored, starting with drawings and paintings, improving with letters and books, up to computers containing data storage devices. Because of the increasing amount of data, larger and faster memory devices of smaller sizes are required. In case of optical data storage, long-term stability, repeatability and reliability need to be improved, as well as the data density and the opto-electronic contrast. Additionally, the costs of the materials should be as low as possible and easy fabrication is required.^{1,2} These criteria are met for phase change materials (PCM).^{3,4} Most phase change materials are based on the pseudo-binary section of the binary compounds GeTe and Sb_2Te_3 yielding compositions like $(\text{GeTe})_m(\text{Sb}_2\text{Te}_3)_n$. Another very interesting composition is AIST,

a combination of the elements Ag, In, Sb and Te.⁵ These materials can rapidly and reversibly be switched between an amorphous and a crystalline state applying a laser with short pulses and high powers. The amorphous and crystalline states have remarkably different optical properties that are easily detected by the laser. For erasing the bit (recrystallization) a longer lasting pulse with lower intensity is used.

During the last decades three different generations of optical data storage devices were developed: compact discs (CD, using a laser wavelength of 830 nm), digital versatile discs (DVDs, 650 nm) and Blu-ray™ discs (BD, 405 nm). Further decreasing the laser wavelength has been proven difficult due to several challenges including the lack of suitable laser diodes, but also a decreasing contrast of phase change materials at shorter wavelengths. Further, phase change materials have been studied for their application potential in non-volatile electronic memories. They can be rapidly and reversibly switched if a low voltage pulse is applied and they have already proven excellent scaling potential. Yet, there are still a number of issues to be addressed in order to understand the full potential of these novel memories. Two questions are of particular interest for applications at elevated temperatures, such as automotive applications, namely: at which temperature will the amorphous phase crystallize and how high is the resistance of the

^aInstitute for Inorganic Chemistry, University of Kiel, Max-Eyth-Str. 2, 24118 Kiel, Germany. E-mail: wbensch@ac.uni-kiel.de

^bInstitute for Materials Science, University of Kiel, Kaiserstr. 2, 24143 Kiel, Germany

^cInstitute of Physics, RWTH Aachen University, Sommerfeldstr. 14, 52056 Aachen, Germany

† Electronic supplementary information (ESI) available. See DOI: 10.1039/c7ra01140g



amorphous phase. While the stability of the amorphous phase is crucial for applications at elevated temperatures, a high resistance of the amorphous state could facilitate realizing a multi-level memory.^{6,7}

In recent years, two major research approaches were followed for further improvement of phase change materials. One research direction is focused on unravelling the atomistic origin of the high switching speeds, the aging of the amorphous state and the pronounced property contrast between the two states.⁸ The structure of the crystalline phase is in most cases a distorted rock salt structure with different vacancy concentrations in the cation sublattice depending on the chemical composition.^{9–12} From a chemical point of view it is not easy to explain that Ge and Sb in $\text{Ge}_2\text{Sb}_2\text{Te}_5$ each are in an octahedral environment of Te^{2-} anions. One approach to rationalize this bonding situation is called resonant bonding where sharing of electrons (covalent bonds) leads to stabilization of highly symmetric coordination. To avoid confusion with the term resonant bonding used in organic chemistry to describe the bonding situation in high symmetric materials like benzene or graphite, resonant bonding in PCMs has a different meaning.^{6,13–15}

The local atomic structures of the different phases were also intensively investigated.^{16–22} Despite many efforts, the short-range coordination of the different atoms in the amorphous structure are still under debate in literature.^{16,23–26} These problems demonstrate that it is not trivial to investigate and understand the reactions on atomic scale of the phase change, yet being the essential issue for designing new materials. Hence, in a second approach, scientists have tried to identify new compounds, which also exhibit the characteristic properties of phase change materials.

So far, many studies have focused on $\text{Ge}_2\text{Sb}_2\text{Te}_5$.^{27–30} Due to its excellent properties it was used as the DVD-RW material. Other well investigated compounds are GeCu_2Te_3 (ref. 31–33) and $\text{Ge}_8\text{Sb}_2\text{Te}_{11}$ being the active material in BD-RW discs or binaries such as $\text{Ge}_{15}\text{Sb}_{85}$,³⁴ GeTe ³⁵ and GaSb ,^{36–39} respectively. Several studies deal with the substitution or doping of established phase change materials.^{40–45} Samples with compositions $(\text{Ge}_2\text{Sb}_2\text{Te}_5)_{1-x}\text{Se}_x$ ($x = 0–0.5$) were recently investigated, showing a significantly different crystallization behavior. For $x \geq 0.1$ the stable hexagonal structure is directly formed at $T \geq 150$ °C, while the metastable cubic phase could only be observed for $x \leq 0.02$. With increasing Se content the optical band gap becomes larger. In addition, the resistance, threshold voltage and thermal stability increased with x . For the Se substituted materials a relatively low crystallinity of the crystalline phases was observed.^{46,47} Compared to $\text{Ge}_2\text{Sb}_2\text{Te}_5$ no significant improvement in properties could be observed and a relationship of properties with structural changes could not be established.

In our ongoing work the impact of the substitution of Te in $\text{Ge}_2\text{Sb}_2\text{Te}_5$ by Se on the material properties was investigated. The substitution in the anion substructure of the metastable cubic rock salt structure should lead to local distortions, a decreased metallic character and a larger electronegativity difference, which increases at the same time hybridization and ionicity. As a result of these pronounced changes of the physico-

chemical properties significant alterations of the optical and electrical behavior are expected. Additionally, the bond strength and therefore the phase change transition temperatures should be altered. The final goal of the present investigation is to establish a relationship between the change in the chemical bonding by chemical substitution of Te by Se and the resulting properties. The results of these experiments and the observed trends concerning the opto-electronic properties and the bonding characteristics are reported.

Experimental section

Thin film samples of $\text{Ge}_2\text{Sb}_2\text{Te}_5$ and $\text{Ge}_2\text{Sb}_2\text{Te}_4\text{Se}$ (I) were prepared by DC magnetron sputtering using stoichiometric targets (Umicore, 99.99%) bonded to water cooled copper plates. The base pressure in the sputter chamber was $< 2 \times 10^{-6}$ mbar, the argon current was fixed at 20 sccm for all deposition runs. $\text{Ge}_2\text{Sb}_2\text{Te}_5$ was deposited by using a single target of 10 cm diameter at 20 W. (I) was prepared *via* co-sputtering of GeSb_2Te_4 (5 cm diameter) at 30 W and GeSe (10 cm diameter) at 25 W.

All substrates had a size of 2×2 cm. Thin film samples of ~ 700 nm thickness were prepared on (1 0 0) silicon single crystal substrates, glass substrates, glass substrates with previously sputtered chromium contacts in the corners (for electrical measurements) and silicon substrates coated with ~ 200 nm aluminum layers (for optical measurements). Thin samples of ~ 35 nm were deposited on nickel TEM-grids, coated with a thin amorphous carbon layer. The deposition times of the thick and thin films were 3688 s (~ 700 nm) and 132 s (~ 35 nm) for $\text{Ge}_2\text{Sb}_2\text{Te}_5$ and 2000 s (~ 700 nm) and 75 s (~ 35 nm) for $\text{Ge}_2\text{Sb}_2\text{Te}_4\text{Se}$ (I).

$\text{Ge}_2\text{Sb}_2\text{Te}_2\text{Se}_3$ (II) was prepared by thermal co-evaporation of single elements in an ultra-high vacuum chamber (Omicron NanoTechnology), using single element Knudsen cells containing the utilized elements (Chempur 99.999%) at different temperatures, listed in Table 1. The base pressure in the chamber was $p < 1 \times 10^{-8}$ mbar. A beam flux monitor was used to ensure stable evaporation rates.

It should be noted that it is very important to find a reliable method to determine the compositions, because the signals of the elements partly overlap in most common analytic techniques due to their similar electronic structure. We found that electron probe micro-analysis (EPMA) is the most promising and precise method for investigating the X-ray emission L-series of the elements, using an acceleration voltage of 10, 16 and 22 kV. The EPMA measurements were taken with a Cameca SX 100, yielding composition values close to the required stoichiometries. A Bruker DektaktXT profilometer was used to determine the film thicknesses.

Table 1 Deposition temperatures of the single elements for preparing $\text{Ge}_2\text{Sb}_2\text{Te}_2\text{Se}_3$

Element	Germanium	Antimony	Tellurium	Selenium
Temperature/°C	1100	348	233	140
Deposition time	9 h (700 nm); 30 min (~ 35 nm)			



X-Ray diffraction (XRD) was performed in θ - θ geometry using an X'Pert Pro MPD diffractometer (PANalytical; Cu $K\alpha_{1,2}$ radiation), equipped with a Göbel mirror and a PIXcel detector. Temperature dependent *in situ* diffraction was performed in an Anton Paar HTK 1200N high temperature chamber in helium (99.999%) atmosphere to prevent oxidation of the samples. The temperature was increased stepwise with a heating rate of 5 K min^{-1} from 28 °C up to 360 °C. The patterns were collected within one hour over a range of 15–65° 2θ at constant temperature. The scans for the Rietveld refinements were performed on a flat stage using the same setup in a range of 10–100° 2θ (step size 0.05°).

Rietveld refinements were carried out using the Program TOPAS Academic (Version 6).⁴⁸ In order to calculate crystallite sizes the fundamental parameter approach was employed.^{49,50} To refine the anisotropic peak broadening caused by strain we used a spherical harmonics to calculate the Lorentz width as a function of $\tan(\theta)$. To correct texture effects, which are typical for thin film analysis, a spherical harmonics was employed.

In situ heating TEM experiments were performed by a FEI Tecnai F30 G² using a GATAN double tilt heating holder 652. The heating rate was set to 10 K min^{-1} . After the desired temperature was reached, a holding time was utilized until minimum sample drift and temperature equilibrium were achieved. Subsequently electron diffraction patterns were recorded at the rim of the grid, close to the measuring and heating device to ensure high accuracy of the actual temperature of the sample. For HRTEM and bright field imaging the heating was interrupted to ensure no sample drift.

To investigate the optical properties FTIR and ellipsometry measurements were done. FTIR spectra have been collected using a Bruker IFS 66v/s with a resolution of 0.12 meV . To exclude drift effects the samples and a gold reference were measured alternately. The measured spectra were renormalized by a gold reference to obtain the final spectrum. For ellipsometry measurements a J. A. Woollam M-2000UI equipped with deuterium and halogen lamps as light sources was used. The incidence angles were 65°, 70° and 75°. The examined energy ranges were 0.05–1 eV for FTIR and 0.7–5.2 eV for ellipsometry. All measurements were performed with the as-deposited amorphous samples as well as the metastable crystalline samples each on aluminum coated silicon substrates at room temperature. These substrates were prepared by sputter deposition of an aluminum target with the same process as described above. The values for the dielectric constants as well as the index of refraction n and the extinction coefficient k were obtained by fitting the spectra using SCOUT software.⁵¹ Therefore the same assumptions as in ref. 42 were made.

Sheet resistance measurements were performed using a four-point-probe setup according to van-der-Pauw^{52–55} with argon (99.996%) as protective gas. ~700 nm thick samples on glass substrates with chromium contacts in each corner were heated with a heating rate of 5 K min^{-1} up to 360 °C. This temperature was held constant for 30 min and then the samples were cooled down to room temperature. Because of the large density change of up to 10% between the amorphous and crystalline phases which unfortunately cannot be investigated

and corrected during the resistivity measurements the resistance of the films instead of the resistivity was investigated.

Results and discussion

Structural characterization by *in situ* XRD and TEM heating experiments

In situ X-ray diffraction and TEM investigations were performed to independently investigate the structure and crystallization of the films. Both methods confirm that all as deposited films are amorphous. Thin films of $\text{Ge}_2\text{Sb}_2\text{Te}_5$ crystallize in the metastable cubic ($Fm\bar{3}m$) and the stable primitive trigonal ($P\bar{3}m1$) phase, respectively.⁵⁶

For the accurate determination of the transition temperatures the intensities of the (002) reflection of the cubic and the (103) reflection of the primitive trigonal phase were analyzed as function of temperature (Fig. 1 and 2). While the 1st transition temperature increases with higher selenium content the temperature of the 2nd transition to the thermodynamically stable phase remains quite constant at around 270–290 °C. All three samples are stable until 360 °C.

In situ TEM heating experiments were performed by monitoring the formation of diffraction spots in the Selected Area Electron Diffraction (SAED) pattern. A representative temperature resolved image of this process is depicted in Fig. 3 for $\text{Ge}_2\text{Sb}_2\text{Te}_2\text{Se}_3$. Crystallization started at 132 °C, 160 °C and 222 °C, for $\text{Ge}_2\text{Sb}_2\text{Te}_5$, $\text{Ge}_2\text{Sb}_2\text{Te}_4\text{Se}$ and $\text{Ge}_2\text{Sb}_2\text{Te}_2\text{Se}_3$, respectively (for details see Fig. S1 and S2†). Further, diffuse streaks in the ED pattern were found for $\text{Ge}_2\text{Sb}_2\text{Te}_2\text{Se}_3$ after reaching the temperature of 250 °C (Fig. 3). These diffuse streaks indicate the formation of planar defects which can be attributed to vacancy layers forming along the (111) planes with respect to the cubic symmetry.^{9,57,58}

A comparison of the transformation temperatures determined by *in situ* XRD and *in situ* TEM are displayed in Table 2. Phase change temperatures exhibit convincing agreement and confirm the monotonous increase of the crystallization temperature with increasing Se content. The values of $\text{Ge}_2\text{Sb}_2\text{Te}_5$ correspond well to those reported in literature.^{27,59,60} Further, the substitution of Te by Se leads to a significant stabilization of the amorphous phase and therefore to a stabilization of amorphous areas/bits in data storage applications. Similar effects were also observed for other Ge–Sb–Te phases upon Se substitution.⁴⁰

Bright field (BF) and high resolution TEM (HRTEM) images of $\text{Ge}_2\text{Sb}_2\text{Te}_5$ after the heating process revealed a mixture of larger grains with 100 nm size and nanocrystals marked by red and blue arrows in Fig. 4a, respectively. In comparison Se substituted films showed significantly smaller crystallites, cf. Fig. 4b and c displaying exclusively nanosized crystallites for (I) and (II).

Room temperature XRD data was analyzed *via* Rietveld refinement of the metastable phase revealing the same tendency for the crystallite size as found in TEM measurements (see Table 3 and Fig. 5).

The refinement indicated a symmetry reduction due to the incorporation of Se and a resulting distortion of the lattice



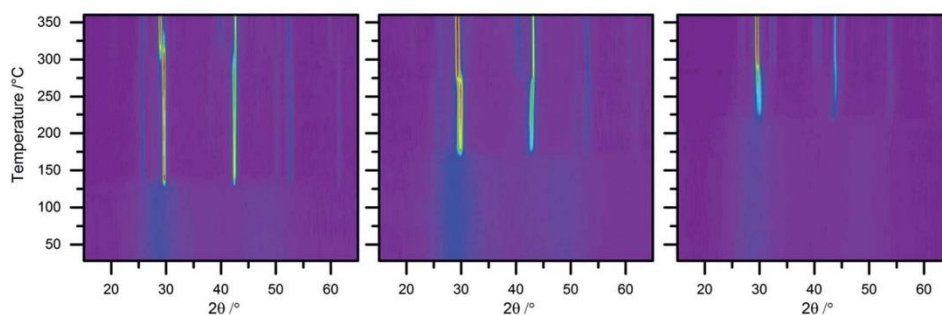


Fig. 1 *In situ* XRD patterns of $\text{Ge}_2\text{Sb}_2\text{Te}_5$ (left), $\text{Ge}_2\text{Sb}_2\text{Te}_4\text{Se}$ (middle) and $\text{Ge}_2\text{Sb}_2\text{Te}_2\text{Se}_3$ (right). Transitions from amorphous to cubic (rhombohedral trigonal) to primitive trigonal phases are seen by the appearance and disappearance of reflections.

along [111]. The latter caused a shift of the (220) reflection and anisotropic strain broadening. In the diffraction pattern of $\text{Ge}_2\text{Sb}_2\text{Te}_2\text{Se}_3$ we finally observe a splitting of the cubic (111) reflection, typically for a reduced symmetry (inset of Fig. 5).

To account for the lower symmetry, the cubic cell was transformed into the trigonal subgroup $R\bar{3}m$ (hexagonal axes). Due to the small crystallite size and the additional strain broadening, a splitting of the (220) reflection could not be observed, but its shift to lower scattering angle clearly represents a reduction of cubic symmetry even if the distortion itself is small. When compared to the transformed undistorted cell, it is apparent that the deviation from the cubic aristotype is more

pronounced for the higher Se content. Calculated d -values based on the Rietveld refinements match closely with measured d -values of ED patterns (Tables S1–S3†).

Optical properties

It was already pointed out that resonant bonding is an indispensable property for high optical contrast of PCMs. As a result of the distortion in the substituted samples the octahedral environment of the atoms is distorted which leads to a misalignment of the p-orbitals and therefore to a significant reduction of the resonant bonding in the metastable phase. This corresponds well with the so called “treasure map” for PCM (Fig. 6).¹⁴

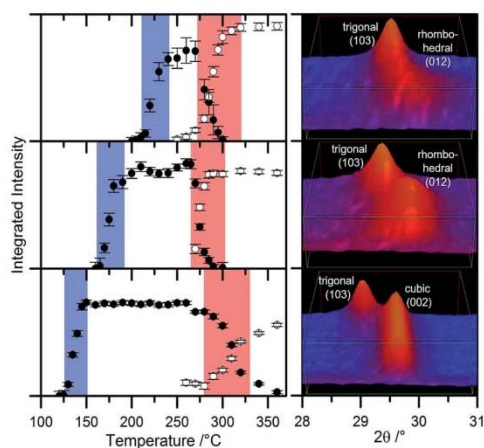


Fig. 2 Left: Determination of the phase change temperatures of $\text{Ge}_2\text{Sb}_2\text{Te}_5$ bottom, (I) middle and (II) top obtained by comparison of the diffraction intensities of the cubic (002)/rhombohedral (012) reflections (black circles) and primitive trigonal (103) reflection (white circles). Blue: phase change from amorphous to cubic (rhombohedral). Red: phase change from cubic to primitive trigonal. Right: Observation of the temperature induced phase transitions by evaluation of the reflection intensities.

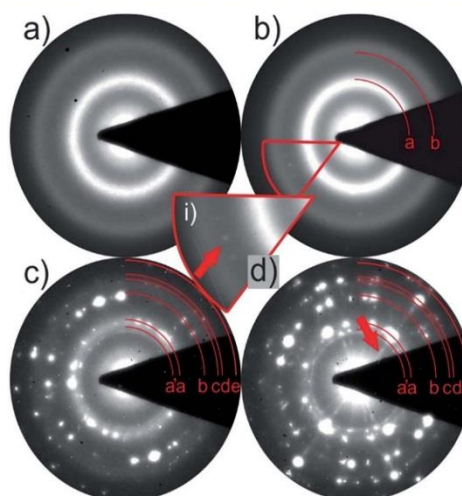


Fig. 3 SAED pattern of $\text{Ge}_2\text{Sb}_2\text{Te}_2\text{Se}_3$ (a) at room temperature; (b) crystallization starts at 222 °C (diffraction spots marked with red arrow); (c) growth of larger grains at 240 °C; (d) C diffuse streaks along [111] (rhombohedral cell) indicate formation of vacancy layers at 250°. Measured d -values fit to the calculated data can be found in Table S3.†





Table 2 Phase change temperatures of the synthesized samples determined by *in situ* XRD and TEM measurements. (1) 1st phase change temperature from amorphous to cubic (rhombohedral); (2) 2nd phase change temperature from cubic (rhombohedral) to primitive trigonal phase

Temperatures determined for	<i>Via in situ</i> XRD measurements		<i>Via in situ</i> TEM measurements
	1	2	1
Ge ₂ Sb ₂ Te ₅	130 °C	290 °C	132 °C
Ge ₂ Sb ₂ Te ₄ Se (I)	165 °C	270 °C	160 °C
Ge ₂ Sb ₂ Te ₂ Se ₃ (II)	220 °C	280 °C	222 °C

All established PCMs for optical data storage devices are located in a well-defined area in the map. It seems that the limit of this area for successful optical data storage materials is reached by the values given by the hybridization of Ge₂Sb₂Te₂Se₃. This assumption is confirmed by investigations of the optical properties.

The dielectric function ϵ contains the two dielectric constants ϵ_1 (real part) and ϵ_2 (imaginary part).

$$\epsilon = \epsilon_1 + i\epsilon_2 \quad (1)$$

A conversion of the dielectric function leads to the index of refraction n (2) and the extinction coefficient k (3):

$$\epsilon_1 = n^2 - k^2 \quad (2)$$

$$\epsilon_2 = 2nk \quad (3)$$

Fig. 7 displays the real and the imaginary part of the dielectric functions of the materials. A significant decrease of the maximum intensity and a shift to higher energies depending on the selenium content is observed. This can be explained by the structural distortions leading to a decrease of resonant bonding, which reduces ϵ_1 of the crystalline samples of (I) and (II) and explains the behavior.

According to formula (1) and (2) the same trend of the energy dependence of n and k is observed (Fig. 7). For typical amorphous phase change materials the index of refraction is ~50% larger in the crystalline state (e.g. Ge₂Sb₂Te₃).^{1,9} The substitution of Te by Se leads to a drastic decrease of the difference between the amorphous and crystalline indices of refraction. It is remarkable that the optical constants of the crystalline Ge₂Sb₂Te₂Se₃ sample are below amorphous Ge₂Sb₂Te₅. This observation implies that the ability of crystalline Ge₂Sb₂Te₂Se₃ to reflect light in the appropriate energy range is even worse compared to amorphous Ge₂Sb₂Te₅.

Table 4 summarizes the values for the optical constant ϵ_∞ and the optical bandgap E_g . The values of the amorphous and crystalline phases of Ge₂Sb₂Te₅ correspond well with the values reported in literature.^{15,62,63}

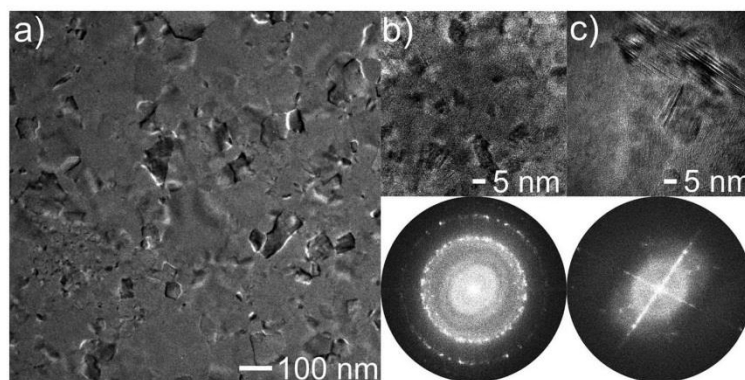


Fig. 4 (a) Bright field image of Ge₂Sb₂Te₅. The red and the blue arrow mark a larger grain of about 100 nm and nanocrystals. (b) HRTEM images and corresponding FFT recorded on Ge₂Sb₂Te₄Se and Ge₂Sb₂Te₂Se₃ (c) after heating to 150 °C, 190 °C and 250 °C, respectively.

Table 3 Rietveld refinement data of the metastable phase. * = transformed undistorted cell. The cell parameters of the rhombohedral trigonal cell ($R\bar{3}m$) are given according to the hexagonal setting of the space group. Further information is given in Table S4

Chemical formula		225	*	I	II
Space group		$Fm\bar{3}m$ (225)	$R\bar{3}m$ (166)	$R\bar{3}m$ (166)	$R\bar{3}m$ (166)
Cell parameter (Å)	<i>a</i>	6.0251	4.2624	4.1976	4.125
	<i>c</i>	—	10.4408	10.4456	10.4364
<i>c/a</i>		—	2.4495	2.4885 (+0.0390)	2.5300 (+0.0805)
Crystallite size (nm)		52	—	18	25
R_{Bragg}		1.78	—	1.01	1.92

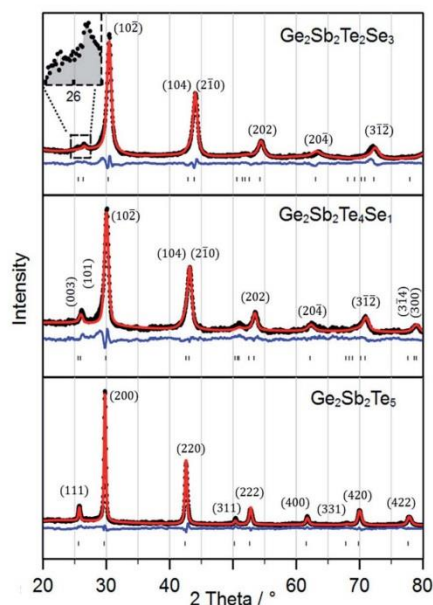


Fig. 5 Powder diffraction pattern of the cubic/rhombohedral trigonal phase after annealing the samples at 180 °C ($\text{Ge}_2\text{Sb}_2\text{Te}_5$), 230 °C (I) and 245 °C (II). Black circles depict the measured data, the red line the refined pattern and the blue line displays the difference of both. Reflection positions are marked by |.

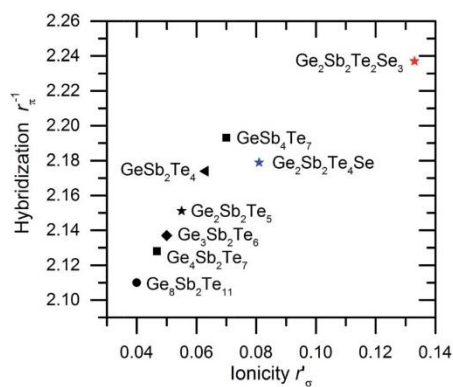


Fig. 6 Calculated values of ionicity and degree of hybridization for some established phase change materials and the substituted compounds.¹⁴ Used radii according to ref. 61.

With increasing selenium content ϵ_∞ decreases while E_g increases due to the reduced metallic behavior as a result of the substitution of Te by Se. Applying eqn (4) the contribution of

resonance bonding can be estimated which is basically the value of the increase of ϵ_∞ in %.¹⁵

$$\frac{\epsilon_\infty^{\text{crystalline}}}{\epsilon_\infty^{\text{amorphous}}} - 1 \quad (4)$$

The resonance bonding decreases with increasing Se content which can be explained (just like the extraordinary low optical constant of the crystalline phase of (II)) *via* the decrease of resonant bonding in the samples (I) and especially (II). The knowledge of all optical constants allows calculation of the absolute reflectivity of the amorphous and crystalline samples. Fig. 8 displays absolute reflectivity and total contrast calculated according to (5).⁴²

$$R_{\text{total}} = \frac{R_{\text{crystalline}} - R_{\text{amorphous}}}{R_{\text{amorphous}}} \quad (5)$$

Due to the pronounced decrease of the absolute reflectivity of the substituted crystalline samples the optical contrast decreases from ~20% for $\text{Ge}_2\text{Sb}_2\text{Te}_5$ to ~17% for (I) and ~8% for (II).

Although a slight shift of the maxima of the dielectric constants to higher energies *e.g.* smaller wavelengths is observed, the Se substituted samples seem to be not suitable for optical phase change data storage. The optical properties confirm the assumption that the limit of the hybridization for materials used in optical data storage devices is reached by values around 2.24.

Sheet resistance measurements

Temperature dependent sheet resistance measurements are shown in Fig. 9. It can be safely assumed that the influence of the slightly different film thicknesses onto resistance data is negligible. The sheet resistances for the amorphous films at room temperature are ~13 M Ω for $\text{Ge}_2\text{Sb}_2\text{Te}_5$, ~73 M Ω for $\text{Ge}_2\text{Sb}_2\text{Te}_4\text{Se}$ and ~11 G Ω for $\text{Ge}_2\text{Sb}_2\text{Te}_2\text{Se}_3$.

In line with the expected enlargement of the band gap the substitution of Te by Se leads to a giant increase of the sheet resistance of the amorphous phase. The large values of the resistance slightly decrease with increasing temperature until an abrupt drop of 2–4 orders of magnitude is observed at the 1st transition temperatures at about 153 °C for $\text{Ge}_2\text{Sb}_2\text{Te}_5$, 190 °C for (I) and 243 °C for (II). These temperatures correspond well with the temperatures revealed by *in situ* XRD measurements, representing a thoroughly crystallized film (Fig. 2). The electrical contrast between the amorphous and the metastable cubic phase increases significantly from 2 orders of magnitude ($\text{Ge}_2\text{Sb}_2\text{Te}_5$) to 2.5 orders of magnitude (I), and 4 orders of magnitude for (II), referring on the sudden drop of the resistance in Fig. 9. Hence, the electrical contrast of $\text{Ge}_2\text{Sb}_2\text{Te}_2\text{Se}_3$ is increased by factor of 100 compared to $\text{Ge}_2\text{Sb}_2\text{Te}_5$. This is an excellent behavior for electrical data storage applications: combining enhanced stability of the amorphous state as well as increasing the readability of the data.

A smooth second drop of the resistivity is caused by the phase change from the cubic into the primitive trigonal phase, which correlates with the slow preformation of the hexagonal



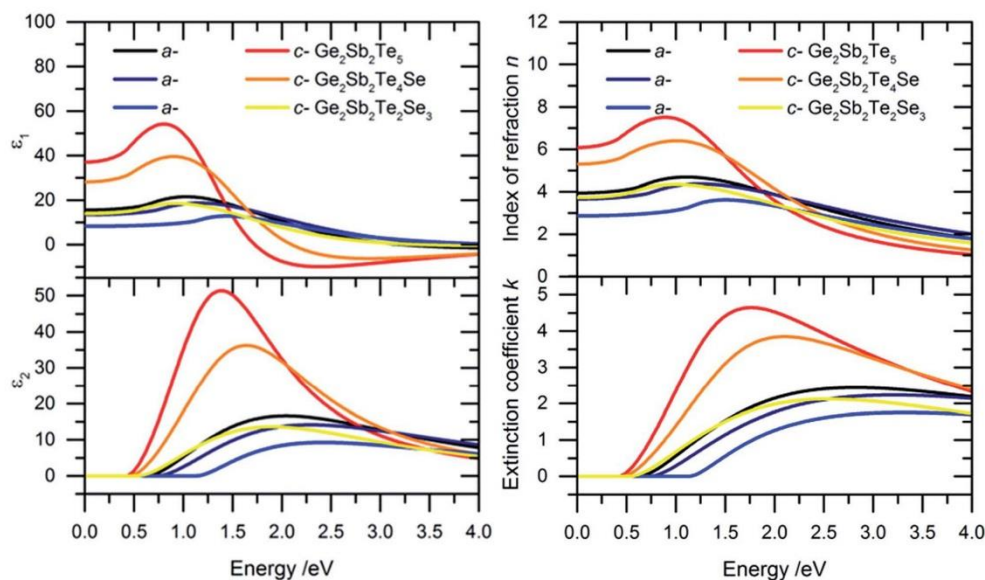


Fig. 7 Left: Dielectric functions ϵ_1 (top) and ϵ_2 (bottom) of the amorphous (a-) and crystalline (c-) samples. ϵ_1 becomes constant for energies below the optical band gap. Functions of ϵ_2 are depicted without the Drude term. Functions of ϵ_2 with the Drude term are seen in Fig. S3.† The crystalline samples were annealed at 160 °C (225), 210 °C (I) and 260 °C (II). Right: Index of refraction n (top) and extinction coefficients k (bottom) of the a- and c-samples. k turns out to be zero at energies below the band gaps.

phase observed by the XRD measurements. This phase transition is visible for $\text{Ge}_2\text{Sb}_2\text{Te}_5$ (327 °C) and for (I) at 315 °C, while (II) only shows a slight change in the resistance. Due to the different heating rates the phase change temperatures measured by *in situ* XRD and *in situ* TEM are smaller than the phase change temperatures determined with the sheet resistance measurements. Thus, the second phase change is not complete at 360 °C, which can be seen as the drop in the resistance at 360 °C. This temperature was held constant for 30 min to complete the second phase change. After annealing the resistances remain quite constant at about 25 Ω for $\text{Ge}_2\text{Sb}_2\text{Te}_5$, 40 Ω for (I) and 68 Ω for (II), respectively, which is typical for degenerated semiconductors with high levels of disorder.⁶⁴

Table 4 Dielectric function ϵ_∞ (degree of polarization) and optical bandgap E_g of the amorphous (a) and crystalline (c) samples. The optical constants were set at energies of 0.05 eV for ϵ_1 while the Drude contribution was subtracted for the crystalline samples. The optical bandgaps were determined *via* α -10 000 method which is exactly the energy where the absorption reaches 10 000 cm^{-1} (ref. 62)

	Optical constant ϵ_∞			Optical bandgap E_g		
	a	c	%increase	a	c	%decrease
225	15.6	37.1	138	0.77	0.53	31
I	13.4	28.1	110	0.88	0.59	33
II	8.2	13.9	70	1.23	0.70	43

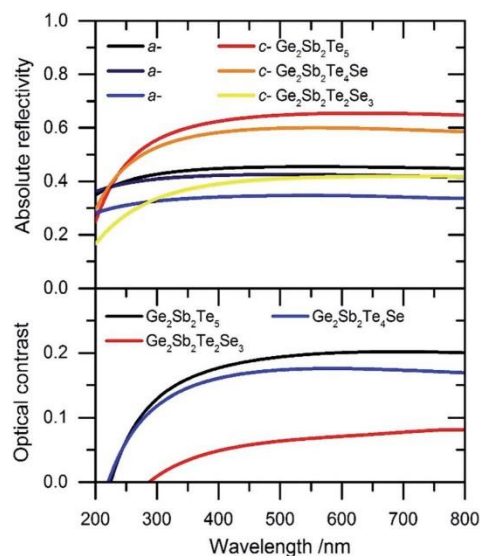


Fig. 8 Calculated absolute reflectivity (top) of the amorphous and crystalline films and total contrast (bottom) of the materials.



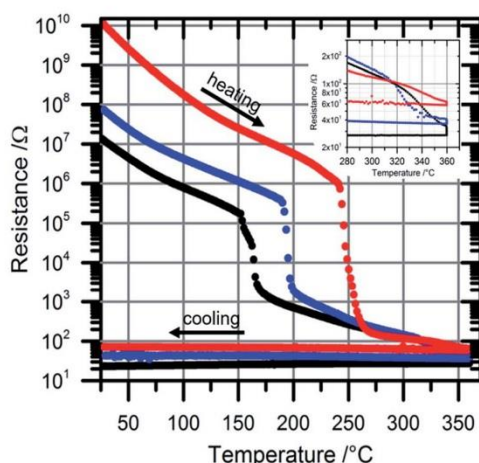


Fig. 9 Sheet resistance measurements of $\text{Ge}_2\text{Sb}_2\text{Te}_5$ (black), $\text{Ge}_2\text{Sb}_2\text{Te}_4\text{Se}$ (blue) and $\text{Ge}_2\text{Sb}_2\text{Te}_2\text{Se}_3$ (red). The phase change is indicated by a large drop of the sheet resistance. With increasing selenium content the 1st phase change temperature increases as well as the electrical contrast. The 2nd phase change is depicted in the inset.

Conclusion and summary

Two new phase change materials were prepared *via* sputter and physical vapor deposition.

The stability of the amorphous phase and the distortion of the metastable cubic phase significantly increased with increasing selenium content.

The optical constants as well as the optical bandgaps for all the presented materials were determined.

The optical contrast decreased with increasing selenium content due to larger structural distortions in selenium rich crystalline phases and therefore the decrease of resonant bonding. The results suggest that the limit of the area for successful optical data storage materials in the treasure map is reached at high ionicity and hybridization of chemical bonds.

The electrical contrast is significantly improved by selenium substitution and is two orders of magnitudes higher than in the unsubstituted material.

Substitution leads to compositions with exceptional good electrical properties for phase change memory devices at the expense of the optical properties.

Acknowledgements

The authors acknowledge the financial support of the State Schleswig-Holstein. Furthermore, the authors would like to thank David C. Johnson and the Center for Advanced Materials Characterization in Oregon (CAMCOR) for the EPMA measurements and kind support.

References

- M. Wuttig, *Nat. Mater.*, 2005, **4**, 265–266.
- W. Bensch and M. Wuttig, *Chem. Unserer Zeit*, 2010, **44**, 92–107.
- M. Wuttig and N. Yamada, *Nat. Mater.*, 2007, **6**, 824–832.
- G. W. Burr, M. J. Breitwisch, M. Franceschini, D. Garetto, K. Gopalakrishnan, B. Jackson, B. Kurdi, C. Lam, L. A. Lastras, A. Padilla, B. Rajendran, S. Raoux and R. S. Shenoy, *J. Vac. Sci. Technol., B: Microelectron. Nanometer Struct.–Process., Meas., Phenom.*, 2010, **28**, 223.
- B.-S. Lee, R. M. Shelby, S. Raoux, C. T. Rettner, G. W. Burr, S. N. Bogle, K. Darmawikarta, S. G. Bishop and J. R. Abelson, *J. Appl. Phys.*, 2014, **115**, 063506.
- D. Lencer, M. Salina and M. Wuttig, *Adv. Mater.*, 2011, **23**, 2030–2058.
- R. Waser, R. Dittmann, M. Salina and M. Wuttig, *Solid-State Electron.*, 2010, **54**, 830–840.
- J. Y. Raty, W. Zhang, J. Lucas, C. Chen, R. Mazzarello, C. Bichara and M. Wuttig, *Nat. Commun.*, 2015, **6**, 7467.
- J. L. F. Da Silva, A. Walsh and H. Lee, *Phys. Rev. B: Condens. Matter Mater. Phys.*, 2008, **78**, 224111.
- T. Matsunaga, R. Kojima, N. Yamada, K. Kifune, Y. Kubota, Y. Tabata and M. Takata, *Inorg. Chem.*, 2006, **45**, 2235–2241.
- T. H. Lee and S. R. Elliott, *Phys. Rev. B: Condens. Matter Mater. Phys.*, 2011, **84**, 094124.
- J. Zhou, Z. Sun, Y. Pan, Z. Song and R. Ahuja, *EPL*, 2011, **95**, 27002.
- A. V. Kolobov, P. Fons, J. Tominaga and M. Hase, *J. Phys. Chem. C*, 2014, **118**, 10248–10253.
- D. Lencer, M. Salina, B. Grabowski, T. Hickel, J. Neugebauer and M. Wuttig, *Nat. Mater.*, 2008, **7**, 972–977.
- K. Shportko, S. Kremers, M. Woda, D. Lencer, J. Robertson and M. Wuttig, *Nat. Mater.*, 2008, **7**, 653–658.
- M. Krbal, A. V. Kolobov, P. Fons, J. Tominaga, S. R. Elliott, J. Hegedus and T. Uruga, *Phys. Rev. B: Condens. Matter Mater. Phys.*, 2011, **83**, 054203.
- M. Krbal, A. V. Kolobov, P. Fons, K. V. Mitrofanov, Y. Tamenori, J. Hegedus, S. R. Elliott and J. Tominaga, *Appl. Phys. Lett.*, 2013, **102**, 111904.
- A. V. Kolobov, J. Haines, A. Pradel, M. Ribes, P. Fons, J. Tominaga, Y. Katayama, T. Hammouda and T. Uruga, *Phys. Rev. Lett.*, 2006, **97**, 035701.
- J. Akola and R. O. Jones, *Phys. Rev. B: Condens. Matter Mater. Phys.*, 2007, **76**, 235201.
- J. Hegedus and S. R. Elliott, *Nat. Mater.*, 2008, **7**, 399–405.
- D. A. Baker, M. A. Paesler, G. Lucovsky, S. C. Agarwal and P. C. Taylor, *Phys. Rev. Lett.*, 2006, **96**, 255501.
- A. V. Kolobov, P. Fons, J. Tominaga and S. R. Ovshinsky, *Phys. Rev. B: Condens. Matter Mater. Phys.*, 2013, **87**, 165206.
- C. Lang, S. Ahn Song, D. Nguyen Manh and D. J. H. Cockayne, *Phys. Rev. B: Condens. Matter Mater. Phys.*, 2007, **76**, 054101.
- S. Kohara, K. Kato, S. Kimura, H. Tanaka, T. Usuki, K. Suzuya, H. Tanaka, Y. Moritomo, T. Matsunaga, N. Yamada, Y. Tanaka, H. Suematsu and M. Takata, *Appl. Phys. Lett.*, 2006, **89**, 201910.



- 25 J. H. Richter, P. Fons, A. V. Kolobov, S. Ueda, H. Yoshikawa, Y. Yamashita, S. Ishimaru, K. Kobayashi and J. Tominaga, *Appl. Phys. Lett.*, 2014, **104**, 061909.
- 26 K. V. Mitrofanov, A. V. Kolobov, P. Fons, X. Wang, J. Tominaga, Y. Tamemori, T. Uruga, N. Ciochini and D. Ielmini, *J. Appl. Phys.*, 2014, **115**, 173501.
- 27 I. Friedrich, V. Weidenhof, W. Njoroge, P. Franz and M. Wuttig, *J. Appl. Phys.*, 2000, **87**, 4130.
- 28 V. Weidenhof, I. Friedrich, S. Ziegler and M. Wuttig, *J. Appl. Phys.*, 2001, **89**, 3168.
- 29 P. Rodenbach, A. Giussani, K. Perumal, M. Hanke, M. Dubsloff, H. Riechert, R. Calarco, M. Burghammer, A. V. Kolobov and P. Fons, *Appl. Phys. Lett.*, 2012, **101**, 061903.
- 30 N. Yamada and T. Matsunaga, *J. Appl. Phys.*, 2000, **88**, 7020.
- 31 Y. Sutou, T. Kamada, M. Sumiya, Y. Saito and J. Koike, *Acta Mater.*, 2011, **60**, 872–880.
- 32 S. Shindo, Y. Sutou, J. Koike, Y. Saito and Y.-H. Song, *Mater. Sci. Semicond. Process.*, 2016, **47**, 1–6.
- 33 Y. Saito, Y. Sutou and J. Koike, *Appl. Phys. Lett.*, 2013, **102**, 051910.
- 34 P. Zalden, C. Bichara, J. van Eijk, C. Braun, W. Bensch and M. Wuttig, *J. Appl. Phys.*, 2010, **107**, 104312.
- 35 G. Bruns, P. Merkelbach, C. Schlockermann, M. Salinga, M. Wuttig, T. D. Happ, J. B. Philipp and M. Kund, *Appl. Phys. Lett.*, 2009, **95**, 043108.
- 36 M. Putero, M.-V. Coulet, T. Ouled-Khachroum, C. Baetz and S. Raoux, *APL Mater.*, 2013, **1**, 062101.
- 37 T. G. Edwards, I. Hung, Z. Gan, B. Kalkan, S. Raoux and S. Sen, *J. Appl. Phys.*, 2013, **114**, 233512.
- 38 M. Putero, M.-V. Coulet, C. Muller, G. Cohen, M. Hopstaken, C. Baetz and S. Raoux, *Appl. Phys. Lett.*, 2014, **105**, 181910.
- 39 M. Putero, M.-V. Coulet, C. Muller, C. Baetz, S. Raoux and H.-Y. Cheng, *Appl. Phys. Lett.*, 2016, **108**, 101909.
- 40 J. Tomforde, S. Buller, M. Ried, W. Bensch, D. Wamwangi, M. Heidelmann and M. Wuttig, *Solid State Sci.*, 2009, **11**, 683–687.
- 41 K. Wang, C. Steimer, D. Wamwangi, S. Ziegler, M. Wuttig, J. Tomforde and W. Bensch, *Microsyst. Technol.*, 2006, **13**, 203–206.
- 42 S. Buller, C. Koch, W. Bensch, P. Zalden, R. Sittner, S. Kremers, M. Wuttig, U. Schürmann, L. Kienle, T. Leichtweiß, J. Janek and B. Schönborn, *Chem. Mater.*, 2012, **24**, 3582–3590.
- 43 K. Wang, C. Steimer, D. Wamwangi, S. Ziegler and M. Wuttig, *Appl. Phys. A*, 2005, **80**, 1611–1616.
- 44 X. Zhou, L. Wu, Z. Song, F. Rao, M. Zhu, C. Peng, D. Yao, S. Song, B. Liu and S. Feng, *Appl. Phys. Lett.*, 2012, **101**, 142104.
- 45 T. Rosenthal, P. Urban, K. Nimmrich, L. Schenk, J. de Boor, C. Stiewe and O. Oeckler, *Chem. Mater.*, 2014, **26**, 2567–2578.
- 46 E. M. Vinod, K. Ramesh and K. S. Sangunni, *Sci. Rep.*, 2014, **5**, 8050.
- 47 E. M. Vinod, K. Ramesh, R. Ganesan and K. S. Sangunni, *Appl. Phys. Lett.*, 2014, **104**, 063505.
- 48 A. A. Coelho, *TOPAS-Academic. Version 6.0*, 2016.
- 49 D. Balzar, N. Audebrand, M. R. Daymond, A. Fitch, A. Hewat, J. I. Langford, A. Le Bail, D. Louër, O. Masson, C. N. McCowan, N. C. Popa, P. W. Stephens and B. H. Toby, *J. Appl. Crystallogr.*, 2004, **37**, 911–924.
- 50 R. W. Cheary and A. A. Coelho, *J. Appl. Crystallogr.*, 1992, **25**, 109–121.
- 51 W. Theiss, *SCOUT Hard- and Software*.
- 52 L. J. A. van der Pauw, *Philips Res. Rep.*, 1958, **13**, 1–9.
- 53 L. J. A. van der Pauw, *Philips Res. Rep.*, 1958, **20**, 220–224.
- 54 F. M. Smits, *Bell Labs Techn. J.*, 1958, **37**, 711–718.
- 55 M. A. Green and M. W. Gunn, *Solid-State Electron.*, 1971, **14**, 1167–1177.
- 56 T. Matsunaga, N. Yamada and Y. Kubota, *Acta Crystallogr.*, 2004, **60**, 685–691.
- 57 Z. Sun, J. Zhou and R. Ahuja, *Phys. Rev. Lett.*, 2006, **96**, 055507.
- 58 W. Zhang, A. Thiess, P. Zalden, R. Zeller, P. H. Dederichs, J.-Y. Raty, M. Wuttig, S. Blügel and R. Mazzarello, *Nat. Mater.*, 2012, **11**, 952–956.
- 59 N. Yamada, E. Ohno, K. Nishiuchi, N. Akahira and M. Takao, *J. Appl. Phys.*, 1991, **69**, 2849.
- 60 B. J. Kooi, W. M. G. Groot, J. Th and M. De Hosson, *J. Appl. Phys.*, 2004, **95**, 924.
- 61 J. R. Chelikowsky and J. C. Phillips, *Phys. Rev. B: Condens. Matter Mater. Phys.*, 1978, **17**, 2453.
- 62 B.-S. Lee, J. R. Abelson, S. G. Bishop, D.-H. Kang, B.-K. Cheong and K.-B. Kim, *J. Appl. Phys.*, 2005, **97**, 093509.
- 63 T. Kato and K. Tanaka, *Jpn. J. Appl. Phys.*, 2005, **44**, 7340–7344.
- 64 T. Siegrist, P. Jost, H. Volker, M. Woda, P. Merkelbach, C. Schlockermann and M. Wuttig, *Nat. Mater.*, 2011, **10**, 202–208.



3. Veröffentlichung ternäre Chromchalkogenide

3.1 Structural properties of the thermoelectric material CuCrS_2 and of deintercalated Cu_xCrS_2 on different length scales: X-ray diffraction, pair distribution function and transmission electron microscopy studies

Um die strukturellen Änderungen durch das gezielte Entfernen von Cu^+ Ionen aus der Verbindung CuCrS_2 zu verstehen, wurden XRD, PDF und TEM Untersuchungen sowohl bei Raumtemperatur, als auch *in situ* bei erhöhten Temperaturen durchgeführt. Ziel hierbei war es durch eine topotaktische Redoxreaktion mittels Jod in Acetonitril, 1/3 der Cu^+ Ionen zwischen den CrS_2 Schichten zu entfernen und somit eine erhöhte Unordnung im Kationengitter zu erzeugen. Eine solche Unordnung soll die Streuung der Phononen in thermoelektrischen Materialien erhöhen und somit einen wesentlichen Beitrag zur Erhöhung des ZT Wertes liefern. Raumtemperatur XRD Untersuchungen offenbarten die Bildung einer bis dahin unbekannt Phase $\text{Cu}_{0.66}\text{CrS}_2$. Die Struktur konnte aus den Röntgenpulverdaten gelöst werden und wies eine monokline Verzerrung des Gitters mit einer $3a$ Überstruktur auf. Des Weiteren deutete die Bildung verzerrter CrS_6 Oktaeder auf die Bildung des Jahn-Teller-Ions Cr^{4+} . PDF Untersuchungen zeigten deutlich eine Abnahme der Cu- Cu Korrelationslänge und eine Reduktion der Cu-S Bindungslängen. *In situ* TEM Untersuchungen verdeutlichten den Verlust der Überstruktur durch eine erhöhte Mobilität der Cu^+ Ionen. Hochtemperatur XRD Experimente zeigten eine signifikante Zunahme der atomaren Auslenkungsparameter (Debye-Waller-Faktoren, DW) von Cu^+ , was eine erhöhte Mobilität der Kationen widerspiegelt. Die DW von Cr-Kationen hingegen nahmen mit steigender Temperatur ab, was durch eine verringerte Verzerrung der Oktaeder verursacht wurde. Oberhalb von 473 K findet eine Phasenumwandlung in CuCrS_2 und CuCr_2S_4 .

A.-L. Hansen, T. Dankwort, H. Groß, M. Etter, J. König, V. Duppel, L. Kienle, W. Bensch, *Journal of Materials Chemistry C*, **2017**, (accepted) DOI: 10.1039/C7TC02983G.



**Structural properties of the thermoelectric material CuCrS₂
and of deintercalated CuxCrS₂ on different length scales: X-
ray diffraction, pair distribution function and transmission
electron microscopy studies**

Journal:	<i>Journal of Materials Chemistry C</i>
Manuscript ID:	Draft
Article Type:	Paper
Date Submitted by the Author:	n/a
Complete List of Authors:	Bensch, Wolfgang; der Universitate Kiel, Institut fur Anorganische Chemie Hansen, Anna; Christian-Albrechts Universitat, Institut fur Anorganische Chemie Dankwort, Torben; Christian-Albrechts Universitat, Institute for Materials Science Groß, Hendrik; Christian-Albrechts-Universitat zu Kiel , Technical Faculty Etter, Martin; Deutsches Elektronen Synchrotron (DESY) König, Jan; Fraunhofer Institute for Physical Measurement Techniques IPM, Thermoelectrics and Integrated Sensor Systems (TES) Duppel, Viola; Max-Planck-INstitut, Kienle, Lorenz; Institute for Material Science, Synthesis and Real Structure

SCHOLARONE™
Manuscripts

Structural properties of the thermoelectric material CuCrS_2 and of deintercalated Cu_xCrS_2 on different length scales: X-ray diffraction, pair distribution function and transmission electron microscopy studies

Anna-Lena Hansen^a, Torben Dankwort^b, Hendrik Groß^b, Martin Etter^c, Jan König^d, Viola Duppel^e
Lorenz Kienle^b, Wolfgang Bensch^a

^aInstitute of Inorganic Chemistry, Kiel University, Max-Eyth-Str. 2, D-24118 Kiel, Germany.

^bInstitute for Materials Science, Kiel University, Kaiserstrasse 2, 24143 Kiel, Germany.

^cDeutsches Elektronen-Synchrotron (DESY), Hamburg 22607, Germany.

^dFraunhofer Institute for Physical Measurement Techniques IPM, Heidenhofstrasse 8, 79110 Freiburg, Germany

^eNanochemistry, Max Planck Institute for Solid State Research, Heisenbergstrasse 1, D-70569 Stuttgart, Germany.

Abstract

We report on the structural alterations of the thermoelectric material CuCrS_2 introduced by the removal of 1/3 of the Cu^+ ions which are located between CrS_2 layers. X-ray diffraction (XRD) and pair distribution function (PDF) analyses revealed a newly formed $\text{Cu}_{0.66}\text{CrS}_2$ phase with monoclinic symmetry and a $3a$ superstructure. Simultaneously, a distortion of CrS_6 octahedra is observed strongly indicating the oxidation of $\text{Cr}^{3+} \rightarrow \text{Cr}^{4+}$ leading to a Jahn-Teller distortion. The structural features extracted from XRD indicate a pronounced disorder in the cationic sub-lattice at moderate temperatures (400 K). Transmission electron microscopy (TEM) examination elucidates the formation of a second $\text{Cu}_{0.66}\text{CrS}_2$ phase without the superstructure, caused by incipient Cu^+ mobility upon beam irradiation. The synergetic combination of high temperature XRD and TEM investigations unveiled the complete mechanism of the phase transition occurring at 503 K, where a transformation into the spinel CuCr_2S_4 and stoichiometric CuCrS_2 occurs.

Introduction

Thermoelectric generators convert heat into usable electrical energy. Therefore, these materials have a high potential contributing to the intensively discussed energy transition, because thermally inefficient processes will never be completely avoidable. The efficiency of thermoelectric materials is assessed by a dimensionless ZT value:

$$ZT = \frac{\sigma \cdot S^2}{\kappa} T \quad (1)$$

where σ is the electrical conductivity, S the Seebeck coefficient (σS^2 is also often called the power factor, PF), T is the absolute temperature, and κ is the thermal conductivity with contributions from charge carriers and phonons. For practically relevant thermoelectric materials σ is about 1000 S/cm, S ca. 200 $\mu\text{V/K}$ resulting in a PF of approximately 40 $\mu\text{W/cmK}^2$ and κ is about 1 W/mK. With a value for ZT of about one, Bi_2Te_3 showed the highest ZT values at room temperature and for decades this material represented the upper limit within thermoelectric research.¹ Besides strategies to enhance the PF of materials, much efforts were made to reduce the thermal conductivity of materials.²⁻⁴ The Phonon Glass-Electron Crystal (PGEC) concept, developed by Slack in the 1990s, postulates that phonons, as the main carrier of thermal energy, should be scattered in an ideal thermoelectric material like in a glass, while the electrons should move freely like in a perfect crystal.⁵ Innovative concepts like nanostructuring of suitable materials led to a renaissance within this field of research. It has been impressively demonstrated that reducing the grain size or introducing nanosized structures or precipitates into a distinct material results in a decrease of the thermal conductivity, thus, the ZT value is greatly enhanced.⁶⁻⁸ Ideal materials possess nanostructures on different length scales to scatter high and low frequency phonons, representing so called hierarchical structures.^{9,10} By applying these new approaches the upper limit of ZT was raised by a factor of ~ 3 , however, the materials applied suffer severely from reduced availability inhibiting large scale applications which would have an impact on global energy transition. Consequently, materials have to be of low cost, nontoxic and environmental friendly. The search for new materials fulfilling these attributes identified sulphides as highly promising with respect to the necessary transition to more sustainable and earth abundant materials.¹¹⁻¹⁷ Classic thermoelectric devices are often based on expensive, rare and toxic elements like Sb, Bi, Pb and Te and obviously are not attractive for large scale usage. Recently, another concept was developed, Phonon-Liquid Electron-Crystal (PLEC), based on studies on the extremely low thermal conductivity and high thermoelectric performance of the superionic phases of Cu_{2-x}Se and Cu_2S .^{13,18} But these materials are not considered to be uncontroversial regarding their large-scale applicability. One major problem is

2

their temperature instability, a tremendous and unwanted migration of Cu^+ ions when subjected to currents and voltages similar to those applied in typical thermoelectric devices.¹⁹ Another sulphide material, CuCrS_2 , exhibit a similar high mobility of Cu^+ ions, which has recently attracted attention as a low cost, environmental friendly thermoelectric material.^{20–24} The layered antiferromagnetic compound CuCrS_2 composed of edge-sharing CuS_2 slabs crystallizes in the α - NaFeO_2 structure type with trigonal R symmetry. Cu^+ cations occupy half of the tetrahedral positions (space group $R\bar{3}m$, $a = 3.4 \text{ \AA}$, $c = 18.7 \text{ \AA}$) in every second van der Waals gap.^{25–27} Rasch *et al.* reported a magneto-elastic coupling, causing a phase transition into a monoclinic structure at $\sim 40 \text{ K}$.²⁸ At temperatures above $\sim 400 \text{ }^\circ\text{C}$, CuCrS_2 shows ionic conductivity.^{27,29–31} The high ionic mobility is discussed as a reason for the very low thermal conductivity at elevated temperatures ($\sim 0.3 \text{ W/m-K}$ at $650 \text{ }^\circ\text{C}$).^{20,30} The material exhibits p-type semiconducting properties with an indirect band gap of 0.58 eV . The charge carrier density varies between 10^{19} and 10^{20} cm^{-3} and the Seebeck coefficient is about $400 \text{ } \mu\text{V K}^{-1}$.³² The good electrical properties of CuCrS_2 combined with an almost glass like thermal conductivity makes it an almost ideal PGEC system and depending on the literature reports, ZT values of 0.01 up to 2 were reported.^{20–24} Theoretical calculations indicate that, besides an occupational disorder of Cu^+ , disordered Cr^{3+} ions should have a large influence on the thermoelectric properties of the material. With an increasingly disordered occupation of the crystallographic Cr sites, a transition from semiconducting to metallic behaviour was postulated.³² These theoretical results are supported by the observation that Cr vacancies can be generated by sintering at higher temperatures. The resulting self-doped material has an increased electrical conductivity and depending on the degree of doping, Seebeck coefficients were reported to be in the range of 150 and $450 \text{ } \mu\text{V/K}$.²¹ There have been attempts to preserve the high temperature Cu^+ disorder at room temperature by quenching single crystals from $850 \text{ }^\circ\text{C}$, however, comparison of the structures of the quenched material and slowly cooled specimens did not show significant differences. The largely differing thermoelectric properties of CuCrS_2 indicate that the structures of the materials investigated exhibit pronounced differences on different length scales. We addressed the question whether Cu disorder can be enhanced at room temperature by successive removal (deintercalation) of Cu^+ ions by a topotactic redox reaction. The deintercalation was done with iodine dissolved in acetonitrile, a method which was successfully used to completely deintercalate ACrS_2 ($A = \text{alkali metal}$).^{33,34} Our attempt was not to fully remove Cu^+ , but to deintercalate a distinct amount in order to enhance the disorder between the CrS_2 layers. Here, we report for the first time on the structural changes caused by the topotactic removal of Cu^+ of the promising thermoelectric material CuCrS_2 using X-ray diffraction, total scattering and

transmission electron microscopy. In previous studies we were able to demonstrate that often highly promising thermoelectric materials cannot withstand elevated temperatures and thermal cycling.^{35–37} Therefore, we performed temperature dependent *in situ* X-ray diffraction experiments and *ex situ* TEM investigations on CuCrS_2 and Cu_xCrS_2 to clarify the temperature stability of the material. Moreover, we carefully investigated the mechanisms of structural transitions by means of *in situ* TEM investigations.

EXPERIMENTAL

Samples were prepared by heating stoichiometric mixtures of pure elements in evacuated quartz ampoules for one week at 1273 K. The elements were supplied by Alfa Aesar (Cu 99.5 %, S 99.5 %) and Sigma Aldrich (Cr 99.5 %). The deintercalation was performed in distilled acetonitrile (water free) and dissolved iodine in excess. Typically 0.5 g of reground CuCrS_2 were used in the experiments. The slurries were stirred for 30 min at ambient conditions, filtered and washed with acetonitrile. The dried filtrate contained CuI , indicating the successful deintercalation of Cu^+ ions. The Cu content of Cu_xCrS_2 was determined applying Energy dispersive X-ray spectroscopic (EDX) measurements. XRD at room temperature and total scattering investigations were performed in Debye-Scherrer geometry at beamline P02.1 at Petra III (DESY, Hamburg) using high-energy synchrotron radiation (60 keV, $\lambda = 0.20722 \text{ \AA}$). A XRD1621 PerkinElmer amorphous silicon image plate detector at 1010 mm for XRD and 371 mm distance for total scattering was used. The powder samples were measured in sealed glass capillaries, which were also measured empty to subtract their contribution to total scattering. Instrumental parameters were refined using a LaB_6 reference sample. High temperature X-ray powder diffraction experiments were performed in sealed quartz capillaries at beamline I15 at Diamond Light Source (DLS, Oxfordshire) from ambient 294 to 533 K utilizing a N_2 blower GSB 1300 (FMB Oxford) at 29.2 keV (0.4246 \AA). Rietveld refinements of XRD data were performed using Topas Academic 6.0.³⁸ Atomic pair distribution function analysis was done with the xPDFsuite.³⁹ LaB_6 was used to account for the instrumental contribution to the dampening of the resulting PDF. Energy dispersive X-ray spectroscopic (EDX) measurements were performed using a Philips Environmental Scanning Electron Microscope ESEM XL30 equipped with an EDAX detector. For nanostructure analysis, two different microscopes have been used. First a Philips CM 30 with LaB_6 cathode operated at 300 kV (C_s 1.15 mm) and a FEI Tecnai F30 STwin with field emission gun operated at 300 kV (C_s 1.2 mm). For HRTEM contrast simulation JEMS based on EMS by Pierre Stadelmann was used⁴⁰. Further for image processing Gatan Digital

Micrograph and scripts described in ⁴¹ have been facilitated. All drawings of the structures were performed using VESTA Version 3.⁴²

Results and Discussion

X-ray powder diffraction experiments

The deintercalation experiments were optimized to achieve the composition $\text{Cu}_{0.66}\text{CrS}_2$. But also samples with larger average Cu contents were investigated with in-house XRD. Measurements with high energy synchrotron radiation revealed the presence of ~2.5 wt.% of Cr_2O_3 in the samples before and after deintercalation (Figure 1), and a very low amount of cubic spinel CuCr_2S_4 (< 1wt.%). Both impurity phases could not be detected in powder patterns collected on a standard laboratory X-ray diffractometer in Bragg-Brentano-Geometry (X'Pert Pro MPD, PANalytical, $\text{Cu K}\alpha_{1,2}$). Rietveld refinement of the starting material CuCrS_2 exhibit very good agreement with the structure described in the literature (space group $R3m$, $a = 3.48 \text{ \AA}$, $c = 18.69 \text{ \AA}$).²⁷ The results of all Rietveld refinements are given in the *Electronic Supporting Information*. The crystallinity of the deintercalated phase ($\text{Cu}_{0.66}\text{CrS}_2$) is drastically reduced as evidenced by decreased intensity of the Bragg reflections in the powder pattern. While a minor amount of reflections could still be assigned to the starting CuCrS_2 phase (~7.5 %), which was only detectable by means of high energy synchrotron radiation, the majority belong to a new unknown phase. The diffraction pattern could not be explained by a classic staging model, describing the periodic arrangement of guest and host layers, accompanied by the typical formation of satellite reflections around the (00 l) series.⁴³ This suggested a more complex change of the structure. The splitting of several reflections like (101), (104), (107), (108), (110) reveals a monoclinic distortion of the unit cell. The powder pattern could be indexed with a C-centered monoclinic cell and because space group $R3m$ is non-centrosymmetric, the direct subgroup Cm was chosen to solve the structure using the simulated annealing approach (space group Cm , $a = 17.67$, $b = 3.42$, $c = 6.42$, $\beta = 107.2^\circ$).⁴⁴ Rietveld refinement and total scattering experiments indicated a higher symmetry, since refinement of the PDF caused high correlations (>85 %) of the atomic positions, indicating a centrosymmetric space group rather than the Cm cell that was used initially. Therefore, the centrosymmetric space group $C2/m$ was used for further investigations. The monoclinic distortion caused by magnetic coupling of the spins at low temperatures mentioned in the introduction ²⁸, differs drastically from the distorted structure that is observed here. The structural relationship between the monoclinic and rhombohedral cell

(hexagonal axes) is shown in Figure 2. A structural transformation to the monoclinic symmetry caused by deintercalation of cations was observed before, especially for well characterized battery materials, e.g. LiCoO_2 and NaTiO_2 .^{45–50} Compared to CuCrS_2 the c lattice parameter is reduced and a superstructure is formed with a three times larger a lattice parameter, with respect to an undistorted monoclinic setting. The distortion of the monoclinic unit cell is independent of the amount of deintercalated Cu^+ , and Rietveld refinements always yielded the composition $\text{Cu}_{0.66}\text{CrS}_2$ with a monoclinic cell and different amounts of the starting material CuCrS_2 (Figure S1).

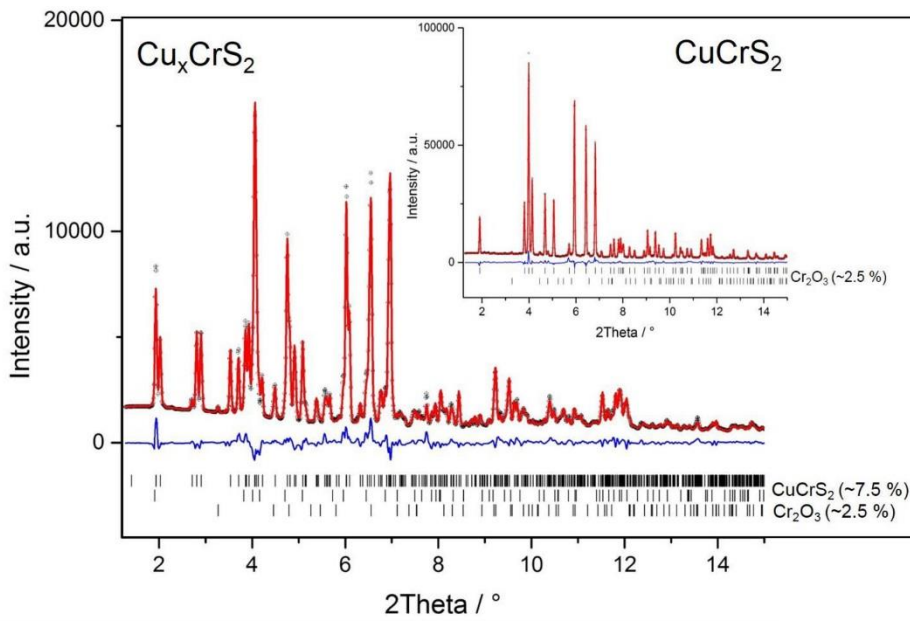


Figure 1: Rietveld refined synchrotron XRD pattern of CuCrS_2 (inset) and deintercalated Cu_xCrS_2 phase, $x=0.66$. Phases are indicated by labelled tic marks. Circles represent measured data, red line calculated curve, blue is the difference curve. Background was refined using a Chebyshev polynomial. $R_{wp}=6.4\%$ (Cu_xCrS_2), $R_{wp}=6.15\%$ (CuCrS_2).

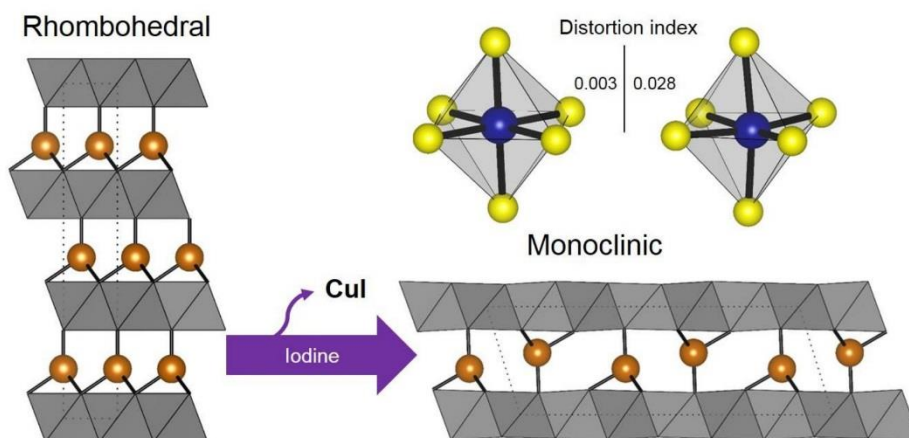


Figure 2: Schematic drawing of the deintercalation mechanism and structural relationship between the high symmetry CuCrS_2 phase on the left and the distorted monoclinic on the right. Both cells are projected onto (010). Dotted lines represent the unit cell. Two types of octahedra are enlarged to illustrate the distortion. Distortion indices were calculated after Baur.

The structure of the monoclinic phase exhibits a modulation of the CrS_2 layer caused by an alternation of distorted and undistorted octahedra (see Figure. 2). Additionally, as a measure for the distortion an index after Baur based on the bond lengths is given.⁵¹ It seems that only one of the two CrS_6 octahedra is affected showing an elongation and a reduced effective coordination number of 5.75. These results strongly indicate an oxidation of Cr^{3+} to Cr^{4+} caused by the removal of Cu^+ ions. The Cr^{4+} (d^2) ion with electronic configuration $t_{2g}^2 e_g^0$ is a Jahn-Teller ion responsible for the distortion and most probably only one of the two independent Cr cations is oxidized.

Total Scattering Analysis

Structural investigations using X-ray diffraction gives information on the averaged long range structure. In order to confirm the local distortion of the CrS_6 octahedra, total scattering experiments to a higher Q range were performed to calculate the corresponding pair distribution function (PDF). The structural model obtained by simulated annealing and Rietveld refinement of the XRD data fitted well with the PDF (Figure S2). The structure obtained by fitting PDF (Table S2), depicted in Figure 3, corresponds well with the results of the XRD analysis, showing a similar modulation of the CrS_2 layer. This indicates a good agreement of both the local and long-range structure.

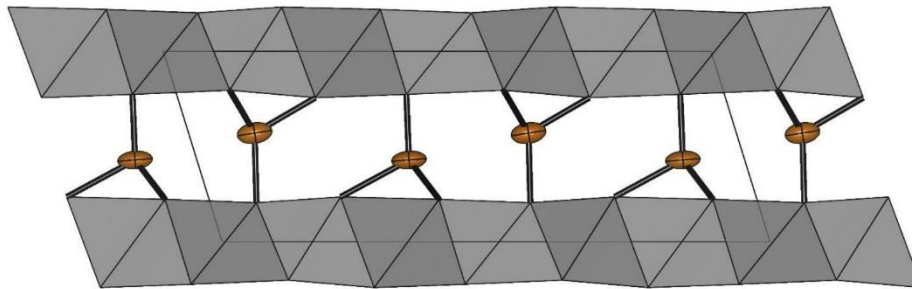


Figure 3: left: schematic illustration of the distorted monoclinic cell, projected onto (010). Anisotropic DW factors are displayed as displacement ellipsoids on the 99% level.

The Debye-Waller factor (DW), representing the average displacement of the atoms around their equilibrium positions, are intrinsically very large for Cu^+ in layered structures. Anisotropic DW factors evidence the displacement of Cu^+ ions between the layers (see Figure 3).

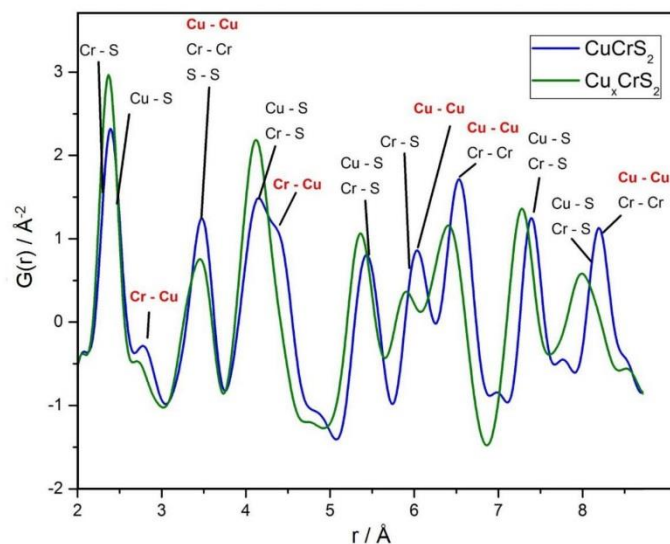


Figure 4: Comparison of pair distribution functions of deintercalated, $x = 0.66$ (green) and starting material (blue). The radial distances of the starting CuCrS_2 phase are marked.

Comparing the PDF of CuCrS_2 and $\text{Cu}_{0.66}\text{CrS}_2$ clearly reveals a decrease of the intensity of radial distributions associated with copper, especially those belonging to Cu-Cu distances and

Cr-Cu (Figure 44, marked red). The mean Cr-S and Cu-S bonds are shortened, indicated by an increase and shift of the corresponding peaks in the PDF. Additionally, a slight broadening of the peaks occurred, especially of Cr-S distances around 6 Å, caused by the distortion of the CrS₆ octahedra.

Temperature stability and phase transformations

The temperature stability of CuCrS₂ was investigated in the past and according to literature data the structure is at least stable up to 1273 K.^{52,53} We performed high temperature XRD measurements up to 737 K, supporting the temperature stability of the starting material CuCrS₂. Temperature dependent XRD measurements of Cu_{0.66}CrS₂ were performed from room temperature to 533 K. A phase transformation occurs between 473 and 503 K as evidenced by the development of new reflections (Figure 5, Figure S3).

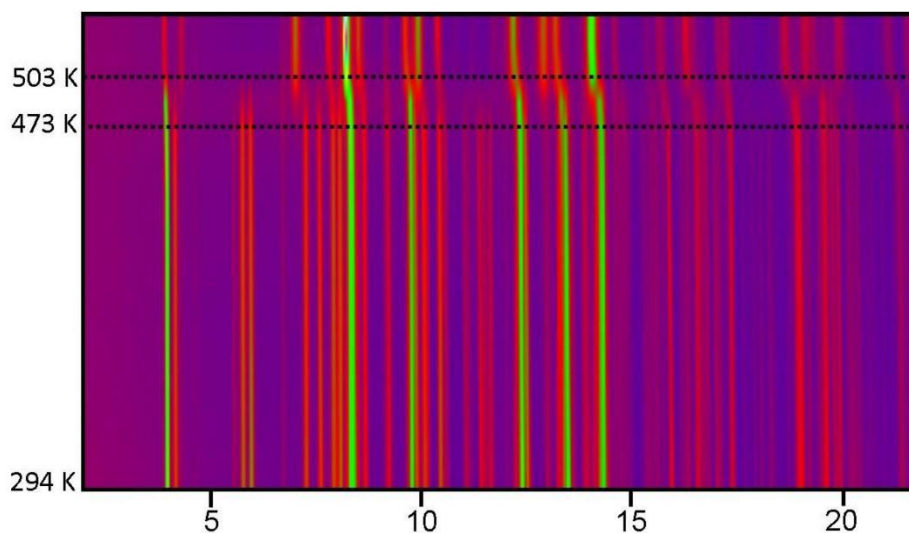
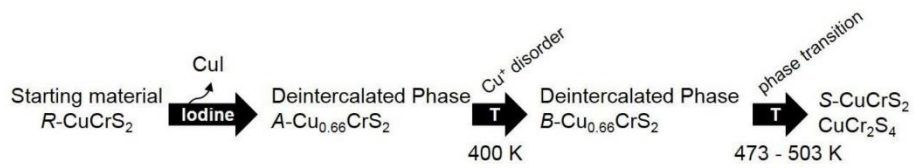


Figure 5: Temperature-dependent 2D Guinier patterns generated from X-ray powder diffraction patterns collected from room temperature to 533K for Cu_{0.66}CrS₂. At 437 K a phase transformation starts which is completed at 503 K.

A quantitative phase analysis based on Rietveld refinements covering the temperature range 294 to 533 K revealed a decrease of the amount of the monoclinic phase Cu_{0.66}CrS₂ (denoted as A-Cu_{0.66}CrS₂) accompanied by an increasing amount of a CuCrS₂ phase with a reduced Cu occupancy (B-Cu_xCrS₂) starting at about 400 K (see Figure 6). Further increase of the

temperature leads to a phase transformation into stoichiometric CuCrS_2 (S- CuCrS_2) and the spinel CuCr_2S_4 beginning at $T \approx 773 \text{ K}$ (Figure 6). Due to a distinct peak overlap, we were not able to judge whether the formed $B\text{-Cu}_x\text{CrS}_2$ was of trigonal R or monoclinic symmetry (without the superstructure), because the differences between these structures are very small and still a certain amount of the starting CuCrS_2 phase (R- CuCrS_2) was present in the sample, as already discussed. Transmission electron microscopy revealed the loss of the superstructure of the monoclinic phase via electron beam heating and interrelated disordering of Cu^+ as discussed in detail in the next chapter. Based on XRD and TEM investigations, the mechanism of the deintercalation, temperature induced loss of the superstructure and phase transition can therefore be denoted as:



We note that the amount of Cr_2O_3 stayed constant at around 2.5 - 3 %.

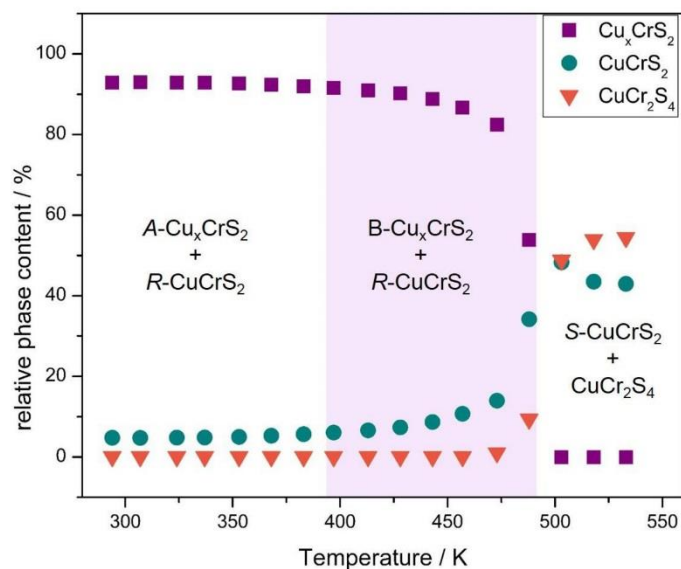


Figure 6: Temperature dependent quantitative phase analysis. The assigned phases are described in detail in the text. Estimated errors are smaller than the symbols.

A comparison of the DW factors of CuCrS_2 and $\text{Cu}_{0.66}\text{CrS}_2$ at room temperature revealed a decreased value for the Cu site (-24 %) and an increased value for the Cr site (+21 %). This change is caused by the elongation of the CrS_6 octahedra and a simultaneous decrease of the average Cu-S bond. While the determination of DW factors can be ambiguous in Rietveld refinements due to correlations with other parameters like e.g. site occupation factors, the changes of the DW factors is immediately observed in the PDF displayed in Figure 4. This highlights the enormous potential of the total scattering approach and its synergistic nature with respect to XRD and TEM methods. With higher temperature the DW factor for Cu^+ increased even more (by a factor of 2), again supporting a very high mobility of the Cu^+ cations. Interestingly, the DW factors of Cr cations decrease with increasing temperatures (Figure 7), most likely caused by a reduced distortion of the CrS_6 octahedra. The distortion indices obtained by Rietveld refinements demonstrate the same trend, *i.e.* a reduction of the distortion of CrS_6 octahedra with increasing temperatures as indicated in Figure 7 by decreasing averaged distortion indices. Most likely the more regular coordination around the Cr centres is caused by electron hopping between the two independent Cr cations.

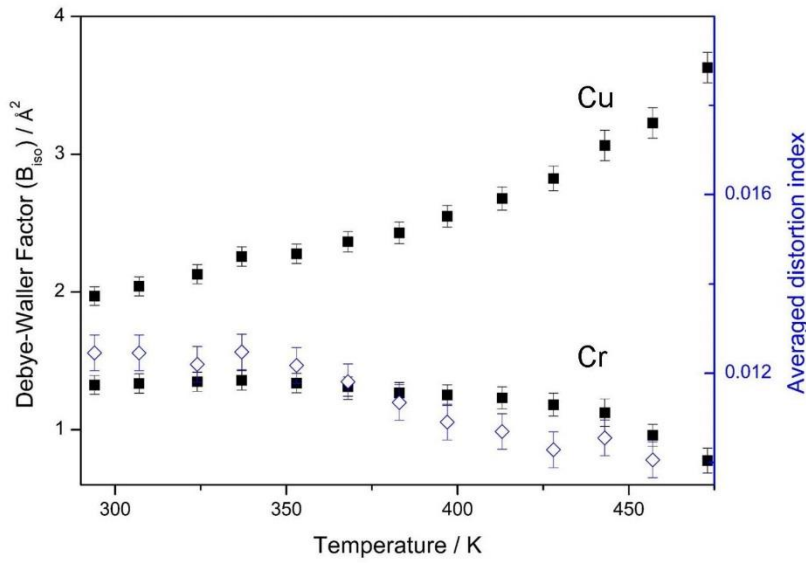


Figure 7: Debye Waller factors of copper and chromium against temperatures obtained by Rietveld refinement. Distortion indices after Baur of the CrS_6 octahedra are displayed in blue.

The phase transformation is not reversible and Rietveld refinement of the room temperature powder pattern of the heated sample yields a phase distribution of ~58% spinel CuCr_2S_4 , ~39% CuCrS_2 and ~3% Cr_2O_3 (Figure S4).

Transmission Electron Microscopy (TEM)

To determine the real structure of $A\text{-Cu}_x\text{CrS}_2$ and the structural transitions, samples were investigated by TEM. The aforementioned monoclinic distortion of $A\text{-Cu}_x\text{CrS}_2$ leads *i.a.* to a change in the c -axis lattice parameter. To directly compare the structures of $R\text{-CuCrS}_2$ and $A\text{-Cu}_x\text{CrS}_2$, the trigonal ($R3m$) CuCrS_2 has been transformed to a monoclinic setting, having the same $3a$ superstructure, by:

$$(a,b,c)_{\text{mon}} = (a,b,c)_{\text{trig}} \cdot \begin{pmatrix} -6 & 0 & 2/3 \\ -3 & 1 & 1/3 \\ 0 & 0 & 1/3 \end{pmatrix} \quad (1)$$

The c lattice parameter of $R\text{-CuCrS}_2$ transformed to the monoclinic setting is 6.550 Å and therefore deviate significantly from that of $A\text{-Cu}_x\text{CrS}_2$, being refined to a value of $c = 6.412$ Å.

Experimentally $c(A-Cu_xCrS_2)$ has been determined from an electron diffraction pattern of zone axis $[130]_{\text{mon}}$ (Figure 8) to 6.42 Å. This value corresponds well with the one determined by Rietveld refinement of XRD room temperature data. Note that no changes of chemical composition (EDX) and $c(A-Cu_xCrS_2)$ were observed upon electron beam irradiation.

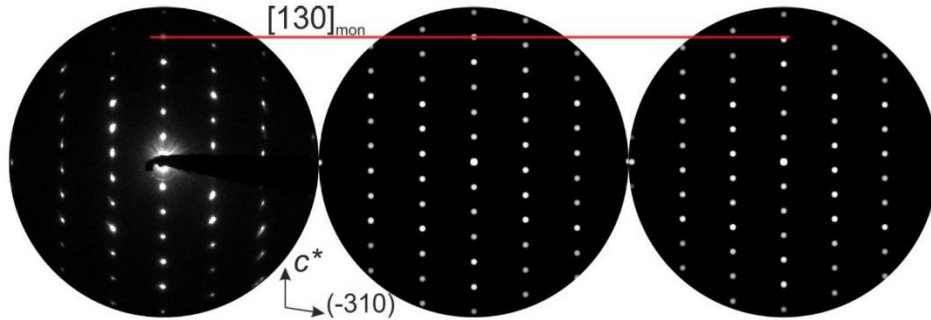


Figure 8: Electron diffraction patterns of the monoclinic $B-Cu_xCrS_2$ in zone axis $[130]$ in comparison to simulated patterns based on the model for Cu_xCrS_2 (middle) and $CuCrS_2$ (right)⁵⁴. The red line highlights the difference in d -spacing along c^* .

However, as it will be shown below the samples are highly beam sensitive with two separate beam induced phase transformations, both correlating well with those observed by XRD. Electron diffraction patterns of pristine $A-Cu_xCrS_2$ exhibit superstructure reflections resulting in a tripling of the a axis (Figure 9a), left, yellow circles). This phase could be convincingly described using the model of $A-Cu_xCrS_2$ obtained by structure solution and Rietveld refinement, as indicated by the convincing correlation of experimental and simulated electron diffraction and pattern. The HRTEM contrast could be simulated facilitating the $A-Cu_xCrS_2$ structure and proves the ordering by corresponding superstructure peaks, cf. Figure 9a), right.

However, after short irradiation (few seconds) the superstructure reflections gradually decay (Figure S5) while only the reflections hkl with $h = 3n$ persist (red circles). As the superlattice reflections and consequently also the alternating contrast along $[100]$ direction stems from the ordering of Cu^+ ions, the vanishing of both indicates that the distribution of Cu ions changes.

Thus to determine the structure of the beam induced phase ($B-Cu_xCrS_2$), different models have been created. As already discussed above, XRD measurements only revealed a loss of the superstructure and a decreased Cu occupancy, with regard to the $R-CuCrS_2$ structure. Based on the observation that the c lattice parameter (cf. Figure 8) is not changed upon beam irradiation, the newly formed $B-Cu_xCrS_2$ structure (monoclinic setting) with cell parameters similar to those

of $A-Cu_xCrS_2$ and lowered Cu occupancy was created as a first model (Figure S6 left). As mentioned above the superstructure ordering is mainly attributed to ordering of Cu ions, thus a second structure model was created by altering the monoclinic phase considering statistically distributed Cu atoms on lattice sites similar to with respect to the trigonal R phase (Figure S6 right). Best fit was obtained for the first model (Figure 9b; HRTEM contrast simulation and simulated electron diffraction coincide well) thus it can be concluded that the beam induced phase is closely related to the rhombohedral phase (no alternating occupation of Cu ions and distorted CrS_6 octahedra) and still maintains the cell parameters of the monoclinic phase. These results suggest that the Cu ions are becoming highly mobile under electron beam illumination, thus eliminating the superstructure of $A-Cu_xCrS_2$. Note that the HRTEM contrast in Figure 9b enables clear identification of the structural motifs. The upper micrograph resembles Scherzer focus, i.e. dark and bright contrasts correlate with high and low values of the projected potential, respectively. The lower micrograph resembles the inverse contrast with respect to the Scherzer focus.

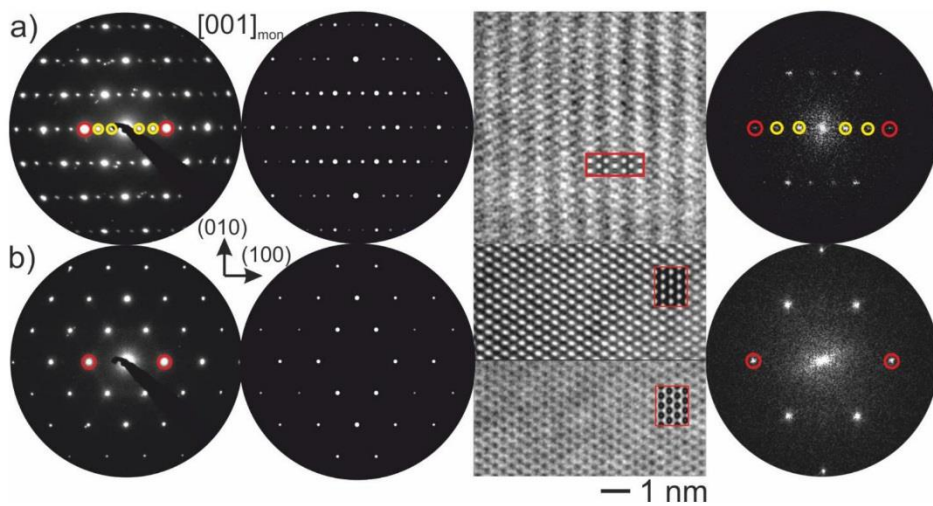
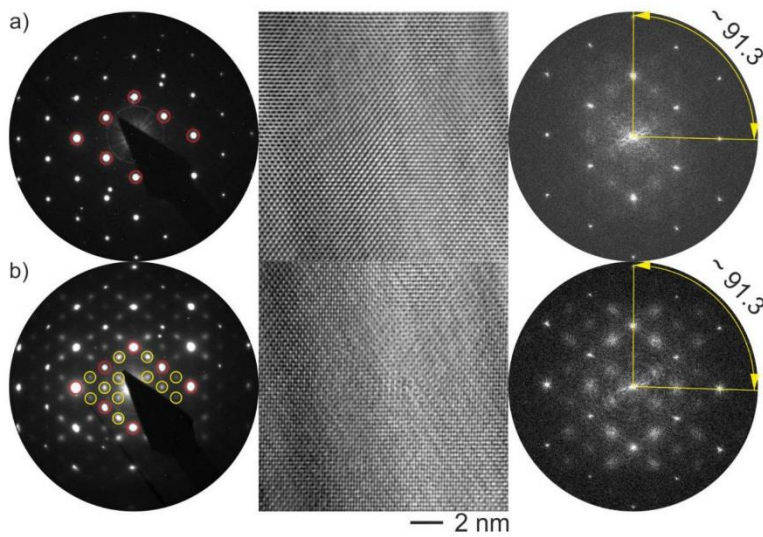


Figure 9: Experimental and simulated electron diffraction patterns, HRTEM micrographs and corresponding FFTs of $A-Cu_xCrS_2$ in zone axis $[001]$. In Figure a, the tripling of the lattice parameter a^* is evident from electron diffraction patterns and HRTEM micrographs (yellow circles) (HRTEM contrast simulation: defocus -75 nm, thickness 46.84 nm). However, this type of superstructure was highly unstable and consequently gradually decayed after short irradiation (b). The structure of the formed $B-CuCrS_2$ phase could be best described by a distorted $CuCrS_2$ -type structure with slight Cu deficiency (HRTEM contrast simulation upper image: defocus -60 nm, thickness 24.38 nm; lower image: defocus -105 nm, thickness 24.38 nm)

After intense electron beam irradiation both $B\text{-Cu}_x\text{CrS}_2$ and $R\text{-CuCrS}_2$ undergo a second transformation, accompanied with the formation of the spinel CuCr_2S_4 phase. The structural changes and thus changes in HRTEM micrographs (and corresponding FFT) and ED patterns before and after irradiation are depicted in Figure 10a) and b), respectively. Upon irradiation the reflections of $R\text{-CuCrS}_2$ (zone axis $[-22\bar{1}]_{\text{trig}}$) persists (marked in red) while diffuse intensities (marked in yellow) can be attributed to the formation of a disordered spinel CuCr_2S_4 phase (zone axis $[110]$). Further, the spinel phase forms nanoscale areas with homogeneous phase contrast (“nanodomains”) which exhibit distorted cubic metrics close to those of CuCrS_2 , with an angle of $\sim 91.3^\circ$ between $(-220)_{\text{spinel}}$ and $(004)_{\text{spinel}}$ (expected for cubic CuCr_2S_4 : 90°). This finding is in contrast to high temperature XRD measurements of CuCrS_2 , which confirm a distinct stability up to at least 773 K. Additionally, Rietveld refinement revealed no evidence, that the spinel formed by temperature induced phase transition is majorly distorted, causing a deviation from its cubic metrics. Note that the transition from the CuCrS_2 to the CuCr_2S_4 can be rationalized by moving Cr ions to occupy lattice sites in the Cu layer. For the sake of completeness, it has to be noted, that the valance distribution in the spinel phase is not as simple as the one proposed by Lodgering *et al.* ($\text{Cu}^+\text{Cr}^{3+}\text{Cr}^{4+}\text{S}_4$) or by Goodenough ($\text{Cu}^{2+}\text{Cr}_2^{3+}\text{S}_4$).^{55,56} But rather be $(\text{Cu}^+\text{Cr}_2^{3+}(\text{S}^{2-})_3\text{S})$, stabilized by delocalized holes in the sulfur orbital dominated valence band.^{57,58} Therefore, no simple phase transition mechanism can be given here with regard to the valence distribution of the phases. Yet, the transformation seems to be universal for CuCrS_2 and thus independent from the degree of deintercalation.



15

Figure 10: a) and b) representing ED, HRTEM and corresponding FFT of R-CuCrS₂ before and after intense electron beam irradiation. Red circles mark fundamental reflections hkl with $h = 3n$ CuCrS₂ (zone axis [-22-1]) and yellow circle mark additional reflections due to the formation of spinel CuCr₂S₄ (zone axis [110]).

Further, an *ex situ* heated (1h at 250 °C) deintercalated sample has been investigated by TEM. For this sample the majority phase was CuCr₂S₄. $\Sigma 3$ twins of CuCr₂S₄ were observed with twin plane (111) (Figure S7). Additionally, lamella-like ingrown domains of trigonal S-CuCrS₂ were identified (Figure 11). According to the ED pattern and the FFT the coinciding planes could be determined to $(-330)_{\text{trig}}$ (or equivalent $(300)_{\text{trig}}$) and (224) for S-CuCrS₂ and CuCr₂S₄, respectively, while the growth directions were found to be $\langle 001 \rangle_{\text{trig}}$ and $\langle 111 \rangle$ for S-CuCrS₂ and CuCr₂S₄, respectively. Consequently, for the lamellar intergrowth of the phases a difference in layer type and stacking sequence perpendicular to the closest packed layer is observed, while for the beam-induced phase transition a more complex segregation based on nanodomains occurs.

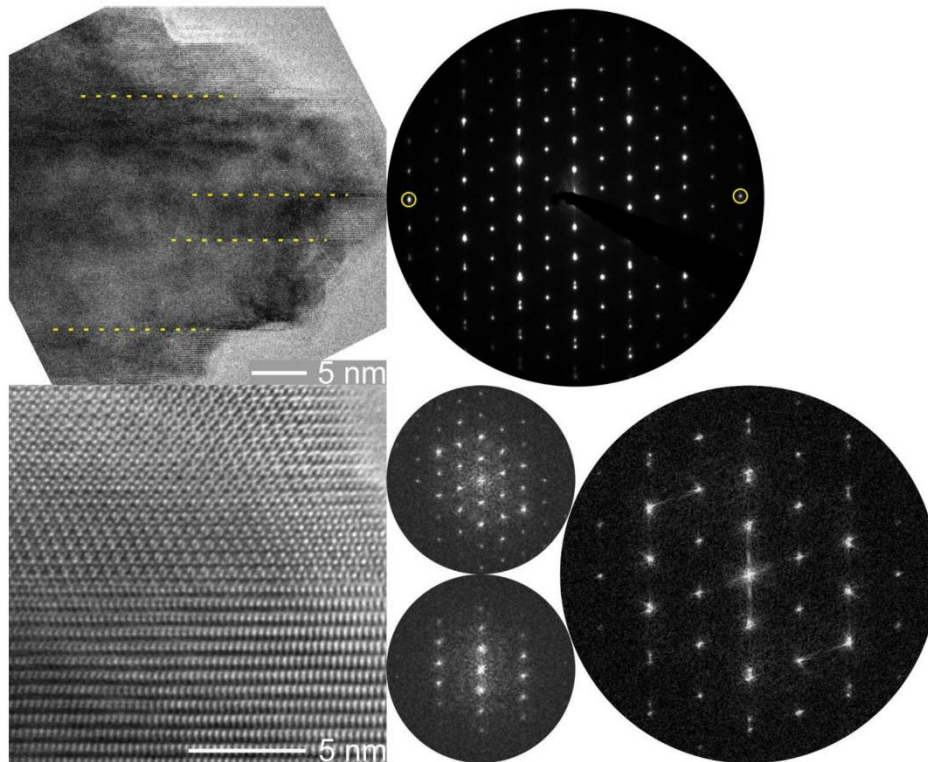


Figure 11: Upper images: Overview image and ED pattern (zone axis $[110]$ for $S\text{-CuCrS}_2$ and CuCr_2S_4) of lamellar ingrown $S\text{-CuCrS}_2$ domains. The dotted yellow lines mark the domain boundaries. Lower image: HRTEM and corresponding FFT of a lamellar ingrown $S\text{-CuCrS}_2$. The yellow encircled planes highlight the coinciding planes namely, (-330) and (224) for $S\text{-CuCrS}_2$ and CuCr_2S_4 , respectively. The domains grow parallel to $\langle 111 \rangle$ and $\langle 001 \rangle$ direction for CuCr_2S_4 and $S\text{-CuCrS}_2$, respectively.

Conclusion

We demonstrated the benefit of a synergistic approach of chemical and structural *in situ* characterization including advanced techniques of X-ray diffraction, total scattering and electron microscopy. For the first time the structural changes occurring on different length scales caused by the topotactic removal of Cu^+ from the thermoelectric material CuCrS_2 could be elucidated in detail. Deintercalation of Cu^+ ions leads to formation of a new monoclinic $A\text{-Cu}_{0.66}\text{CrS}_2$ phase which exhibits a modulation of distorted and undistorted CrS_6 octahedra caused by the formation of Cr^{4+} ions. Additionally, the removal of Cu^+ from the host lattice leads to the formation of a $3a$ superstructure. At elevated temperatures a significant increase of the Debye Waller factor

suggests an enhanced mobility of Cu⁺, while that for Cr ions decreases due to reduction of the distortion of the CrS₆ octahedra. *In situ* XRD and TEM investigations revealed the instability of the superstructure, leading to the formation of a second phase, B-Cu_{0.66}CrS₂. Above 503 K a phase transformation into the spinel CuCr₂S₄ and stoichiometric CuCrS₂ occurred.

Acknowledgements

The authors thank the German Electron Synchrotron (DESY) and Diamond Light Source (DLS, UK) for beamtime allocation. We also thank the German Research Foundation (DFG) within the research grant KI 1263/16-1 and BE1653/37-1. Thanks also to Sanna Sommer, Nils Lau Nyborg Broge for the help with PDF analysis and fruitful discussions.

References

- 1 D. M. Rowe, *CRC Handbook of Thermoelectrics*, CRC Press, 1995.
- 2 A. Mehdizadeh Dehkordi, M. Zebarjadi, J. He and T. M. Tritt, *Mater. Sci. Eng. R Rep.*, 2015, **97**, 1–22.
- 3 J. R. Sootsman, D. Y. Chung and M. G. Kanatzidis, *Angew. Chem. Int. Ed.*, 2009, **48**, 8616–8639.
- 4 A. Shakouri, *Annu. Rev. Mater. Res.*, 2011, **41**, 399–431.
- 5 Glen A Slack, in *CRC Handbook of Thermoelectrics*, CRC Press, 1995.
- 6 J. Androulakis, C.-H. Lin, H.-J. Kong, C. Uher, C.-I. Wu, T. Hogan, B. A. Cook, T. Caillat, K. M. Paraskevopoulos and M. G. Kanatzidis, *J. Am. Chem. Soc.*, 2007, **129**, 9780–9788.
- 7 C. J. Vineis, A. Shakouri, A. Majumdar and M. G. Kanatzidis, *Adv. Mater.*, 2010, **22**, 3970–3980.
- 8 M. G. Kanatzidis, *Chem. Mater.*, 2010, **22**, 648–659.
- 9 K. Biswas, J. He, I. D. Blum, C.-I. Wu, T. P. Hogan, D. N. Seidman, V. P. Dravid and M. G. Kanatzidis, *Nature*, 2012, **489**, 414–418.
- 10 M. G. Kanatzidis, *MRS Bull.*, 2015, **40**, 687–695.
- 11 R. Amatya and R. J. Ram, *J. Electron. Mater.*, 2011, **41**, 1011–1019.
- 12 O. Falkenbach, J. Tinz, A. S. Schulze, E. Mueller and S. Schlecht, *Phys. Status Solidi A*, 2016, **213**, 699–705.
- 13 Y. He, T. Day, T. Zhang, H. Liu, X. Shi, L. Chen and G. J. Snyder, *Adv. Mater.*, 2014, **26**, 3974–3978.
- 14 S. Bhattacharya, R. Chmielowski, G. Dennler and G. K. H. Madsen, *J. Mater. Chem. A*, 2016, **4**, 11086–11093.
- 15 G. Tan, S. Hao, J. Zhao, C. Wolverton and M. G. Kanatzidis, *J. Am. Chem. Soc.*, 2017, **139**, 6467–6473.
- 16 R. Chmielowski, S. Bhattacharya, S. Jacob, D. Péré, A. Jacob, K. Moriya, B. Delatouche, P. Roussel, G. Madsen and G. Dennler, *Sci. Rep.*, 2017, **7**, srep46630.
- 17 Y. Li, T. Zhang, Y. Qin, T. Day, G. Jeffrey Snyder, X. Shi and L. Chen, *J. Appl. Phys.*, 2014, **116**, 203705.
- 18 H. Liu, X. Shi, F. Xu, L. Zhang, W. Zhang, L. Chen, Q. Li, C. Uher, T. Day and G. J. Snyder, *Nat. Mater.*, 2012, **11**, 422–425.
- 19 G. Dennler, R. Chmielowski, S. Jacob, F. Capet, P. Roussel, S. Zastrow, K. Nielsch, I. Opahle and G. K. H. Madsen, *Adv. Energy Mater.*, 2014, **4**, 1301581.
- 20 Y.-X. Chen, B.-P. Zhang, Z.-H. Ge and P.-P. Shang, *J. Solid State Chem.*, 2012, **186**, 109–115.
- 21 G. C. Tewari, T. S. Tripathi, P. Kumar, A. K. Rastogi, S. K. Pasha and G. Gupta, *J. Electron. Mater.*, 2011, **40**, 2368–2373.
- 22 G. C. Tewari, T. S. Tripathi and A. K. Rastogi, *Z. Krist. Cryst. Mater.*, 2010, **225**, 471–474.
- 23 C.-G. Han, B.-P. Zhang, Z.-H. Ge, L.-J. Zhang and Y.-C. Liu, *J. Mater. Sci.*, 2013, **48**, 4081–4087.

- 24 A. Kaltzoglou, P. Vaqueiro, T. Barbier, E. Guilmeau and A. V. Powell, *J. Electron. Mater.*, 2014, **43**, 2029–2034.
- 25 H. Hahn and C. D. Lorent, *Z. Anorg. Allg. Chem.*, 1957, **290**, 68–81.
- 26 P. F. Bongers, C. F. Van Bruggen, J. Koopstra, W. P. F. A. M. Omloo, G. A. Wiegers and F. Jellinek, *J. Phys. Chem. Solids*, 1968, **29**, 977–984.
- 27 N. Le Nagard, G. Collin and O. Gorochov, *Mater. Res. Bull.*, 1979, **14**, 1411–1417.
- 28 J. C. E. Rasch, M. Boehm, C. Ritter, H. Mutka, J. Schefer, L. Keller, G. M. Abramova, A. Cervellino and J. F. Löffler, *Phys. Rev. B*, , DOI:10.1103/PhysRevB.80.104431.
- 29 R. A. Yakshibaev, G. R. Akmanova, R. F. Almukhametov and V. N. Konev, *Phys. Status Solidi A*, 1991, **124**, 417–426.
- 30 G. C. Tewari, T. S. Tripathi and A. K. Rastogi, *J. Electron. Mater.*, 2010, **39**, 1133–1139.
- 31 I. G. Vassilieva, T. Y. Kardash and V. V. Malakhov, *J. Struct. Chem.*, 2009, **50**, 288–295.
- 32 D. Srivastava, G. C. Tewari, M. Karppinen and R. M. Nieminen, *J. Phys. Condens. Matter*, 2013, **25**, 105504.
- 33 R. Schöllhorn, in *Reactivity of Solids*, eds. J. Wood, O. Lindqvist, C. Helgesson and N.-G. Vannerberg, Springer US, 1977, pp. 719–723.
- 34 H. Boller, *Solid State Ion.*, 2001, **141–142**, 53–56.
- 35 T. Dankwort, A.-L. Hansen, M. Winkler, U. Schürmann, J. D. Koenig, D. C. Johnson, N. F. Hinsche, P. Zahn, I. Mertig, W. Bensch and L. Kienle, *Phys. Status Solidi A*, 2016, 662–671.
- 36 J. Koenig, M. Winkler, T. Dankwort, A.-L. Hansen, H.-F. Pernau, V. Duppel, M. Jaegle, K. Bartholomé, L. Kienle and W. Bensch, *Dalton Trans*, 2015, **44**, 2835–2843.
- 37 A.-L. Hansen, T. Dankwort, M. Winkler, J. Ditto, D. C. Johnson, J. D. Koenig, K. Bartholomé, L. Kienle and W. Bensch, *Chem. Mater.*, 2014, **26**, 6518–6522.
- 38 A. A. Coelho, *Comput. Programme Rietveld Anal.*
- 39 P. Juhás, T. Davis, C. L. Farrow and S. J. L. Billinge, *J. Appl. Crystallogr.*, 2013, **46**, 560–566.
- 40 P. A. Stadelmann, *Ultramicroscopy*, 1987, **21**, 131–145.
- 41 D. R. G. Mitchell and B. Schaffer, *Ultramicroscopy*, 2005, **103**, 319–332.
- 42 K. Momma and F. Izumi, *J. Appl. Crystallogr.*, 2011, **44**, 1272–1276.
- 43 M. S. Dresselhaus and G. Dresselhaus, *Adv. Phys.*, 1981, **30**, 139–326.
- 44 A. A. Coelho, *J. Appl. Crystallogr.*, 2000, **33**, 899–908.
- 45 D. Wu, X. Li, B. Xu, N. Twu, L. Liu and G. Ceder, *Energy Env. Sci*, 2015, **8**, 195–202.
- 46 Y. Shao-Horn, S. Levasseur, F. Weill and C. Delmas, *J. Electrochem. Soc.*, 2003, **150**, A366–A373.
- 47 K. Mukai, Y. Kishida, H. Nozaki and K. Dohmae, *Chem. Mater.*, 2013, **25**, 2828–2837.
- 48 M. E. Arroyo y de Dompablo and G. Ceder, *J. Power Sources*, 2003, **119–121**, 654–657.
- 49 J. P. Peres, F. Weill and C. Delmas, *Solid State Ion.*, 1999, **116**, 19–27.
- 50 X. Li, X. Ma, D. Su, L. Liu, R. Chisnell, S. P. Ong, H. Chen, A. Toumar, J.-C. Idrobo, Y. Lei, J. Bai, F. Wang, J. W. Lynn, Y. S. Lee and G. Ceder, *Nat. Mater.*, 2014, **13**, 586–592.
- 51 W. H. Baur, *Acta Crystallogr. B*, 1974, **30**, 1195–1215.
- 52 M. A. Boutbila, J. Rasneur and M. El Aatmani, *J. Alloys Compd.*, 1999, **283**, 88–90.
- 53 P. Perrot, M. S. I. Team and M. ®, in *Refractory metal systems*, eds. G. Effenberg and S. Ilyenko, Springer Berlin Heidelberg, 2010, pp. 138–149.
- 54 R. A. Yakshibaev, G. R. Akmanova, R. F. Almukhametov and V. N. Konev, *Phys. Status Solidi A*, 1991, **124**, 417–426.
- 55 F. K. Lotgering and R. P. van Staple, *Solid State Commun.*, 1967, **5**, 143–146.
- 56 J. B. Goodenough, *J. Phys. Chem. Solids*, 1969, **30**, 261–280.
- 57 R. Schöllhorn, *Angew. Chem. Int. Ed. Engl.*, 1988, **27**, 1392–1400.
- 58 V. Bodenez, L. Dupont, L. Laffont, A. R. Armstrong, K. M. Shaju, P. G. Bruce and J.-M. Tarascon, *J. Mater. Chem.*, 2007, **17**, 3238–3247.

4. Weitere Veröffentlichungen

4.1 Elucidation of the Conversion Reaction of CoMnFeO₄ Nanoparticles in Lithium Ion Battery Anode via Operando Studies

Die nanokristalline Verbindung CoMnFeO₄ (Spinell-Struktur) wurde als Anodenmaterial untersucht. Die Konversion des Materials durch die Reaktion mit Lithium wurde mit *operando* XRD, Röntgenabsorptionsspektroskopie (XAS), *ex situ* TEM, Li-NMR und Molekulardynamik Simulationen aufgeklärt. Im Gegensatz zu Untersuchungen an mikrokristallinen Spinellen konnte die Aufnahme größerer Mengen Li in das Wirtsgitter ausgeschlossen werden. Während der Reduktion der Kationen wechseln diese von Tetraeder- auf Oktaederplätze. Dies führt zu einer Umwandlung von der Spinell- in die Kochsalzstruktur ($Fd\bar{3}m \rightarrow Fm\bar{3}m$). Die (*hkl*)-abhängigen Domänengrößen ergaben eine (gemittelte) oktaedrische Kristallmorphologie, die auch im TEM zu beobachten war. Die Morphologie blieb zur „Aufnahme“ von ~ 0.5 Li pro Formeleinheit erhalten. Im weiteren Reaktionsverlauf war eine sphärische Form der Partikel zu beobachten (Abbildung 15). Eine analoge sphärische Morphologie wurde für die

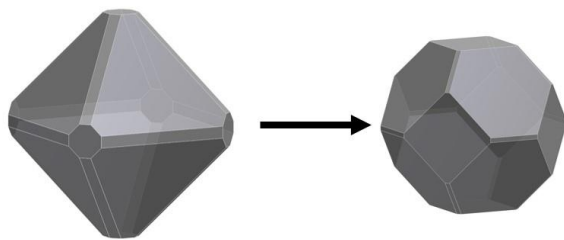


Abbildung 15: Schematische Darstellung der Änderung der Partikelmorphologie während der Konversionsreaktion.

Monoxidphase gefunden. Die Analyse der logarithmischen Domänengrößenverteilung ergab eine Abnahme der kleineren Spinellkristallite zugunsten des neu gebildeten Monoxids. Am Ende der Entladung liegen metallische Co-, Fe- und Mn-Nanopartikel eingebettet in einer Li₂O-Matrix vor. Mittels XAS konnte aufgeklärt werden, dass dem für Mn³⁺-Spinelle typische

partielle Kapazitätsverlust eine nicht vollständig verlaufende Redoxreaktion zu Grunde liegt: $Mn^{3+} \rightarrow Mn \leftrightarrow Mn^{2+}$.

Reprinted with permission from S. Permien, S. Indris, A.-L. Hansen, M. Scheuermann, D. Zahn, U. Schürmann, G. Neubüser, L. Kienle, E. Yegudin, W. Bensch, *ACS Appl. Mater. Interfaces* **2016**, 8, 15320–15332. Copyright 2016 American Chemical Society.

Elucidation of the Conversion Reaction of CoMnFeO_4 Nanoparticles in Lithium Ion Battery Anode via Operando Studies

Stefan Permien,[†] Sylvio Indris,[‡] Anna-Lena Hansen,[†] Marco Scheuermann,[‡] Dirk Zahn,^{||} Ulrich Schürmann,[§] Gero Neubüser,[§] Lorenz Kienle,[§] Eugen Yegudin,[†] and Wolfgang Bensch^{*,†}

[†]Institute of Inorganic Chemistry, University of Kiel, Max-Eyth-Straße 2, 24118 Kiel, Germany

[‡]Institute for Applied Materials, Karlsruhe Institute of Technology, P.O. Box 3640, 76021 Karlsruhe, Germany

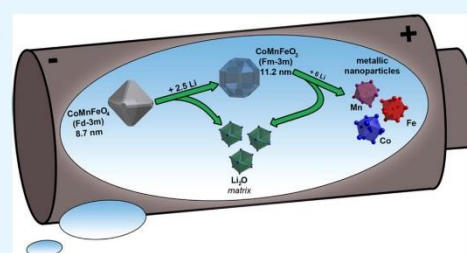
[§]Institute for Materials Science, University of Kiel, Kaiserstraße 2, 24143 Kiel, Germany

^{||}Chair for theoretical Chemistry/Computer Chemistry Centrum, Friedrich-Alexander University Erlangen-Nürnberg, Nagelsbachstraße 25, 91052 Erlangen, Germany

Supporting Information

ABSTRACT: Conversion reactions deliver much higher capacities than intercalation/deintercalation reactions of commercial Li ion batteries. However, the complex reaction pathways of conversion reactions occurring during Li uptake and release are not entirely understood, especially the irreversible capacity loss of Mn(III)-containing oxides. Here, we report for the first time on the electrochemical Li uptake and release of $\text{Co}^{\text{II}}\text{Mn}^{\text{III}}\text{Fe}^{\text{III}}\text{O}_4$ spinel nanoparticles and the conversion reaction mechanisms elucidated by combined operando X-ray diffraction, operando and ex-situ X-ray absorption spectroscopy, transmission electron microscopy, ^7Li NMR, and molecular dynamics simulation. The combination of these techniques enabled uncovering the pronounced electronic changes and structural alterations on different length scales in a unique way. The spinel nanoparticles undergo a successive phase transition into a mixed monoxide caused by a movement of the reduced cations from tetrahedral to octahedral positions. While the redox reactions $\text{Fe}^{3+} \leftrightarrow \text{Fe}^0$ and $\text{Co}^{2+} \leftrightarrow \text{Co}^0$ occur for many charge/discharge cycles, metallic Mn nanoparticles formed during the first discharge can only be oxidized to Mn^{2+} during charge. This finding explains the partial capacity loss reported for Mn(III)-based spinels. Furthermore, the results of the investigations evidence that the reaction mechanisms on the nanoscale are very different from pathways of microcrystalline materials.

KEYWORDS: lithium ion battery, spinel oxide, conversion, operando XRD, operando XAS, anode



1. INTRODUCTION

Massive efforts are under way to develop new rechargeable batteries and to identify new electrode materials, because there is a pronounced need for compact sources for portable electricity, transportation, and energy storage of renewables such as solar and wind power.^{1,2} The commercialized rechargeable Li batteries are characterized by a specific capacity between ~ 120 and 180 mAh g^{-1} , and it seems that there is an upper capacity limit for systems where one Li per formula unit is intercalated/deintercalated.³ Hence, intense research is going on to identify new materials for lithium ion batteries (LIBs),^{1,4} and a large variety of materials including layered transition metal oxides, phosphates with olivine structure, or spinels are investigated.^{5–7} To improve the performance of LIBs based on intercalation/deintercalation reactions, ex situ and in situ/operando studies were performed with a large variety of analytic tools.^{1,8–13} Reasonably good understanding of the reaction mechanisms occurring during discharge/charge in commer-

cially used electrode materials helped to improve the performance of LIBs.

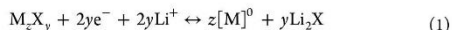
However, as mentioned above, the capacity is limited, and therefore, to overcome such limitation, conversion reactions were investigated in the past. Nowadays, they are more intensively studied. During a conversion reaction many more Li atoms can be transferred between the cathode and anode thus leading to capacities that are 2–5 times larger than for, for example, commercially used LiCoO_2 /graphite.^{14,15} Transition metal (TM) oxides, sulfides, nitrides, fluorides, or phosphides M_xX_y ($\text{M} = \text{Mn, Fe, Co, Ni, Cu, Zn, ...}$; $\text{X} = \text{O, S, N, F, P}$) were investigated as electrode materials, and during discharge (Li uptake) the cations are reduced to metal nanoparticles embedded in a Li_nX_b salt matrix.^{15–18} During charging (Li

Received: March 15, 2016

Accepted: May 24, 2016

Published: May 24, 2016

release), it is postulated that binary compounds M_xX_y are formed and Li is recovered as described in eq 1:



(M = transition metal, X = O, S)

This type of reaction is more complex than presented in eq 1 with occurrence of several intermediate phases for distinct materials.^{19–23} Operando/in situ investigations demonstrated that the reactions proceed via different steps.^{24–26} One advantage of operando/in situ experiments is that unwanted side reactions with air or moisture and undesirable altering products are avoided. Using X-ray powder diffraction (XRD) the long-range order of the material as well as new phases can be identified during discharge/charge processes. Combining XRD with X-ray absorption spectroscopy (XAS), structural alterations and changes of the electronic structure as well as local environments of the transition metals (irrespective of whether the material is crystalline, amorphous, or nanocrystalline) can be monitored simultaneously. Recently, we investigated the reaction mechanisms of Li uptake and release using $MnFe_2O_4$, $CoFe_2O_4$, and $MgFe_2O_4$ nanoparticles as electrode materials.^{21–23} The reaction proceeds in distinct steps: (i) consumption of a small amount of Li by reaction with amorphous oxides on the particle surface; (ii) formation of a monoxide with NaCl-type structure after uptake of ~ 2 Li per formula unit; (iii) reduction of TM cations to the metallic state and simultaneous formation of Li_2O ; (iv) formation of the metal oxides for M = Mn, Fe, Co during the charge process.

Spinel oxides containing one (Co_3O_4 ,²⁷ Mn_3O_4 ,²⁸ Fe_3O_4 ,²⁹) or two ($CoFe_2O_4$,^{30,31} $NiFe_2O_4$,³² $MnFe_2O_4$,³³ $ZnFe_2O_4$,³⁴ $ZnMn_2O_4$,³⁵) transition metals used as anode materials exhibit high specific capacities of ~ 1100 – 1400 mAh g^{-1} (first discharge), because eight Li can be converted per formula unit. Zn-containing TM oxides enable even storage of one additional Li per formula unit by formation of a LiZn alloy. It was demonstrated that special morphologies of the oxide particles and/or composites with graphene or carbon nanotubes led to stable capacities of 800 to 1000 mAh g^{-1} , for example, in the 100th cycle.^{36,37}

While several mono- and bimetallic spinel oxides were investigated as electrode materials in LIBs, comparable experiments on trimetallic spinels are scarce. Lavela et al.³⁸ synthesized $NiFeMnO_4$ by a reverse micelle method, and the capacity after 20 cycles was ~ 900 mAh g^{-1} being competitive with the performance of mono- and bimetallic spinels. $CoMn_2O_4$,^{39,40} and $CoFe_2O_4$ ^{30,31,41} spinels were reported as high-capacity anode materials, but Li uptake into $CoMnFeO_4$ has not been investigated, yet. $CoMnFeO_4$ was synthesized as thin films^{42,43} and as powders for determination of the cation distribution and magnetic and catalytic properties.^{44,45} Here we report for the first time on the electrochemical performance of $CoMnFeO_4$ nanoparticles as anode material. Furthermore, we investigate the reaction mechanism during Li insertion into the quaternary spinel by operando synchrotron-based XRD and XAS allowing monitoring the individual structural and electronic events occurring during the reaction. The XRD/XAS experiments are complemented by ex situ 7Li magic-angle spinning (MAS) NMR and transmission electron microscopy (TEM) investigations. To the best of our knowledge, operando studies on quaternary spinels were never reported before. The elucidation of an exact reaction mechanism helps to understand

the behavior of the constituents of the anode material thus enabling optimization for potential application in LIBs.

2. RESULTS

2.1. Structural Characterization. The XRD powder pattern of $CoFeMnO_4$ is presented in Figure 1, top. The

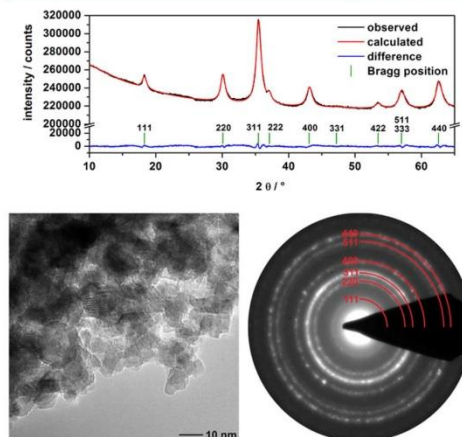


Figure 1. (top) XRD powder pattern of $CoFeMnO_4$ nanoparticles (black), Pawley Fit (red), and difference curve (blue). (bottom) HRTEM image (left) and SAED pattern (right).

position of the Bragg reflections and their relative intensities match very well with the cubic spinel, space group $Fd\bar{3}m$. The refinements of the pattern revealed that the observed broadening of the reflections are caused predominantly by particle size effects. The volume-weighted average particle size was determined to be $8.5(2)$ nm, and the lattice parameter a was refined to $8.387(2)$ Å. The value for a is slightly shorter than that reported in ref 46 ($a = 8.402$ Å) and ref 44 ($a = 8.41$ Å for 42 nm particles), indicating that the synthesis conditions affect the lattice parameters.

Scanning electron microscope (SEM) pictures show large particles composed of agglomerated smaller particles (Figure S1). Energy-dispersive X-ray (EDX) analysis confirmed the presence of Co, Fe, Mn, and O (Mn: 37.8 atom %, Fe: 30.9 atom %, and Co: 32.3 atom %). The slight deviation of the theoretical value for Fe can be explained by an overlap of the Fe $K\alpha$ line with the Mn $K\beta$ emission and an overlap of the Fe $K\beta$ line with the Co $K\alpha$ line (Figure S1). Because the deviation is only ~ 3 atom % the sample is named $CoFeMnO_4$ in the manuscript.

The high-resolution transmission electron microscopy (HRTEM) image of $CoFeMnO_4$ nanoparticles shows a particle size distribution with average sizes of ~ 8 nm (Figure 1, bottom). A statistical analysis was hindered by the fact that the particles formed aggregates. The representative selected area electron diffraction (SAED) pattern (Figure 1, bottom) can be unambiguously assigned to the cubic spinel without impurity phases (Table S2). A closer view demonstrates that crystalline cores are covered by a thin noncrystalline surface layer (magnification: Figure S2).

The CoMnFeO_4 nanoparticles were further chemically analyzed in the TEM demonstrating a homogeneous dispersion of Co, Fe, and Mn (Figure 2, top). The intensity distributions

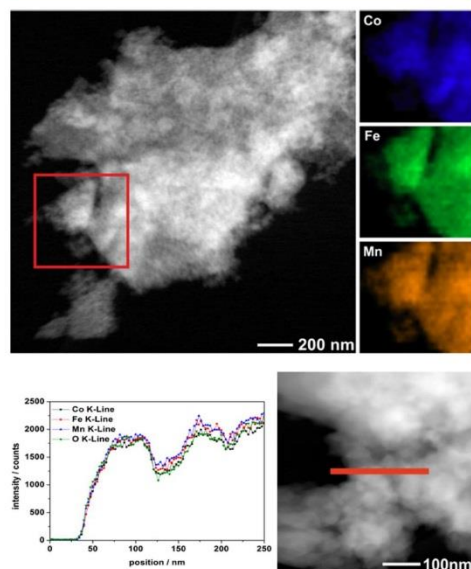


Figure 2. (top) STEM image (top, left), EDX mapping at the area marked with a red square (top, right). EDX line scan (bottom, left) of pristine CoMnFeO_4 particles (bottom, right). Dark-field STEM image (right) with line scan position marked by the red bar.

in the elemental maps are very similar, and EDX point measurements yielded a TM ratio close to 1:1:1 (Figure 2, top). These results were confirmed by an EDX line scan performed on a neighboring particle (see Figure 2, bottom) evidencing the coincidence with the X-ray intensities for Fe, Co, and Mn (see Figure 2, left) and rendering the homogeneous dispersion of the elements.

2.2. Electrochemical Performance of Nanosized CoFeMnO_4 . The electrochemical performance of the CoFeMnO_4 nanoparticles in a potential range from 0.1 to 3 V is shown in Figure 3. During the first discharge process, a not well-resolved plateau at ~ 1.2 V is visible followed by a long plateau located at 0.8 V (Figure 3a). The overall capacity of the first discharge process of 1448 mAh g^{-1} corresponds to an uptake of ~ 12.7 Li per formula unit (f.u.).

Capacities larger than the theoretically expected one (917 mAh g^{-1}) are characteristic for nanosized spinel oxides^{27,29–38,41} caused by irreversible reactions of the electrode materials with the electrolyte and formation of the solid electrolyte interphase (SEI). These unwanted processes are responsible for irreversible capacity loss during charge processes, for which a sloping plateau at ~ 1.7 V is observed (Figure 3a). The reversible capacity of the first cycle of 968 mAh g^{-1} (capacity loss: 480 mAh g^{-1}) is in the range reported for other spinel oxides $\text{M}^{\text{I}}\text{M}^{\text{II}}_2\text{O}_4$ ($\text{M}^{\text{I}} = \text{Co, Fe, Ni, Mn, Zn}$; $\text{M}^{\text{II}} = \text{Co, Mn, Fe}$).^{27–41} The slightly larger capacity than the theoretically expected one may be explained by reversible

reactions with the electrolyte and/or capacitive effects at the surface of the nanoparticles.^{47–49}

Cyclic voltammetry (CV) exhibits two anodic peaks during the first discharge (Figure 3b), of which a less intense one occurs at 1.0 V (Figure 3b, inset), and a very intense signal is located at 0.5 V. During the charge process a broad cathodic peak ranging from 1.5 to 2.0 V is observed, which consists of more than one event. The discharge process of the second and following cycles are different from the first one, and only a weak anodic event occurs at 1.2 V; a second more intense signal occurs at 0.8 V (Figure 3b). With increasing cycle number the events slightly shift to lower cell potentials. The voltage profile during the first discharge process is completely different from the following as can be seen for cycling with constant current and CV (compare Figure 3a,b). Obviously, during the first charge process new phases are formed exhibiting different electronic and structural characteristics.

In Figure 3c the charge and discharge capacity as a function of the cycle number at C/10 rate is displayed. The capacity remains stable during the first 12 cycles, while a slight decrease is observed in subsequent cycles, and after 50 cycles the capacity is still 717 mAh g^{-1} , that is, 74% of the first cycle. A comparison with literature data demonstrates that the cycle stability of the CoFeMnO_4 nanoparticles are better or at least competitive with other transition metal oxides like NiFe_2O_4 nanoparticles³² (345 mAh g^{-1} , after 40th cycle), Mn_3O_4 ²⁸ (720 mAh g^{-1} , after 40th cycle), CoFe_2O_4 ³⁰ (730 mAh g^{-1} , after 50 cycles), $\text{ZnFe}_2\text{O}_4/\text{C}$ ³⁴ (713 mAh g^{-1} , after 50 cycles), and NiMnFeO_4 ³⁸ (750 mAh g^{-1} , after 50 cycles). We note that optimization of the particle morphology as well as addition of suitable additives like carbon species should lead to an even better performance of the material.

Figure 3d illustrates the capacity at different C-rates from C/10 to 1.4 C. For C/10, C/5, C/2, 1, and 1.4 C rates the capacity is 1011, 853, 661, 495, and 375 mAh g^{-1} , respectively, being larger than for graphite even at high currents. After it cycles at high current density the material is at least partially destroyed, and cycle stability is lost as can be seen in Figure 3d for the C/10 data measured after cycling at 1.4 C.

2.3. Operando XRD. The refinement of the powder pattern of the pristine material yielded $a = 8.388(2) \text{ \AA}$ and a volume-weighted particle size $d = 8.7(1) \text{ nm}$. The differences of the values between *in house* diffraction experiments and the synchrotron-based investigation are marginal (0.1%).

The evolution of the potential of the *in situ* cell during first discharge is similar to that recorded for the Swagelok cell (Figure 4, bottom left). According to the potential profile three regions can be distinguished: (a) region I: uptake of the first 2.5 Li per formula unit, (b) region II: uptake of >2.5 Li until end of discharge, (c) region III: charge process. The operando XRD patterns recorded during region I are presented in Figure 4 (top). At the beginning of Li uptake (ca. 0.5 Li per f.u., region Ia) a slight shift of all reflections occurred due to an expansion of the a axis of $\sim 0.2\%$. (Figure 4, bottom right). The integrated intensity of all reflections of the powder patterns collected up to 0.5 Li exhibit no change evidencing that the crystalline material is not converted into a new product at this stage. The (hkl)-dependent domain sizes yield octahedral crystal morphology for the pristine material being in good accordance with TEM image (Figure S2). The morphology is preserved until ~ 0.5 Li/f.u. (Figure 4 top, red line), while a truncation of the octahedra occurs for >0.5 Li/f.u. yielding a more spherical

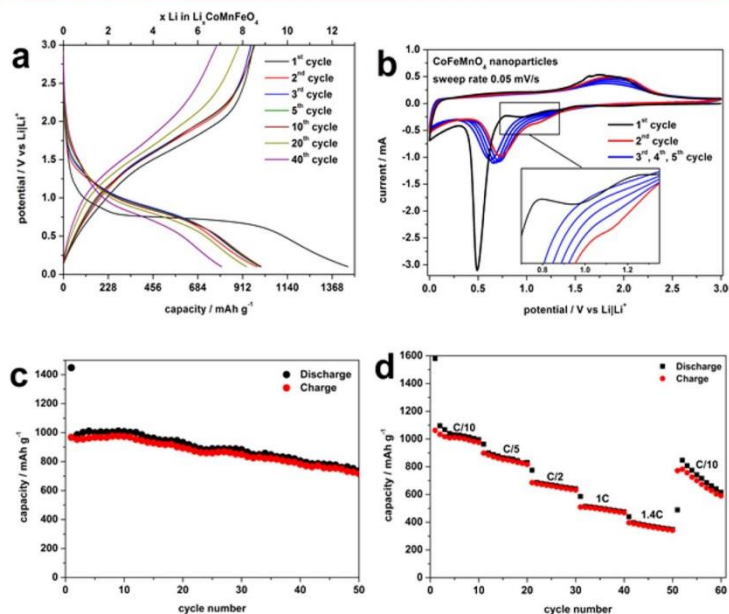


Figure 3. Electrochemical performance of CoFeMnO₄ nanoparticles. (a) Potential vs capacity of the first three cycles and of cycles 5, 10, 20, and 40. (b) CV of the first five cycles at a sweep rate of 0.05 mV/s. (c) Capacity of the first 50 cycles at a C/10 rate. (d) Cycle stability at different cycling rates.

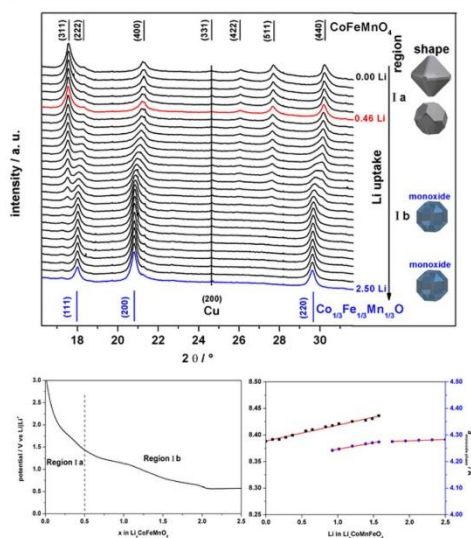


Figure 4. Operando XRD of region I during uptake of the first 2.5 Li per formula unit (top), potential process of region I (bottom left), and expansion of the *a* axes during Li uptake for spinel phase as well as monoxide phase (bottom right).

shape. An analogous spherical morphology is found for the monoxide phase (Figure 4).

Increasing the Li content beyond 0.5 Li/f.u., the (311) and (511) reflections start to lose intensity, while at the position of the (222) reflection an intensity gain can be observed. Simultaneously, the (400) and (440) reflections are broadened indicating an overlap of reflections, that is, new Bragg reflections appeared, which are assigned to a monoxide adopting space group *Fm* $\bar{3}$ *m* with *a* = 4.239(3) Å (for uptake of ~0.6 Li). A linear expansion of the *a* axis of the spinel phase occurs until the refinement of the lattice parameter is not reliable anymore, due to low intensity of the reflections. Simultaneously, the lattice parameter of the monoxide phase is increasing continuously up to 2 Li per f.u., and afterward it remains constant. The reflections of the starting material disappeared, and the powder pattern can be refined with only one phase, that is, a monoxide with a NaCl-type structure Co_{1/3}Fe_{1/3}Mn_{1/3}O; *a* = 4.275(1). The NaCl-type structure can only be realized by the movement of ions located on tetrahedral sites to neighboring empty octahedral sites and simultaneous reduction of M^{III} cations to M^{II} (see Section 2.4). A challenging question is whether phase separation and formation of FeO, CoO, and MnO particles occurred. Such a phase separation requires a directed movement and reduction of M^{III} located on tetrahedral sites to those empty octahedral sites having M^{II} in octahedral site as direct neighbor; that is, Fe^{III}/Mn^{III} are reduced and jump to those empty octahedral sites where Fe^{II}/Mn^{II} are the next nearest neighbor. Because the tetrahedral sites are statistically occupied by the trivalent ions such a concerted

mechanism/movement seems not to be plausible under the experimental conditions.

In addition, the presence of three separated oxides would lead to much broader reflections in the powder patterns because the coherently scattering domains of the individual oxides are much smaller than those of a mixed monoxide. Additionally, cubic MnO exhibits a larger lattice parameter compared to Fe_{1-x}O and CoO leading to an asymmetric shape of the reflections (simulated powder pattern: Figure S3). On the basis of the present results and those reported in the literature it is most likely that Li uptake gradually forces the formation of a mixed monoxide.^{43,45–47} Between 2.0 and 2.5 Li/f.u. a further growth of the particles was not observed.

Analysis of log-normal domain size distribution revealed a decrease of small spinel crystallites in favor of the newly formed monoxide during the chemical reaction. A comparison of the spinel (0 Li) and the monoxide after uptake of ~ 2.5 Li clearly displays the loss of smaller particles and a shift in the distribution toward larger crystallites (Figure S4, volume weighted particle size $d = 11.2(1)$ nm).

The continuing uptake of Li (long plateau at 0.6 V, region IIa) leads to a successive decrease of the reflection intensities and a continuous broadening of the reflections; that is, either the intermediate phase is converted to an amorphous product or the coherent scattering domains are too small to be detected by XRD (Figure 5). No reflections are observed after uptake of 8 Li/f.u. suggesting that all metal ions are reduced to the metallic state and the metallic particles are too small to be detected by XRD (Figure 5, red pattern). Accommodation of additional Li in region IIb can be explained by reversible/irreversible reactions with the electrolyte and/or surface charge transfer mechanism (discussed in Section 2.2). The diffraction

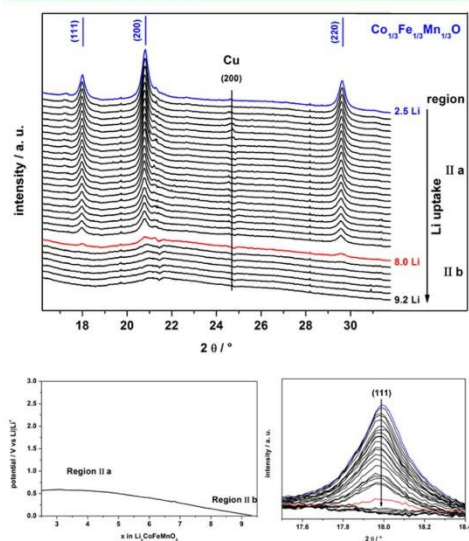
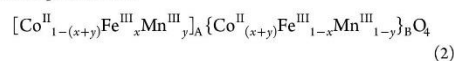


Figure 5. Operando XRD patterns recorded in region II during uptake of more than two Li until end of discharge (top), voltage profile of region II (bottom left), and magnified view of the region of the 111 reflection (bottom right).

patterns collected during the charge process and after the first cycle (not presented here) give evidence that the particles are either amorphous or that the crystalline domains are smaller than the coherence length of the X-rays.

2.4. Operando X-ray Absorption Spectroscopy. The small energy differences of the Mn, Fe and Co, K absorption edges allow quick XAS measurements with just one cell, reducing the risk of varying data, which may occur if individual cells are used for every absorption edge. The spectra of the pristine material at all three K edges show a pre-edge peak (Figure 6 thick blue line) delivering information about the local structure of the absorber atom. Pre-edge features are a result of $1s \rightarrow 3d/4p$ (hybridized orbitals) transitions, which may appear with large intensity in a non-centrosymmetric environment. For the centrosymmetric octahedral (B) environment the pre-edge signal is very weak and a result of mainly quadrupole transitions of very low intensity.

The occurrence of $1s \rightarrow 3d/4p$ transitions for all three metal ions is a clear hint that they are at least partially located on tetrahedral sites.^{50,51} The energy of the Mn K-edge at 6550 eV (determined by the maximum of the first derivative) is identical with that of $\alpha\text{-Mn}^{III}_2\text{O}_3$,⁵² evidencing that Mn in CoFeMnO_4 nanoparticles is in the expected oxidation state Mn^{III} . For the Fe K-edge a value of 7125 eV is obtained in agreement with the value for Fe^{III} in MFe_2O_4 ($M = \text{Ni}, \text{Co}, \text{Mn}$).⁵¹ The Co K-edge energy at 7716 eV is in line with that of Co^{II} in CoFe_2O_4 .⁵³ Summarizing, the expected oxidation states could be confirmed by XAS for pristine CoFeMnO_4 . Hence, the chemical formula can be presented as



(A: tetrahedral sites and B = octahedral sites).

In Figure 7, the potential curve of the operando XAS cell is shown, displaying processes similar to the first cycle discussed in Section 2.2. Below the potential curve the energy position of the Mn K-, Fe K-, and Co K-edges are displayed. In region I, the position of the Co K-edge is only slightly affected by Li uptake, while both the Fe K-edge and Mn K-edge exhibit a strong shift to lower energy. We note that in region I Mn^{III} is reduced first, and at later stage reduction of Fe^{III} starts (Figure 7).

After uptake of ~ 2.5 Li per f.u. the Mn K-edge energy at 6545 eV is identical with that of MnO (Figure 6, top).⁵⁴ Also a strong shift of the Fe K-edge occurred, that is, Fe^{III} is reduced to Fe^{II} (Figure 6), as also observed during Li uptake into Fe_2O_3 .⁵⁵

Not only shifts of the absorption edges are obvious but also their shapes are altered during Li uptake. The pre-edge features for all three elements disappeared when ~ 2.5 Li/f.u. are inserted because the ions moved from the tetrahedral to neighbored octahedral sites. At this stage of discharge, X-ray absorption near edge structure (XANES) spectra of all three elements display the largest intensity of the $1s \rightarrow 4p$ transition (Figure 6, thick blue line). In region II (during the long plateau at ~ 0.6 V), the intermediately formed monoxide is transformed to an amorphous respectively nanocrystalline product (Section 2.3). Co^{II} , Mn^{II} , and Fe^{II} are reduced to the metallic state during the long plateau in region II (Figure 7). In the spectra of all three metals a rotation around isosbestic points is visible at 6545 eV for Mn, at 7123 eV for Fe, and at 7718 eV for Co (Figure 6) giving evidence that the three metals are transformed in a one-step reaction without formation of

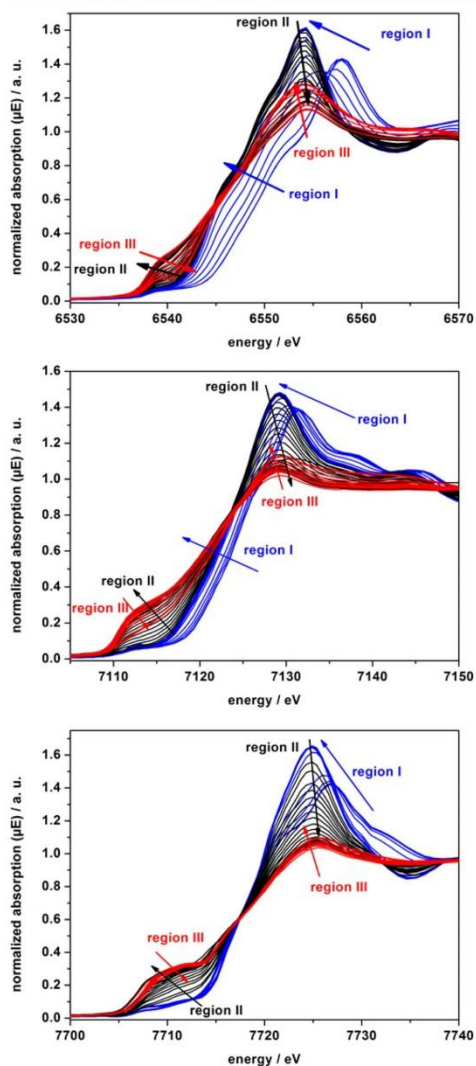


Figure 6. Operando XANES spectra at Mn (top), Fe (middle), and Co K-edge (bottom) during uptake of the first 2.5 Li per f.u. (region I, blue lines), during uptake of more than 2.5 Li (region II, black lines), and during charge process (region III, red lines).

intermediates. At the end of region II (end of discharge process), the spectra of all three elements resemble those of metallic reference foils, that is, the metallic states of Mn, Fe, and Co are reached. Similar observations were made for the Li uptake by NiCo_2O_4 . But this material contains Co^{III} , which is reduced in the first step followed by simultaneous reduction of Ni^{II} and Co^{II} to the metallic state.⁵⁶

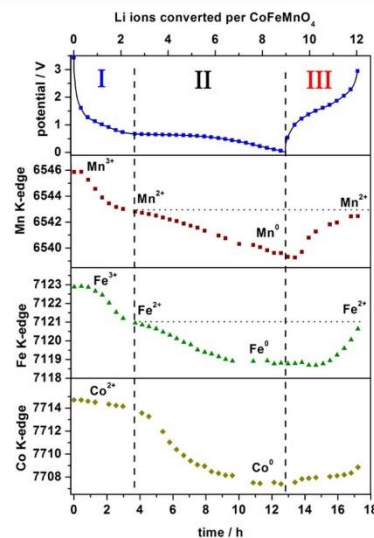


Figure 7. Potential curve of the in situ cell (top) and K-edge position of Mn, Fe, and Co (from top).

The charge process is accompanied by a strong shift of the Mn K-edge to higher energy, that is, Mn^0 is oxidized, followed by oxidation of Fe. The beginning of oxidation of metallic Co is only partially visible at the end of the charge process (see Figures 6 and 7).

Fourier transformation (FT R-space) of the spectra of the pristine state and at the end of regions I, II, and III was performed to interpret the changes in the local environment of the ions (Figure 8; the normalized XAS spectra covering the pre-edge, XANES, and extended X-ray absorption fine structure region are displayed in Figure S5). For pristine CoMnFeO_4 two signals are visible in the FT R-space plot for each element representing the M–O bonds (1.5 Å) and M–O–M paths (2.5 Å). The asymmetry of the shape of the first signal is caused by overlapping paths of the cations located on tetrahedral (shorter path) and octahedral sites (longer path) in the spinel structure. At the end of region I, the distance of all three elements to the first neighbor increases slightly caused by formation of the monoxide phase characterized by longer M–O bonds (M = Co, Fe, Mn). At the end of region II a new signal at 2 Å developed corresponding to interatomic distances for metallic Co, Fe, and Mn (Figure 8), while signals at 1.5 and 2.5 Å disappeared. During the first two scans of the charge process (region III) the K-edge positions of the elements are not shifting (Figure 6), suggesting a reversible additional storage mechanism affecting the capacity at the early stages of Li release.^{48,49}

The FT R-space curves at the end of region III (charged state) are characterized by an intensity reduction of the M–M paths at ca. 2 Å for all three elements and the development of the two signals assigned to M–O and M–O–M scattering paths. The maxima of the Mn/Fe–O and Mn/Fe–O–M signals occur at nearly identical distances as in the monoxide intermediate phase. Furthermore, as can be seen in Figure 7 only 3.1 Li (capacity: 355 mAhg^{-1}) could be removed during

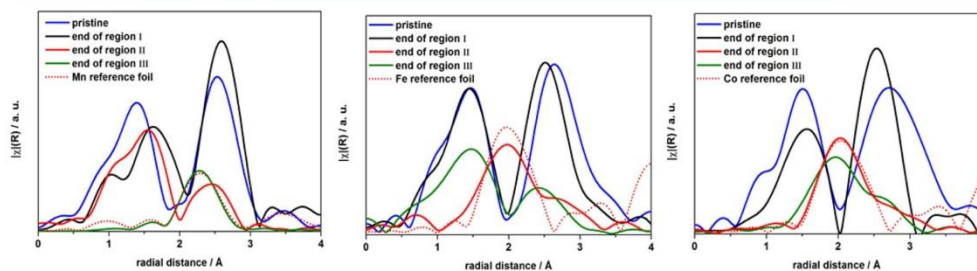


Figure 8. FT R-space spectra of Mn (left), Fe (middle), and Co (right). Note: no phase shift correction was applied.

charge demonstrating that the charge process was incomplete (see Section 2.2). Most probably, the setup of the in situ cell does not compensate the volume expansion during cycling, and parts of the active material may become inactive. Indeed the last spectra of the operando study evidence that the final oxidation states of the transition metal ions are not reached. Nevertheless, operando XAS during the charge process provides information in which sequence the transition metals are oxidized from the metallic state. The final oxidation state of the transition metals was determined by ex situ XANES spectra of a fully cycled sample (Figure S6). The XANES data evidence that metallic Mn is oxidized to Mn^{II} and remains in this oxidation state. This observation is in line with results obtained on Mn_3O_4 , where during charge MnO is formed instead of Mn^{III} .²⁰ The XANES spectra at the Fe K-edge indicate that trivalent Fe^{III} is obtained after the first cycle. Co is also oxidized, and the K-edge absorption energy gives hints for the presence of Co^{II} after the first cycle. The results are in agreement with observations recently made for CoFe_2O_4 nanoparticles.²³ The presence of weak pre-edge features in the K-edge spectra suggests a local symmetry without an inversion center.

2.5. Ex Situ ^7Li Magic-Angle Spinning Nuclear Magnetic Resonance. The ex situ ^7Li MAS NMR spectra of the lithiated CoMnFeO_4 samples and of the sample obtained after one complete electrochemical cycle are displayed in Figure 9. The samples with small Li contents (0.3 Li, 0.6 Li, 1 Li) exhibit very broad spinning sideband patterns and very broad isotropic peaks. The intensity of the isotropic peaks is covering the range from +100 to -400 ppm. Such large ^7Li NMR shift values occur only in samples with paramagnetic neighbors in the direct environment of the Li ions.⁵⁷ Thus, these large shifts reflect the presence of Li–O–(Fe/Mn/Co) bonds. The extremely broad contributions in the patterns obtained in spite of the very fast MAS spinning (60 kHz) show that the Li ions experience a large variety of local environments, that is, many different compositions and arrangements of the transition metal neighbors (Co, Mn, Fe). This is consistent with a random arrangement of the different transition metal elements in the amorphous phase on the surface of the nanoparticles. After conversion of two Li ions, the spinning sideband pattern in the ^7Li NMR spectrum shows a clear narrowing and a major isotropic peak close to 0 ppm with strongly reduced width. This reveals the formation of a Li-containing phase without transition metal neighbors around the Li, and thus this peak can be assigned to the Li_2O phase that is formed together with the $\text{Co}_{1/3}\text{Fe}_{1/3}\text{Mn}_{1/3}\text{O}$ rock salt phase. Additionally, in this spectrum broad contributions covering the range from +200 to -100 ppm are visible (marked with arrows in Figure 9). These

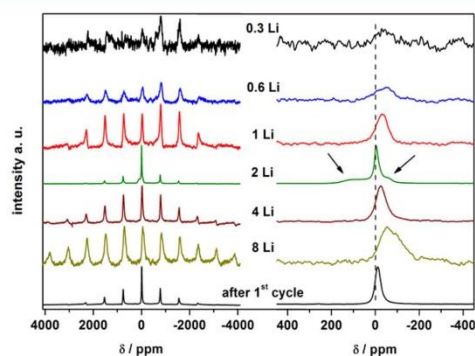


Figure 9. ^7Li MAS NMR spectra of CoFeMnO_4 nanoparticles after uptake of 0.3, 0.6, 1, 2, 4, 8 Li per formula unit and after the first cycle. (left) Full spinning sideband patterns. (right) Magnified view of the region of the isotropic peaks.

are caused either by residuals of the spinel phase or small amounts of Li in the rock salt phase. Further increasing of the Li content, the width of the spinning sideband pattern increases again, and the isotropic peaks also show a strong broadening. This behavior is consistent with our earlier observations on MnFe_2O_4 ²¹ and MgFe_2O_4 ,²² and it is caused by the increasing amount and size of Mn, Fe, and Co metal particles. The spectrum of the sample obtained after one full cycle shows again a quite narrow peak and a rather narrow spinning sideband pattern. This spectrum confirms that the overall reaction is not reversible; that is, the transition metal particles are converted back to oxides, but the initial spinel phase is not reformed.

2.6. Ex Situ Transmission Electron Microscopy of Lithium-Containing Samples. TEM investigations were performed on CoMnFeO_4 nanoparticles that were discharged to 10 mV and cycled (0.1–3.0 V, charged state) three times (potential profiles are shown in Figure S7). Figure 10 (top, left) shows a dark-field STEM image of a completely discharged sample. The Co-, Mn-, and Fe-containing particles (with strong Z-contrast) are randomly dispersed in an amorphous matrix. STEM-EDX mapping (Figure 10, top right) performed on a single particle reveals that iron, cobalt, and manganese are not homogeneously dispersed (cf. Mn-rich and Fe-poor area marked in Figure 10, top right) within the metal oxide; however, phase separation of single metal (oxide) nanoparticles

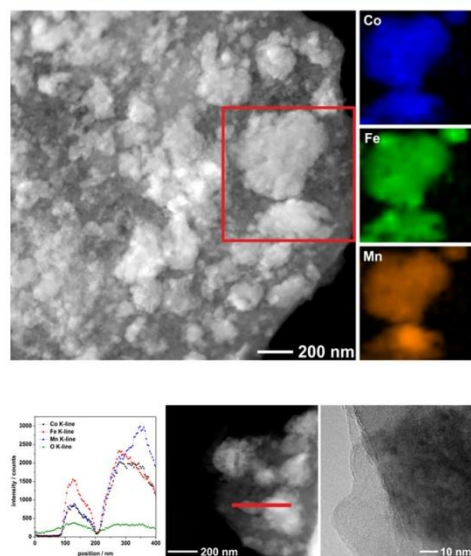


Figure 10. Dark-field STEM image (top left), EDX mapping at the area marked with a red square. EDX line scan (bottom left) of CoMnFeO₄ particles after cycling three times between 3.0 and 0.1 V. Dark-field STEM image (bottom middle) with line scan marked by the red bar. HRTEM micrograph at the edge of an amorphous particle with SEI on the left side (bottom, right).

is not observed. Very recently a local segregation of chemical elements on the nanometer scale was reported, which significantly improved the electrochemical performance.⁵⁸ Whether the inhomogeneous distribution of the metals is

beneficial for the electrochemical performance of the material cannot be answered on the basis of the present data.

After three cycles an EDX line scan (Figure 10, bottom left) over two particles (see Figure 10 middle, red bar) demonstrates the equal distribution of oxygen and metals content in both particles. On the left side of the measuring area an oxygen excess arising from the SEI is visible. At high resolution the amorphous SEI covering the surface of a particle is visible (see Figure 10, bottom right). After the cycles, the metal-containing particles lose their crystalline character. HRTEM and SAED investigations revealed that the product is amorphous, also visible by FFT transformation of the image (Figure S8; Moreover, carbon could be found due to the sample preparation and its presence in the SEI).

2.7. Molecular Dynamics Simulation of Li Ion Intercalation and Mobility in Fe₃O₄. To explore the early stage of Li intercalation into the spinel structure of M₃O₄ we performed molecular dynamics simulations on an Fe₃O₄ nanocube initially prepared as an ideal crystal. Upon relaxation at 300 K the nanocube evolved into a slightly more rounded shape, exhibiting partial amorphous arrangements at its edges and corners, which is in good agreement with amorphous surface visible in TEM. Subsequently five Li⁺ were incorporated into neighboring 8b and 48f tetrahedral sites, and relaxation was explored (i) without charge compensation and (ii) with charge compensation by reducing an adjacent Fe^{III} ion. In both cases, structural relaxation of the defect involves only local rearrangements keeping the overall lattice intact. At 300 K the average distance of Li–O contacts was found as 2.2 Å, while the Fe^{II}–O and Fe^{III}–O nearest neighbor distances are 2.9 and 2.7 Å, respectively. In turn, the metal ions are shifted to expand the distance with respect to the tetrahedral sites from less than 2 Å (for empty tetrahedral sites) to ~2.7 Å (Li–Fe^{II} contact after intercalation).

By filling of five neighboring tetrahedral sites, our starting model was prepared to locally mimic intercalation by one Li per Fe₃O₄ f.u. However, in both setups (i) and (ii), that is, with and without charge Fe^{III} reduction, we identified Li⁺ diffusion steps

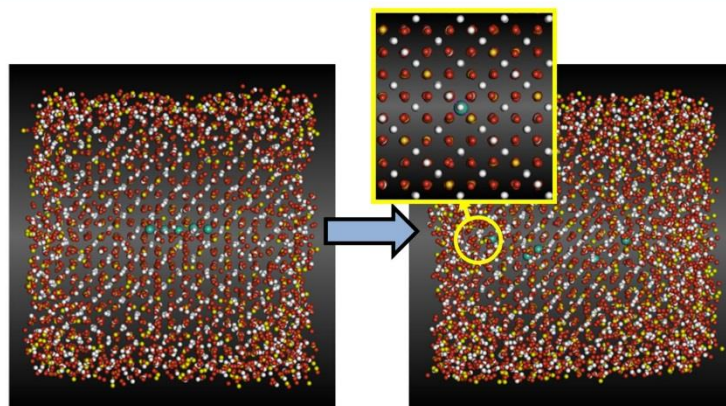


Figure 11. Snapshots from molecular dynamics runs of a Fe₃O₄ nanocube intercalated by five Li ions (left). Relaxation occurs in two steps: rapid separation of the Li ions, by at least one vacant tetrahedral site, and much slower Li⁺ diffusion within the nanoparticle. (inset) A single Li intercalation site after model quenching to 0 K. Colors: Fe^{III} (white), Fe^{II} (yellow), O (red), Li (cyan).

leading to larger Li–Li separation after ~100 ps. Upon Li separation by at least one vacant tetrahedral site, ion mobility decreased, and diffusion steps were observed on the 1 ns scale (Figure 11). Our simulations hence suggest that intercalation by 0.5 Li per Fe_3O_4 f.u. constitutes a limiting scenario. Full intercalation of all tetrahedral sites would hinder the beforehand described relaxation of Li–Fe and Li–O distances and result in a sharp increase in potential energy.

3. DISCUSSION

CoMnFeO_4 nanoparticles crystallize as a partially inverse spinel with formula $[\text{Co}^{II}_{1-(x+y)}\text{Fe}^{III}_x\text{Mn}^{III}_y]_A\{\text{Co}^{II}_{(x+y)}\text{Fe}^{III}_{1-x}\text{Mn}^{III}_{1-y}\}_B\text{O}_4$. XANES spectra of the pristine nanoparticles confirm the presence of Fe^{III} , Mn^{III} , and Co^{II} . In the spinel structure, two different tetrahedral sites (8b and 48f) and one octahedral site (16d) are empty. If Li^+ enters the structure either on 8b or 48f the Fe/Mn/Co–Li distances are shorter than 2 Å leading to strong repulsive interactions if the structure is assumed as a stiff lattice. An alternative scenario is the uptake of Li^+ on one of these sites followed by a movement of the M cations located on 8a to empty 16d sites accompanied by reduction of M^{III} and a jump of Li ions to 16d sites. Obviously, all octahedral sites are occupied after uptake of 1 Li per formula unit, and a NaCl-like structure should be generated. We note that this scenario was postulated for the Li uptake by Fe_3O_4 .⁵⁹

Molecular dynamics (MD) simulation showed this scenario can be excluded for nanoparticles: Li^+ ions intercalated on tetrahedral sites (8b and 48f) clearly favor this position and only temporarily visit empty octahedral 16d sites when diffusing from one tetrahedral site to another.

Strong repulsive interactions are compensated by a shift of metal ions to expand the distance with respect to the tetrahedral sites from less than 2 Å to ~2.7 Å (Li–Fe^{II} contact after intercalation). Hence, the MD simulation suggests that up to 0.5 Li may be incorporated into the structure. This is in agreement with the operando XRD investigations (Section 2.3). In the beginning the integrated and normalized reflection areas of the powder patterns exhibit no variation up to 0.5 Li/ CoFeMnO_4 indicating that the spinel phase is not converted into a new product. The unit cell expansion of the spinel phase is only 0.2%, which is in agreement with the marginal enlargement observed in the MD simulation. The ⁷Li MAS NMR spectra after uptake of 0.3 and 0.6 Li exhibit large shifts indicating the presence of Li–O–M (M = Fe, Co, Mn) bonds, which is in agreement with Li ions being either inserted into the spinel structure or on the surface of the particles. In the operando XANES spectra a slight shift of the Mn K-edge energy is observed indicating that Mn^{III} ions are reduced first. Summarizing these results, a possible scenario is an uptake of small amounts of Li into the spinel structure being accompanied by reduction of some Mn^{III} ions and expansion of tetrahedral sites, while direct neighbored empty tetrahedral sites are contracted (Section 2.7). This reaction step seems to be partially reversible as demonstrated by repeated cycling between 1.3 and 3.0 V (Figure S9).

For Li contents beyond 0.5/ CoFeMnO_4 an abrupt rise in potential energy is observed in the MD simulation. This increase is induced by the beginning of the transformation of crystalline spinel phase into a NaCl-type oxide as evidenced by XRD. During further Li uptake the M^{III} ions are successively reduced, and the M^{II} ions on the tetrahedral site move to empty octahedra. Where are the Li^+ ions located? One may assume

that Li^+ ions also occupy empty octahedral site. But the observation that up to 1.5 Li/f.u. two crystalline phases coexist (XRD), while at this Li content all 16c/16d sites are occupied, requiring an explanation. A narrowing of the ⁷Li NMR signal for the sample containing one Li/ CoFeMnO_4 suggests formation of Li_2O with only weak or no Li–O–M bridges. On the basis of this finding we conclude that Li^+ does not occupy octahedral sites, but rather Li_2O is formed. We note that the reaction proposed here is not in accordance with that reported for microcrystalline spinel materials.^{59–62} The XANES spectra clearly demonstrate that Mn^{III} is reduced first to Mn^{II} followed by simultaneous reduction of remaining Mn^{III} and Fe^{III} to Mn^{II} /Fe^{II}. The reduction of the trivalent ions is finished at the end of region I in the galvanostatic discharge curve. All metal ions are now in the centrosymmetric octahedral environment as evidenced by the disappearance of the pre-edge features in the XANES spectra. According to operando XRD data the spinel structure is now completely converted to the NaCl-type structure (Section 2.3). Occupation of all 16c/16d site leaves behind a network of empty tetrahedral sites, resembling that observed for Li_2O (Li is tetrahedrally surrounded by oxygen atoms). In the ⁷Li MAS NMR spectrum a narrow line is observed, which is typical for Li_2O . The observation of formation of a monoxide as an intermediate during discharge is not unique and was also reported or postulated for a number of spinel materials.^{19–22} But compared to these studies we are able to present evidence for Li_2O formation during discharge, the stepwise reduction of M^{III} to M^{II} , and the successive transformation of the spinel into a NaCl-type structure. The elaborate evaluation of operando XRD demonstrates the successive morphology change and alteration of crystallite size distribution of the nanoparticles. Interestingly, the size of coherently scattering domains of the monoxide after uptake of ~2.5 Li clearly displays a shift in the log-normal size distribution toward larger crystallites (Section 2.3).

Further discharge (cf. long plateau at 0.8 V in galvanostatic cycling, the intense peak in the CV (Figure 3)) leads to simultaneous reduction of all M^{II} ions to the metallic state (Section 2.3); that is, no further intermediates are formed. The TEM/EDX investigations of particles formed after three cycles evidence that the nanoparticles contain Co, Mn, Fe, and O; thus, a phase separation can be safely excluded. From thermodynamics the occurrence of the monoxide containing all three cations is surprising and may be explained by the nanosized nature of the spinel particles.

After the first charge process no long-range ordered crystalline materials is formed as evidenced by XRD. But one cannot exclude formation of nanocrystallites being smaller than the coherence length of the X-rays. The results of the XAS experiments demonstrate that metallic Mn is oxidized first, followed by Fe and then Co. Oxidation of metallic Fe to Fe^{III} during charge could be definitely answered by accompanying ex situ XAS investigation (Figure S6). Because Mn nanoparticles can only be oxidized to Mn^{2+} the partial capacity loss reported for Mn(III)-based spinels can be explained with this finding.⁴⁸

4. CONCLUSION

Phase-pure CoMnFeO_4 nanoparticles were synthesized via a new synthesis route and investigated for the first time with respect to the electrochemical performance. The material exhibits excellent cycling stability (717 mAh g⁻¹, i.e., 74% after 50 cycles) outperforming many other binary and ternary oxides.

For the first time an oxidic spinel consisting of three transition metal cations was investigated by a combination of operando XRD, operando and ex-situ XAS, HRTEM/EDX, ^7Li MAS NMR, and MD simulation allowing formulation of a very detailed picture of the complex reactions occurring during Li uptake and release. On the basis of all results we safely exclude intercalation of larger quantities of Li in contrast to what was reported for microcrystalline particles.^{19,59,62} The spinel phase is successively transformed to rock salt structured $\text{Co}_{1/3}\text{Mn}_{1/3}\text{Fe}_{1/3}\text{O}$, which is accompanied by formation of Li_2O . We also investigated for the first time the change of the log-normal domain size distribution and of the particle morphologies. At the end of discharge metallic Co, Fe, and Mn nanoparticles are embedded in a Li_2O matrix. During cycling of the material, metallic nanoparticles and oxidized species are reversibly formed. The oxidized samples most probably consist of oxide(s), while only the local structure of the oxide(s) is known. In summary, CoMnFeO_4 nanoparticles are a highly promising new anode material both from a fundamental and application point of view. Addition of graphene or carbon coating and/or special morphology will improve the cycling stability and is a topic of further investigations.

5. METHODS

Synthesis. CoFeMnO_4 nanoparticles were synthesized by dissolving $\text{Co}(\text{NO}_3)_2 \cdot 6\text{H}_2\text{O}$ (97%, Merck Millipore), $\text{Fe}(\text{NO}_3)_3 \cdot 9\text{H}_2\text{O}$ (98%, Riedel-de Haen), and $\text{Mn}(\text{NO}_3)_2 \cdot 4\text{H}_2\text{O}$ (98%, Grüssing) in 20 mL of deionized water. Nitric acid (5 mL, 65%, p.A., Grüssing) was added to the solution by stirring at room temperature. Afterward 10 mL of ethylene glycol (99%, Merck Millipore) was added, and the mixture was heated at 80 °C until a viscous gel formed. Afterward the gel was dried at 120 °C for 24 h. The solid was ground in an agate mortar and heated at 400 °C in a preheated oven in air for 3 h. The synthesis presented here is similar to that of NiFeMnO_4 nanoparticles reported in ref 63.

Materials Characterizations. XRD patterns were recorded with an X'pert PRO diffractometer (PANalytical) equipped with a PIXcel detector using $\text{Cu K}\alpha$ radiation. The refinement of the powder pattern was performed employing the fundamental parameter approach in combination with a Pawley fit using Topas Academic.⁶⁴ EDX spectra were collected in a Philips ESEM XL 30 with an EDAX New XL-30 Detecting Unit. An acceleration voltage of 20 kV was used to detect the K-lines. TEM investigations were performed with a Tecnai F30 G2-STwin microscope at 300 kV with a field emission gun cathode and a Si/Li detector (Thermo Fisher, NSS). For TEM investigations CoFeMnO_4 nanoparticles were suspended in *n*-butanol and treated in ultrasonic bath to induce particle separation. Afterward the dispersion was dropped onto a holey-carbon copper grid.

Electrochemical Measurements. Electrochemical tests were performed in Swagelok cells. The cells were prepared by mixing 70 wt % active material with 20 wt % SUPER C65 Carbon (Timcal, Switzerland) and 10 wt % sodium carboxy methylcellulose (Sigma-Aldrich, Germany). The mixture was dispersed in deionized water, deposited on dendritic copper foil (Schlenk, Germany), and dried overnight at room temperature and at 80 °C for 24 h. Afterward 10 mm discs were cut with ~1 mg of active material. Lithium metal was used as counter electrode, glass microfiber filters (Whatman, United Kingdom) as the separator, and a solution of 1 M LiPF_6 in an ethylene carbonate/dimethyl carbonate mixture (Merck, Germany) as electrolyte. The cells were assembled in an argon-filled glovebox (<1 ppm of O_2 , <1 ppm of H_2O) and were discharged/charged with a MMates 510 DC galvanostat.

Operando X-ray Diffraction and X-ray Absorption Spectroscopy. For operando XRD and XAS investigations a custom-built cell ($40 \times 40 \times 15$ mm) consisting of two aluminum plates with rectangular apertures (14×3 mm) in the center and two sheets of

Kapton foil windows glued on both sides was used. 80 wt % active material was mixed with 10 wt % SUPER C65 Carbon (Timcal, Switzerland) and 10 wt % polyvinylidene fluoride (Solvay, Germany). The mixture was suspended in *N*-methyl-2-pyrrolidone, deposited on 8 μm Cu foil, and dried. Li metal as counter electrode was attached to a Cu foil. A microporous polyethylene/polypropylene membrane (Celgard 2325) was used as separator, and 1 M LiPF_6 in an ethylene carbonate/dimethyl carbonate mixture was used as electrolyte. For operando XRD, the PDIFF beamline at synchrotron source ANKA (Karlsruhe, Germany) was operated at 16 keV ($\lambda = 0.774901 \text{ \AA}$) with a Princeton CCD detector. Powder patterns were collected within 3 min. Reflections of copper were masked, and two-dimensional patterns were transformed with Area Diffraction Machine.⁶⁵ To determine the line profile of the instrument, a LaB_6 standard material (NIST 660a) was measured under the same conditions. The operando XRD patterns were analyzed using Whole Powder Pattern Modeling macros implemented in TOPAS Academic 5.0.^{64,66} The log-normal size distribution of the coherently scattering domains (modeled as spheres) are displayed in the Supporting Information (Figure S4). Additionally, the anisotropic [*hkl*]-dependent crystallite sizes were determined in combination with a Pawley Fit.⁶⁷ These results were utilized to model the crystallite morphologies.

Operando XAS analysis was performed at XAS beamline at ANKA applying repeated quick XAS scans at the Mn, Fe, and Co K-edges. The energy was calibrated with Fe foil before the experiment. Additional Mn, Fe, and Co reference foils were measured simultaneously between the second and third ionization chambers. Spectra were background-corrected, normalized, k^2 -weighted, and Fourier transformed with the Athena Software package.⁶⁸ In situ cells were discharged/charged at a C/12 rate with a Biologic VSP 300 potentiostat/galvanostat. (C/12 rate corresponds to 12 h for the charge and discharge process, and the calculation is based on the theoretical capacity of 917 mAh g^{-1} corresponding to a current density of 77 mA g^{-1}).

Ex Situ Investigation by ^7Li Nuclear Magnetic Resonance and Transmission Electron Microscopy. For ex situ ^7Li NMR investigations nanoparticles were mixed with SUPER C65 carbon and PVDF (80/10/10 wt %). Approximately 25 mg were pressed into 8 mm pellets and assembled in a Swagelok cell. The test cells were prepared with electrolyte, separator, and lithium as described above. After it reached the desired (overall) composition $\text{Li}_x\text{CoFeMnO}_4$, the discharge process was stopped, and the cells were opened in an argon-filled glovebox. ^7Li MAS NMR spectroscopy was performed at room temperature on a Bruker Avance 200 MHz spectrometer at a magnetic field of 4.7 T corresponding to a Larmor frequency of $\nu_L = 77.8$ MHz. A spinning speed of 60 kHz was applied using 1.3 mm rotors in a dry nitrogen atmosphere. An aqueous 1 M LiCl solution served as ^7Li reference (0 ppm). The typical value for the recycling delay was 1 s. ^7Li MAS NMR experiments were implemented with a rotor-synchronized Hahn-echo sequence ($\pi/2 - \tau - \pi - \tau$ -acquisition) and a typical $\pi/2$ pulse length of 2 μs . For ex situ TEM investigations an in situ preparation method was used as described by Lin et al.⁶⁹ Instead of using coin cells we used Swagelok cells.

Molecular Dynamics Simulations. Molecular dynamics simulations were performed on a magnetite nanocube model using a $5 \times 5 \times 5$ supercell as a starting point. The interatomic potentials were calculated on the basis of the 12-6 interaction model of Zhao et al. using explicit Coulomb summation.⁷⁰ Constant-temperature molecular dynamics simulations with a time step of 1 fs were performed at a variety of different temperature conditions ($T = 300, 600,$ and 900 K) to explore nanoparticle relaxation, which typically converged after less than 0.1 ns. After intercalation of five Li^+ ions structural relaxation (using $T = 300$ K) and Li^+ mobility were investigated at $T = 600$ and 900 K from independent simulation runs each comprising 5 ns, respectively.

■ ASSOCIATED CONTENT

● Supporting Information

The Supporting Information is available free of charge on the ACS Publications website at DOI: 10.1021/acsami.6b03185.

SEM image of the as-prepared sample with corresponding EDX spectrum, EDX results, details of TEM investigations, detailed view on powder pattern after uptake of 2.5 Li per f.u., log-normal size distribution of as-prepared and sample after uptake of 2.5 Li per f.u., XAS spectra of CoMnFeO₄ and at the end of regions I, II, and III, ex situ XANES spectra, preparation of lithiated TEM samples, FFT TEM image, repeated cycling at high potentials (1.3–3.0 V) (PDF)

■ AUTHOR INFORMATION

Corresponding Author

*E-mail: wbesch@ac.uni-kiel.de.

Author Contributions

The manuscript was written through contributions of all authors. All authors have given approval to the final version of the manuscript.

Notes

The authors declare no competing financial interest.

■ ACKNOWLEDGMENTS

We are grateful to the Deutsche Forschungsgemeinschaft and to the German Federal Ministry of Education and Research for financial support. Beamtime allocation by ANKA (Karlsruhe) is thankfully acknowledged. We are also very thankful to Dr. S. Doyle and Dr. S. Mangold for their great support during experiments at ANKA PDIFF and XAS beamlines.

■ ABBREVIATIONS

LIB, lithium ion battery
f.u., formula unit
MD, molecular dynamics

■ REFERENCES

- (1) Goodenough, J. B.; Park, K.-S. The Li-Ion Rechargeable Battery: A Perspective. *J. Am. Chem. Soc.* **2013**, *135*, 1167–1176.
- (2) Panwar, N. L.; Kaushik, S. C.; Kothari, S. Role of Renewable Energy Sources in Environmental Protection: A Review. *Renewable Sustainable Energy Rev.* **2011**, *15*, 1513–1524.
- (3) Whittingham, M. S. Ultimate Limits to Intercalation Reactions for Lithium Batteries. *Chem. Rev.* **2014**, *114*, 11414–11443.
- (4) Scrosati, B.; Garche, J. Lithium Batteries: Status, Prospects and Future. *J. Power Sources* **2010**, *195*, 2419–2430.
- (5) Wagemaker, M.; Mulder, F. M. Properties and Promises of Nanosized Insertion Materials for Li-Ion Batteries. *Acc. Chem. Res.* **2013**, *46*, 1206–1215.
- (6) Kaus, M.; Issac, I.; Heinzmann, R.; Doyle, S.; Mangold, S.; Hahn, H.; Chakravadhanula, V. S. K.; Kübel, C.; Ehrenberg, H.; Indris, S. Electrochemical Delithiation/Relithiation of LiCoPO₄: A Two-Step Reaction Mechanism Investigated by *in Situ* X-Ray Diffraction, *in Situ* X-Ray Absorption Spectroscopy, and *ex Situ* ⁷Li/³¹P NMR Spectroscopy. *J. Phys. Chem. C* **2014**, *118*, 17279–17290.
- (7) Bezza, I.; Kaus, M.; Heinzmann, R.; Yavuz, M.; Knapp, M.; Mangold, S.; Doyle, S.; Grey, C. P.; Ehrenberg, H.; Indris, S.; Saadoun, I. Mechanism of the Delithiation/Lithiation Process in LiFe_{0.4}Mn_{0.6}PO₄: *in Situ* and *Ex Situ* Investigations on Long-Range and Local Structures. *J. Phys. Chem. C* **2015**, *119*, 9016–9024.
- (8) Liu, H.; Strobridge, F. C.; Borkiewicz, O. J.; Wiaderek, K. M.; Chapman, K. W.; Chupas, P. J.; Grey, C. P. Capturing Metastable Structures during High-Rate Cycling of LiFePO₄ Nanoparticle Electrodes. *Science* **2014**, *344*, 1252817–1252817.
- (9) Zhang, X.; van Hulzen, M.; Singh, D. P.; Brownrigg, A.; Wright, J. P.; van Dijk, N. H.; Wagemaker, M. Direct View on the Phase Evolution in Individual LiFePO₄ Nanoparticles during Li-Ion Battery Cycling. *Nat. Commun.* **2015**, *6*, 8333.
- (10) Zhang, X.; van Hulzen, M.; Singh, D. P.; Brownrigg, A.; Wright, J. P.; van Dijk, N. H.; Wagemaker, M. Rate-Induced Solubility and Suppression of the First-Order Phase Transition in Olivine LiFePO₄. *Nano Lett.* **2014**, *14*, 2279–2285.
- (11) Chueh, W. C.; El Gabaly, F.; Sugar, J. D.; Bartelt, N. C.; McDaniel, A. H.; Fenton, K. R.; Zavadil, K. R.; Tyliczszak, T.; Lai, W.; McCarty, K. F. Intercalation Pathway in Many-Particle LiFePO₄ Electrode Revealed by Nanoscale State-of-Charge Mapping. *Nano Lett.* **2013**, *13*, 866–872.
- (12) Etacheri, V.; Marom, R.; Elazari, R.; Salitra, G.; Aurbach, D. Challenges in the Development of Advanced Li-Ion Batteries: A Review. *Energy Environ. Sci.* **2011**, *4*, 3243–3262.
- (13) Li, D.; Zhou, H. Two-Phase Transition of Li-Intercalation Compounds in Li-Ion Batteries. *Mater. Today* **2014**, *17*, 451–463.
- (14) Tarascon, J.-M.; Laruelle, S.; Grugeon, S.; Dupont, L.; Poizat, P. Nano-Sized Transition-Metal Oxides as Negative-Electrode Materials for LiB. *Nature* **2000**, *407*, 496–499.
- (15) Reddy, M. V.; Subba Rao, G. V.; Chowdari, B. V. R. Metal Oxides and Oxyalts as Anode Materials for LiB. *Chem. Rev.* **2013**, *113*, 5364–5457.
- (16) Cabana, J.; Monconduit, L.; Larcher, D.; Palacin, M. R. Beyond Intercalation-Based Li-Ion Batteries: The State of the Art and Challenges of Electrode Materials Reacting Through Conversion Reactions. *Adv. Mater.* **2010**, *22*, E170–E192.
- (17) Rui, X.; Tan, H.; Yan, Q. Nanostructured Metal Sulfides for Energy Storage. *Nanoscale* **2014**, *6*, 9889–9924.
- (18) Wang, F.; Robert, R.; Chernova, N. A.; Pereira, N.; Omenya, F.; Badway, F.; Hua, X.; Ruotolo, M.; Zhang, R.; Wu, L.; Volkov, V.; Su, D.; Key, B.; Whittingham, M. S.; Grey, C. P.; Amatucci, G. G.; Zhu, Y.; Graetz, J. Conversion Reaction Mechanisms in Lithium Ion Batteries: Study of the Binary Metal Fluoride Electrodes. *J. Am. Chem. Soc.* **2011**, *133*, 18828–18836.
- (19) Bresser, D.; Paillard, E.; Kloepsch, R.; Krueger, S.; Fiedler, M.; Schmitz, R.; Baither, D.; Winter, M.; Passerini, S. Carbon Coated ZnFe₂O₄ Nanoparticles for Advanced Lithium-Ion Anodes. *Adv. Energy Mater.* **2013**, *3*, 513–523.
- (20) Lowe, M. A.; Gao, J.; Abruña, H. D. *In Operando* X-Ray Studies of the Conversion Reaction in Mn₃O₄ Lithium Battery Anodes. *J. Mater. Chem. A* **2013**, *1*, 2094–2103.
- (21) Permien, S.; Hain, H.; Scheuermann, M.; Mangold, S.; Mereacre, V.; Powell, A. K.; Indris, S.; Schürmann, U.; Kienle, L.; Duppel, V.; Harm, S.; Bensch, W. Electrochemical Insertion of Li into Nanocrystalline MnFe₂O₄: A Study of the Reaction Mechanism. *RSC Adv.* **2013**, *3*, 23001–23014.
- (22) Permien, S.; Indris, S.; Scheuermann, M.; Schürmann, U.; Mereacre, V.; Powell, A. K.; Kienle, L.; Bensch, W. Is There a Universal Reaction Mechanism of Li Insertion into Oxidic Spinels: A Case Study Using MgFe₂O₄. *J. Mater. Chem. A* **2015**, *3*, 1549–1561.
- (23) Permien, S.; Indris, S.; Schürmann, U.; Kienle, L.; Zander, S.; Doyle, S.; Bensch, W. What Happens Structurally and Electronically during the Li Conversion Reaction of CoFe₂O₄ Nanoparticles: An *Operando* XAS and XRD Investigation. *Chem. Mater.* **2016**, *28*, 434–444.
- (24) Liu, X.; Wang, D.; Liu, G.; Srinivasan, V.; Liu, Z.; Hussain, Z.; Yang, W. Distinct Charge Dynamics in Battery Electrodes Revealed by *in Situ* and *Operando* Soft X-Ray Spectroscopy. *Nat. Commun.* **2013**, *4*, 2568.
- (25) Marino, C.; Fraisse, B.; Womes, M.; Villeveuille, C.; Monconduit, L.; Stievano, L. At the Heart of a Conversion Reaction An *Operando* X-ray Absorption Spectroscopy Investigation of NiSb₂, a Negative Electrode Material for Li-Ion Batteries. *J. Phys. Chem. C* **2014**, *118*, 27772–27780.

- (26) Boesenberg, U.; Marcus, M. A.; Shukla, A. K.; Yi, T.; McDermott, E.; Teh, P. F.; Srinivasan, M.; Moewes, A.; Cabana, J. Asymmetric Pathways in the Electrochemical Conversion Reaction of NiO as Battery Electrode with High Storage Capacity. *Sci. Rep.* **2014**, *4*, 7133.
- (27) Wu, Z.-S.; Ren, W.; Wen, L.; Gao, L.; Zhao, J.; Chen, Z.; Zhou, G.; Li, F.; Cheng, H.-M. Graphene Anchored with Co₃O₄ Nanoparticles as Anode of Lithium Ion Batteries with Enhanced Reversible Capacity and Cyclic Performance. *ACS Nano* **2010**, *4*, 3187–3194.
- (28) Gao, J.; Lowe, M. A.; Abruña, H. D. Sponglike Nanosized Mn₂O₄ as a High-Capacity Anode Material for Rechargeable Lithium Batteries. *Chem. Mater.* **2011**, *23*, 3223–3227.
- (29) Zhou, G.; Wang, D.-W.; Li, F.; Zhang, L.; Li, N.; Wu, Z.-S.; Wen, L.; Lu, G. Q.; Cheng, H.-M. Graphene-Wrapped Fe₃O₄ Anode Material with Improved Reversible Capacity and Cyclic Stability for Lithium Ion Batteries. *Chem. Mater.* **2010**, *22*, 5306–5313.
- (30) Yoon, S. Facile Microwave Synthesis of CoFe₂O₄ Spheres and Their Application as an Anode for Lithium-Ion Batteries. *J. Appl. Electrochem.* **2014**, *44*, 1069–1074.
- (31) Yao, X.; Kong, J.; Tang, X.; Zhou, D.; Zhao, C.; Zhou, R.; Lu, X. Facile Synthesis of Porous CoFe₂O₄ Nanosheets for Lithium-Ion Battery Anodes with Enhanced Rate Capability and Cycling Stability. *RSC Adv.* **2014**, *4*, 27488–27492.
- (32) Cherian, C. T.; Sundaramurthy, J.; Reddy, M. V.; Suresh Kumar, P.; Mani, K.; Pliszka, D.; Sow, C. H.; Ramakrishna, S.; Chowdari, B. V. R. Morphologically Robust NiFe₂O₄ Nanofibers as High Capacity Li-Ion Battery Anode Material. *ACS Appl. Mater. Interfaces* **2013**, *5*, 9957–9963.
- (33) Xiao, Y.; Zai, J.; Tao, L.; Li, B.; Han, Q.; Yu, C.; Qian, X. MnFe₂O₄-graphene Nanocomposites with Enhanced Performances as Anode Materials for Li-Ion Batteries. *Phys. Chem. Chem. Phys.* **2013**, *15*, 3939–3945.
- (34) Lin, L.; Pan, Q. ZnFe₂O₄@C/graphene Nanocomposites as Excellent Anode Materials for Lithium Batteries. *J. Mater. Chem. A* **2015**, *3*, 1724–1729.
- (35) Wang, G.; Chen, R.; Zhou, Y.; Wang, H.; Bai, J. One-Pot Template-Free Fabrication of ZnMn₂O₄ Hollow Microspheres as High-Performance Lithium-Ion Battery Anodes. *J. Nanopart. Res.* **2014**, *16*, 2300.
- (36) Zhang, Z.; Wang, Y.; Zhang, M.; Tan, Q.; Lv, X.; Zhong, Z.; Su, F. Mesoporous CoFe₂O₄ Nanospheres Cross-Linked by Carbon Nanotubes as High-Performance Anodes for Lithium-Ion Batteries. *J. Mater. Chem. A* **2013**, *1*, 7444–7450.
- (37) Wang, N.; Xu, H.; Chen, L.; Gu, X.; Yang, J.; Qian, Y. A General Approach for MFe₂O₄ (M = Zn, Co, Ni) Nanorods and Their High Performance as Anode Materials for Lithium Ion Batteries. *J. Power Sources* **2014**, *247*, 163–169.
- (38) Lavela, P.; Kyeremateng, N. A.; Tirado, J. L. NiMn_{2-x}Fe_xO₄ Prepared by a Reverse Micelles Method as Conversion Anode Materials for Li-Ion Batteries. *Mater. Chem. Phys.* **2010**, *124*, 102–108.
- (39) Zhang, G.; Lou, X. W. D. General Synthesis of Multi-Shelled Mixed Metal Oxide Hollow Spheres with Superior Lithium Storage Properties. *Angew. Chem., Int. Ed.* **2014**, *53*, 9041–9044.
- (40) Zhou, L.; Zhao, D.; Lou, X. W. Double-Shelled CoMn₂O₄ Hollow Microcubes as High-Capacity Anodes for Lithium-Ion Batteries. *Adv. Mater.* **2012**, *24*, 745–748.
- (41) Wu, L.; Xiao, Q.; Li, Z.; Lei, G.; Zhang, P.; Wang, L. CoFe₂O₄/C Composite Fibers as Anode Materials for Lithium-Ion Batteries with Stable and High Electrochemical Performance. *Solid State Ionics* **2012**, *215*, 24–28.
- (42) Lu, Z. M.; Li, Z. W.; Shen, J.; Meng, F. B.; Liu, H. Y.; Li, Y. X.; Li, C. Y. Magnetic and Structural Properties of Co_{0.8}Mn_{0.2-x}Fe_xO₄ (x = 0.2, 0.4, 0.6, 0.8) Polycrystalline Powders Synthesized by Sol-Gel Process. *J. Appl. Phys.* **2009**, *105*, 519–520.
- (43) Oudrhiri-Hassani, F.; Presmanes, L.; Barnabe, A.; Tailhades, P. Microstructural Characterization of CoMnFeO₄ Thin Films Deposited by Radio-Frequency Sputtering. *MATEC Web Conf.* **2013**, *5*, 04041.
- (44) Goyal, A.; Bansal, S.; Singh, J.; Singhal, S. Mn Substituted Cobalt Ferrites (CoMn_xFe_{2-x}O₄ (x = 0.0, 0.2, 0.4, 0.6, 0.8, 1.0)) As Magnetically Separable Heterogeneous Nanocatalyst for Thereduction of Nitrophenols. *Appl. Surf. Sci.* **2015**, *324*, 877–889.
- (45) Jauhar, S.; Singhal, S.; Dhiman, M. Manganese Substituted Cobalt Ferrites as Efficient Catalysts for H₂O₂ Assisted Degradation of Cationic and Anionic Dyes: Their Synthesis and Characterization. *Appl. Catal., A* **2014**, *486*, 210–218.
- (46) Chassaing, I.; Presmanes, L.; Tailhades, P.; Rousset, A. Submicron Mn_{1-x}Co_xFe_{2-x}O₄ Spinel Ferrites Cationic Distribution and Reactivity. *Solid State Ionics* **1992**, *58*, 261–267.
- (47) Laruelle, S.; Grugeon, S.; Poizot, P.; Dollé, M.; Dupont, L.; Tarascon, J.-M. On the Origin of the Extra Electrochemical Capacity Displayed by MO/Li Cells at Low Potential. *J. Electrochem. Soc.* **2002**, *149*, A627–A634.
- (48) Ponrouch, A.; Taberna, P.-L.; Simon, P.; Palacin, M. R. On the Origin of the Extra Capacity at Low Potential in Materials for Li Batteries Reacting through Conversion Reaction. *Electrochim. Acta* **2012**, *61*, 13–18.
- (49) Maier, J. Nanoionics: Ion Transport and Electrochemical Storage in Confined Systems. *Nat. Mater.* **2005**, *4*, 805–815.
- (50) Zhang, Z. J.; Wang, Z. L.; Chakoumakos, B. C.; Yin, J. S. Temperature Dependence of Cation Distribution and Oxidation State in Magnetic Mn-Fe Ferrite Nanocrystals. *J. Am. Chem. Soc.* **1998**, *120*, 1800–1804.
- (51) Carta, D.; Casula, M. F.; Falqui, A.; Loche, D.; Mountjoy, G.; Sangregorio, C.; Corrias, A. A Structural and Magnetic Investigation of the Inversion Degree in Ferrite Nanocrystals MFe₂O₄ (M = Mn, Co, Ni). *J. Phys. Chem. C* **2009**, *113*, 8606–8615.
- (52) Aitchison, P.; Amundsen, B.; Jones, D. J.; Burns, G.; Rozière, J. Cobalt Substitution in Lithium Manganate Spinel: Examination of Local Structure and Lithium Extraction by XAFS. *J. Mater. Chem.* **1999**, *9*, 3125–3130.
- (53) Artus, M.; Ben Tahar, L.; Herbst, F.; Smiri, L.; Villain, F.; Yaacoub, N.; Grenèche, J.-M.; Ammar, S.; Fiévet, F. Size-Dependent Magnetic Properties of CoFe₂O₄ Nanoparticles Prepared in Polyol. *J. Phys.: Condens. Matter* **2011**, *23*, 506001.
- (54) Zhong, K.; Zhang, B.; Luo, S.; Wen, W.; Li, H.; Huang, X.; Chen, L. Investigation on Porous MnO Microsphere Anode for Lithium Ion Batteries. *J. Power Sources* **2011**, *196*, 6802–6808.
- (55) Jain, G.; Balasubramanian, M.; Xu, J. J. Structural Studies of Lithium Intercalation in a Nanocrystalline α-Fe₂O₃ Compound. *Chem. Mater.* **2006**, *18*, 423–434.
- (56) Chadwick, A. V.; Savin, S. L. P.; Fiddy, S.; Alcantara, R.; FernandezLisbona, D.; Lavela, P.; Ortiz, G. F.; Tirado, J. L. Formation and Oxidation of Nanosized Metal Particles by Electrochemical Reaction of Li and Na with NiCo₂O₄: X-Ray Absorption Spectroscopic Study. *J. Phys. Chem. C* **2007**, *111*, 4636–4642.
- (57) Grey, C. P.; Dupré, N. NMR Studies of Cathode Materials for Lithium-Ion Rechargeable Batteries. *Chem. Rev.* **2004**, *104*, 4493–4512.
- (58) Lin, F.; Nordlund, D.; Li, Y.; Quan, M. K.; Cheng, L.; Weng, T.-C.; Liu, Y.; Xin, H. L.; Doeff, M. M. Metal Segregation in Hierarchically Structured Cathode Materials for High-Energy Lithium Batteries. *Nat. Energy* **2016**, *1*, 15004.
- (59) Thackeray, M. M.; David, W. I. F.; Goodenough, J. B. Structural Characterization of the Lithiaed Iron Oxides Li_{1-x}Fe_{2-x}O₄ and Li_xFe₂O₃ (0 < x < 2). *Mater. Res. Bull.* **1982**, *17*, 785–793.
- (60) Chen, C.; Greenblatt, M.; Waszczak, J. Lithium Insertion into Spinel Ferrites. *Solid State Ionics* **1986**, *18–19*, 838–846.
- (61) Thackeray, M. M.; David, W. I. F.; Bruce, P. G.; Goodenough, J. B. Lithium Insertion into Manganese Spinel. *Mater. Res. Bull.* **1983**, *18*, 461–472.
- (62) Thackeray, M.; Baker, S.; Adendorff, K.; Goodenough, J. Lithium Insertion into Co₃O₄: A Preliminary Investigation. *Solid State Ionics* **1985**, *17*, 175–181.
- (63) Khosravi, I.; Yazdanbakhsh, M.; Goharshadi, E. K.; Youssefi, A. Preparation of Nanospinel NiMn_{2-x}Fe_xO₄ Using Sol-gel Method and Their Applications on Removal of Azo Dye from Aqueous Solutions. *Mater. Chem. Phys.* **2011**, *130*, 1156–1161.
- (64) Coelho, A. A. *Topas Academic*; Coelho Software, 2012.

- (65) Lande, J. *Area Diffraction Machine*; 2013. Free and open-source software available online.
- (66) Leoni, M.; Maggio, R.; Polizzi, S.; Scardi, P. X-Ray Diffraction Methodology for the Microstructural Analysis of Nanocrystalline Powders: Application to Cerium Oxide. *J. Am. Ceram. Soc.* **2004**, *87*, 1133–1140.
- (67) Evans, J. S. O. Advanced Input Files & Parametric Quantitative Analysis Using Topas. *Mater. Sci. Forum* **2010**, *651*, 1–9.
- (68) Ravel, B.; Newville, M. ATHENA, ARTEMIS, HEPHAESTUS: Data Analysis for X-Ray Absorption Spectroscopy Using IFEFFIT. *J. Synchrotron Radiat.* **2005**, *12*, 537–541.
- (69) Lin, F.; Nordlund, D.; Weng, T.-C.; Zhu, Y.; Ban, C.; Richards, R. M.; Xin, H. L. Phase Evolution for Conversion Reaction Electrodes in Lithium-Ion Batteries. *Nat. Commun.* **2014**, *5*, 3358–3367.
- (70) Zhao, L.; Liu, L.; Sun, H. Semi-Ionic Model for Metal Oxides and Their Interfaces with Organic Molecules. *J. Phys. Chem. C* **2007**, *111*, 10610–10617.

4.2 CuV₂S₄: A high rate-capacity and stable anode material for sodium-ion batteries

Die Verbindung CuV₂S₄ (Spinell-Struktur) wurde als Anodenmaterial für die Natriumioneneinlagerung untersucht. Der Mechanismus der Konversion wurde *ex situ* mit XRD, ²³Na MAS NMR und TEM untersucht. Während der Konversion des Materials werden Cu⁺-Ionen zu nanokristallinem metallischem Kupfer (~20 nm) reduziert, während mit XRD keine Reflexe von metallischem Vanadium nachweisbar sind. Dies lässt auf die Bildung einer röntgenamorphen oder nanokristallinen Phase schließen, deren kohärent streuende Domänen zu klein waren, um mit Kupferstrahlung ($\lambda = 1.54 \text{ \AA}$) detektiert zu werden. Rietveld-Verfeinerungen ergaben bereits für Proben nach einer Aufnahme von 0.5 und 1 Na pro Formeleinheit eine Abnahme der Cu-Besetzung. Die Gitterparameter waren jedoch identisch (0.5 Na: $a = 9.811(1) \text{ \AA}$ und 1 Na: $a = 9.811(2) \text{ \AA}$). Allerdings konnte eine zunehmende Gitterverzerrung bei zunehmender Na-Aufnahme beobachtet werden. Im vollständig entladenen Zustand lag das Elektrodenmaterial als röntgenamorphe Phase vor und nur Reflexe von kristallinem Kupfer und Na₂S waren detektierbar. Die Bildung von nanokristallinen metallischen Cu-Partikeln während der ersten Entladung führte zu einem verbesserten Elektronentransport, der die außerordentlich Zyklusstabilität im Vergleich zu anderen Übergangsmetallsulfiden erklärt. Während der Ladung konnte keine Rekristallisation von CuV₂S₄ beobachtet werden. In späteren Zyklen konnte ein bisher einzigartiges Phänomen einer Veränderung der Lade-/Entladeprofile beobachtet werden. Wahrscheinlich wurde Cu_{2-x}S gebildet, was die Auflösung von Polysulfidspezies im Elektrolyten behindert, wodurch ein häufig auftretender Kapazitätsverlust verhindert wird.

Reprinted with permission from M. Krenkel, A.-L. Hansen, M. Kaus, S. Indris, N. Wolff, L. Kienle, D. Westfal, W. Bensch, *ACS Appl. Mater. Interfaces* **2017**, 9, 21283–21291.

Copyright 2017 American Chemical Society.

CuV₂S₄: A High Rate Capacity and Stable Anode Material for Sodium Ion Batteries

Markus Kregel,[†] Anna-Lena Hansen,[†] Maximilian Kaus,[‡] Sylvio Indris,[‡] Niklas Wolff,[§] Lorenz Kienle,[§] David Westfal,[†] and Wolfgang Bensch^{*,†}

[†]Institute for Inorganic Chemistry, Christian-Albrechts-Universität zu Kiel, Max-Eyth-Str.2, 24118 Kiel, Germany

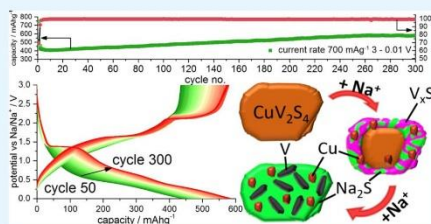
[‡]Institute for Applied Materials – Energy Storage Systems (IAM-ESS), Karlsruhe Institute of Technology (KIT), Hermann-von-Helmholtz-Platz 1, 76344 Eggenstein-Leopoldshafen, Germany

[§]Institute for Materials Science, Christian-Albrechts-Universität zu Kiel, Kaiserstr. 2, 24143 Kiel, Germany

Supporting Information

ABSTRACT: The ternary compound CuV₂S₄ exhibits an excellent performance as anode material for sodium ion batteries with a high reversible capacity of 580 mAh g⁻¹ at 0.7 A g⁻¹ after 300 cycles. A Coulombic efficiency of ≈99% is achieved after the third cycle. Increase of the C-rate leads to a drop of the capacity, but a full recovery is observed after switching back to the initial C-rate. In the early stages of Na uptake first Cu⁺ is reduced and expelled from the electrode as nanocrystalline metallic Cu. An increase of the Na content leads to a full conversion of the material with nanocrystalline Cu particles and elemental V embedded in a Na₂S matrix. The formation of Na₂S is evidenced by ²³Na MAS NMR spectra and X-ray powder diffraction. During the charge process the nanocrystalline Cu particles are retained, but no crystalline materials are formed. At later stages of cycling the reaction mechanism changes which is accompanied by the formation of copper(I) sulfide. The presence of nanocrystalline metallic Cu and/or Cu₂S improves the electrical conductivity, leading to superior cycling and rate capability.

KEYWORDS: sodium ion battery, anode material, ternary sulfides, CuV₂S₄, ex situ MAS NMR



INTRODUCTION

Portable electronic devices, electric vehicles, or stationary energy storage systems require batteries with different performances. For the first two applications Li ion batteries (LIBs) with high energy densities are available which were successively improved during the past decades. For large scale energy storage systems LIBs seem to be less promising due to the limited abundance of Li and the associated high costs. Hence, a growing interest to develop efficient, environmentally friendly energy storage devices leads to the exploration of new electrode materials for sodium ion batteries (SIBs) due to the higher availability, lower cost, and wider distribution of Na compared to Li.^{1–7} Considering sulfide-based materials, mainly binary transition metal compounds like TiS₂,⁸ MoS₂,^{9,10} WS₂,¹¹ FeS₂,^{12–14} Co₃S₄,¹⁵ Ni₃S₂,¹⁶ or main group sulfides like SnS₂,^{17,18} and Sb₂S₃^{19–21} were investigated. Ternary transition metal oxides^{22–32} have been intensively studied as electrode materials in lithium and sodium ion batteries, but there are just a few reports of ternary transition metal sulfide compounds investigated as electrode materials.^{33–36}

To compete with today's available LIBs, new materials for SIBs should have high specific capacities, long-term stability, and very good cyclability. These requirements may be achieved by application of electrodes in so-called conversion reactions. In

contrast to commercial LIBs which operate on intercalation/deintercalation reactions leaving the host materials structurally intact, the electrodes are converted during a conversion reaction and new phases are formed. Such conversion electrodes often show poor long time cycle stability and fast capacity loss. To ensure highly reversible sodium insertion and extraction, mainly nano-scaled materials are examined. The improved cyclability of such materials is explained by enhanced diffusion due to a more homogeneous atom contribution upon cycling.¹² To further improve rate and cycle stability, reduced graphene oxide (rGO) composites are primarily used.^{11,15,17,35} Besides the obvious benefits of such composite materials concerning their electrical characteristics, there is a major disadvantage. rGO is commonly synthesized from graphite via a modified Hummers method.³⁷ Until now, this method is not suitable for preparation of rGO on an industrial scale, preventing the use of this material in commercial batteries.³⁸ But the advantage of adding rGO to the electrode material was demonstrated for Cu and V sulfides. Pure copper sulfides showed a poor rate and cycle stability, e.g., 261 mAh g⁻¹ after

Received: April 4, 2017

Accepted: June 8, 2017

Published: June 8, 2017

20 cycles³⁹ and 41.8 mAh g⁻¹ after 100 cycles.⁴⁰ A similar behavior was reported for V₅S₈ displaying a continuous loss of capacity during cycling.⁴¹ In recently published papers, it was shown that binary copper or vanadium sulfides as anode materials for SIBs only showed good rate and cycle stability when using rGO composites.^{41–43}

The role of rGO in conversion electrodes is not fully understood, but it is assumed that the electrical contact between metallic nanoparticles formed during the first discharge is improved, thus leading to better cyclability. The role of rGO may be accomplished by electrically conducting nanoparticles which are generated using suitable ternary compounds. Because more phases are formed during the first Na or Li uptake, a more finely distributed nanostructure is generated with the constituents being in close contact. This might enable an improved cyclability and stability of the capacity, and therefore using ternary instead of binary compounds as starting materials might be beneficial to overcome the necessity of adding additives like rGO.

On the basis of these ideas, we investigated the electrochemical performance of CuV₂S₄ as a potential anode material for SIBs. The results demonstrate that the material exhibits an outstanding cycling stability and high specific capacity.

EXPERIMENTAL SECTION

Material Synthesis. The CuV₂S₄ sample was synthesized via a solid state reaction method. Stoichiometric amounts of copper (Alfa Aesar, 99.9%), vanadium (Chempur, 99.5+%), and sulfur (Chempur, 99.999%) were mixed together and ground in a mortar. The mixture was placed into a quartz tube and sealed under vacuum (<10⁻⁴ mbar). It was heated to 873 K at a rate of 100 K/h, maintained at this temperature for 24 h, and then heated up to 1123 K for an additional 5 days. The powder was pelletized, and the procedure described above was repeated.

Characterization of the Materials. XRD patterns were collected using Cu Kα₁ radiation with a Stoe Stadi-P equipped with a germanium monochromator and a Mythen 1K detector and with a Panalytical XPert Pro diffractometer equipped with a PIXCEL Detector. Rietveld refinement⁴⁴ of the powder pattern was performed with FULLPROF⁴⁵ using a pseudo-Voigt function with axial divergence asymmetry. Linear interpolation between a set of selected points was used to model the background. The lattice parameter *a* and all general atom positions were refined.

For *ex situ* XRD analysis the prepared electrodes or pellets of about 30 mg consisting of 70% CuV₂S₄ and 30% carbon black were used. The material was recovered from the Swagelok cells in an argon-filled glovebox and put onto an X-ray sample holder sealed with a Kapton window or in a quartz capillary with a diameter of 0.5 mm.

Transmission electron microscopy was performed on a FEI Tecnai F30 STWIN microscope on samples inserted with 2 Na and 6 Na. Samples were prepared by gentle grinding and dispersion on carbon-laced grids made out of molybdenum or gold to avoid overlap of Mo⁴⁺ and S²⁻ peaks in the EDX spectrum. EDX measurements and scanning TEM elemental maps were obtained with the attached EDAX SiLi detector with an energy resolution of 134 eV. The electron diffraction experiment was performed by limiting the area of diffraction by an aperture of 500 nm in diameter.

SEM images and EDX were obtained with a Philips ESEM XL 30 with EDAX New XL-30 detecting unit. Acceleration voltage of 20 kV was used to detect the K-lines.

²³Na magic-angle spinning (MAS) nuclear magnetic resonance (NMR) spectroscopy was performed on a Bruker spectrometer at a magnetic field of 4.7 T, corresponding to a Larmor frequency of 52.9 MHz. Sample spinning was done in 2.5 mm rotors at a spinning speed of 30 kHz. Spectra were acquired with a rotor-synchronized Hahn-echo pulse sequence with a $\pi/2$ pulse length of 2.3 μ s and a recycle delay of 1 s. The spectra were referenced to an aqueous solution of 1

M NaCl at 0 ppm. ⁶³Cu resonances observed during these ²³Na NMR measurements were additionally referenced to CuCl powder as a secondary reference (−333.2 ppm at 298 K).⁴⁶

Electrochemical Test. CuV₂S₄ electrodes were prepared from 80 wt % CuV₂S₄, 10 wt % SUPER C6S Carbon (Timcal, Switzerland), and 10 wt % PVdF (Solvay, Germany) suspended in NMP (*N*-methyl-2-pyrrolidone). The mixture was spread on a copper or aluminum foil using doctor-blade casting method. Drying of the electrode foil was carried out in a vacuum oven at 60 °C for 24 h. Afterward, 10 mm discs with about 2 mg/cm² active material were punched out. Assembly of the Swagelok type cells was carried out in an argon-filled glovebox with water and oxygen contents below 1 ppm using sodium metal as the anode, glass fiber filter disks (Whatman, United Kingdom), and Celgard membrane as separator and a solution of 1 M NaCF₃SO₃ (Sigma, 98%) in diethylene glycol dimethyl ether (Sigma, 99.5%, anhydrous) as electrolyte. Galvanostatic measurements were carried out with a Materials mates 510 DC or a MTI 8 channel battery analyzer. Cyclic voltametric measurements were carried out with a Zahner XPot at a scan rate of 0.1 mV s⁻¹ between 0.001 and 3 V.

RESULTS AND DISCUSSION

CuV₂S₄ has been intensively studied concerning its magnetic, electronic, and structural properties but not as an anode material in sodium or lithium ion batteries so far.^{47–54} CuV₂S₄ is a metallic thiospinel and crystallizes in the cubic space group *Fd* $\bar{3}m$. The copper cations occupy the tetrahedral 8a sites, the vanadium cations occupy the octahedral 16d sites, and sulfur is located on the 32e sites (inset Figure 1). In contrast to most

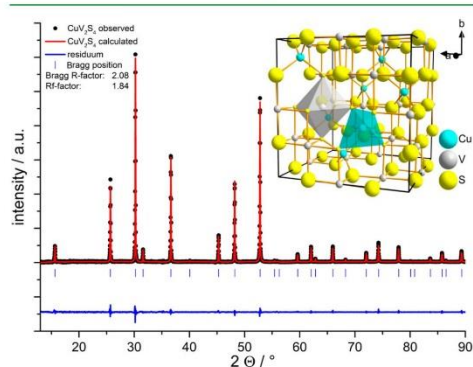


Figure 1. Rietveld refinement results of the XRD pattern of CuV₂S₄. Observed (dots), calculated (red), and difference (blue) profiles. Reflection positions are marked as vertical bars. The inset shows the spinel type unit cell.

spinel compounds with the general formula M₁²⁺M₂³⁺A₄²⁻ (M: metal cation; A: chalcogenide anion), copper has the oxidation state +1.^{54–56} Charge balance is achieved by a delocalized hole in the valence band.

The Rietveld refinement of the X-ray powder data reveals a phase pure material (Figure 1). The lattice parameter was determined as *a* = 9.796(9) Å, very close to the data reported in the literature.⁵⁰ Electron diffraction (ED) performed in a transmission electron microscope (TEM) shown in Figure S1A confirms the single crystallinity of CuV₂S₄ particles with the cubic *Fd* $\bar{3}m$ structure. The elemental analyses performed via energy dispersive X-ray spectroscopy (EDX) on a scanning electron microscope (SEM) and TEM yields a composition close to stoichiometric material (SEM EDX: Cu_{1.07}V₂S_{4.01},

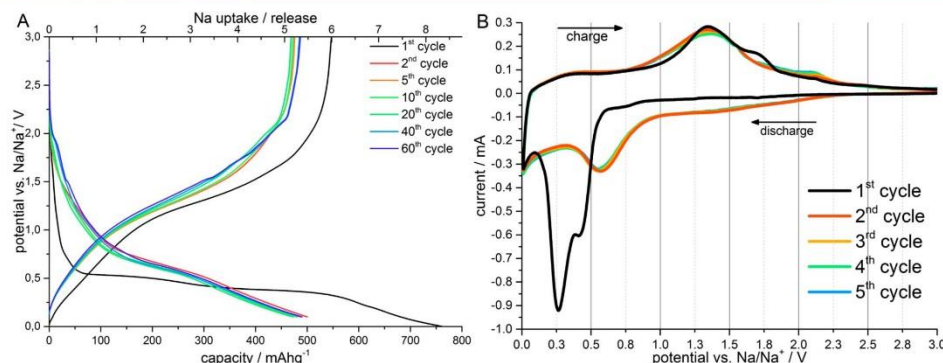


Figure 2. Electrochemical measurements of CuV_2S_4 against Na. (A) Galvanostatic charge/discharge curves at a current rate of 150 mA g^{-1} cycled from 3 to 0.1 V. (B) Cyclic voltammogram measurement with a scan rate of 0.1 mV s^{-1} cycled from 3 to 0.01 V.

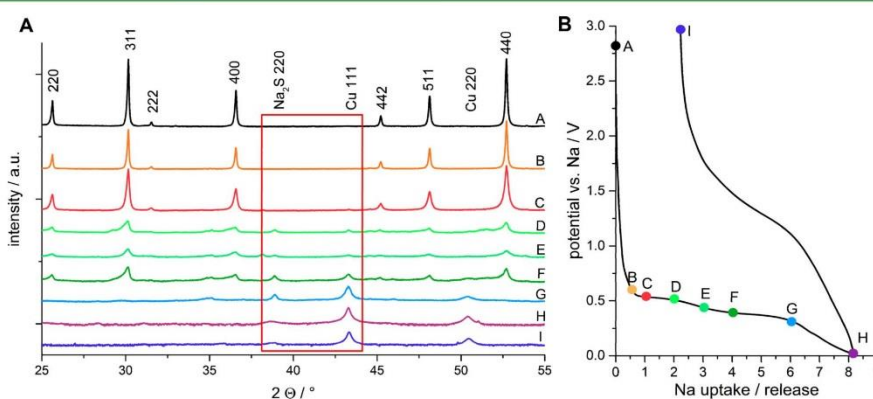


Figure 3. *Ex situ* XRD patterns of the CuV_2S_4 electrode collected at various points (A), as indicated in the corresponding charge–discharge profile (B).

Table S1; TEM EDX $\text{Cu}_{1.2}\text{V}_{1.84}\text{S}_{3.95}$ (Figures S1B and S2). SEM images show a broad size distribution of the as prepared particles between 5 and $50 \mu\text{m}$ (Figure S3).

Assuming a full conversion of the material with a reduction of Cu^+ and V^{3+} to their elemental state as shown in eq 1 and the uptake of one electron into the valence band hole, CuV_2S_4 has a theoretical specific capacity of 730 mAh g^{-1} .

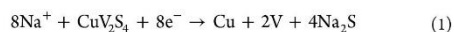


Figure 2a displays a selection of galvanostatic charge–discharge profiles of the CuV_2S_4 cell. Because of the use of a microcrystalline material and to ensure a full conversion of the electrode material in the first cycle, we choose a current density of 73 mA g^{-1} and a cutoff potential of 0.01 mV. During the subsequent cycles, the cell was cycled between 3 and 0.1 V at a current density of 150 mA g^{-1} to minimize electrolyte decomposition. The first discharge occurs stepwise, with a fast decrease of the voltage at the beginning followed by a first plateau at 0.55 V until two Na are inserted. Another not well-pronounced voltage drop leads to the pseudoplateau in the

region of 0.4–0.3 V. After the insertion of six Na the voltage steadily decreases until the cutoff of 0.01 V is reached. A very similar behavior was reported for the Li insertion into CuCr_2Se_4 ⁵⁷ and CuTi_2S_4 , but in this case the materials showed a severe capacity loss for every cycle.³⁶

The voltage profiles (Figure 2A) demonstrate a highly reversible process involving the uptake of about 8 Na per formula unit upon the first discharge in which a capacity of 753 mAh g^{-1} has been achieved, followed by the removal of 6 Na during the charge process. The first discharge capacity is slightly larger than the theoretically expected value caused by solid electrolyte interphase (SEI) formation and electrolyte decomposition. The irreversible capacity loss is 207 mAh g^{-1} , yielding an efficiency of 72.5% in the first cycle. From the third cycle an efficiency >99% is achieved.

The cyclic voltammetry (CV) curves are displayed in Figure 2B. In the first cycle two strong reduction peaks at 0.41 and 0.28 V and one weak reduction signal from 0.6 to 0.8 V are visible. During charge two broad oxidation peaks at 1.4 and 1.75 V are observed in accordance with the plateaus of the galvanostatic measurement. The shift of the reduction peak in

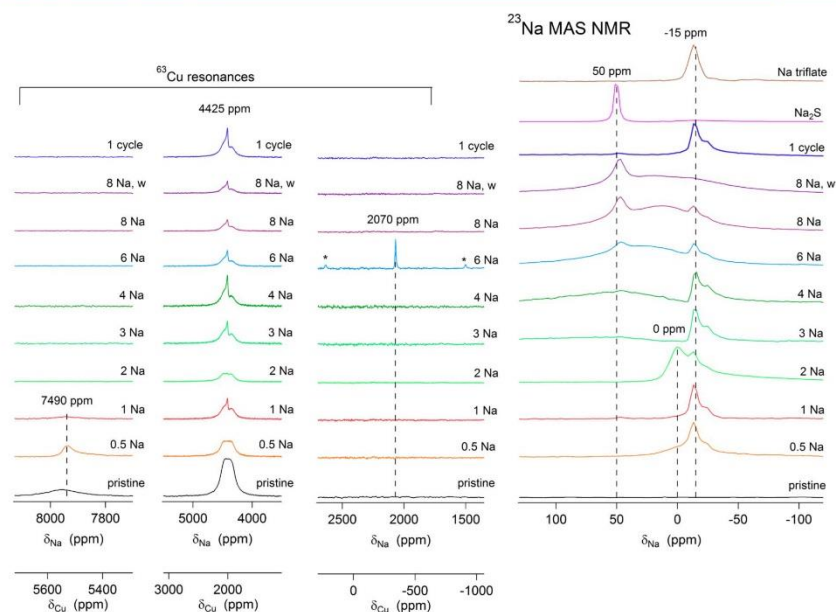


Figure 4. ^{23}Na MAS NMR spectra of CuV_2S_4 for different Na contents obtained during discharging and charging against Na metal. The sample with 8 Na washed with diglyme/*n*-hexane is labeled with "8 Na w." The spectra of Na_2S and Na triflate are shown for comparison at the top.

the CV cycle can be explained by the larger overpotential within the cell due to the higher current density. Considering the *ex situ* XRD and ^{23}Na MAS NMR measurements (Figures 3 and 4, see above), the first reduction event at 0.41 V can be attributed to the reduction of Cu^+ . The broad peak from 0.6 to 0.8 V may be caused by the first SEI formation. The following strong reduction peak is due to the conversion reaction. A not well developed small shoulder at 0.15 V occurs which might be caused by a second formation of a SEI due to the volume expansion during the conversion reaction. The reduction event near 0 V can be explained by electrolyte decomposition. The following cycles strongly differ from the first one showing a very broad reduction peak at 1.4 V and a more pronounced signal at 0.45 V. This behavior is typical for conversion reactions due to irreversible processes occurring during the first cycle. The oxidation peak at 1.4 V is still visible, whereas the oxidation peak at 1.75 V vanished and a new oxidation signal occurs at 2.1 V. The second to fifth cycle are nearly superimposable, indicating a very good reversibility of the electrode material.

Figure 3A displays *ex situ* XRPD patterns collected at the different voltages during the electrochemical discharge/charge reaction marked in Figure 3B. The reduction of Cu^+ to elemental Cu is observed by the appearance of the (111) reflection of Cu after an uptake of 1 Na (a magnification is shown in Figure S4). Besides the formation of Na_2S , an intermediate phase can be observed at point D (2 Na) and gets more pronounced after the uptake of 3 Na per formula unit. The broad reflections cannot be unambiguously assigned to a distinct compound because most vanadium sulfides show the most intense reflections in this region (Figure S5). The

formation of Na_2S was confirmed by additional *ex situ* XRD (Figure S6) and ^{23}Na MAS NMR (Figure 4). Because of an overlap of reflections of CuV_2S_4 and the intermediate phase Rietveld refinements of the occupancies of Cu and V were not unambiguous after uptake of more than 2 Na per formula unit. But the refinements clearly show a decrease of Cu occupancy already for samples with 0.5 and 1 Na per formula unit. The refined lattice parameters for these two materials are identical with $a = 9.811(1)$ Å (0.5 Na) and $a = 9.811(2)$ Å (1 Na), but an increase of the strain can be observed for larger Na uptake (e_0 from strain: 0.00046 (0.5 Na), 0.00112 (1 Na), and 0.00137 (2 Na)). For the sample with 2 Na per formula unit a slight decrease of the a -axis to 9.799(3) Å is obtained. Interestingly, the lattice parameter does not change after uptake of 0.5 and 1 Na but is slightly larger than for the pristine material ($a = 9.796(9)$ Å). This small expansion of the cell parameter can be explained by the uptake of an electron into the valence band hole in the early stage of discharge leading to a slightly larger sulfur anion radius overcompensating the loss of Cu^+ as observed in XRD patterns (Figure S3). A similar behavior was observed for the uptake of Li in CuCr_2Se_4 .⁵⁷

The successive conversion of CuV_2S_4 is revealed by a constant decrease of the intensity and broadening of the reflections after an uptake of 2 Na. The broadening is most likely caused by a reduction of the size of coherently scattering domains during the conversion reaction. During further Na uptake, the intensity of reflections of Na_2S and Cu steadily increases. At the fully discharged state the electrode material is converted to an X-ray amorphous phase or into particles being too small to be detected by X-ray diffraction, and only the Cu-related reflections (111) and (200) as well as the (220)

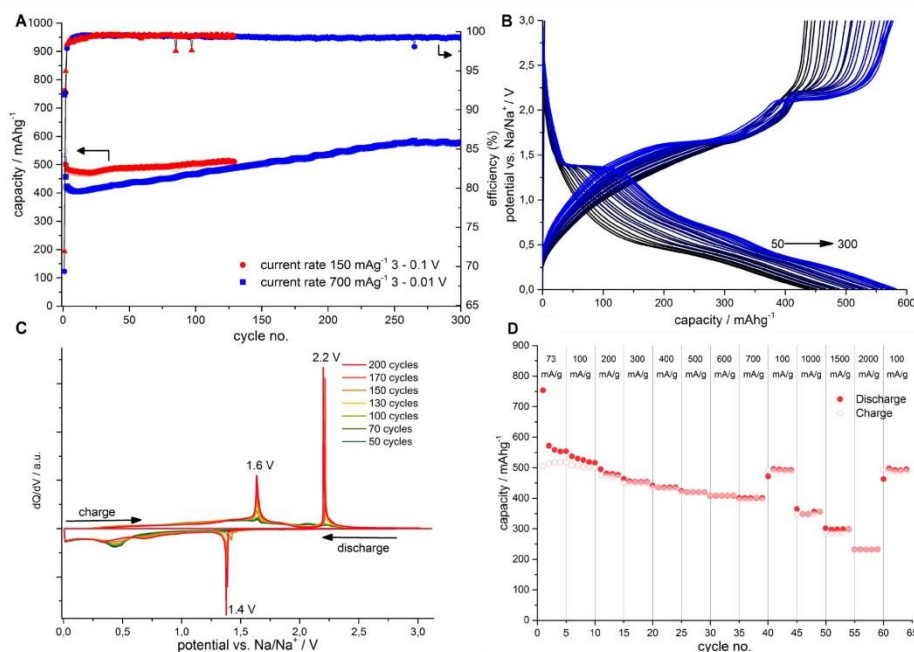


Figure 5. (A) Cycling performance and charge efficiency of CuV₂S₄ cells, using galvanostatic cycling at 0.15 Ag⁻¹ between 3 and 0.1 V and 3 and 0.01 V at 0.7 Ag⁻¹ (B) Discharge–charge profile evolution of CuV₂S₄ cycling at 0.7 Ag⁻¹ between 3 and 0.1 V for the 50th to 300th cycle. Every 10th cycle is displayed. (C) dQ/dV analysis for selected cycles. (D) Rate capability at various current densities from 0.073 to 2 A g⁻¹.

reflection of Na₂S are visible. No recrystallization of CuV₂S₄ can be observed during charge. The crystallite size of the metallic Cu particles is estimated by Scherrer's formula to be in the range of 20 nm. It is remarkable that the Cu⁺ ions are reduced to nanocrystalline particles, while the V³⁺ ions are converted into an X-ray amorphous phase or nano-sized particles which could not be seen in the XRD patterns. At the fully charged state (point I in Figure 3) the intensity of the Na₂S reflection decreased, whereas the reflections of elemental Cu are still clearly visible.

The ²³Na MAS NMR spectra of CuV₂S₄ are shown in Figure 4 for different Na contents. In all NMR spectra, a peak is visible at about -15 ppm which can be assigned to residues of the Na salt of the electrolyte used in the batteries (Na triflate). For a sample washed with diglyme/*n*-hexane this signal cannot be observed. After uptake of 2 Na per formula unit, a new peak is visible at 0 ppm which can be assigned to an intermediate unknown phase since for further cycling this signal disappears again. When the Na content is further increased, a broad component emerges in the range between +70 and -50 ppm. Furthermore, for Na contents larger than 6 per formula unit, a narrower peak is observed at +50 ppm. This signal can clearly be assigned to the formation of Na₂S during discharging. When the material is charged again, the peak at +50 ppm disappears, revealing the reversibility of Na₂S formation. The weak peak at -25 ppm could not be clearly identified, but since it seems to be correlated to the peak of Na triflate, it might be an electrolyte decomposition product.

It is remarkable that additional signals can be observed at very large positive shifts, shown on the left side of Figure 4. For the pristine material and a Na content of 0.5 one broad peak is clearly visible at 7490 ppm, which then becomes much weaker and even broader at a content of 1 Na and for larger Na contents disappears completely. This signal is caused by a ⁶³Cu resonance because the resonance frequencies of ²³Na and ⁶³Cu are very similar (52.9 and 53.0 MHz, respectively, at 4.7 T). Both ²³Na and ⁶³Cu have a nuclear spin *I* = 3/2 and thus experience quadrupolar interactions with electric field gradients being present at the site of these nuclei. This interaction accounts for some of the observed line broadenings and spinning sidebands. The presence of the signal at 7490 ppm in the pristine material and at very low Na contents is generated by the presence of Cu⁺. This confirms the *ex situ* XRD measurement results which demonstrated that Cu⁺ is reduced to the metallic form during the uptake of 2 Na. A very broad signal is present at +4400 ppm. This signal belongs to metallic Cu, and it stems from the NMR RF coil which is made of Cu and which is located around the sample. The large positive shift is a so-called Knight shift caused by the interactions of the ⁶³Cu nuclei with delocalized electrons in the metal. For the cycled samples (and *only* for the cycled samples) on top of this broad peak another signal with much smaller width is visible. This signal belongs again to metallic Cu, but this time it represents the metallic Cu that is formed inside the sample during discharging. While the broad signal stems from the static RF coil, the narrow signal can be clearly assigned to the rotating

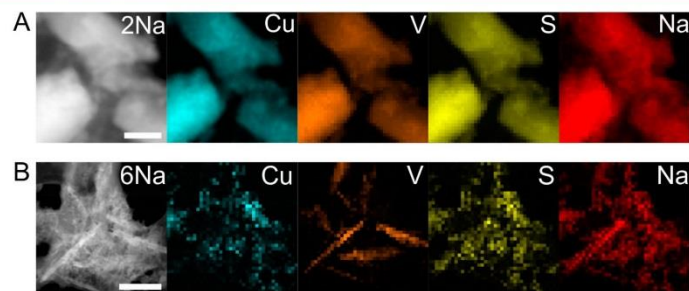


Figure 6. Scanning TEM images (first column) and corresponding EDX elemental maps of the pristine material after the uptake of (A) 2 Na and (B) 6 Na. The scale bars show 200 nm and 1 μm , respectively.

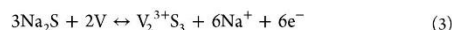
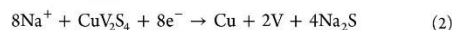
sample. Furthermore, for the sample obtained after conversion of 6 Na, a narrow signal at 2070 ppm is visible with clear spinning sidebands (marked with an asterisk). This clearly shows that this signal stems from the sample and the position shows that it is generated from a diamagnetic Cu environment, i.e., Cu^{1+} far away from V neighbors. This signal is thus assigned to Cu_2S . It disappears after further conversion of Na. Cu_2S thus represents an intermediate phase which is further converted to Na_2S and metallic Cu during further discharging. The NMR spectrum obtained after one complete cycle also confirms that the initial CuV_2S_4 phase is not re-formed.

The cycling performance of the CuV_2S_4 electrodes at different current rates and cutoff potentials is presented in Figure 5A. In both cases, the tested cells reach a Coulombic efficiency of $\approx 99\%$ after the third cycle with a capacity of 490 mAh g^{-1} at 0.15 Ag^{-1} and 410 mAh g^{-1} at 0.7 Ag^{-1} . These values correspond to 5.4 $\text{Na/CuV}_2\text{S}_4$ and 4.5 $\text{Na/CuV}_2\text{S}_4$, respectively. The cells show a constant gain in capacity during the first 50 cycles which is not accompanied by a change in the discharge–charge profile as can be seen in Figure 2A. This behavior might be explained by remaining inactive electrode material throughout the first cycles due to blocked diffusion pathways for Na. By repeated cycling, a more homogeneous distribution of the involved elements is achieved that might enable a better Na diffusion to the former inactive parts of the electrode. On higher cycle numbers, a change in the discharge–charge profile becomes visible (Figure 5B), which is clearly seen by the dQ/dV analysis displayed in Figure 5C. A new plateau at about 1.35 V evolves during the discharge and two plateaus at 1.65 V and around 2.2 V during charge occur which become more pronounced with increasing cycle number. These observations indicate a change of the reaction mechanism. This suggests that the former inactive Na_2S matrix starts to participate in the redox process leading to a constant capacity increase up to 580 mAh g^{-1} (6.4 Na per formula unit can be cycled) at 700 mA g^{-1} for the 250th cycle, remaining constant at this level during the next 50 cycles.

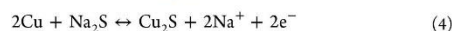
It is known that upon cycling of sulfide based materials against Na or Li, Na_2S_x or Li_2S_x species are formed which are soluble in the electrolyte. It was reported that the addition of metallic Cu powder into a lithium sulfur battery system captures intermediate polysulfides by formation of Cu_xS ($x = 1$ or 2) depending on the chain length of polysulfides.⁵⁸ It is very likely that this process can also take place in a Na based system. Since we have shown the presence of metallic Cu via *ex situ* XRD measurements, we assume that Cu_2S is formed during

higher cycle numbers. This assumption is supported by the dQ/dV analysis in Figure 5C. The potential profile of the evolving cathodic and anodic peaks are in very good agreement with the reduction and oxidation of Cu_2S , leading to a gain in capacity.^{39,43,59,60} This assumption is supported by additional *ex situ* XRD measurements (Figure S7) recorded after 100 cycles showing a loss in intensity of the Cu reflections while new broad reflections of Cu_{2-x}S appeared. We note that this phenomenon was observed in all cells tested during this study and has never been reported for transition metal sulfides in sodium ion batteries until now.

Considering the results of the investigations and analyses in this work, we assume the following reactions for the first discharge (eq 2) and charge (eq 3). Based on our results, most probably a V(III) sulfide is formed during the charge process according to eq 3.



During higher cycle numbers a small amount of the Cu starts participating in the sodiation process, and two different reactions may be envisaged including a reversible formation of Cu_2S and Cu (e.g., eq 4)



or an intercalation reaction as proposed in ref 56 (eq 5)

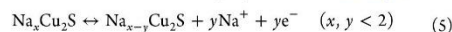


Figure 5D displays the rate performance of CuV_2S_4 at different C-rates. The cell delivered a reversible capacity of 500, 473, 453, 435, 420, 410, 400, 350, 300, and 232 mAh g^{-1} for current densities ranging from 100 to 2000 mA g^{-1} . When the current density is reset to 100 mA g^{-1} , a capacity of 500 mAh g^{-1} could be recovered. This high rate stability is remarkable since we investigated a bare, non-graphene/rGO composite material with only 10 wt % carbon black added to the electrode slurry.

The elemental mapping using scanning (S)TEM EDX for the analysis of Cu, V, S, and Na content after the uptake of 2 Na and 6 Na in the pristine material is presented in Figure 6. After the uptake of 2 Na (A) the elemental maps of remaining crystalline material confirm the presence of so far inactive pristine material. However, the lateral distribution of Na is more extended which is explainable by SEI formation and the electrolyte slurry encapsulating the microcrystals. However,

special care in interpretation of the Na signal has to be taken into account since the intensity of the Na^K (1.04 keV) peak might be enhanced due to the nearby Cu^L (0.93 keV) peak and its L^{β3} (1.02 keV) transition as indicated in Figure S1B. A clear decomposition of the crystallite structures is observable after the uptake of 6 Na (B). From the elemental maps the separation of V from equal distributed Cu and S is apparent, forming low quality crystals which are sensitive for crystallization processes under the electron beam. Certain correlations with respect to the distribution of the elements were found for Cu with S and Na signals supporting the arguments of Cu₂S or Na_xCu₂S formation from pure metallic Cu particles. However, clear evidence for the presence of pure metallic Cu may be inhibited due to electron beam induced reaction.

Compared to other sulfides and composites CuV₂S₄ exhibits an excellent performance as anode material. For MoS₂ on amorphous carbon nanotubes a reversible capacity of 461 mAh g⁻¹ was obtained after 150 cycles (current density: 500 mA g⁻¹).⁶¹ About 450 mAh g⁻¹ was obtained for WS₂ nanosheets after 50 cycles at 0.1 A g⁻¹.⁶² For FeS₂ a capacity of 170 mAh g⁻¹ was reported for a current density of 20 A g⁻¹ and a value of about 200 mAh g⁻¹ was obtained at 1 A g⁻¹.⁶³ Composites of layered nickel sulfide and reduced graphene oxide achieved a maximum reversible specific capacity of about 392 mAh g⁻¹ (current density: 100 mA g⁻¹) after 50 cycles with a high rGO content of 35 wt %.⁶⁴ VS₄ on rGO delivered a reversible capacity of 362 mAh g⁻¹ at 100 mA g⁻¹.⁴² In a recently published paper dealing with chemically exfoliated V₅S₈ and graphite-V₅S₈ hybrid nanosheets comparable capacities were achieved for the hybrid material (496 mAh g⁻¹ at 1 A g⁻¹ after 500 cycles), whereas the graphite free material showed a constant loss of the capacity (<100 mAh g⁻¹ at 1 A g⁻¹ after 500 cycles).⁴¹ These comparisons impressively demonstrate the outstanding performance of CuV₂S₄ as anode material in SIBs.

CONCLUSION

We demonstrated that CuV₂S₄ is an excellent anode material for sodium ion storage. A superior high and stable capacity of 580 mAh g⁻¹ is achieved at high C rates in the 300th cycle. The evolution of nanocrystalline metallic Cu particles during the first discharge leads to an improved electron transport, which explains the superior rate stability compared to other transition metal sulfides. We also demonstrated a unique phenomenon of a change of the charge/discharge profiles occurring at later stages of cycling. Most probably, Cu_{2-x}S is formed hindering dissolution of polysulfide species in the electrolyte, thus preventing capacity fading caused by this phenomenon.²³ Na NMR spectra and XRD patterns of the discharged anode material clearly evidence the formation of Na₂S and metallic Cu. During the charge process Na₂S disappears while nanocrystalline Cu is still present.

ASSOCIATED CONTENT

Supporting Information

The Supporting Information is available free of charge on the ACS Publications website at DOI: 10.1021/acsami.7b04739.

TEM electron diffraction pattern, TEM-EDX and EDX measurements, additional *ex situ* XRD powder patterns (PDF)

AUTHOR INFORMATION

Corresponding Author

*E-mail: wbensch@ac.uni-kiel.de (W.B.).

ORCID

Sylvio Indris: 0000-0002-5100-113X

Wolfgang Bensch: 0000-0002-3111-580X

Notes

The authors declare no competing financial interest.

REFERENCES

- Panwar, N. L.; Kaushik, S. C.; Kothari, S. Role of Renewable Energy Sources in Environmental Protection: A Review. *Renewable Sustainable Energy Rev.* **2011**, *15*, 1513–1524.
- Larcher, D.; Tarascon, J.-M. Towards Greener and More Sustainable Batteries for Electrical Energy Storage. *Nat. Chem.* **2014**, *7*, 19–29.
- Slater, M. D.; Kim, D.; Lee, E.; Johnson, C. S. Sodium-Ion Batteries. *Adv. Funct. Mater.* **2013**, *23*, 947–958.
- Yabuuchi, N.; Kubota, K.; Dahbi, M.; Komaba, S. Research Development on Sodium-Ion Batteries. *Chem. Rev.* **2014**, *114*, 11636–11682.
- Pan, H.; Hu, Y.-S.; Chen, L. Room-Temperature Stationary Sodium-Ion Batteries for Large-Scale Electric Energy Storage. *Energy Environ. Sci.* **2013**, *6*, 2338–2360.
- Ong, S. P.; Chevrier, V. L.; Hautier, G.; Jain, A.; Moore, C.; Kim, S.; Ma, X.; Ceder, G. Voltage, Stability and Diffusion Barrier Differences between Sodium-Ion and Lithium-Ion Intercalation Materials. *Energy Environ. Sci.* **2011**, *4*, 3680–3688.
- Luo, W.; Shen, F.; Bommier, C.; Zhu, H.; Ji, X.; Hu, L. Na-Ion Battery Anodes: Materials and Electrochemistry. *Acc. Chem. Res.* **2016**, *49*, 231–240.
- Newman, G. H. Ambient Temperature Cycling of an Na-TiS₂ Cell. *J. Electrochem. Soc.* **1980**, *127*, 2097.
- Zhu, C.; Mu, X.; van Aken, P. A.; Yu, Y.; Maier, J. Single-Layered Ultrasmall Nanoplates of MoS₂ Embedded in Carbon Nanofibers with Excellent Electrochemical Performance for Lithium and Sodium Storage. *Angew. Chem.* **2014**, *126*, 2184–2188.
- Wang, Y.-X.; Seng, K. H.; Chou, S.-L.; Wang, J.-Z.; Guo, Z.; Wexler, D.; Liu, H.-K.; Dou, S.-X. Reversible Sodium Storage via Conversion Reaction of a MoS₂ – C Composite. *Chem. Commun.* **2014**, *50*, 10730.
- Choi, S. H.; Kang, Y. C. Sodium Ion Storage Properties of WS₂-Decorated Three-Dimensional Reduced Graphene Oxide Microspheres. *Nanoscale* **2015**, *7*, 3965–3970.
- Douglas, A.; Carter, R.; Oakes, L.; Share, K.; Cohn, A. P.; Pint, C. L. Ultrafine Iron Pyrite (FeS₂) Nanocrystals Improve Sodium-Sulfur and Lithium-Sulfur Conversion Reactions for Efficient Batteries. *ACS Nano* **2015**, *9*, 11156–11165.
- Zhu, Y.; Suo, L.; Gao, T.; Fan, X.; Han, F.; Wang, C. Ether-Based Electrolyte Enabled Na/FeS₂ Rechargeable Batteries. *Electrochem. Commun.* **2015**, *54*, 18–22.
- Walter, M.; Zünd, T.; Kovalenko, M. V. Pyrite (FeS₂) Nanocrystals as Inexpensive High-Performance Lithium-Ion Cathode and Sodium-Ion Anode Materials. *Nanoscale* **2015**, *7*, 9158–9163.
- Du, Y.; Zhu, X.; Zhou, X.; Hu, L.; Dai, Z.; Bao, J. Co₂S₃ Porous Nanosheets Embedded in Graphene Sheets as High-Performance Anode Materials for Lithium and Sodium Storage. *J. Mater. Chem. A* **2015**, *3*, 6787–6791.
- Kim, J.-S.; Ahn, H.-J.; Ryu, H.-S.; Kim, D.-J.; Cho, G.-B.; Kim, K.-W.; Nam, T.-H.; Ahn, J. H. The Discharge Properties of Na/Ni₃S₂ Cell at Ambient Temperature. *J. Power Sources* **2008**, *178*, 852–856.
- Qu, B.; Ma, C.; Ji, G.; Xu, C.; Xu, J.; Meng, Y. S.; Wang, T.; Lee, J. Y. Layered SnS₂-Reduced Graphene Oxide Composite - A High-Capacity, High-Rate, and Long-Cycle Life Sodium-Ion Battery Anode Material. *Adv. Mater.* **2014**, *26*, 3854–3859.
- Sun, W.; Rui, X.; Yang, D.; Sun, Z.; Li, B.; Zhang, W.; Zong, Y.; Madhavi, S.; Dou, S.; Yan, Q. Two-Dimensional Tin Disulfide

- Nanosheets for Enhanced Sodium Storage. *ACS Nano* **2015**, *9*, 11371–11381.
- (19) Hou, H.; Jing, M.; Huang, Z.; Yang, Y.; Zhang, Y.; Chen, J.; Wu, Z.; Ji, X. One-Dimensional Rod-Like Sb_2S_3 -Based Anode for High-Performance Sodium-Ion Batteries. *ACS Appl. Mater. Interfaces* **2015**, *7*, 19362–19369.
- (20) Zhu, Y.; Nie, P.; Shen, L.; Dong, S.; Sheng, Q.; Li, H.; Luo, H.; Zhang, X. High Rate Capability and Superior Cycle Stability of a Flower-like Sb_2S_3 Anode for High-Capacity Sodium Ion Batteries. *Nanoscale* **2015**, *7*, 3309–3315.
- (21) Hwang, S. M.; Kim, J.; Kim, Y.; Kim, Y. Na-Ion Storage Performance of Amorphous Sb_2S_3 Nanoparticles: Anode for Na-Ion Batteries and Seawater Flow Batteries. *J. Mater. Chem. A* **2016**, *4*, 17946–17951.
- (22) Wang, Y.; Wang, M.; Chen, G.; Dong, C.; Wang, Y.; Fan, L.-Z. Surfactant-Mediated Synthesis of ZnCo_2O_4 Powders as a High-Performance Anode Material for Li-Ion Batteries. *Ionics* **2015**, *21*, 623–628.
- (23) Wang, N.; Ma, X.; Wang, Y.; Yang, J.; Qian, Y. Porous MnFe_2O_4 Microrods as Advanced Anodes for Li-Ion Batteries with Long Cycle Lifespan. *J. Mater. Chem. A* **2015**, *3*, 9550–9555.
- (24) Zhang, W.; Hou, X.; Lin, Z.; Yao, L.; Wang, X.; Gao, Y.; Hu, S. Hollow Microspheres and Nanoparticles MnFe_2O_4 as Superior Anode Materials for Lithium Ion Batteries. *J. Mater. Sci.: Mater. Electron.* **2015**, *26*, 9535–9545.
- (25) Xing, Z.; Ju, Z.; Yang, J.; Xu, H.; Qian, Y. One-Step Solid State Reaction to Selectively Fabricate Cubic and Tetragonal CuFe_2O_4 Anode Material for High Power Lithium Ion Batteries. *Electrochim. Acta* **2013**, *102*, 51–57.
- (26) Brown, Z. L.; Smith, S.; Obrovac, M. N. Mixed Transition Metal Titanate and Vanadate Negative Electrode Materials for Na-Ion Batteries. *J. Electrochem. Soc.* **2015**, *162*, A15–A20.
- (27) Kang, W.; Tang, Y.; Li, W.; Yang, X.; Xue, H.; Yang, Q.; Lee, C.-S. High Interfacial Storage Capability of Porous $\text{NiMn}_2\text{O}_4/\text{C}$ Hierarchical Tremella-like Nanostructures as the Lithium Ion Battery Anode. *Nanoscale* **2015**, *7*, 225–231.
- (28) Courtel, F. M.; Duncan, H.; Abu-Lebdeh, Y.; Davidson, I. J. High Capacity Anode Materials for Li-Ion Batteries Based on Spinel Metal Oxides AMn_2O_4 (A = Co, Ni, and Zn). *J. Mater. Chem.* **2011**, *21*, 10206.
- (29) Yao, X.; Kong, J.; Tang, X.; Zhou, D.; Zhao, C.; Zhou, R.; Lu, X. Facile Synthesis of Porous CoFe_2O_4 Nanosheets for Lithium-Ion Battery Anodes with Enhanced Rate Capability and Cycling Stability. *RSC Adv.* **2014**, *4*, 27488.
- (30) Yoon, S. Facile Microwave Synthesis of CoFe_2O_4 Spheres and Their Application as an Anode for Lithium-Ion Batteries. *J. Appl. Electrochem.* **2014**, *44*, 1069–1074.
- (31) Wu, X.; Li, S.; Wang, B.; Liu, J.; Yu, M. Controllable Synthesis of Micro/nano-Structured MnCo_2O_4 with Multiporous Core-shell Architectures as High-Performance Anode Materials for Lithium-Ion Batteries. *New J. Chem.* **2015**, *39*, 8416–8423.
- (32) Lavela, P.; Tirado, J. L. CoFe_2O_4 and NiFe_2O_4 Synthesized by Sol-gel Procedures for Their Use as Anode Materials for Li Ion Batteries. *J. Power Sources* **2007**, *172*, 379–387.
- (33) Bhattacharjya, D.; Sinhamahapatra, A.; Ko, J.-J.; Yu, J.-S. High Capacity and Exceptional Cycling Stability of Ternary Metal Sulfide Nanorods as Li Ion Battery Anodes. *Chem. Commun.* **2015**, *51*, 13350–13353.
- (34) Krengel, M.; Adelhelm, P.; Klein, F.; Bensch, W. FeV_2S_4 as a High Capacity Electrode Material for Sodium-Ion Batteries. *Chem. Commun.* **2015**, *51*, 13500–13503.
- (35) Choi, S. H.; Kang, Y. C. Synergetic Compositional and Morphological Effects for Improved Na^+ Storage Properties of $\text{Ni}_3\text{Co}_2\text{S}_6$ -Reduced Graphene Oxide Composite Powders. *Nanoscale* **2015**, *7*, 6230–6237.
- (36) Bodenez, V.; Dupont, L.; Morcrette, M.; Surcin, C.; Murphy, D. W.; Tarascon, J.-M. Copper Extrusion/Reinjection in Cu-Based Thiopins by Electrochemical and Chemical Routes. *Chem. Mater.* **2006**, *18*, 4278–4287.
- (37) Hummers, W. S., Jr.; Offeman, R. E. Preparation of Graphitic Oxide. *J. Am. Chem. Soc.* **1958**, *80*, 1339–1339.
- (38) Raccichini, R.; Varzi, A.; Passerini, S.; Scrosati, B. The Role of Graphene for Electrochemical Energy Storage. *Nat. Mater.* **2014**, *14*, 271–279.
- (39) Kim, J.-S.; Kim, D.-Y.; Cho, G.-B.; Nam, T.-H.; Kim, K.-W.; Ryu, H.-S.; Ahn, J.-H.; Ahn, H.-J. The Electrochemical Properties of Copper Sulfide as Cathode Material for Rechargeable Sodium Cell at Room Temperature. *J. Power Sources* **2009**, *189*, 864–868.
- (40) Shi, B.; Liu, W.; Zhu, K.; Xie, J. Synthesis of Flower-like Copper Sulfides Microspheres as Electrode Materials for Sodium Secondary Batteries. *Chem. Phys. Lett.* **2017**, *677*, 70–74.
- (41) Yang, C.; Ou, X.; Xiong, X.; Zheng, F.; Hu, R.; Chen, Y.; Liu, M.; Huang, K. V_2S_5 - graphite Hybrid Nanosheets as a High Rate-Capacity and Stable Anode Material for Sodium-Ion Batteries. *Energy Environ. Sci.* **2017**, *10*, 107–113.
- (42) Sun, R.; Wei, Q.; Li, Q.; Luo, W.; An, Q.; Sheng, J.; Wang, D.; Chen, W.; Mai, L. Vanadium Sulfide on Reduced Graphene Oxide Layer as a Promising Anode for Sodium Ion Battery. *ACS Appl. Mater. Interfaces* **2015**, *7*, 20902–20908.
- (43) Li, J.; Yan, D.; Lu, T.; Qin, W.; Yao, Y.; Pan, L. Significantly Improved Sodium-Ion Storage Performance of CuS Nanosheets Anchored into Reduced Graphene Oxide with Ether-Based Electrolyte. *ACS Appl. Mater. Interfaces* **2017**, *9*, 2309–2316.
- (44) Rietveld, H. M. A Profile Refinement Method for Nuclear and Magnetic Structures. *J. Appl. Crystallogr.* **1969**, *2*, 65–71.
- (45) Rodriguez-Carvajal, J. Recent Advances in Magnetic Structure Determination by Neutron Powder Diffraction. *Phys. B (Amsterdam, Neth.)* **1993**, *192*, 55–69.
- (46) Yu, H.; Tan, X.; Bernard, G. M.; Terskikh, V. V.; Chen, J.; Wasylshen, R. E. Solid-State ^{63}Cu , ^{65}Cu , and ^{31}P NMR Spectroscopy of Photoluminescent Copper(I) Triazole Phosphine Complexes. *J. Phys. Chem. A* **2015**, *119*, 8279–8293.
- (47) Hahn, H.; De Lorent, C.; Harder, B. Untersuchungen über ternäre Chalkogenide. VIII. über die Struktur des CuV_2S_4 , CuCr_2S_4 , CuCr_2Se_4 und CuCr_2Te_4 . *Z. Anorg. Allg. Chem.* **1956**, *283*, 138–142.
- (48) Kawaguchi, S.; Ishibashi, H.; Tsuji, N.; Kim, J.; Kato, K.; Takata, M.; Kubota, Y. Structural Properties in Incommensurately Modulated Spinel Compound CuV_2S_4 . *J. Phys. Soc. Jpn.* **2013**, *82*, 064603.
- (49) Okada, H.; Koyama, K.; Nakatake, M.; Shimada, K.; Namatame, H.; Taniguchi, M.; Watanabe, K. Photoemission Spectroscopy of Spinel-Type CuV_2S_4 Single Crystal. *J. Phys. Soc. Jpn.* **2008**, *77*, 114711.
- (50) Müttsch, M.; Krimmel, A.; Koza, M. M.; Mutka, H.; Horn, S. Neutron Scattering Study on CuV_2S_4 and CuTi_2S_4 . *Phys. B (Amsterdam, Neth.)* **2006**, *378–380*, 1070–1071.
- (51) Horny, R.; Klimm, S.; Klemm, M.; Ebbinghaus, S.; Eicklering, G.; Horn, S. Electronic Transport and Structural Properties of Electronically Correlated CuV_2S_4 . *J. Magn. Mater.* **2004**, *272–276*, E307–E309.
- (52) Lu, Z. W.; Klein, B. M.; Kurmaev, E. Z.; Cherkashenko, V. M.; Galakhov, V. R.; Shamin, S. N.; Yarmoshenko, Y. M.; Trofimova, V. A.; Neumann, M.; Furubayashi, T. others. Electronic Structure of CuV_2S_4 . *Phys. Rev. B: Condens. Matter Mater. Phys.* **1996**, *53*, 9626.
- (53) Sekine, T.; Uchinokura, K.; Iimura, H.; Yoshizaki, R.; Matsuura, E. Electrical and Thermal Properties in CuV_2S_4 . *Solid State Commun.* **1984**, *51*, 187–189.
- (54) Mähli, D.; Pickardt, J.; Reuter, B. Züchtung Und Untersuchung von Einkristallen Einiger Ternärer Und Quaternärer Kupferthiospinelle. *Z. Anorg. Allg. Chem.* **1982**, *491*, 203–207.
- (55) Riedel, E.; Horvath, E. Kationen-anionen-abstände in Kupfer- und Chromthiospinellen. *Mater. Res. Bull.* **1973**, *8*, 973–982.
- (56) Folmer, J. C.; Jellinek, F. The Valence of Copper in Sulphides and Selenides: An X-Ray Photoelectron Spectroscopy Study. *J. Less-Common Met.* **1980**, *76*, 153–162.
- (57) Bensch, W.; Opey, J.; Hain, H.; Gesswein, H.; Chen, D.; Mönig, R.; Gruber, P. A.; Indris, S. Chemical and Electrochemical Insertion of Li into the Spinel Structure of CuCr_2Se_4 : Ex Situ and in Situ Observations by X-Ray Diffraction and Scanning Electron Microscopy. *Phys. Chem. Chem. Phys.* **2012**, *14*, 7509.

(58) Jia, L.; Wu, T.; Lu, J.; Ma, L.; Zhu, W.; Qiu, X. Polysulfides Capture-Copper Additive for Long Cycle Life Lithium Sulfur Batteries. *ACS Appl. Mater. Interfaces* **2016**, *8*, 30248–30255.

(59) Fu, Y.; Manthiram, A. Electrochemical Properties of Cu_2S with Ether-Based Electrolyte in Li-Ion Batteries. *Electrochim. Acta* **2013**, *109*, 716–719.

(60) Lai, C.-H.; Huang, K.-W.; Cheng, J.-H.; Lee, C.-Y.; Hwang, B.-J.; Chen, L.-J. Direct Growth of High-Rate Capability and High Capacity Copper Sulfide Nanowire Array Cathodes for Lithium-Ion Batteries. *J. Mater. Chem.* **2010**, *20*, 6638.

(61) Xu, X.; Yu, D.; Zhou, H.; Zhang, L.; Xiao, C.; Guo, C.; Guo, S.; Ding, S. MoS_2 Nanosheets Grown on Amorphous Carbon Nanotubes for Enhanced Sodium Storage. *J. Mater. Chem. A* **2016**, *4*, 4375–4379.

(62) Zhou, J.; Qin, J.; Guo, L.; Zhao, N.; Shi, C.; Liu, E.; He, F.; Ma, L.; Li, J.; He, C. Scalable Synthesis of High-Quality Transition Metal Dichalcogenide Nanosheets and Their Application as Sodium-Ion Battery Anodes. *J. Mater. Chem. A* **2016**, *4*, 17370–17380.

(63) Hu, Z.; Zhu, Z.; Cheng, F.; Zhang, K.; Wang, J.; Chen, C.; Chen, J. Pyrite FeS_2 for High-Rate and Long-Life Rechargeable Sodium Batteries. *Energy Environ. Sci.* **2015**, *8*, 1309–1316.

(64) Qin, W.; Chen, T.; Lu, T.; Chua, D. H. C.; Pan, L. Layered Nickel Sulfide-Reduced Graphene Oxide Composites Synthesized via Microwave-Assisted Method as High Performance Anode Materials of Sodium-Ion Batteries. *J. Power Sources* **2016**, *302*, 202–209.

5. Unveröffentlichte Projekte (*to be published*)

High and low temperature investigations of the layered trichalcogenide CrTe₃ – combined XRD and PDF study

Anna-Lena Hansen^a, Bastian Dietl^a, Martin Etter^b, Reinhard K. Kremer^c, David C. Johnson^d, Wolfgang Bensch^{a,*}

^aInstitut für Anorganische Chemie, Universität Kiel, Olshausenstr. 40, D-24098 Kiel, Germany.

^bDeutsches Elektronen-Synchrotron (DESY), Hamburg 22607, Germany.

^cMax-Planck-Institut für Festkörperforschung, Heisenbergstr. 1, D-70506 Stuttgart, Germany.

^dDepartment of Chemistry, University of Oregon, Eugene, OR 97403, USA.

Introduction

The discovery of emergent properties in monolayers of graphite - graphene ^[1] has considerably revived the interest in system featuring layers weakly coupled by a van der Waals interaction. The opportunity to expand the set of properties by combining insulating, semiconducting, metallic and magnetic 2D layers has opened new perspectives for potential devices^[2–4] To this end, transition metal chalcogenides offer a rich playground to study such phenomena. For example, the evolution from an indirect band gap in the bulk to a direct band gap in monolayers was realized with molybdenum disulfide.^[5,6] However, the properties of monolayers are very sensitive to the properties of the substrate and details of the interaction of the monolayer with the substrate^[7–10] This challenge led to the concept of designed 2D heterostructures, where different 2D layers are stacked together interconnected by van der Waals bonding, which eliminates the constraints imposed by direct epitaxy.^[11–14] The desire to expand the selection of 2D materials to obtain a wide variety of properties has resulted in a growing complexity in the structures of the layers being investigated.

Generally, for layered systems it is prerequisite to have a pronounced anisotropy of the bonds, *i.e.* strong intralayer covalent bonds and substantially weaker interlayer van der Waals bonds. Many known layered compounds satisfy this condition. Initial research focused on 2D layers structurally similar to the hexagonal sheets of graphene,^[1,15] including elemental allotropes like silicene^[16], germanene^[17] and phosphorene^[18], and related compounds like hexagonal boron nitride (hBN).^[12,19,20] Soon thereafter, monolayers of transition metal dichalcogenides (TMDCs) MX₂ where M = Ti, Zr, Hf, V, Nb, Ta, Mo, W and X = S, Se, Te were targeted.^[2,4] First investigations of structurally related ternary MPX₃ compounds (M = Ag, Cu, In, Fe, Mn, Cr, Ni and X = S, Se) have recently appeared.^[21,22] More structurally complex transition metal trichalcogenides (TMTCs), MX₃ where M = Ti, Zr, Hf, and Nb and X = S, Se and Te have also gained attention as possible optoelectronic materials,^[23,24] as catalysts for hydrogen evolution^[25,26], as thermoelectric materials^[27–29], or as a potential sources to prepare monolayers.^[30]

The group IV-V TMTCs, such as TiS₃ or ZrTe₃, crystallize in chain like layered structures of trigonal prismatic coordinated TM chalcogenides. Within the family of group IV-V TMTC

CrTe₃ is unique since it represents, so far, the only crystalline group VI trichalcogenide.^[31–33] CrTe₃ crystallizes in a complex layered structure (space group $P2_1/c$; $a = 7.88 \text{ \AA}$, $b = 11.22 \text{ \AA}$, $c = 11.56 \text{ \AA}$ und $\beta = 118.41^\circ$) built up by layers of CrTe₆ octahedra stacked along the crystallographic a axis as illustrated in Figure 1.^[34] Only weak van-der-Waals bonds interconnect the layers. The octahedra within each layer are arranged in clusters of edge sharing Cr₄Te₁₆ rhombi like tetramers, highlighted in Figure 1. The layers can be described as ordered chromium deficient derivatives of Cr-ditelluride layers found in CrTe₂ (Cr_{2/3}Te₂). In this configuration, Cr has an oxidation state +III. An ionic notation would therefore be $[\text{Cr}^{3+}]_2[\text{Te}]^{2-}[\text{Te}_2]^{2-}[\text{Te}_3]^{2-}$, illustrating that charge balance leads to the formation of a polymerized mixed valent anion network (Te²⁻, Te₂²⁻, Te₃²⁻).^[34–36]

Bulk samples of CrTe₃ are accessible via conventional solid state synthesis. Interestingly, thin films of CrTe₃ can also be prepared using *modulated elemental reactants*.^[37–40]

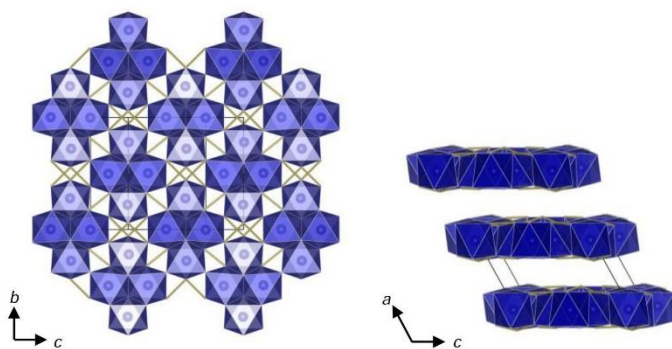


Figure 1: Structure of CrTe₃. Projection onto the (bc)-plane (left). Projection onto the (ac)-plane (right).^[41]

While the Cr-Te phase diagram and CrTe₃ homogeneity range were first investigated over three decades ago, important questions concerning the stability of CrTe₃ still remain open.^[41,42] Ipser *et al.* assumed that for compositions containing less than 74.9 % tellurium “CrTe₃” above 735 – 737 K peritectically decomposes into an unknown polytelluride (CrTe_x) phase and elemental Te at temperatures. For phases with a higher Te content peritectic decomposition starts already at 718 K. The additional signatures found in the differential thermal analysis (DTA) traces, however, occurred in heating cycles only. Therefore the authors suggested that CrTe₃ is a line phase, but comment that even after annealing single crystals for several months it was not possible to eliminate tiny residues of elemental Te.^[42] Recently, McGuire *et al.* reported that CrTe₃ is easily cleavable and single layers may be useful as a semiconducting 2D layer material. The high temperature magnetic properties were interpreted in terms of a spin $S = 3/2$ tetramer model including antiferromagnetic intra- and ferromagnetic inter-tetramer Heisenberg-type spin exchange interaction.^[40] Below 55 K McGuire *et al.* found antiferromagnetic long-range ordering and some unconventional low temperature behavior of the interlayer spacing.

These observations and the open questions concerning the exact stoichiometry inspired us to investigate the low and high temperature behavior of this unique polytelluride. Our analysis of X-ray diffraction and total scattering data collected as function of temperature provides insight why it is apparently impossible to gain phase pure CrTe₃. Our investigations identify minute structural distortions, which are hard to detect by coherent X-ray scattering only.

Experimental

Samples were prepared in evacuated quartz ampules by heating stoichiometric mixtures of chromium and tellurium to a temperature of 573 K. After one day the temperature was slowly raised to 723 K and held there for 4 d. Slow cooling of the samples to room temperature yielded phase pure CrTe₃. High temperature powder diffraction experiments were performed at photon energies of 29.2 keV ($\lambda = 0.4246 \text{ \AA}$) on polycrystalline samples enclosed in sealed quartz glass capillaries at the I15 beamline at the Diamond Light Source (DLS, Oxfordshire) from ambient (294 K) temperatures to 794 K utilizing a nitrogen hot gas blower GSB 1300 (FMB Oxford). Low temperature x-ray powder diffraction (XRPD) and pair distribution function (PDF) analysis was conducted on patterns collected using photons with energies of 60 keV ($\lambda = 0.20722 \text{ \AA}$) at the beamline P02.1 at PETRA III (DESY, Hamburg) between room temperature and 100 K obtained using a liquid N₂ cryo streamer. Pawley and Rietveld refinements of the XRPD data were performed using the TOPAS Academic 6.0 software.^[43] To analyze the strain contribution to the broadening of the Bragg peaks the strain value ϵ_0 was obtained after carefully including the instrumental resolution (measured with NIST standard material for line broadening LaB₆ SRM 660c).^[44] The analysis of the atomic pair distribution function was performed utilizing the xPDF software suite.^[45] To subtract the contribution of the quartz glass capillaries to the total scattering data, an empty capillary was measured under identical conditions. To account for the instrumental contribution to the damping of the resulting PDF a LaB₆ standard sample was measured. Scanning electron microscopic (SEM) and energy dispersive X-ray spectroscopic (EDX) measurements were performed using a Philips Environmental Scanning Electron Microscope ESEM XL30 equipped with an EDAX detector.

Results and Discussion

Room temperature powder diffraction data collected at beamline P02.1 (Petra III, DESY) (Figure 2) of CrTe₃ compound were refined using the Rietveld method. We found no evidence of any crystalline impurity phase and the refined structural parameters matched well the published CrTe₃ structure data (Supplemental Information, Table 1). We noticed that the background contained a periodic modulation which suggests either the presence of an additional amorphous phase, deviations from the known structure due to deformations on a

short-range order (SRO) scale (Figure 2) or the presence of stacking faults. Therefore, additional measurements at higher Q values were performed to access the PDF.

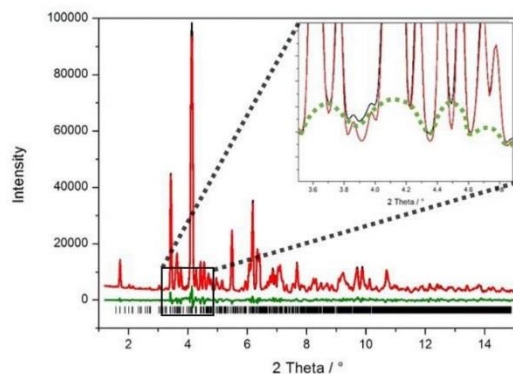


Figure 2: X-ray powder diffraction pattern of CrTe_3 collected at beamline P02.1 (DESY). Measured (black), Rietveld refined (red) and difference curve (green) are given, as well as (black) vertical ticks to mark the positions of the Bragg reflections used to simulate the pattern. A closer inspection of the pattern reveals a modulated background (light green curve in the inset) either due to an additional amorphous phase, deviations from the known structure due to deformations on a short-range order scale (Figure 2) or to stacking faults.

A comparison of the experimental and the calculated PDF is shown in Figure 3. The experimental data could be reasonably well fitted ($R_{wp} = 11.6\%$) on the basis of the CrTe_3 structure data obtained from the Rietveld profile refinement. The very good accordance of the structural model on large length-scales excludes the existence of substantial stacking faults. Stacking faults would lead to a better consensus in the SRO and larger deviations on the long range. A closer inspection rather revealed a discrepancy between the experimental and the calculated data at short distances visible in the increased amplitude of the difference curve (green line, Figure 3). Since the sample was synthesized with an excess tellurium, our first approach was to check for an amorphous Te phase, which should have maxima in the radial distribution at 2.83, 4.28 and 6.23 Å.^[46] Apparently, these bond lengths are also present in the CrTe_3 structure making it hard to discriminate whether amorphous Te is present or not. Since the discrepancies of the modelled PDF are not only at the proposed r -values, the deviation between the model and the observed data below ~ 11 Å could just as well be caused by disagreements between local and averaged crystallographic structure.

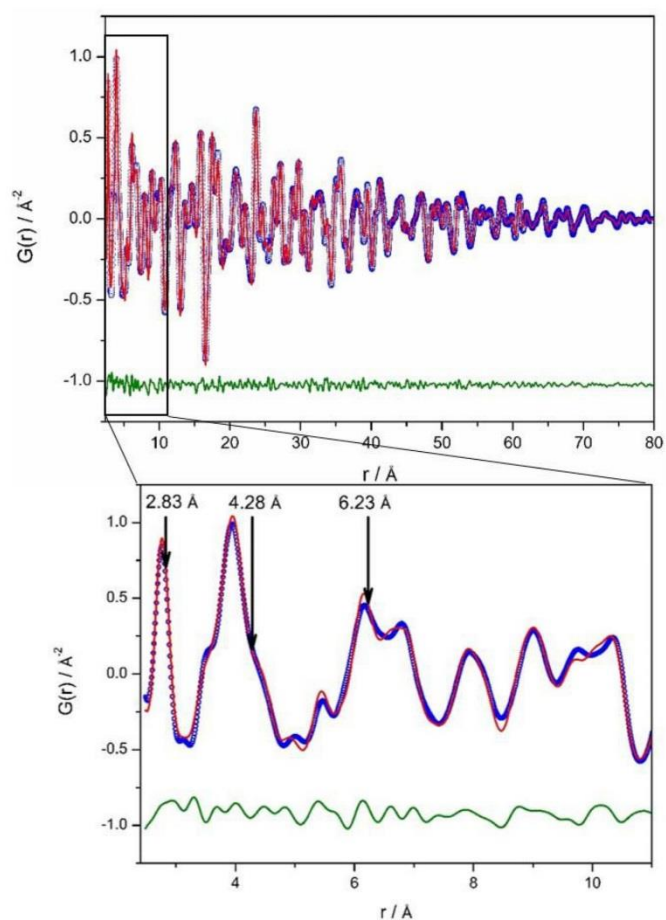


Figure 3: Experimental PDF (blue circles) and the calculated PDF (red line) based on the structural model of CrTe_3 . Measurements were performed at room temperature. $R_{wp} = 11.6\%$. Arrows in the enlarged short r region indicate maxima in the radial distribution of amorphous Te published by Akola and Jones.

Scanning electron microscopy investigations provide additional evidence for the existence of an amorphous phase (Figure 4). Stoichiometric CrTe_3 crystallites were covered and interconnected all across the sample by a glassy slightly off stoichiometric secondary phase (~ 77 at.% Te). It has to be noted that energy dispersive X-ray spectroscopic measurements (EDX) provide an averaged composition depending on the actual penetration depth of electrons into the investigated material, which should be a few hundred nm in the present case. We can therefore not exclude that the cover layer is even more enriched in Te or even pure tellurium.

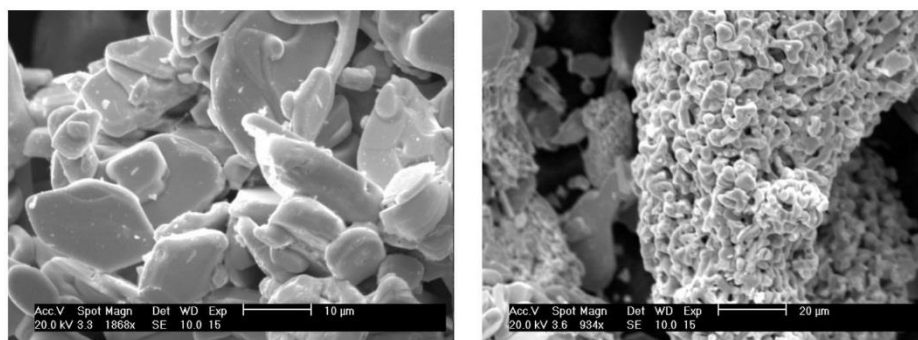


Figure 4: SEM images of as synthesized CrTe_3 . Left: Region with pure CrTe_3 crystallites. Right: Additional phase with higher Te content and a more glassy appearance.

In order to understand the behavior of the additional Te rich phase at higher temperatures and to check for an unknown polytelluride phase above 734 K, high temperature diffraction data were collected (Figure 5). A close look at the region near $2\Theta \sim 7.5^\circ$ revealed a Bragg reflection growing out above ~ 454 K which can be ascribed to crystallized tellurium (Figure 6). Quantitative phase analysis yielded a maximum content of $< 1\%$ Te. Due to this low content and a slight overlap with CrTe_3 reflections, no further structural information of this phase could be deduced. We found no evidence for the proposed phase transition of CrTe_3 into an unknown telluride phase. The cell parameter increase almost linearly (with a minor deviation of the b -axis, see Figure 11) and the atomic positions change only marginally with increasing temperature (supplemental information). A closer look at the Debye-Waller-factors (DW), representing the average displacement of atoms around their equilibrium positions, revealed large differences between the various Te positions (Figure 8). The unusually large DW factor of Te3 being prominent already at room temperatures suggests a possible distortion of the corresponding CrTe_6 octahedra, which is schematically shown in Figure 7. The different Te3 positions in the structure are averaged over the measured sample volume, leading to the observed high DW factors. A comparison of the distortion indices, based on bond lengths defined by Baur, of the octahedra, obtained by XRD and PDF strongly supports this finding.^[47] The indices of the corresponding Cr2 octahedra are noticeably larger in the structural model obtained by PDF. Even if, as it has been done here, averaged over a radius of 80 Å, the PDF structure model is less averaged on a global scale than XRD. It has to be noted that the deviations from the XRD values are even more pronounced, when the r range is smaller. But due to the fact, that we have strong indications of an additional amorphous phase, we refrained from analyzing the low r range more precisely to not overemphasize the structural distortions.

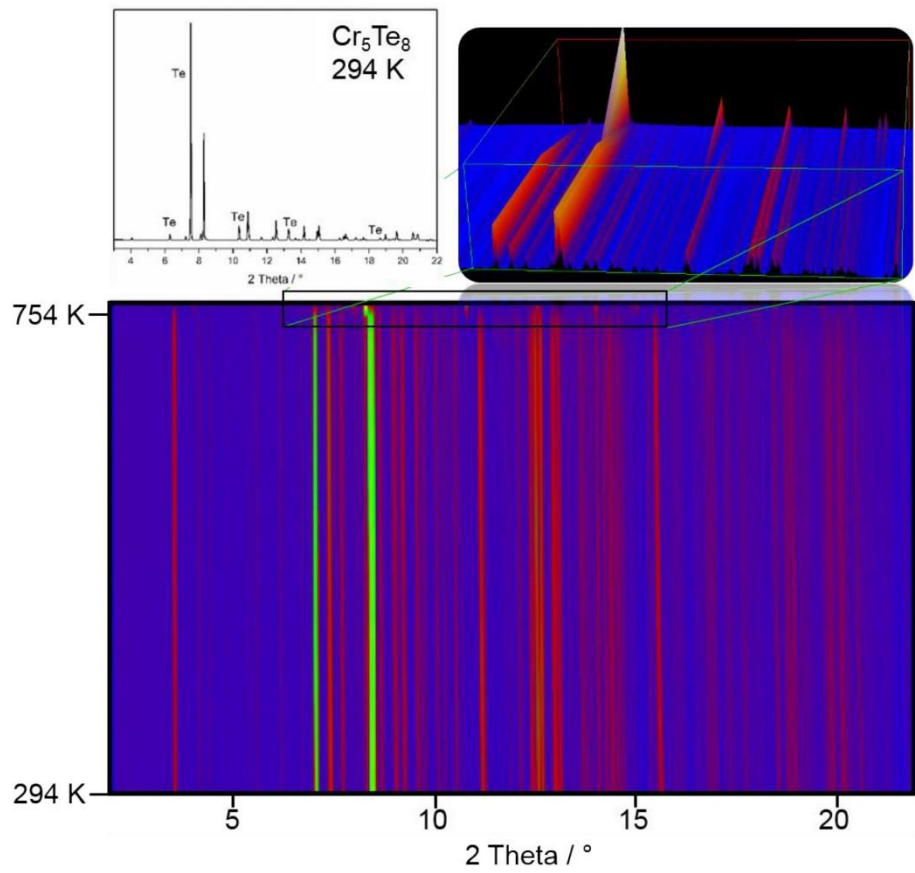


Figure 5: Simulated 2D Guinier pattern of in situ XRPD measurements from room temperature to 794 K (below) with an inset zooming into the phase transition taking place around 754 K. A single XRPD pattern of Cr_5Te_8 and recrystallized Te at ambient temperatures (above left) is given for comparison.

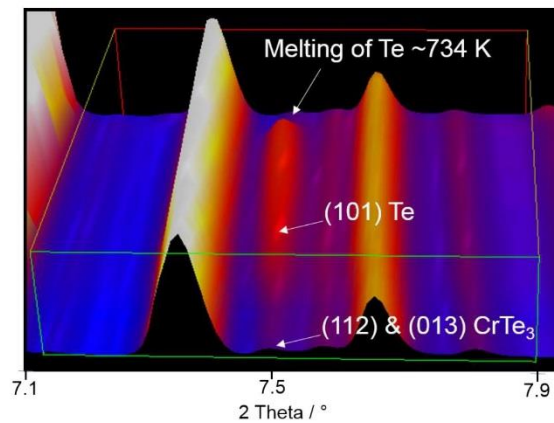


Figure 6: Temperature evolution of the Te (101) peak between 434 K and 754 K.

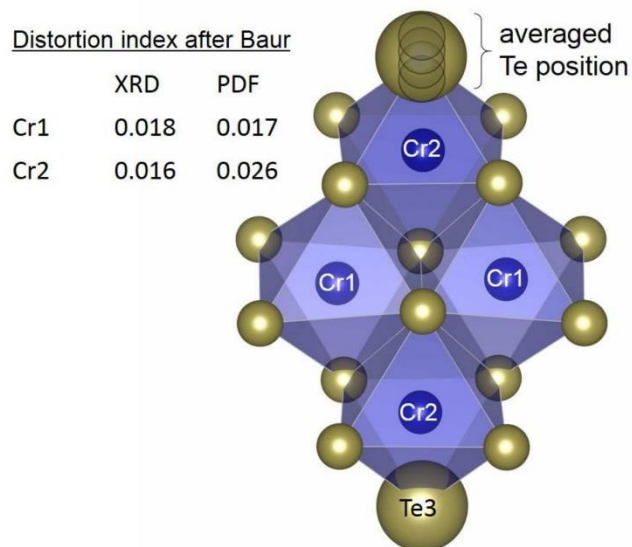


Figure 7: (Main frame) Schematic illustration of a Cr_4Te_{16} rhombus. Averaging of different Te positions could explain the unusual high DW factors of the Te3 position. Distortion indices of the octahedra calculated according to Baur support this finding (upper left).

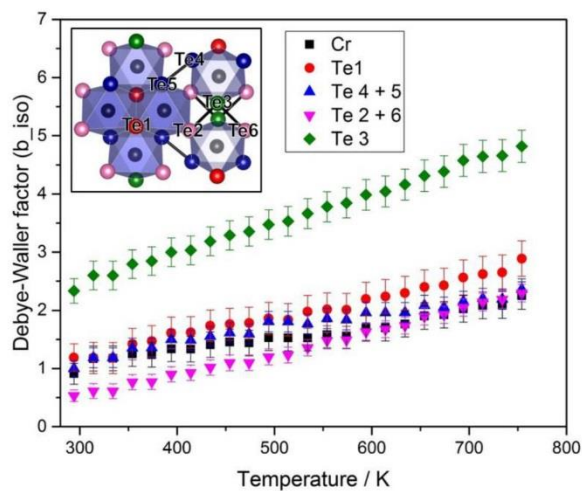


Figure 8: Isotropic Debye-Waller factors obtained by Rietveld profile refinement of the high temperature XRPD patterns.

At higher temperatures, the DW factors could also be caused by an increased mobility of tellurium at the Te3 position. This high mobility could be an indicator that Te3 atoms are prone to leaving their position and recrystallizing in the observed additional Te phase. The disappearance of the additional Te reflections at 734 K viz. the melting temperature of Te,

occurs exactly in the temperature region proposed for the peritectic decomposition of CrTe_3 into an unknown polytelluride. This coincidence supports the proposal that melting of Te is more likely. Above 753 K, CrTe_3 decomposes into Cr_5Te_8 and Te as reported previously.^[48] To clarify whether Te leaves its atomic position or whether we observed a recrystallization of an amorphous Te rich secondary phase, we performed a secondary *ex situ* annealing (24h, 523 K, cooled 1 K/min) of the as synthesized sample and investigated it via SEM, XRD and PDF. SEM revealed a different appearance of the overall sample. The majority consisted of pure CrTe_3 crystallites, but still regions of a glassy phase could be found. Additionally, a few pure tellurium crystallites were spotted (Figure 9). Rietveld profile refinement of the diffraction pattern collected at P02.1 (Petra III, DESY) of the annealed sample again revealed a phase content of max. 1% tellurium, making it almost impossible to rely on a refinement of the Te occupancy.

The lattice parameters (Supplemental Information, Table 1) are slightly smaller than those of the as-synthesized sample, yet the deviations are in a range which we found to be common for repeated measurements of the same sample. These findings support the inhomogeneous nature of the compound. It has to be noted, that the DW factors in the annealed sample remain exceptionally large, indicating that the structural distortions are an intrinsic feature of CrTe_3 and cannot be reduced by an additional annealing of the sample. To calculate the corresponding PDF, measurements were performed with a $Q_{\text{max}} = 25 \text{ \AA}^{-1}$. The regions of the marked radial distributions of the amorphous tellurium phase slightly change in the annealed sample, particularly a decrease around 6.23 \AA is noticeable, a region where crystalline Te structure does not have Bragg peaks. Overall a narrowing of the peaks is observable in the low r range. The increase of the intensity in certain parts of the PDF fit well to the calculated PDF of crystalline Te. Above $\sim 7 \text{ \AA}$ the intensity of the PDF of the annealed sample exceeds the PDF of the as synthesized CrTe_3 up to high r values, indicating the existence of well crystallized tellurium (supplemental information). Therefore, we assume that structural changes occurred on a local scale supporting recrystallization of an amorphous Te rich secondary phase.

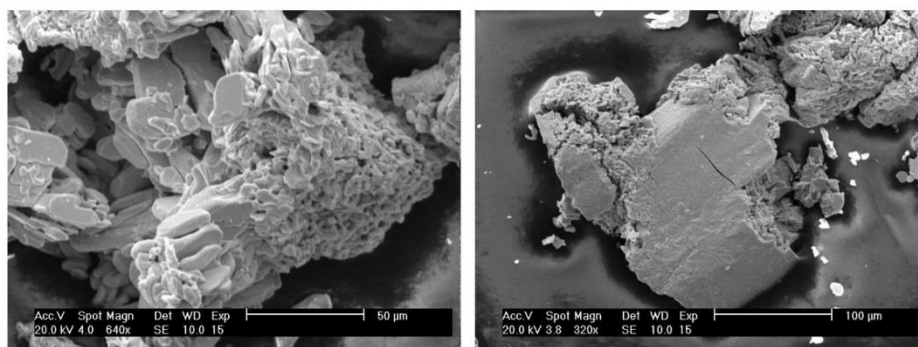


Figure 9: SEM images of ex situ annealed CrTe₃. Left: Region with pure CrTe₃ crystallites interconnected by glassy Te rich phase. Right: Te crystallite.

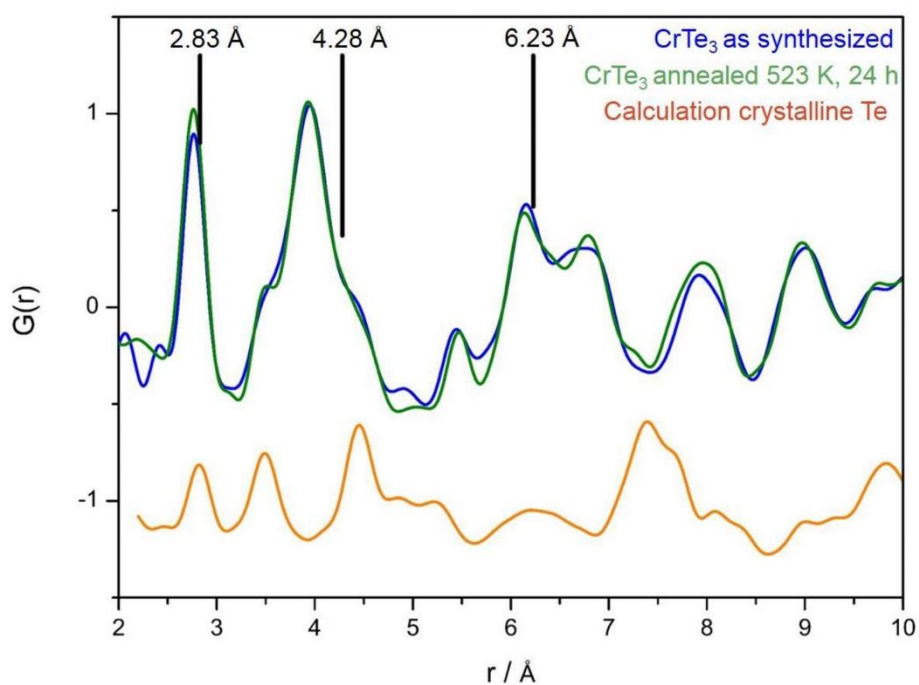


Figure 10: Experimental PDF of as synthesized CrTe₃ (blue) and the annealed sample (green), in comparison with a calculated PDF based on the structural model of crystalline tellurium (orange).

To gain more information on the structural changes with decreasing temperatures, sequential Rietveld profile refinement of the diffraction data was performed. As shown in Figure 11 CrTe₃ exhibits a pronounced anisotropic thermal expansion. The cell parameters contract with decreasing temperature with a deviation from linearity starting at about 250 K.

Whereas the b axis shows a expansion of $\sim 2\%$ as the temperature is raised from 100K to 700K, both a and c axis increase significantly less, about 0.7 and 0.8 %, respectively. Anisotropic thermal expansion parallel and perpendicular to the layers is a typical behavior of layered structures, with the small expansion of the a -axis reflecting the weak van der Waals bonding between the layers. The small thermal expansion along the c -axis is unusual and most likely caused by the different types of bonds within the layer. The anisotropic thermal expansion was discussed in detail by McGuire *et al.*^[40]

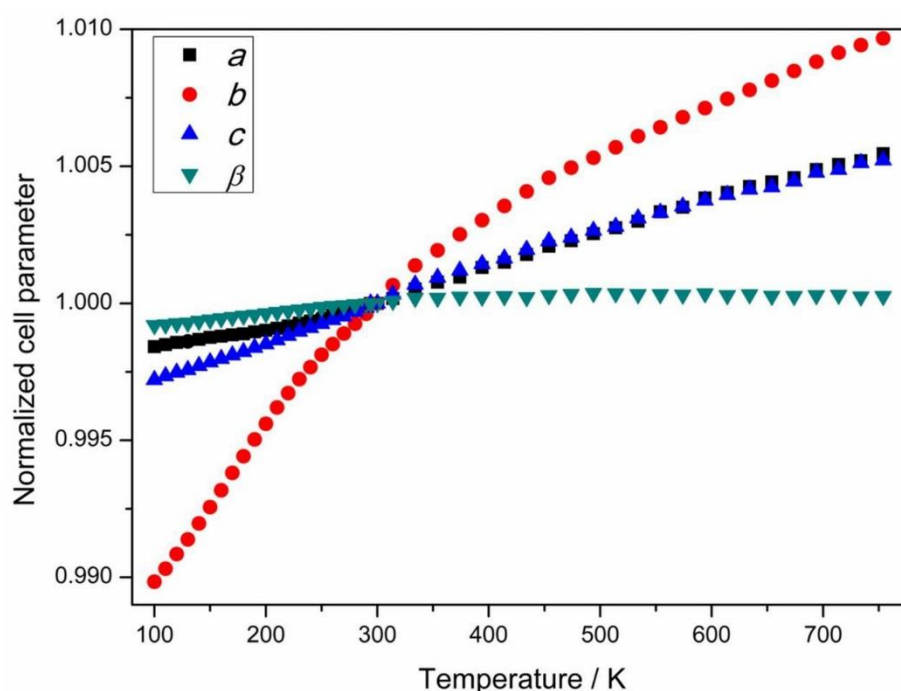


Figure 11: Normalized cell parameter of CrTe_3 against temperature. The figure represents two datasets (heating and cooling), therefore, a minor change of the slope at 300 K occurred.

Rietveld refinement of the diffraction patterns collected at each temperature step provides information on the structural changes occurring with temperature. We defined the following bond length ratio as a measure of the anisotropy of the $(\text{Cr}_4\text{Te}_{16})$ rhombi, which make up the in-plane structure of CrTe_3 :

$$r = \frac{\text{bond length (Cr1 - Cr1)}}{\text{bond length (Cr2 - Cr2)}}$$

The change in the bond length ratio r with temperature is displayed in Figure 12. Instead of a continuous decrease of the ratio we observe an abrupt distortion of the structure at ~ 250 K.

While McGuire *et al.* also noticed the distortion of the rhombi, they were not able to detect the abrupt change in the structure as they performed *ex situ* measurements only at three distinct temperatures. The change in the in-plane structure resulting in the distortion of the rhombi causes the deviation from linearity, which is most pronounced for the b-axis. The interlayer distance was also found to vary more rapidly between 200 and 300K, which agrees with the change in the interlayer distances with temperature reported by McGuire.^[40] While structural components within the CrTe_3 structure change systematically with temperature, we did not find any evidence for a distinct phase in the low or high temperature diffraction data.

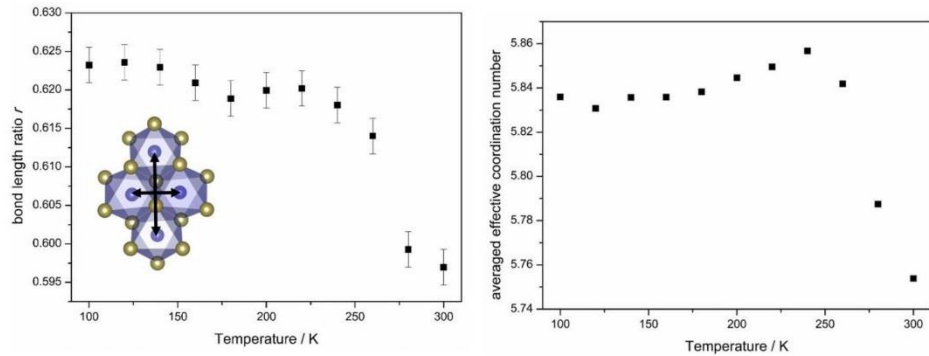


Figure 12: Left: bond length ratio of $\text{Cr}_4\text{Te}_{16}$ rhombus with decreasing temperature. Right: averaged effective coordination number of chromium.

As indicated by the variation of the bond length ratios, the average effective coordination number of chromium changes with decreasing temperature (see Figure 12). This should also affect the spin exchange coupling of the Cr^{3+} cations and become noticeable in the magnetic susceptibility. Figure 13 displays the magnetic susceptibilities, $\chi_{\text{mol}}(T, H) = M_{\text{mol}}(T, H)/H$ versus temperature measured in magnetic fields between 0.01T and 7 T on a polycrystalline powder sample. Especially for small magnetic fields the magnetic susceptibility exhibits a strong field and history dependence with a splitting between field cooled (fc) and zero field cooled (zfc) traces below about 200 K. For small fields there is the built-up of substantial spontaneous magnetization reminiscent of a ferro- or ferrimagnet showing up as a step-like increase below ~ 240 K. The fc-zfc splitting is suppressed and the step-like increase is smeared out when the measuring field is increased. For sufficiently strong fields the susceptibilities are almost identical with a broad hump similar to that reported by McGuire *et al.*, however centered at significantly lower temperature.

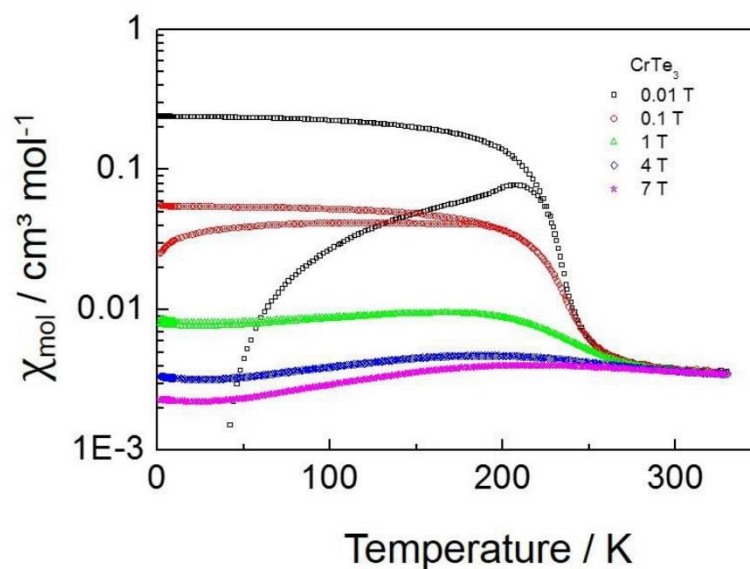


Figure 13: Temperature dependent field cooled (fc) and zero-field cooled magnetic susceptibilities measured with varying magnet field strength as indicated.

Fig 14 shows the magnetic susceptibility of our sample in comparison with the susceptibility data published by *McGuire et al.*⁴¹ together with the susceptibilities for a spin $S=3/2$ tetramer and a $S=3/2$ dimer both normalized to one mole Cr atoms coupled by spin exchange coupling according to the following Heisenberg Hamiltonians:

For the tetramer

$$\mathcal{H} = -2J_1 (\mathbf{S}_1 + \mathbf{S}_2 + \mathbf{S}_3 + \mathbf{S}_4) - 2J_2 \mathbf{S}_2 \mathbf{S}_4$$

where a cyclic notation for the indices was used, and for the dimer

$$\mathcal{H} = -2J \mathbf{S}_1 \mathbf{S}_2.$$

For the tetramer we took the exchange parameters, $J_1 = -40$ K and $J_2 = +35$ K similar as derived by *McGuire et al.* and for the dimer the spin exchange J was taken as -66 K.

As already note by *McGuire et al.* the tetramer susceptibilities agree well above 350 K. Dimer and tetramer susceptibility deviate below and cannot capture our susceptibility data. Especially, the maxima of the theoretical data are substantially broader, as also noted by

McGuire *et al.* before. Indication of any anomalous magnetization behavior at ~53 K where McGuire *et al.* have found long-range antiferromagnetic ordering by neutron diffraction cannot be observed in our data.

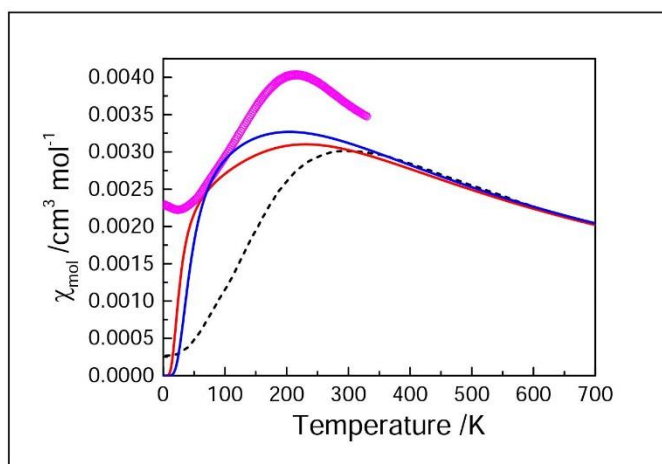


Figure 14: Magnetic susceptibilities of CrTe₃. Our data taken at 7 T external field are represented by the magenta circles and McGuire's data by the dashed line. The solid blue and red lines depict the magnetic susceptibilities of a spin $S=3/2$ tetramer and a dimer, respectively, with spin exchange coupling parameters given in the text.

Figure 15 summarizes the heat capacity measurements obtained on the same sample as used for the susceptibility experiment. We do neither discern the small magnetic anomaly at ~65 K resolved by McGuire *et al.*⁴¹ nor is there indication of a magnetic anomaly near ~240 K. The lower inset in Figure 15 displays the low-temperature heat capacity of our sample of CrTe₃ together with a fit to a polynomial according to

$$C_p(T)/T = \beta T^2 + \delta T^4 + \varepsilon T^6. \quad (1)$$

The coefficient β amounts to 0.00219(5) J/mol K⁴ corresponding to a Debye temperature of

$$\Theta_{\text{Debye}}(T \rightarrow 0) = 153(1) \text{ K}.$$

The heat capacity across the whole temperature range can be well modeled by a superposition of a Debye contribution with a Debye temperature of ~150 K and three Einstein oscillators at 30 K, 100 K and 280 K and respective weights of 0.23, 0.12 and 1.40 (see Figure 15, lower inset). The Einstein term at 30 K is fitted with a weight of 0.23 per formula unit CrTe₃, or 0.92 per Cr₄Te₁₂, i.e. approximately one atom in a tetramer. We tentatively

ascrbe the low Einstein temperature to the weakly bonded Te3 atoms in the rhombi as indicated by the x-ray measurements.

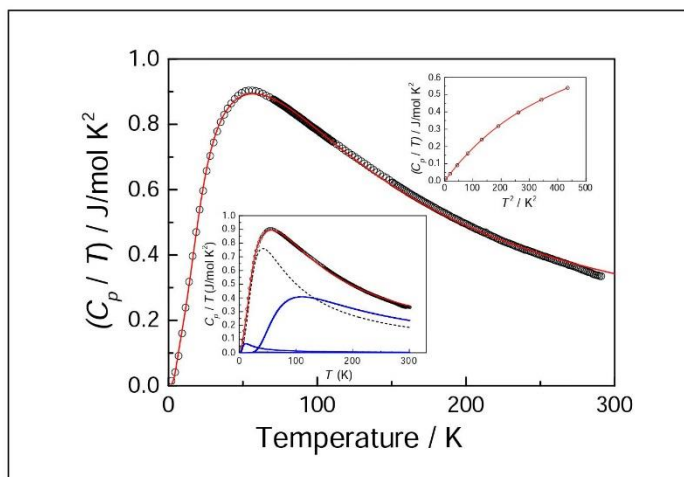


Figure 16: (main frame) Heat capacity of our CrTe_3 sample (identical to the magnetic susceptibility sample). The solid red line is the result of a fit of the experimental data to a sum of a Debye heat capacity and three Einstein terms with Debye and Einstein temperatures quoted in the text. Upper inset: Low temperature heat capacity, C_p/T , ('Sommerfeld plot') with a polynomial fit (solid red line). The slope to the contribution $\propto T^3$ to the heat capacity corresponds to a Debye temperature, $\Theta_{\text{Debye}} (T \rightarrow 0)$ of 153(1) K. The lower inset shows the individual Debye and Einstein contributions: The black dashed line represents a Debye contribution with a Debye temperature of 150 K and a weight of 2.25, the solid blue line represent three Einstein contributions with Einstein temperatures of 30 K, 100, and 280 K with weights of 0.23, 0.12 and 1.40, respectively.

Acknowledgement

We thank Mrs. E. Brücher and Mrs G. Siegle for expert experimental assistance.

References

- [1] K. S. Novoselov, A. K. Geim, S. V. Morozov, D. Jiang, Y. Zhang, S. V. Dubonos, I. V. Grigorieva, A. A. Firsov, *Science* **2004**, *306*, 666–669.
- [2] M. Xu, T. Liang, M. Shi, H. Chen, *Chem. Rev.* **2013**, *113*, 3766–3798.
- [3] K. S. Novoselov, D. Jiang, F. Schedin, T. J. Booth, V. V. Khotkevich, S. V. Morozov, A. K. Geim, *Proc. Natl. Acad. Sci. U. S. A.* **2005**, *102*, 10451–10453.
- [4] Q. H. Wang, K. Kalantar-Zadeh, A. Kis, J. N. Coleman, M. S. Strano, *Nat. Nanotechnol.* **2012**, *7*, 699–712.
- [5] R. A. Gordon, D. Yang, E. D. Crozier, D. T. Jiang, R. F. Frindt, *Phys. Rev. B* **2002**, *65*, 125407.
- [6] K. F. Mak, C. Lee, J. Hone, J. Shan, T. F. Heinz, *Phys. Rev. Lett.* **2010**, *105*, 136805.
- [7] A. Koma, K. Sunouchi, T. Miyajima, *Microelectron. Eng.* **1984**, *2*, 129–136.
- [8] A. Koma, K. Ueno, K. Saiki, *J. Cryst. Growth* **1991**, *111*, 1029–1032.
- [9] J.-H. Chen, C. Jang, S. Xiao, M. Ishigami, M. S. Fuhrer, *Nat. Nanotechnol.* **2008**, *3*, 206–209.

- [10] C. R. Dean, A. F. Young, I. Meric, C. Lee, L. Wang, S. Sorgenfrei, K. Watanabe, T. Taniguchi, P. Kim, K. L. Shepard, et al., *Nat. Nanotechnol.* **2010**, *5*, 722–726.
- [11] A. Koma, *Thin Solid Films* **1992**, *216*, 72–76.
- [12] L. A. Ponomarenko, A. K. Geim, A. A. Zhukov, R. Jalil, S. V. Morozov, K. S. Novoselov, I. V. Grigorieva, E. H. Hill, V. V. Cheianov, V. I. Fal'ko, et al., *Nat. Phys.* **2011**, *7*, 958–961.
- [13] K. S. Novoselov, A. Mishchenko, A. Carvalho, A. H. C. Neto, *Science* **2016**, *353*, aac9439.
- [14] A. K. Geim, I. V. Grigorieva, *Nature* **2013**, *499*, 419–425.
- [15] K. S. Novoselov, V. I. Fal'ko, L. Colombo, P. R. Gellert, M. G. Schwab, K. Kim, *Nature* **2012**, *490*, 192–200.
- [16] P. Vogt, P. De Padova, C. Quaresima, J. Avila, E. Frantzeskakis, M. C. Asensio, A. Resta, B. Ealet, G. Le Lay, *Phys. Rev. Lett.* **2012**, *108*, 155501.
- [17] M. E. Dávila, L. Xian, S. Cahangirov, A. Rubio, G. L. Lay, *New J. Phys.* **2014**, *16*, 095002.
- [18] H. Liu, A. T. Neal, Z. Zhu, D. Tomanek, P. D. Ye, *ACS Nano* **2014**, *8*, 4033–4041.
- [19] I. Meric, C. Dean, A. Young, J. Hone, P. Kim, K. L. Shepard, in *2010 Int. Electron Devices Meet.*, **2010**, p. 23.2.1-23.2.4.
- [20] L. Song, L. Ci, H. Lu, P. B. Sorokin, C. Jin, J. Ni, A. G. Kvashnin, D. G. Kvashnin, J. Lou, B. I. Yakobson, et al., *Nano Lett.* **2010**, *10*, 3209–3215.
- [21] K. Du, X. Wang, Y. Liu, P. Hu, M. I. B. Utama, C. K. Gan, Q. Xiong, C. Kloc, *ACS Nano* **2016**, *10*, 1738–1743.
- [22] R. Brec, *Solid State Ion.* **1986**, *22*, 3–30.
- [23] J. O. Island, A. J. Molina-Mendoza, M. Barawi, R. Biele, E. Flores, J. M. Clamagirand, J. R. Ares, C. Sanchez, H. S. J. van der Zant, R. D'Agosta, et al., *ArXiv170201865 Cond-Mat* **2017**.
- [24] K. Wu, E. Torun, H. Sahin, B. Chen, X. Fan, A. Pant, D. P. Wright, T. Aoki, F. M. Peeters, E. Soignard, et al., *Nat. Commun.* **2016**, *7*, 12952.
- [25] M. Barawi, E. Flores, I. J. Ferrer, J. R. Ares, C. Sánchez, *J. Mater. Chem. A* **2015**, *3*, 7959–7965.
- [26] E. Flores, J. R. Ares, I. J. Ferrer, C. Sánchez, *Phys. Status Solidi RRL – Rapid Res. Lett.* **2016**, *10*, 802–806.
- [27] P. R. N. Misse, D. Berthebaud, O. I. Lebedev, A. Maignan, E. Guilmeau, *Materials* **2015**, *8*, 2514–2522.
- [28] Y. Saeed, A. Kachmar, M. A. Carignano, *J. Phys. Chem. C* **2017**, *121*, 1399–1403.
- [29] E. Guilmeau, D. Berthebaud, P. R. N. Misse, S. Hébert, O. I. Lebedev, D. Chateigner, C. Martin, A. Maignan, *Chem. Mater.* **2014**, *26*, 5585–5591.
- [30] J. Dai, M. Li, X. C. Zeng, *Wiley Interdiscip. Rev. Comput. Mol. Sci.* **2016**, *6*, 211–222.
- [31] F. Lévy, H. Berger, *J. Cryst. Growth* **1983**, *61*, 61–68.
- [32] K. S. Liang, J. P. deNaufville, A. J. Jacobson, R. R. Chianelli, F. Betts, *J. Non-Cryst. Solids* **1980**, *35*, 1249–1254.
- [33] P. Afanasiev, *Comptes Rendus Chim.* **2008**, *11*, 159–182.
- [34] E. Canadell, S. Jobic, R. Brec, J. Rouxel, *J. Solid State Chem.* **1992**, *98*, 59–70.
- [35] K. O. Klepp, H. Ipser, *Monatshefte Für Chem. Chem. Mon.* **1979**, *110*, 499–501.
- [36] K. O. Klepp, H. Ipser, *Angew. Chem.* **1982**, *94*, 931–932.
- [37] S. Kraschinski, S. Herzog, W. Bensch, *Solid State Sci.* **2002**, *4*, 1237–1243.
- [38] M. Behrens, J. Tomforde, E. May, R. Kiebach, W. Bensch, D. Häußler, W. Jäger, *J. Solid State Chem.* **2006**, *179*, 3330–3337.
- [39] D. C. Johnson, *Curr. Opin. Solid State Mater. Sci.* **1998**, *3*, 159–167.
- [40] M. A. McGuire, V. O. Garlea, S. KC, V. R. Cooper, J. Yan, H. Cao, B. C. Sales, *ArXiv170108621 Cond-Mat* **2017**.
- [41] K. O. Klepp, H. Ipser, *Monatshefte Für Chem. Chem. Mon.* **n.d.**, *110*, 499–501.
- [42] H. Ipser, K. L. Komarek, K. O. Klepp, *J. Common Met.* **1983**, *92*, 265–282.
- [43] A. A. Coelho, *Comput. Programme Rietveld Anal.* **2004**.
- [44] D. Balzar, N. Audebrand, M. R. Daymond, A. Fitch, A. Hewat, J. I. Langford, A. Le Bail, D. Louër, O. Masson, C. N. McCowan, et al., *J. Appl. Crystallogr.* **2004**, *37*, 911–924.

- [45] P. Juhás, T. Davis, C. L. Farrow, S. J. L. Billinge, *J. Appl. Crystallogr.* **2013**, *46*, 560–566.
 [46] J. Akola, R. O. Jones, *Phys. Rev. B* **2012**, *85*, 134103.
 [47] W. H. Baur, *Acta Crystallogr. B* **1974**, *30*, 1195–1215.
 [48] G. Chattopadhyay, *J. Phase Equilibria* **1994**, *15*, 431–440.

Supporting information

Table 1: Results of Rietveld Refinement at DESY and PDF analyses.

<u>XRD</u>	$a / \text{Å}$	$b / \text{Å}$	$c / \text{Å}$	$\beta / ^\circ$	$R_{\text{WP}} / \%$
as synthesized	7.8985(3)	11.2316(5)	11.5610(6)	118.493(4)	4.6
annealed	7.8887(3)	11.2244(5)	11.5516(5)	118.490(3)	4.15
<u>PDF</u>					
as synthesized	7.88(2)	11.21(2)	11.54(2)	118.4(2)	11.6

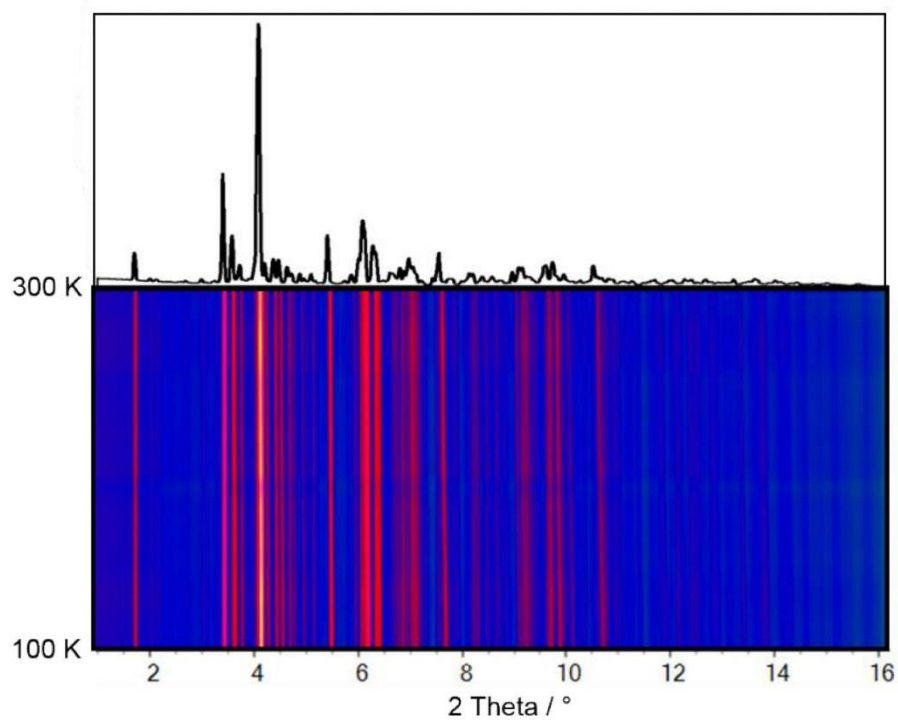


Figure 14: Simulated 2D Guinier pattern of in situ XRD measurements from room temperature to 100 K (below) and single PXRD pattern of CrTe_3 at ambient temperatures (above) for comparison.

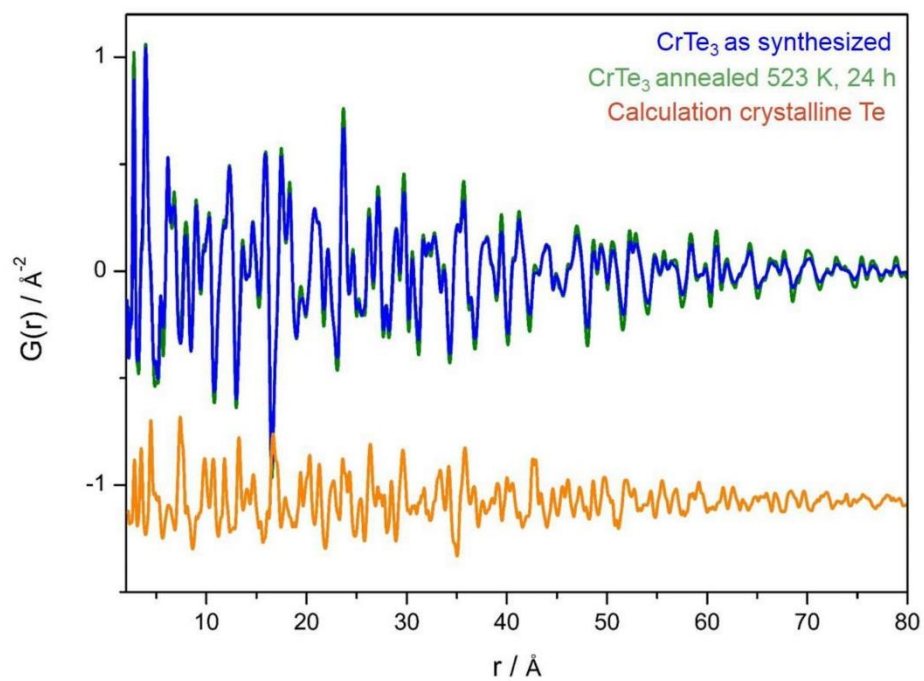


Figure 15: Comparison of PDF of as synthesized and annealed CrTe₃ in comparison with a calculated PDF of crystalline tellurium.

D Zusammenfassender Ausblick

Im Rahmen dieser Arbeit wurden überwiegend thermoelektrische Materialien mit unterschiedlichen analytischen Methoden charakterisiert. Die Materialien umfassen Dünnschichten und Übergitter basierend auf klassischen thermoelektrischen Verbindungen wie Bi_2Te_3 und Sb_2Te_3 (C 1.1 - 1.3) und Materialien, in denen die thermoelektrische Performance gezielt durch Nanoausscheidungen verbessert werden konnte (C 2.1). Ein wesentliches Ergebnis der Charakterisierungen ist, dass deren viel versprechende strukturelle Eigenschaften nicht temperaturstabil sind. Experimente mit *in situ* XRD und TEM sowie *ex situ* PDF konnten eindrücklich diese thermische Instabilität nachweisen. Erst die synergistischen Effekte dieser Analysemethoden ermöglichen eine umfassende Materialcharakterisierung auf allen Längenskalen und diese sollten zukünftig als Standardmethoden für die umfassende Charakterisierung dieser Materialklasse eingesetzt werden. Neben einer vollständigen Charakterisierung, die erst Aussagen über Langzeitstabilität zulassen, ist auch ein Umdenken bei der Auswahl der zu untersuchenden Materialien notwendig. Wenn Thermoelektrika eine entscheidende Rolle bei der Verbesserung der thermischen Effizienz von Prozessen sein

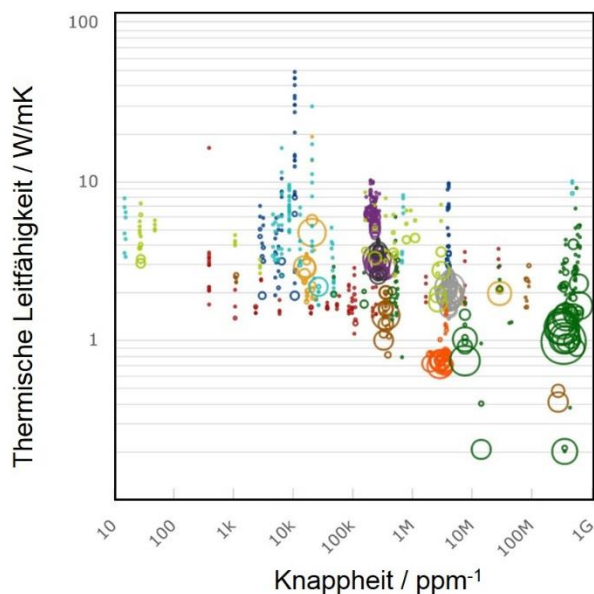


Abbildung 16: Thermische Leitfähigkeit in Abhängigkeit von der Knappheit der enthaltenen Elemente. Je größer die dargestellten Kreise, desto höher der ZT Wert des Materials. Thermoelektrische Materialien sind nach Farben klassifiziert: rot: Manganoxide, hellbraun: Chlathrate, dunkelblau: ZnO , SrTiO_3 , lila: Halb-Heusler, hell orange: Cobaltoxide, dunkel orange Zintl-Phasen, hellblau: andere Oxide, grau: Skutterudite, schwarz: Si-Ge Verbindungen, hellgrün: Silizide, dunkelgrün: Chalkogenide. Nach [127]

sollen um damit zur Reduzierung des CO_2 Ausstoßes beizutragen, müssen diese großindustriell herstellbar sein. Dies wird nur möglich sein, wenn die Materialien kostengünstig sind und auf toxikologisch unbedenklichen und häufigen Elementen basieren. Die Seltenheit von Elementen und besonders deren Versorgungssicherheit in Bezug auf die Herkunftsländer geraten immer weiter in den Fokus der Forschung. Zusammengefasst werden solche geopolitischen und ökonomischen Fakten im Herfindahl-Hirschmann Index (HHI). Für die Erstellung des HHI werden die Konzentration der Elemente in der Erdkruste, die Produktion der Elemente (welches Herkunftsland) und die Reserven des Elements herangezogen.^[127,128] In Abbildung 16 ist exemplarisch die Knappheit, welche die Häufigkeit der Elemente in der Erdkruste in Bezug auf den

Gewichtsanteilanteil im Material wider-spiegelt, gegen die thermische Leitfähigkeit für eine große Auswahl thermoelektrischer Materialien dargestellt. Aus der Abbildung wird deutlich, dass die Materialien mit niedriger thermischer Leitfähigkeit gleichzeitig aus den seltensten Elementen bestehen. Das bedeutet, dass bei der Entwicklung zukunftsfähiger thermoelektrischer Materialien ein Kompromiss zwischen thermoelektrischer Performance und der Verfügbarkeit der Elemente gefunden werden muss. Für die Forschung an Chalkogeniden bedeutet das eine zwangsläufige Abkehr von Telluriden zu den wesentlich häufigeren Sulfiden. Erste Ergebnisse struktureller Untersuchungen sind im Abschnitt C 3.1 dieser Arbeit zusammengefasst.

Literaturverzeichnis

- [1] G. I. Finch, S. Fordham, *Proc. Phys. Soc.* **1936**, *48*, 85.
- [2] R. M. Bozorth, *J. Am. Chem. Soc.* **1922**, *44*, 2232–2236.
- [3] L. Pauling, J. L. Hoard, *Z. Für Krist. - Cryst. Mater.* **1930**, *74*, 546–551.
- [4] J. L. Verble, T. J. Wietling, P. R. Reed, *Solid State Commun.* **1972**, *11*, 941–944.
- [5] E. Mooser, F. Lévy, *Crystallography and Crystal Chemistry of Materials with Layered Structures.*, Springer Netherlands, Dordrecht, **2011**.
- [6] B. Schönfeld, J. J. Huang, S. C. Moss, *Acta Crystallogr. B* **1983**, *39*, 404–407.
- [7] K. S. Novoselov, A. K. Geim, S. V. Morozov, D. Jiang, Y. Zhang, S. V. Dubonos, I. V. Grigorieva, A. A. Firsov, *Science* **2004**, *306*, 666–669.
- [8] K. F. Mak, C. Lee, J. Hone, J. Shan, T. F. Heinz, *Phys. Rev. Lett.* **2010**, *105*, 136805.
- [9] A. Splendiani, L. Sun, Y. Zhang, T. Li, J. Kim, C.-Y. Chim, G. Galli, F. Wang, *Nano Lett.* **2010**, *10*, 1271–1275.
- [10] A. K. Geim, I. V. Grigorieva, *Nature* **2013**, *499*, 419–425.
- [11] A. Koma, *Thin Solid Films* **1992**, *216*, 72–76.
- [12] L. A. Ponomarenko, A. K. Geim, A. A. Zhukov, R. Jalil, S. V. Morozov, K. S. Novoselov, I. V. Grigorieva, E. H. Hill, V. V. Cheianov, V. I. Fal'ko, K. Watanabe, T. Taniguchi, R. V. Gorbachev, *Nat. Phys.* **2011**, *7*, 958–961.
- [13] K. S. Novoselov, A. Mishchenko, A. Carvalho, A. H. C. Neto, *Science* **2016**, *353*, aac9439.
- [14] D. C. Johnson, *Curr. Opin. Solid State Mater. Sci.* **1998**, *3*, 159–167.
- [15] D. Golberg, Y. Bando, Y. Huang, T. Terao, M. Mitome, C. Tang, C. Zhi, *ACS Nano* **2010**, *4*, 2979–2993.
- [16] R. Ma, T. Sasaki, *Adv. Mater.* **2010**, *22*, 5082–5104.
- [17] M. Osada, T. Sasaki, *J. Mater. Chem.* **2009**, *19*, 2503–2511.
- [18] M. Osada, T. Sasaki, *Adv. Mater.* **2012**, *24*, 210–228.
- [19] M. A. Bizeto, A. L. Shiguihara, V. R. L. Constantino, *J. Mater. Chem.* **2009**, *19*, 2512–2525.
- [20] P. Nalawade, B. Aware, V. J. Kadam, R. S. Hirlekar, *JSIR Vol6804 April 2009* **2009**.
- [21] P. F. Luckham, S. Rossi, *Adv. Colloid Interface Sci.* **1999**, *82*, 43–92.
- [22] B. Velde, *Introduction to Clay Minerals: Chemistry, Origins, Uses and Environmental Significance*, Springer Netherlands : Imprint : Springer, Dordrecht, **1992**.
- [23] E. Manias, A. Touny, L. Wu, K. Strawhecker, B. Lu, T. C. Chung, *Chem. Mater.* **2001**, *13*, 3516–3523.
- [24] V. Grasso, Ed., *Electronic Structure and Electronic Transitions in Layered Materials*, D. Reidel; Boston : Norwell, MA, U.S.A., **1986**.
- [25] H. Hahn, C. D. Lorent, *Z. Für Anorg. Allg. Chem.* **1957**, *290*, 68–81.
- [26] B. A. Boukamp, G. A. Wiegers, *Solid State Ion.* **1983**, *9–10, Part 2*, 1193–1196.
- [27] R. Quint, H. Boller, H. Blaha, *Monatshefte Für Chem. Chem. Mon.* **1986**, *117*, 1387–1397.
- [28] R. Quint, H. Boller, H. Blaha, *Monatshefte Für Chem. Chem. Mon.* **1984**, *115*, 975–985.
- [29] J. A. Wilson, A. D. Yoffe, *Adv. Phys.* **1969**, *18*, 193–335.
- [30] M. Chhowalla, H. S. Shin, G. Eda, L.-J. Li, K. P. Loh, H. Zhang, *Nat. Chem.* **2013**, *5*, 263–275.
- [31] Q. H. Wang, K. Kalantar-Zadeh, A. Kis, J. N. Coleman, M. S. Strano, *Nat. Nanotechnol.* **2012**, *7*, 699–712.
- [32] J. Dai, M. Li, X. C. Zeng, *Wiley Interdiscip. Rev. Comput. Mol. Sci.* **2016**, *6*, 211–222.
- [33] V. Nicolosi, M. Chhowalla, M. G. Kanatzidis, M. S. Strano, J. N. Coleman, *Science* **2013**, *340*, 1226419–1226419.
- [34] G. J. Snyder, E. S. Toberer, *Nat. Mater.* **2008**, *7*, 105–114.
- [35] A. F. Ioffe, “Semiconductor thermoelements and thermoelectric cooling,” <http://cds.cern.ch/record/232753>, **1957**.
- [36] D. M. Rowe, *CRC Handbook of Thermoelectrics*, CRC Press, **1995**.

- [37] W. G. Zeier, A. Zevalkink, Z. M. Gibbs, G. Hautier, M. G. Kanatzidis, G. J. Snyder, *Angew. Chem. Int. Ed.* **2016**, *55*, 6826–6841.
- [38] N. Savvides, H. J. Goldsmid, *J. Phys. C Solid State Phys.* **1980**, *13*, 4657.
- [39] H. J. Goldsmid, A. W. Penn, *Phys. Lett. A* **1968**, *27*, 523–524.
- [40] D. M. Rowe, Ed., *Thermoelectrics Handbook: Macro to Nano*, CRC/Taylor & Francis, Boca Raton, **2006**.
- [41] L. D. Hicks, M. S. Dresselhaus, *Phys. Rev. B* **1993**, *47*, 16631–16634.
- [42] L. D. Hicks, M. S. Dresselhaus, *Phys. Rev. B* **1993**, *47*, 12727–12731.
- [43] Glen A. Slack, in *CRC Handb. Thermoelectr.*, CRC Press, **1995**.
- [44] R. Venkatasubramanian, E. Siivola, T. Colpitts, B. O'Quinn, *Nature* **2001**, *413*, 597–602.
- [45] G. Chen, *Phys. Rev. B* **1998**, *57*, 14958–14973.
- [46] M. Winkler, X. Liu, U. Schürmann, J. D. König, L. Kienle, W. Bensch, H. Böttner, *Z. Für Anorg. Allg. Chem.* **2012**, *638*, 2441–2454.
- [47] C. Chiritescu, D. G. Cahill, N. Nguyen, D. Johnson, A. Bodapati, P. Koblinski, P. Zschack, *Science* **2007**, *315*, 351–353.
- [48] A. Shakouri, *Annu. Rev. Mater. Res.* **2011**, *41*, 399–431.
- [49] J. R. Sootsman, D. Y. Chung, M. G. Kanatzidis, *Angew. Chem.* **2009**, *121*, 8768–8792.
- [50] C. J. Vineis, A. Shakouri, A. Majumdar, M. G. Kanatzidis, *Adv. Mater.* **2010**, *22*, 3970–3980.
- [51] K. Biswas, J. He, I. D. Blum, C.-I. Wu, T. P. Hogan, D. N. Seidman, V. P. Dravid, M. G. Kanatzidis, *Nature* **2012**, *489*, 414–418.
- [52] S. Nakajima, *J. Phys. Chem. Solids* **1963**, *24*, 479–485.
- [53] T. Caillat, M. Carle, D. Perrin, H. Scherrer, S. Scherrer, *J. Phys. Chem. Solids* **1992**, *53*, 227–232.
- [54] N. K. Abrikosov, A. Tybulewicz, *Semiconducting II-VI, IV-VI, and V-VI Compounds*, **1969**.
- [55] T. L. Anderson, H. B. Krause, *Acta Crystallogr. B* **1974**, *30*, 1307–1310.
- [56] J. L. F. Da Silva, A. Walsh, H. Lee, *Phys. Rev. B* **2008**, *78*, 224111.
- [57] T. C. Harman, J. M. Honig, *J. Appl. Phys.* **1963**, *34*, 189–194.
- [58] T. C. Harman, J. M. Honig, B. M. Tarmy, *J. Appl. Phys.* **1963**, *34*, 2225–2229.
- [59] A. G. Samoilovich, M. V. Nitsovich, V. M. Nitsovich, *Phys. Status Solidi B* **1966**, *16*, 459–465.
- [60] M. Chitroub, S. Scherrer, H. Scherrer, *J. Phys. Chem. Solids* **2000**, *61*, 1693–1701.
- [61] H. Scherrer, B. Hammou, J. P. Fleurial, S. Scherrer, *Phys. Lett. A* **1988**, *130*, 161–165.
- [62] T. C. Harman, *Bull Amer Phys Soc* **1955**, *30*, 35.
- [63] G. R. Miller, C.-Y. Li, *J. Phys. Chem. Solids* **1965**, *26*, 173–177.
- [64] C. H. Champness, P. T. Chiang, P. Parekh, *Can. J. Phys.* **1965**, *43*, 653–669.
- [65] H. J. Goldsmid, R. W. Douglas, *Br. J. Appl. Phys.* **1954**, *5*, 386.
- [66] H. J. Goldsmid, *Proc. Phys. Soc.* **1958**, *71*, 633.
- [67] B. Poudel, Q. Hao, Y. Ma, Y. Lan, A. Minnich, B. Yu, X. Yan, D. Wang, A. Muto, D. Vashaee, X. Chen, J. Liu, M. S. Dresselhaus, G. Chen, Z. Ren, *Science* **2008**, *320*, 634–638.
- [68] T. Chattopadhyay, J. X. Boucherle, H. G. von Schnering, *J. Phys. C Solid State Phys.* **1987**, *20*, 1431.
- [69] K. Schubert, H. Fricke, *Z. Für Naturforschung A* **1951**, *6*, 781–782.
- [70] K. Schubert, H. Fricke, *Z. Met.* **1953**, *44*, 457–461.
- [71] G. R. Gurbanov, *Russ. J. Inorg. Chem.* **2013**, *58*, 91–95.
- [72] L. E. Shelimova, O. G. Karpinsky, M. A. Kretova, E. S. Avilov, *J. Alloys Compd.* **1996**, *243*, 194–201.
- [73] U. Schürmann, V. Duppel, S. Buller, W. Bensch, L. Kienle, *Cryst. Res. Technol.* **2011**, *46*, 561–568.
- [74] T. Rosenthal, M. N. Schneider, C. Stiewe, M. Döblinger, O. Oeckler, *Chem. Mater.* **2011**, *23*, 4349–4356.

- [75] T. Matsunaga, R. Kojima, N. Yamada, K. Kifune, Y. Kubota, Y. Tabata, M. Takata, *Inorg. Chem.* **2006**, *45*, 2235–2241.
- [76] T. Matsunaga, H. Morita, R. Kojima, N. Yamada, K. Kifune, Y. Kubota, Y. Tabata, J.-J. Kim, M. Kobata, E. Ikenaga, K. Kobayashi, *J. Appl. Phys.* **2008**, *103*, 093511.
- [77] T. Schröder, M. N. Schneider, T. Rosenthal, A. Eisele, C. Gold, E.-W. Scheidt, W. Scherer, R. Berthold, O. Oeckler, *Phys. Rev. B* **2011**, *84*, 184104.
- [78] L. E. Shelimova, P. P. Konstantinov, O. G. Karpinsky, E. S. Avilov, M. A. Kretova, V. S. Zemskov, *J. Alloys Compd.* **2001**, *329*, 50–62.
- [79] G. C. Christakudis, S. K. Plachkova, L. E. Shelimova, E. S. Avilov, *Phys. Status Solidi A* **1991**, *128*, 465–471.
- [80] M. Wuttig, N. Yamada, *Nat. Mater.* **2007**, *6*, 824–832.
- [81] W. Bensch, M. Wuttig, *Chem. Unserer Zeit* **2010**, *44*, 92–107.
- [82] G. I. Meijer, *Science* **2008**, *319*, 1625–1626.
- [83] S. R. Ovshinsky, *Phys. Rev. Lett.* **1968**, *21*, 1450–1453.
- [84] A. V. Kolobov, P. Fons, A. I. Frenkel, A. L. Ankudinov, J. Tominaga, T. Uruga, *Nat. Mater.* **2004**, *3*, 703–708.
- [85] E. Canadell, S. Jobic, R. Brec, J. Rouxel, *J. Solid State Chem.* **1992**, *98*, 59–70.
- [86] K. O. Klepp, H. Ipser, *Monatshefte Für Chem. Chem. Mon.* **1979**, *110*, 499–501.
- [87] K. O. Klepp, H. Ipser, *Angew. Chem.* **1982**, *94*, 931–932.
- [88] H. Ipser, K. L. Komarek, K. O. Klepp, *J. Common Met.* **1983**, *92*, 265–282.
- [89] M. A. McGuire, V. O. Garlea, S. KC, V. R. Cooper, J. Yan, H. Cao, B. C. Sales, *ArXiv170108621 Cond-Mat* **2017**.
- [90] S. Kraschinski, S. Herzog, W. Bensch, *Solid State Sci.* **2002**, *4*, 1237–1243.
- [91] M. Behrens, J. Tomforde, E. May, R. Kiebach, W. Bensch, D. Häußler, W. Jäger, *J. Solid State Chem.* **2006**, *179*, 3330–3337.
- [92] P. F. Bongers, C. F. Van Bruggen, J. Koopstra, W. P. F. A. M. Omloo, G. A. Wiegers, F. Jellinek, *J. Phys. Chem. Solids* **1968**, *29*, 977–984.
- [93] N. Le Nagard, G. Collin, O. Gorochov, *Mater. Res. Bull.* **1979**, *14*, 1411–1417.
- [94] R. A. Yakshibaev, G. R. Akmanova, R. F. Almukhametov, V. N. Konev, *Phys. Status Solidi A* **1991**, *124*, 417–426.
- [95] G. C. Tewari, T. S. Tripathi, A. K. Rastogi, *J. Electron. Mater.* **2010**, *39*, 1133–1139.
- [96] Y.-X. Chen, B.-P. Zhang, Z.-H. Ge, P.-P. Shang, *J. Solid State Chem.* **2012**, *186*, 109–115.
- [97] D. Srivastava, G. C. Tewari, M. Karppinen, R. M. Nieminen, *J. Phys. Condens. Matter* **2013**, *25*, 105504.
- [98] G. C. Tewari, T. S. Tripathi, P. Kumar, A. K. Rastogi, S. K. Pasha, G. Gupta, *J. Electron. Mater.* **2011**, *40*, 2368–2373.
- [99] G. C. Tewari, T. S. Tripathi, A. K. Rastogi, *Z. Für Krist. Cryst. Mater.* **2010**, *225*, 471–474.
- [100] C.-G. Han, B.-P. Zhang, Z.-H. Ge, L.-J. Zhang, Y.-C. Liu, *J. Mater. Sci.* **2013**, *48*, 4081–4087.
- [101] A. Kaltzoglou, P. Vaqueiro, T. Barbier, E. Guilmeau, A. V. Powell, *J. Electron. Mater.* **2014**, *43*, 2029–2034.
- [102] R. E. Dinnebier, S. J. L. Billinge, Eds. , *Powder Diffraction*, Royal Society Of Chemistry, Cambridge, **2008**.
- [103] E. J. Mittemeijer, U. Welzel, Eds. , *Modern Diffraction Methods*, Wiley-VCH, Weinheim, **2013**.
- [104] H. M. Rietveld, *Acta Crystallogr.* **1967**, *22*, 151–152.
- [105] R. Dinnebier, M. Müller, in *Mod. Diffr. Methods* (Eds.: E.J. Mittemeijer, U. Welzel), Wiley-VCH Verlag GmbH & Co. KGaA, Weinheim, Germany, **2013**, pp. 27–60.
- [106] L. B. McCusker, R. B. Von Dreele, D. E. Cox, D. Louër, P. Scardi, *J. Appl. Crystallogr.* **1999**, *32*, 36–50.
- [107] D. S. Young, B. S. Sachais, L. C. Jefferies, *The Rietveld Method*, **1993**.
- [108] H. P. Klug, L. E. Alexander, *X-Ray Diffraction Procedures for Polycrystalline and Amorphous Materials*, Wiley, New York, **1974**.
- [109] R. W. Cheary, A. Coelho, *J. Appl. Crystallogr.* **1992**, *25*, 109–121.

- [110] W. H. Hall, *Proc. Phys. Soc. Sect. A* **1949**, *62*, 741.
- [111] G. K. Williamson, W. H. Hall, *Acta Metall.* **1953**, *1*, 22–31.
- [112] P. Scardi, M. Leoni, *Acta Crystallogr. A* **2002**, *58*, 190–200.
- [113] P. Scardi, M. Leoni, in *Diffr. Anal. Microstruct. Mater.* (Eds.: E.J. Mittemeijer, P. Scardi), Springer Berlin Heidelberg, **2004**, pp. 51–91.
- [114] P. Scardi, M. Leoni, Y. H. Dong, *Eur. Phys. J. B - Condens. Matter Complex Syst.* **2000**, *18*, 23–30.
- [115] B. L. Averbach, B. E. Warren, *J. Appl. Phys.* **1949**, *20*, 885–886.
- [116] B. E. Warren, *X-Ray Diffraction*, Dover Publications, New York, **1990**.
- [117] Coelho, A. A. Topas Academic (Version 6); Coelho Software, Australia, **2016**.
- [118] A. A. Coelho, J. S. O. Evans, J. W. Lewis, *J. Appl. Crystallogr.* **2016**, *49*, 1740–1749.
- [119] S. J. L. Billinge, M. G. Kanatzidis, *Chem. Commun.* **2004**, 749–760.
- [120] T. Egami, *Mater. Trans. JIM* **1990**, *31*, 163–176.
- [121] T. Egami, S. J. L. Billinge, *Underneath the Bragg Peaks: Structural Analysis of Complex Materials*, Elsevier, Amsterdam, **2012**.
- [122] T. Proffen, S. J. L. Billinge, T. Egami, D. Louca, *Z. Für Krist. - Cryst. Mater.* **2009**, *218*, 132–143.
- [123] K. Ramesha, A. Llobet, T. Proffen, C. R. Serrao, C. N. R. Rao, *J. Phys. Condens. Matter* **2007**, *19*, 102202.
- [124] K. Page, T. Kolodiaznyi, T. Proffen, A. K. Cheetham, R. Seshadri, *Phys. Rev. Lett.* **2008**, *101*, 205502.
- [125] X. Qiu, T. Proffen, J. F. Mitchell, S. J. L. Billinge, *Phys. Rev. Lett.* **2005**, *94*, 177203.
- [126] K. L. Page, T. Proffen, R. B. Neder, in *Mod. Diffr. Methods* (Eds.: E.J. Mittemeijer, U. Welzel), Wiley-VCH Verlag GmbH & Co. KGaA, Weinheim, Germany, **2013**, pp. 61–86.
- [127] M. W. Gaultois, T. D. Sparks, C. K. H. Borg, R. Seshadri, W. D. Bonificio, D. R. Clarke, *Chem. Mater.* **2013**, *25*, 2911–2920.
- [128] A. O. Hirschman, *National Power and the Structure of Foreign Trade*, University Of California Press, Berkeley, **1980**.

E Anhang

Liste der Veröffentlichungen und Tagungsbeiträge

1. M. Winkler, X. Liu, A.-L. Hansen, J. D. König, W. Bensch, L. Kienle, H. Böttner, K. Bartholomé, *Nanothermoelectrics* **2013**, *1*, 1–9.
2. A.-L. Hansen, T. Dankwort, M. Winkler, J. Ditto, D. C. Johnson, J. D. König, K. Bartholomé, L. Kienle, W. Bensch, *Chem. Mater.* **2014**, *26*, 6518–6522.
3. J. König, M. Winkler, T. Dankwort, A.-L. Hansen, H.-F. Pernau, V. Duppel, M. Jaegle, K. Bartholomé, L. Kienle, W. Bensch, *Dalton Trans* **2015**, *44*, 2835–2843.
4. T. Dankwort, A.-L. Hansen, M. Winkler, U. Schürmann, J. D. König, D. C. Johnson, N. F. Hinsche, P. Zahn, I. Mertig, W. Bensch, L. Kienle, *Phys. Status Solidi A* **2016**, *213*, 662–671.
5. S. Permien, S. Indris, A.-L. Hansen, M. Scheuermann, D. Zahn, U. Schürmann, G. Neubüser, L. Kienle, E. Yegudin, W. Bensch, *ACS Appl. Mater. Interfaces* **2016**, *8*, 15320–15332.
6. C. Koch, A.-L. Hansen, T. Dankwort, G. Schienke, M. Paulsen, D. Meyer, M. Wimmer, M. Wuttig, L. Kienle, W. Bensch, *RSC Adv.* **2017**, *7*, 17164–17172.
7. M. Krengel, A.-L. Hansen, M. Kaus, S. Indris, N. Wolff, L. Kienle, D. Westfal, W. Bensch, *ACS Appl. Mater. Interfaces* **2017**, *9*, 21283–21291.
8. A.-L. Hansen, T. Dankwort, H. Groß, M. Etter, J. König, V. Duppel, L. Kienle, W. Bensch, *Journal of Materials Chemistry C*, **2017**, (accepted) DOI: 10.1039/C7TC02983G.

9. *In-situ* X-ray diffraction of superlattice thin film thermoelectrics (Invited talk)

European XRD Days, Dresden

04. – 06.03.2015

10. Chalcogenide based thermoelectric materials

15th European Powder Diffraction Conference, Bari

12. – 15.06.2016

11. Chalcogenide based thermoelectric materials – Microstructure and thermoelectric performance (Poster)

Thick and thin Multifaceted Properties of Layered Materials

18. Conference of the GDCh Division

Solid State Chemistry and Materials Research Innsbruck,

Austria September 19–21, 2016

Z. Für Anorg. Allg. Chem. **2016**, 642, 989–996

12. Chalkogenid-basierte Thermoelektrika - Mikrostruktur und Performance

AC-Kolloquium Wintersemester 2016/17

22.11.2016

Electronic supporting information

(Entsprechend der laufenden Nummer der Liste der Veröffentlichungen und Tagungsbeiträge)

3. J. König, M. Winkler, T. Dankwort, A.-L. Hansen, H.-F. Pernau, V. Duppel, M. Jaegle, K. Bartholomé, L. Kienle, W. Bensch, *Dalton Trans* **2015**, *44*, 2835–2843.

Electronic Supplementary Material (ESI) for Dalton Transactions.
This journal is © The Royal Society of Chemistry 2014

Supporting Information

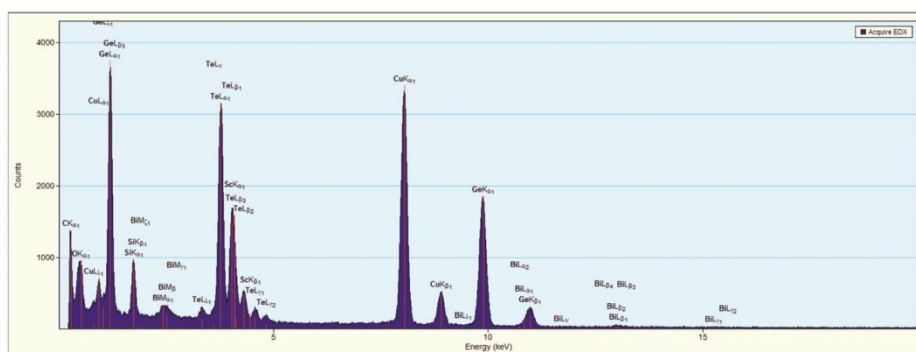


Figure S1. A representative EDX spectra for 0.962(GeTe) 0.038(Bi₂Se_{0.2}Te_{2.8}) (the sample with the lowest Bi content). As also stated in the manuscript the Bi M-line is observed.

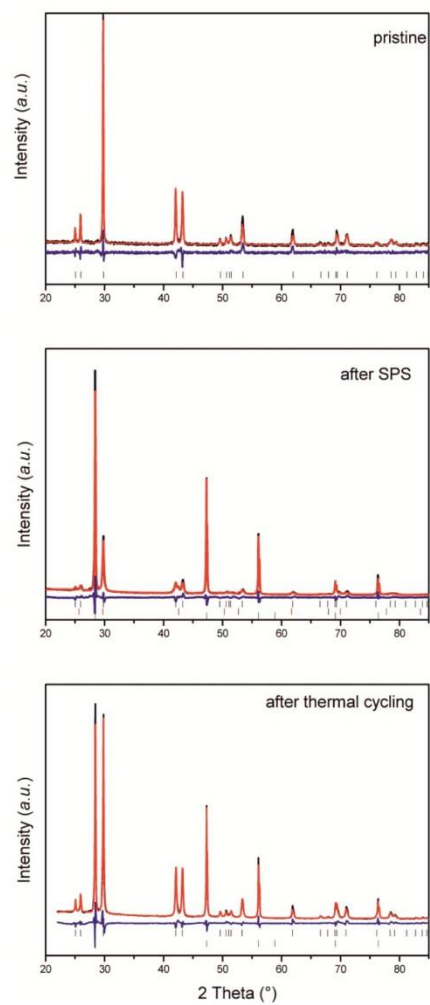


Figure S2. Fitted XRD pattern of $(\text{GeTe})_{0.937}(\text{Bi}_2\text{Te}_{2.8}\text{Se}_{0.2})_{0.063}$ at 28 °C in the pristine stage, after SPS and after thermal cycling. Observed (black), calculated (red) and difference curves (blue) are shown, reflection positions indicated by vertical bars.

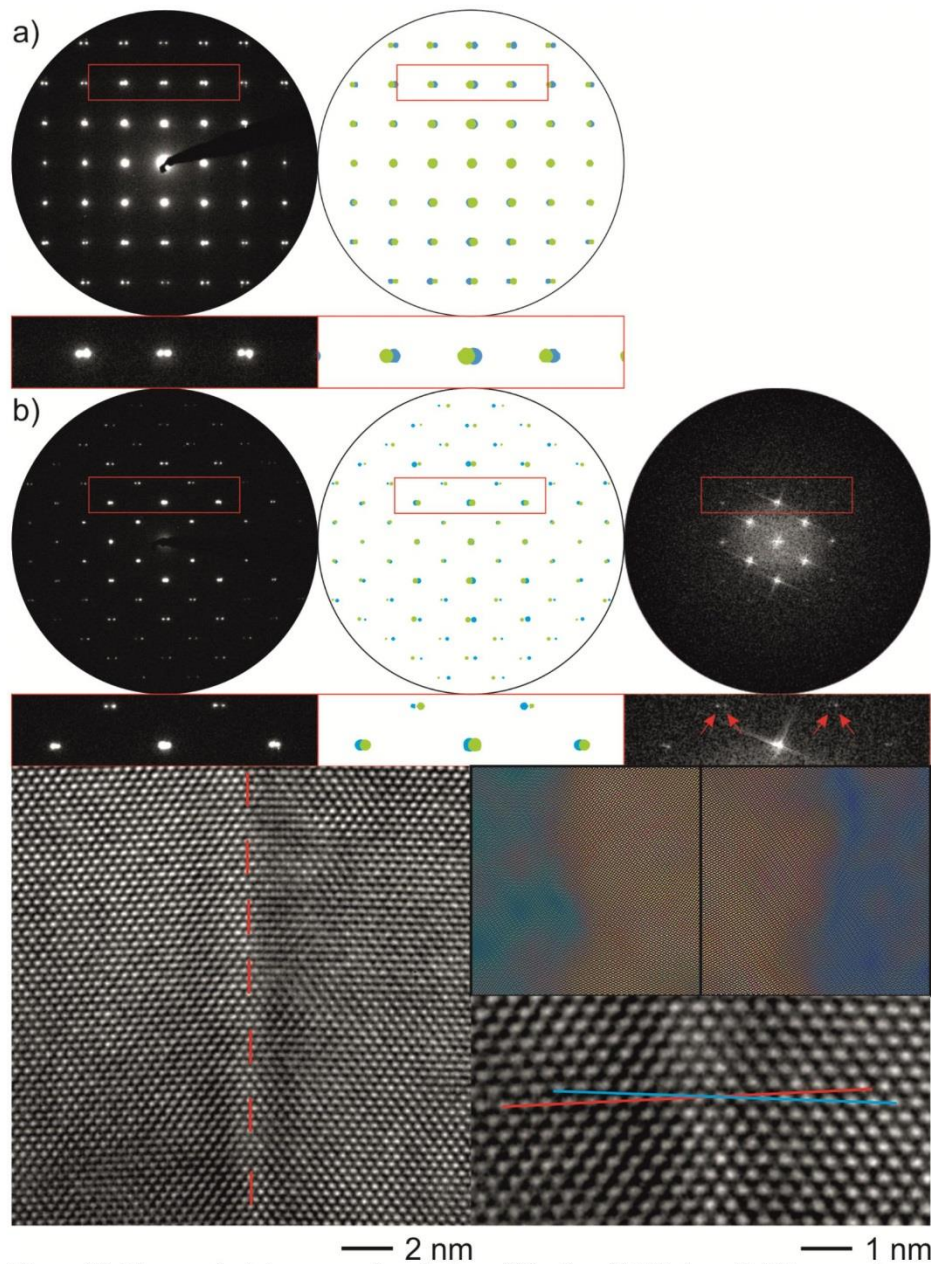


Figure S3. Figure a depicts a precession electron diffraction (PED) along $[1-11]$ zone axis with a twin boundary along (110) . The right image represents the respective superimposed calculated diffraction patterns for the different twin domains. Figure b depicts a PED, superimposed calculated diffraction pattern, FFT and HRTEM along $[-110]$ with a twin boundary along (112) . The HRTEM micrograph depicts an on edge twin boundary (marked with a red dashed line). The right images represent the inverse fourier filtering of the different

twin domains. The image below shows an enlarged section of the twin boundary with the red and the blue lines guiding the eye along the two twin domains.

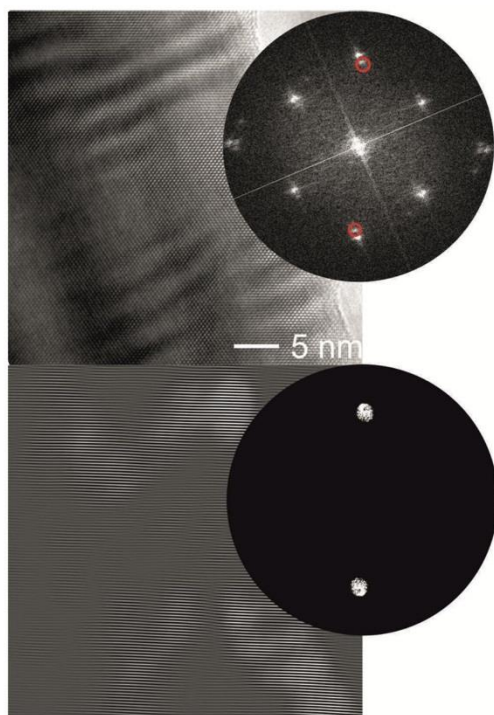


Figure S4. IFFT filtering of fringes in $(\text{GeTe})_{0.937}(\text{Bi}_2\text{Se}_{0.2}\text{Te}_{2.8})_{0.063}$. The top and the bottom images depict the HRTEM micrograph and the IFFT filtered image, respectively. The red circle in the FFT marks the diffraction spot used for IFFT filtering.

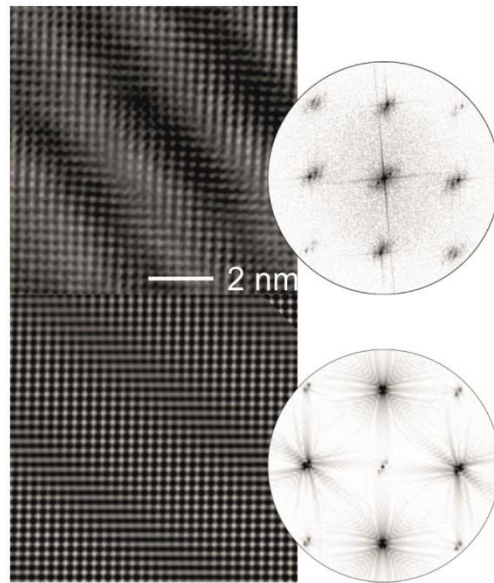


Figure S5. The top image represents a HRTEM micrograph and FFT of the observed fringes in $\langle -110 \rangle$ zone axis. The image below represents the superposition of calculated HRTEM micrographs of α and β phase and the corresponding FFT.

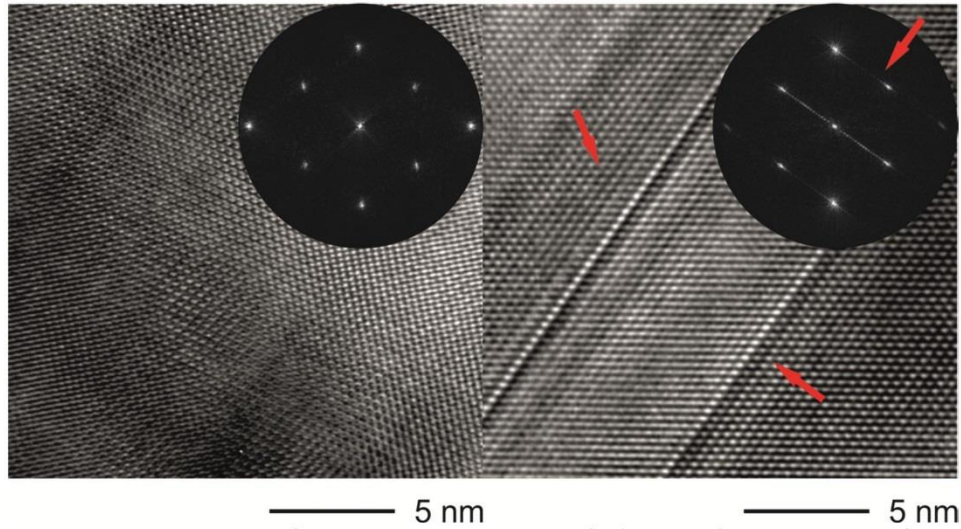


Figure S6: Comparison of representative regions of the samples in state 3 for $(\text{GeTe})_{0.962}(\text{Bi}_2\text{Se}_{0.2}\text{Te}_{2.8})_{0.038}$ (left) and $(\text{GeTe})_{0.937}(\text{Bi}_2\text{Se}_{0.2}\text{Te}_{2.8})_{0.063}$ (right). For sample $(\text{GeTe})_{0.937}(\text{Bi}_2\text{Se}_{0.2}\text{Te}_{2.8})_{0.063}$ formation of planar defects along $\langle 111 \rangle$ and $\langle 001 \rangle$ directions are observed which are absent in the sample $(\text{GeTe})_{0.962}(\text{Bi}_2\text{Se}_{0.2}\text{Te}_{2.8})_{0.038}$ (right). The insets show FFTs of the corresponding areas. In the case of $(\text{GeTe})_{0.937}(\text{Bi}_2\text{Se}_{0.2}\text{Te}_{2.8})_{0.063}$ diffuse intensities correlate to the planar defects (marked with red arrows).

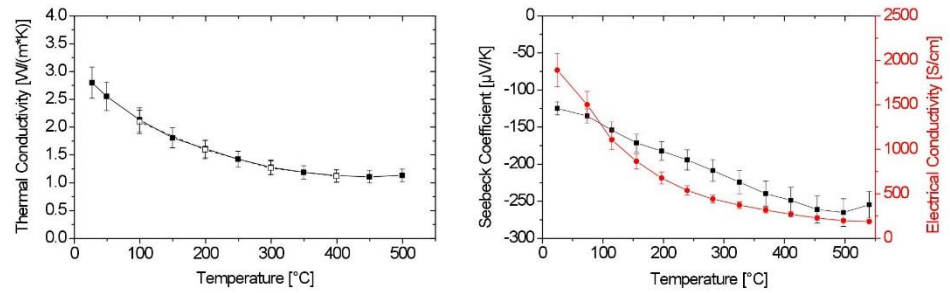


Figure S7. Transport data of SPS-compacted Bi-doped PbTe in dependence on temperature. Left: Thermal conductivity. Right: Seebeck coefficient (black) and electrical conductivity (red). Full data points: heating, empty points: cooling

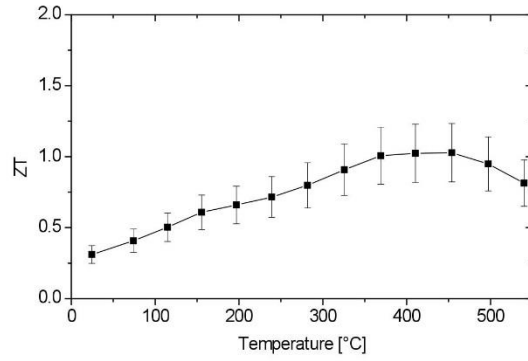


Figure S8. Figure of merit ZT of SPS-compacted Bi-doped PbTe in dependence on temperature. For calculating the ZT value for the highest temperature, the thermal conductivity value was extrapolated from the data obtained up to 500°C.

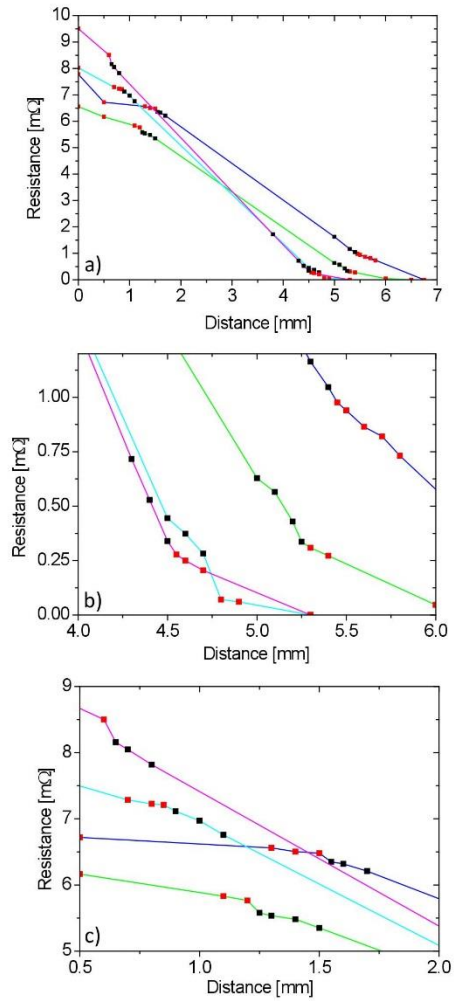


Figure S9. Plot of resistance versus distance between probing needle and front contact for different material / contact combinations. Black points = $(\text{GeTe})_{1-x}(\text{Bi}_2\text{Se}_{0.2}\text{Te}_{2.8})_x$ (thermoelectric material), red points = SnTe (contact). Near the leg/contact interface, the number of acquired data points was significantly increased in order to accurately determine the voltage drop corresponding to contact resistance. a) Resistance / distance plot for whole leg + contacts, b) leg + front contact, c) leg + back contact, both magnified sections from plot a.

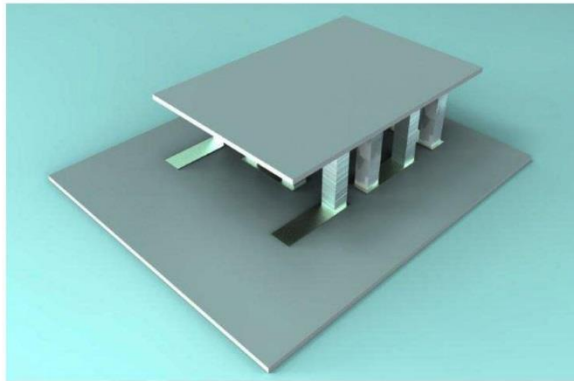


Figure S10. Drawing of assembled thermoelectric module.

5. S. Permien, S. Indris, A.-L. Hansen, M. Scheuermann, D. Zahn, U. Schürmann, G. Neubüser, L. Kienle, E. Yegudin, W. Bensch, *ACS Appl. Mater. Interfaces* **2016**, *8*, 15320–15332.

Supporting Information

Elucidation of the Conversion Reaction of CoMnFeO_4 Nanoparticles in Lithium Ion Battery Anode via *Operando* Studies

Stefan Permien¹, Sylvio Indris², Anna-Lena Hansen¹, Marco Scheuermann², Dirk Zahn⁴, Ulrich Schürmann³, Gero Neubüser³, Lorenz Kienle³, Eugen Yegudin¹, Wolfgang Bensch^{1*}

¹Institute of Inorganic Chemistry, University of Kiel, Max-Eyth-Straße 2, 24118 Kiel, Germany

²IAM-ESS, Karlsruhe Institute of Technology, P.O. box 3640, 76021 Karlsruhe, Germany

³Institute for Materials Science, University of Kiel, Kaiserstraße 2, 24143 Kiel, Germany

⁴Chair for theoretical Chemistry/Computer Chemistry Centrum, Friedrich-Alexander Universität Erlangen-Nürnberg, Nagelsbachstraße 25, 91052 Erlangen, Germany

Email: wbensch@ac.uni-kiel.de

SEM image of the as-prepared material is presented in Figure S1, left, and the EDX spectrum is shown in Figure S1, right. Mn, Fe and Co K line are close to each other. The Fe K $_{\alpha}$ line is overlapping with the Mn K $_{\beta}$ line and the Fe K $_{\beta}$ line with Co K $_{\alpha}$ line.

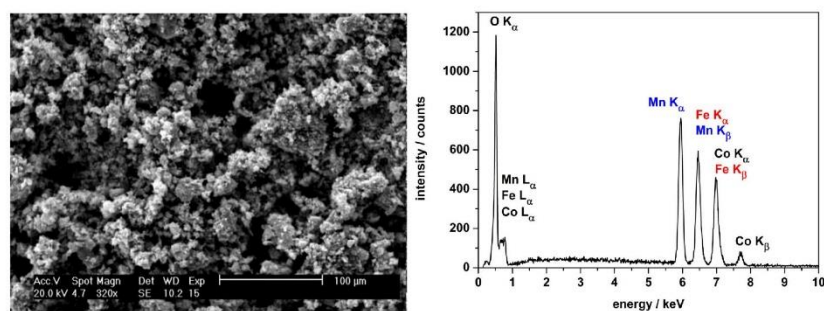


Figure S1: SEM image (left) and EDX spectra (right) of CoFeMnO₄ nanoparticles.

Data of the EDX analysis at different positions is shown in Table S1.

Table S1: EDX analysis of Mn, Fe and Co K line at 6 different positions.

position	Mn K / At %	Fe K / At %	Co K / At %
1	37.03	31.9	31.06
2	37.61	30.43	31.96
3	36.17	30.79	33.04
4	35.79	30.37	33.85
5	36.82	31.2	31.98
6	37.29	30.52	32.19
Average	36.79	30.87	32.35

SAED pattern comparison of experimental and calculated reflections is presented in Table S2.

Table S2: SAED pattern (space group $Fd\bar{3}m$, a = axis: 8.380 Å)

d (hkl)	experimental	calculated
111	4.89	4.84
220	2.95	2.96
311	2.52	2.53
400	2.10	2.10
333/511	1.60	1.61
440	1.47	1.48

Magnification of HRTEM image, arrows point to the amorphous surface on the nanoparticles (Figure S2).

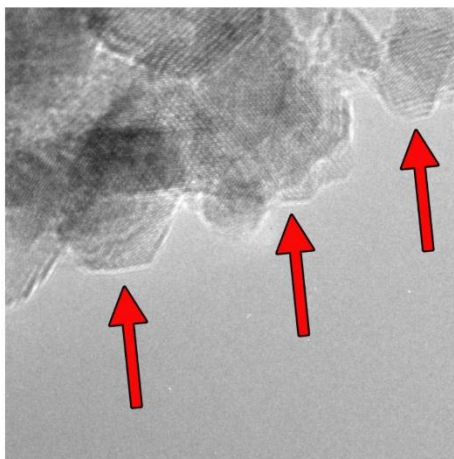


Figure S2: Magnification of HRTEM image, at the surface of crystalline particles (area with grid lines) an amorphous surface is visible.

In Figure S3 *operando* XRD scan 30 (after uptake of 2.5 Li per formula unit) is presented and compared with simulated powder patterns of a mixture of MnO ($Fm\bar{3}m$, $a = 4.441 \text{ \AA}$), CoO ($Fm\bar{3}m$, $a = 4.258 \text{ \AA}$) and $Fe_{1-x}O$ ($Fm\bar{3}m$, $a = 4.300 \text{ \AA}$) ratio 1:1:1 for 3 nm and 8 nm particle size. The simulated pattern shows asymmetric reflections, which can be excluded for the observed powder pattern (scan 30). This observation supports the assumption that just a monoxide phase is formed after uptake of 2.5 Li per formula unit.

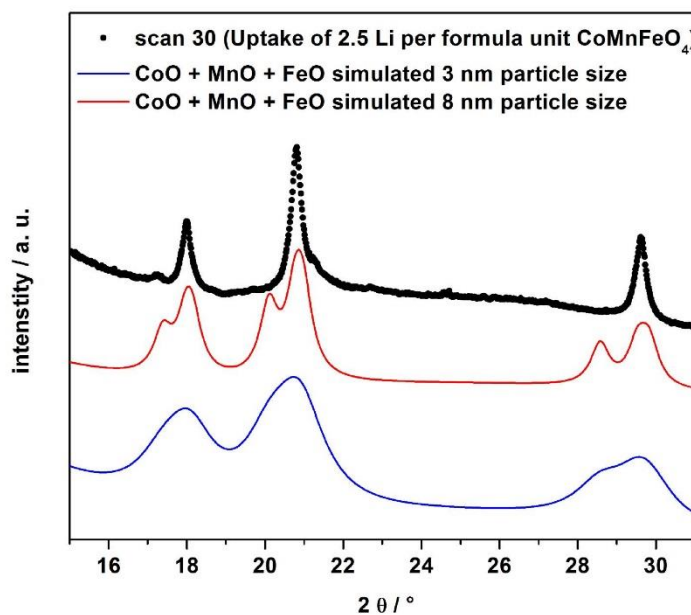


Figure S3: *operando* XRD scan 30 (black) and simulated powder patterns of a 1:1:1 mixture of MnO, CoO and $Fe_{1-x}O$ with 8 nm (red) and 3 nm (blue) particle size.

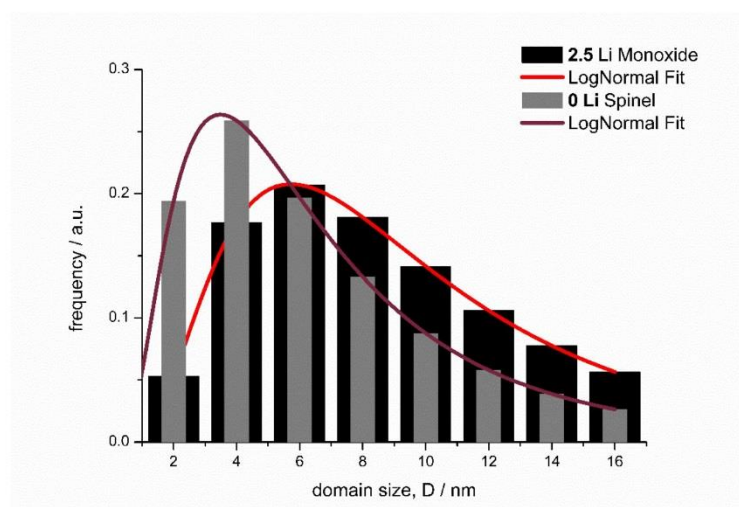


Figure S4: LogNormal size distribution of the coherent scattering domains calculated employing whole powder pattern modelling (WPPM). Comparison of pristine stage (= 0 Li) and after 2.5 Li uptake.

XAS spectra of pristine CoMnFeO_4 and at the end of region I, II and III at Mn, Fe and Co K-edge are presented in Figure S5.

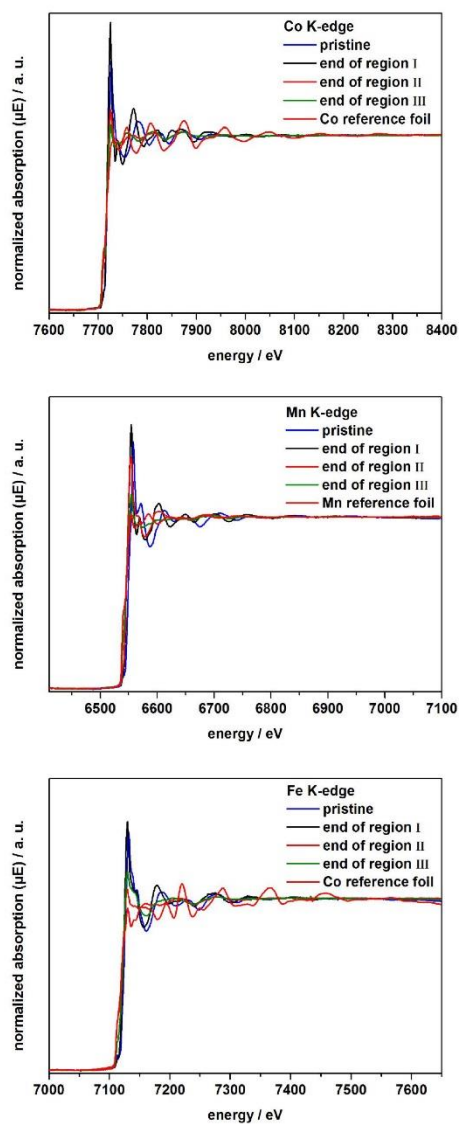


Figure S5: XAS spectra of pristine CoMnFeO_4 (blue) and at the end of region I (black), region II (red) and region III (green) of Mn K-edge (top), Fe K-edge (bottom) and Co K-edge (top) with corresponding reference foils (red).

Ex situ XANES spectra of pristine CoMnFeO_4 and after first cycle at Mn, Fe and Co K-edge. To illustrate the energy shift, Mn, Fe and Co reference foils are shown as dashed lines (Figure S6).

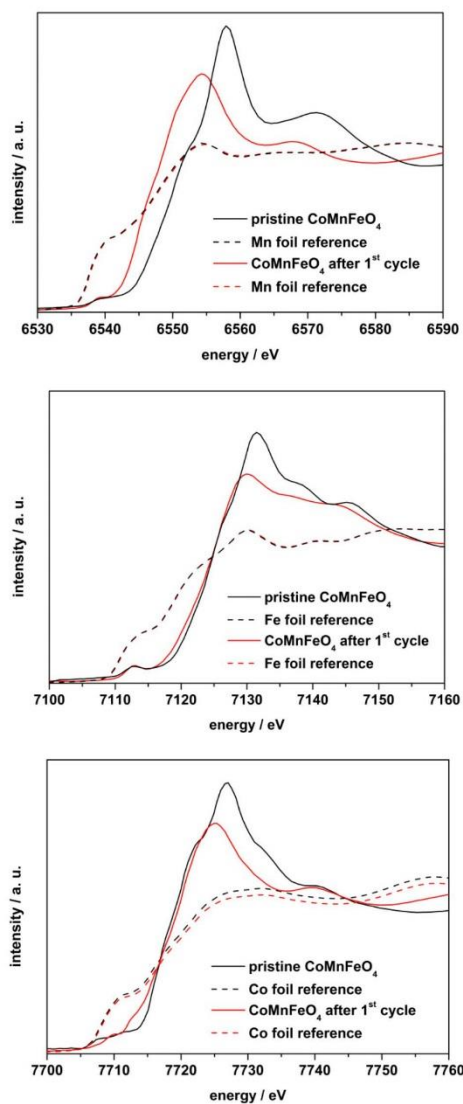


Figure S6: XANES spectra of pristine CoMnFeO_4 (black line) and after first cycle (red line) of Mn K-edge (top), Fe K-edge (middle) and Co K-edge (bottom) with corresponding reference foils (dashed lines).

Preparation of lithiated samples for TEM: 80 wt% CoMnFeO_4 Nanoparticles (active material) were mixed with 10 wt% binder (sodium carboxy methylcellulose) and 10 wt% carbon. The mixture was mixed with water to form a viscous slurry and dropped onto the TEM grid. Afterwards, the TEM grid was mounted in a Swagelock cell as described in section 2. Cell A was discharged to 10 mV and cell B was cycled three times between 10 mV and 3 V. In Figure S7 the cell potential is plotted against the time. Both cells were discharged with $5 \mu\text{A}$.

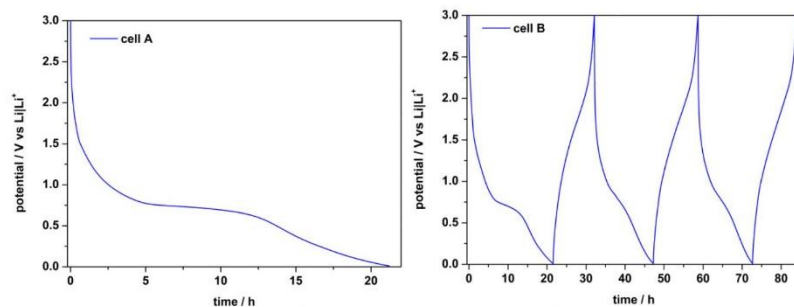


Figure S7: Potential curve of the Swagelock cells with coated TEM grid inside discharged/charged with $5 \mu\text{A}$ cell A (left) and cell B (right).

FFT transformation of HRTEM image is shown in Figure S8 revealing that the obtained product is amorphous.

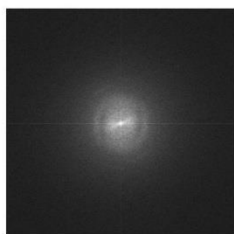


Figure S8: FFT transformation of HRTEM image.

Repeated cycling in a potential range from 1.3 to 3.0 V (Figure S9).

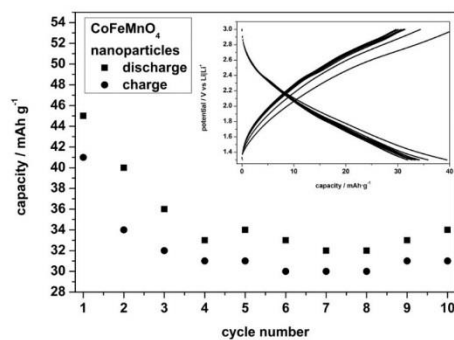


Figure S9: Capacity of the first 10 cycles in a potential range from 3.0 to 1.3 V. Inset: voltage profiles acquired during cycling.

6. C. Koch, A.-L. Hansen, T. Dankwort, G. Schienke, M. Paulsen, D. Meyer, M. Wimmer, M. Wuttig, L. Kienle, W. Bensch, *RSC Adv.* **2017**, *7*, 17164–17172.

Electronic Supplementary Material (ESI) for RSC Advances.
This journal is © The Royal Society of Chemistry 2017

Enhanced Temperature Stability and exceptionally high electrical Contrast of Selenium substituted $\text{Ge}_2\text{Sb}_2\text{Te}_5$ Phase Change Materials

Christine Koch,^a Anna-Lena Hansen,^a Torben Dankwort,^b Gerrit Schienke,^a Melf Paulsen,^a Dominik Meyer,^c Martin Wimmer,^c Matthias Wuttig,^c Lorenz Kienle,^b Wolfgang Bensch^a

^a Institute for Inorganic Chemistry, University of Kiel, Max-Eyth-Str. 2, 24118 Kiel, Germany

^b Institute for Materials Science, University of Kiel, Kaiserstr. 2, 24143 Kiel, Germany

^c Institute of Physics, RWTH Aachen University, Sommerfeldstr. 14, 52056 Aachen, Germany

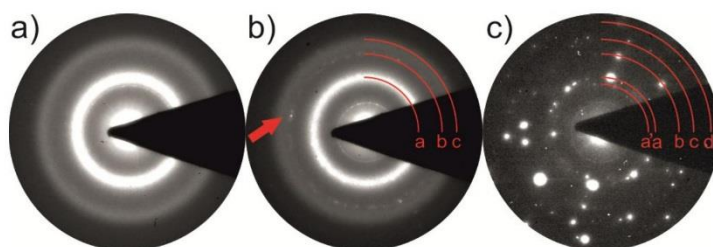


Fig. S1 $\text{Ge}_2\text{Sb}_2\text{Te}_5$ ED: a) at room temperature; b) crystallization starts at 132 °C; c) electron diffraction at 150 °C. The red arrow marks first visible diffraction spots.

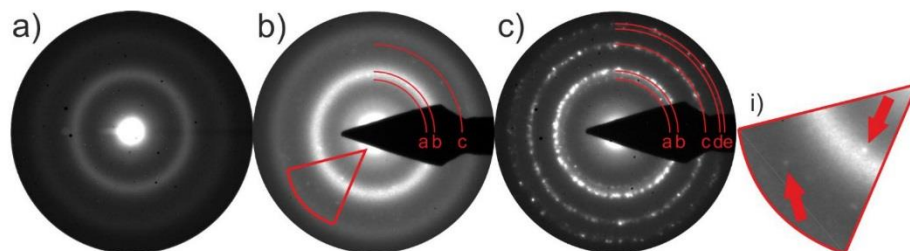


Fig. S2 $\text{Ge}_2\text{Sb}_2\text{Te}_4\text{Se}$ ED: a) at room temperature; b) at 160 °C c) at 190 °C. The red arrow marks first visible diffraction spots. Further the red curves show the rotational average of the respective electron diffraction pattern.

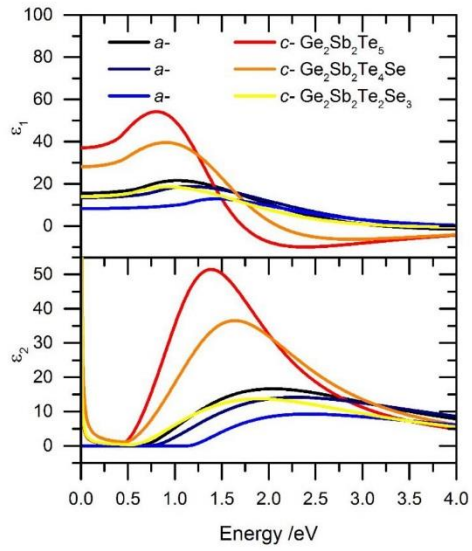


Fig. S3 Functions of ϵ_1 and ϵ_2 including the Drude term.

Table S1 d-values of $\text{Ge}_2\text{Sb}_2\text{Te}_5$ according to the caption in Figure S1.

	d-value / \AA	plane
a'	3.57	(111)
a	2.96	(002)
b	2.11	(022)
c	1.75	(222)
d	1.51	(004)

Table S2 d-values of $\text{Ge}_2\text{Sb}_2\text{Te}_4\text{Se}$ according to the caption in Figure S2.

	d-value / \AA	plane
a	3.43	(003)
b	3.05	(012)
c	2.14	(-114)
d	1.79	(006)
e	1.73	(-222)

Table S3 d-values of $\text{Ge}_2\text{Sb}_2\text{Te}_2\text{Se}_3$ according to the caption in Figure 3.

	d-value / Å	plane
a'	3.44	(003)
a	3.01	(012)
b	2.09	(-114)
c	1.78	(006)
d	1.69	(-222)
e	1.48	(024)

Table S4 Rhombohedral setting.

rhombohedral setting	a / Å	α / °
$\text{Ge}_2\text{Sb}_2\text{Te}_4\text{Se}_1$	4.2404	59.34
$\text{Ge}_2\text{Sb}_2\text{Te}_2\text{Se}_3$	4.2156	58.57

7. M. Kregel, A.-L. Hansen, M. Kaus, S. Indris, N. Wolff, L. Kienle, D. Westfal, W. Bensch, *ACS Appl. Mater. Interfaces* **2017**, *9*, 21283–21291.

Supporting Information

CuV₂S₄: A high Rate-Capacity and Stable Anode Material for Sodium-ion Batteries

Markus Kregel¹, Anna-Lena Hansen¹, Maximilian Kaus², Sylvio Indris², Niklas Wolff³, Lorenz Kienle³, David Westfal¹ and Wolfgang Bensch^{1*}

¹ Institute for Inorganic Chemistry, Christian-Albrechts-Universität zu Kiel, Max-Eyth-Str.2, 24118 Kiel, Germany

² Institute for Applied Materials – Energy Storage Systems (IAM-ESS), Karlsruhe Institute of Technology (KIT), Hermann-von-Helmholtz-Platz 1, 76344 Eggenstein-Leopoldshafen, Germany

³ Institute for Materials Science, Christian-Albrechts-Universität zu Kiel, Kaiserstr. 2, 24143 Kiel, Germany

*To whom correspondence should be addressed. E-mail: wbench@ac.uni-kiel.de

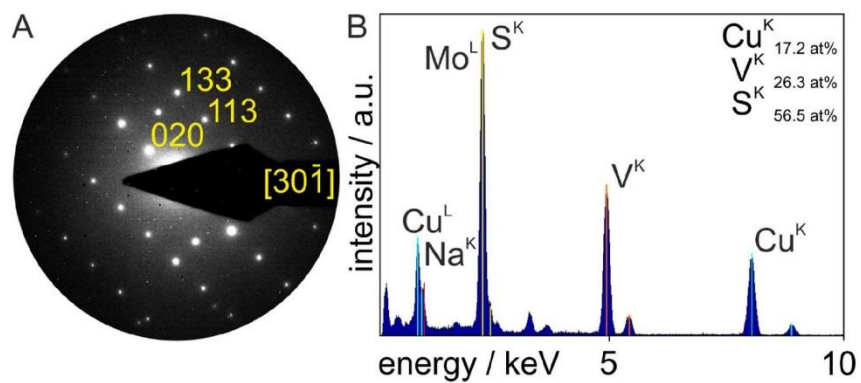


Fig. S1: (A) ED pattern recorded on a selected area containing a larger crystallite of CuV_2S_4 (Fd3-m, $[30\bar{1}]$ zone axis orientation). (B) TEM EDX spectrum depicting all relevant transition lines for CuV_2S_4 +Na.

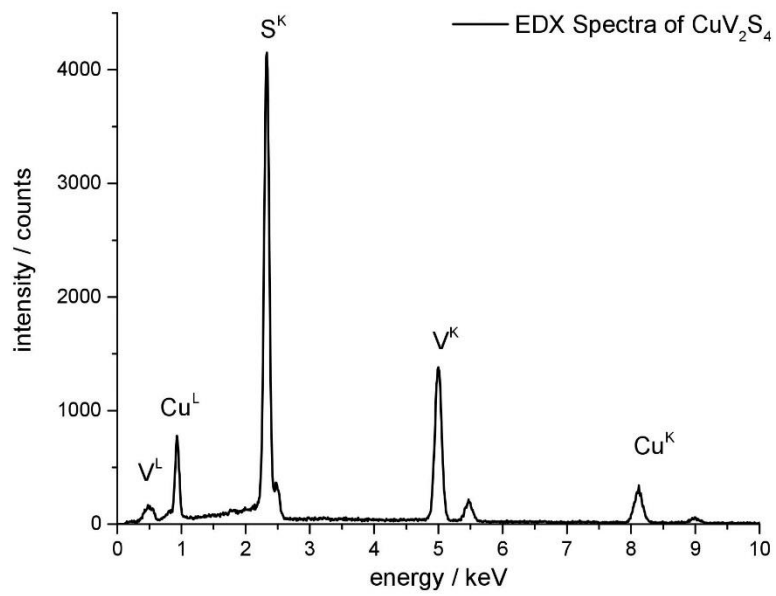


Fig. S 2 EDX spectrum of the prepared CuV_2S_4 sample.

Table S1 Calculated sum formula from the EDX measurements of the synthesized CuV_2S_4 powder.

Position	Cu	V	S
1	1.14	2	3.913
2	0.99	2	4.342
3	1.06	2	3.784
\emptyset	1.07	2	4.01

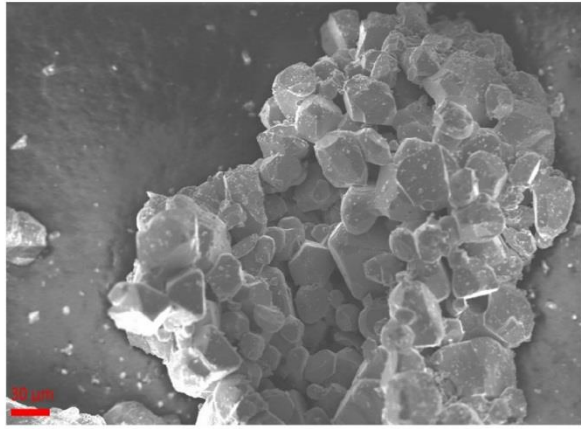


Fig. S3: SEM image of CuV₂S₄

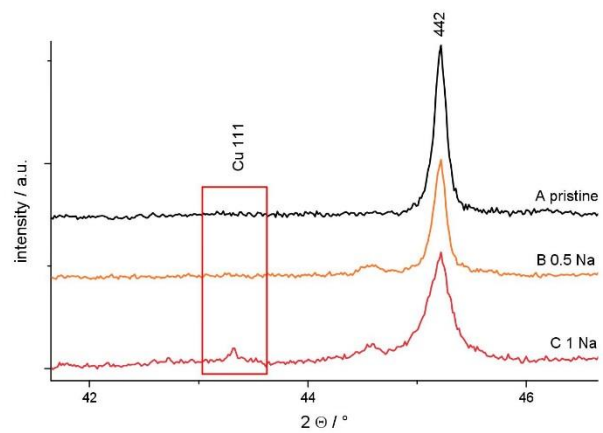


Fig. S4: Magnification of the ex situ XRD patterns for the pristine material, and after the uptake of 0.5 and 1 Na.

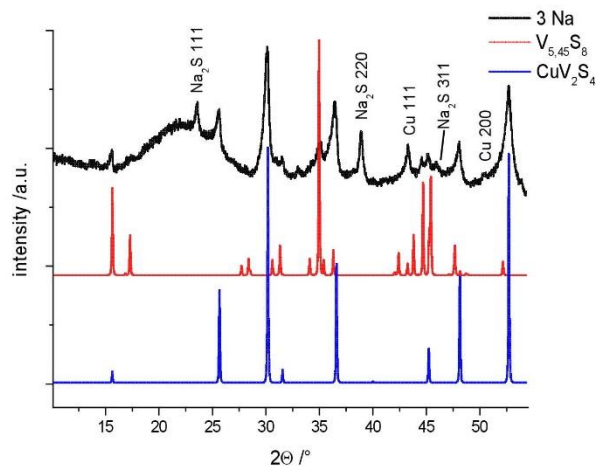


Fig. S5: *ex situ* XRD patterns after the uptake of 3 Na (black) and the calculated patterns for $V_{5.45}S_8$ (red) and CuV_2S_4 (blue).

Fig. S5 displays the *ex situ* XRD pattern for CuV_2S_4 after the uptake of 3 Na. Besides the reflections of Na_2S , metallic Cu and residual CuV_2S_4 additional reflections can be observed that may be explained by the formation $V_{5.45}S_8$. Because most vanadium sulfides show the most intense reflections in this region the evolving phase cannot be unambiguously assigned to a distinct compound.

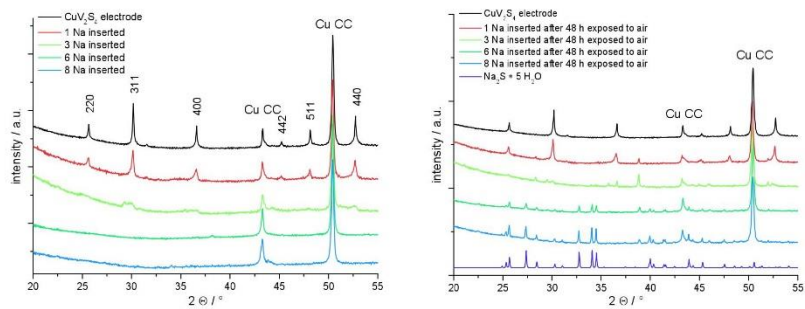


Fig. S6: *Ex situ* XRD patterns of CuV_2S_4 electrodes on a copper current collection. The reflections of the current collector are marked with Cu CC.

Fig. S6: *ex situ* XRD patterns of CuV_2S_4 electrodes on Cu current collectors. The formation of the Na_2S matrix upon discharge is not visible in the XRD patterns of the electrodes measured under air exclusion. But due to the hygroscopic nature of Na_2S , reflections of $\text{Na}_2\text{S} \cdot 5\text{H}_2\text{O}$ become visible when the electrodes are exposed to air for 48 h giving the indirect evidence of the formation of an X-ray amorphous Na_2S matrix during the first discharge.

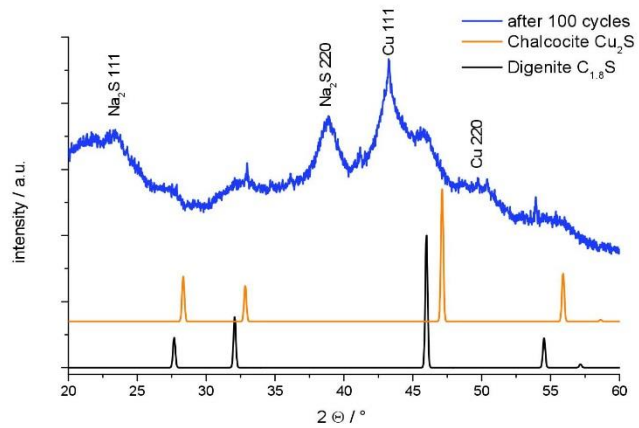


Fig. S7: Ex situ XRD patterns of CuV_2S_4 after 100 cycles (blue) and calculated patterns for Cu_2S (orange) and $\text{Cu}_{1.8}\text{S}$ (black)

8. A.-L. Hansen, T. Dankwort, H. Groß, M. Etter, J. König, V. Duppel, L. Kienle, W. Bensch, *J. Mater. Chem. C*, submitted.

Electronic Supporting Information

Structural properties of the thermoelectric material CuCrS_2 and of deintercalated Cu_xCrS_2 on different length scales: X-ray diffraction, pair distribution function and transmission electron microscopy studies

Anna-Lena Hansen^a, Torben Dankwort^b, Hendrik Groß^b, Martin Etter^c, Jan König^d, Viola Duppel^e
Lorenz Kienle^b, Wolfgang Bensch^a

^aInstitute of Inorganic Chemistry, Kiel University, Max-Eyth-Str. 2, D-24118 Kiel, Germany.

^bInstitute for Materials Science, Kiel University, Kaiserstrasse 2, 24143 Kiel, Germany.

^cDeutsches Elektronen-Synchrotron (DESY), Hamburg 22607, Germany.

^dFraunhofer Institute for Physical Measurement Techniques IPM, Heidenhofstrasse 8, 79110 Freiburg, Germany

^eNanochemistry, Max Planck Institute for Solid State Research, Heisenbergstrasse 1, D-70569 Stuttgart, Germany.

Figures

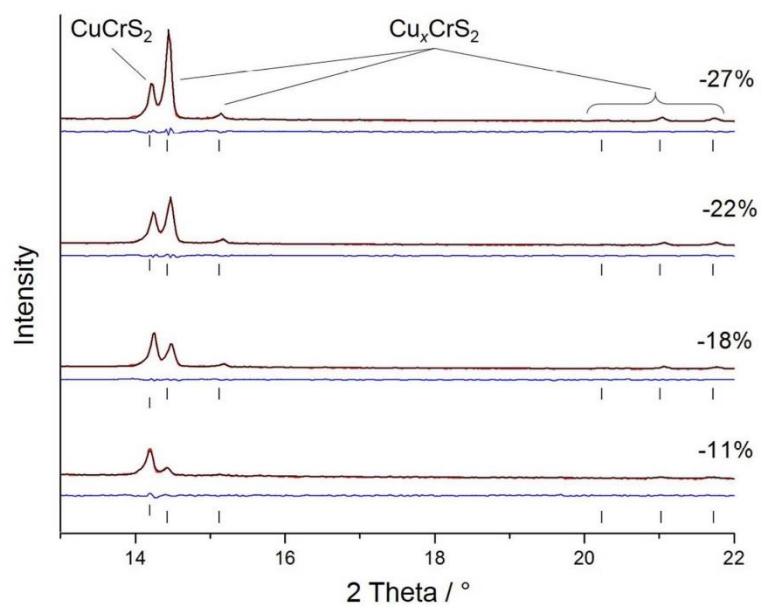


Figure S1: Section of Rietveld refined (red curve) XRD pattern (black) of samples with different deintercalation grade, given on the right (oriented on the copper content after deintercalation). Difference curve is depicted in blue. Measured using an X'Pert Pro MPD diffractometer (PANalytical), $\lambda = 1.5405$.

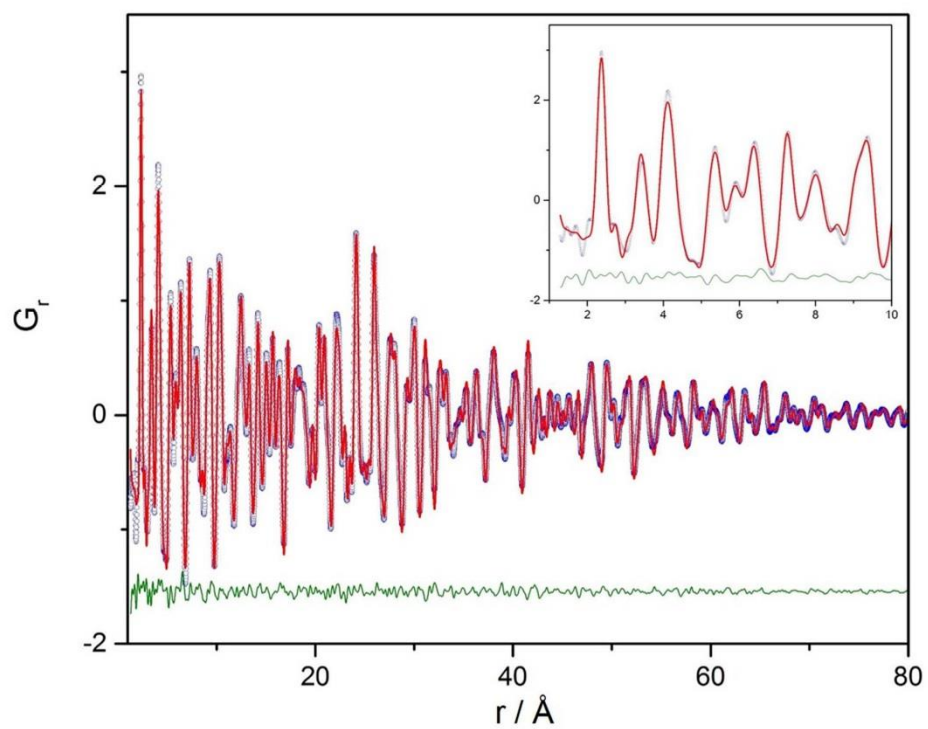


Figure S2: Observed pair distribution function (blue circles), calculated PDF based on the model given in the text (red line) and difference curve (green). Inset shows a good agreement of short range order. $R_{\text{WP}} = 15.6\%$.

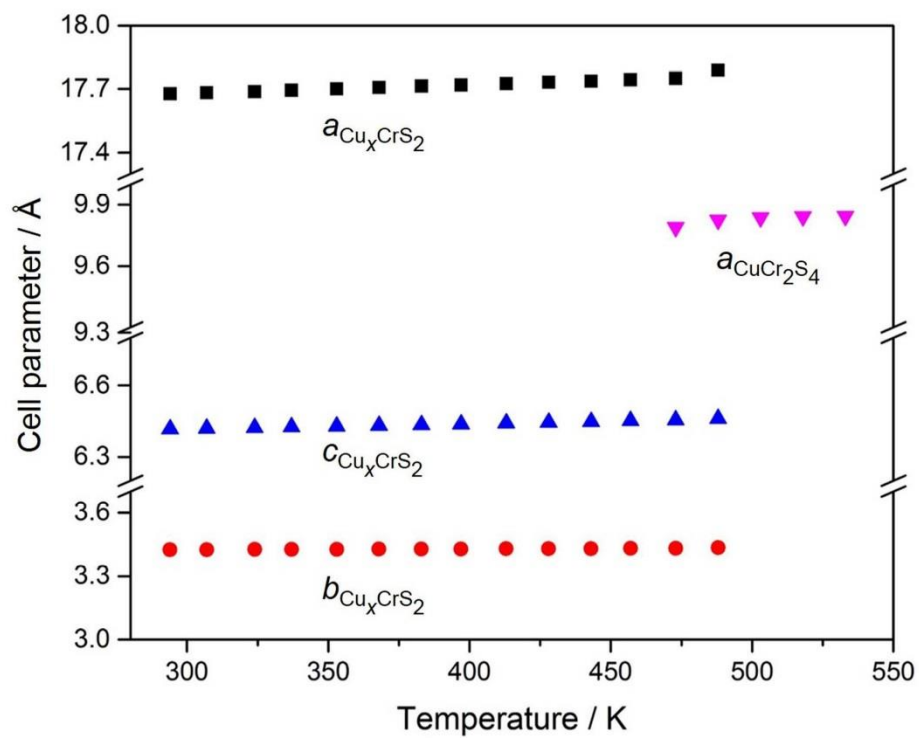


Figure S3: cell parameter against temperature. Estimates standard deviations are smaller than given symbols.

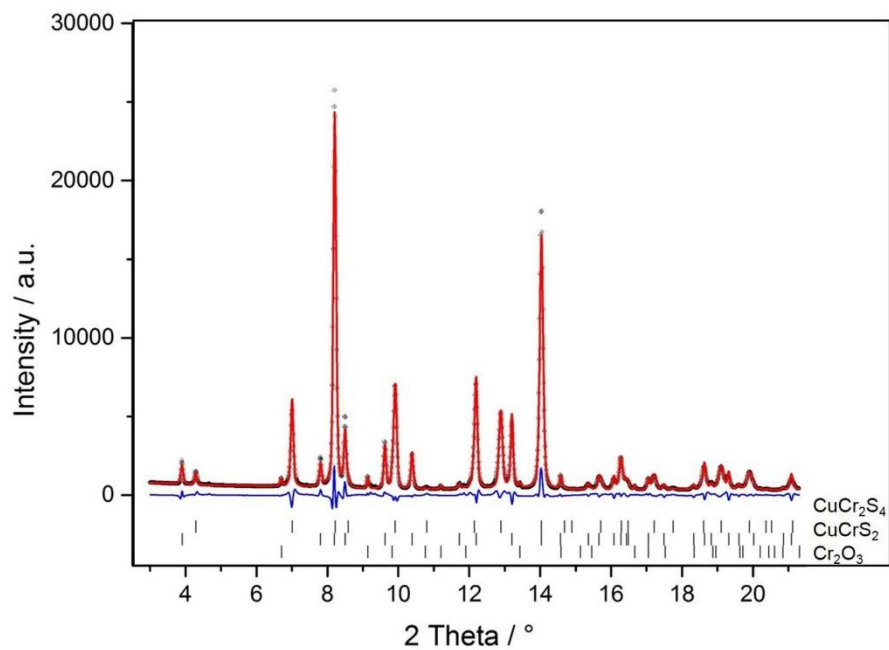


Figure S4: Rietveld refined synchrotron XRPD pattern of deintercalated sample heated above 533 K and cooled to room temperature. Phases are indicated by labelled tic marks. Wavelength $\lambda = 0.4246 \text{ \AA}$. Circles represents measured data, red line calculated curve, blue difference curve. $R_{wp} = 6.8 \%$.

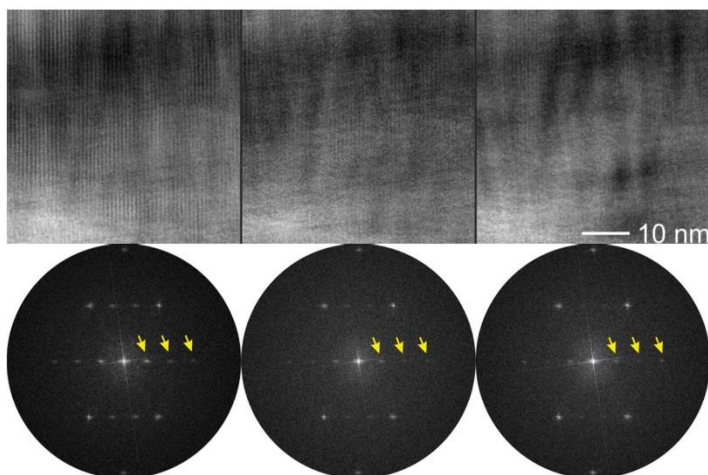


Figure S5: Gradual decay of the superlattice reflections along a^* due to short electron beam irradiation.

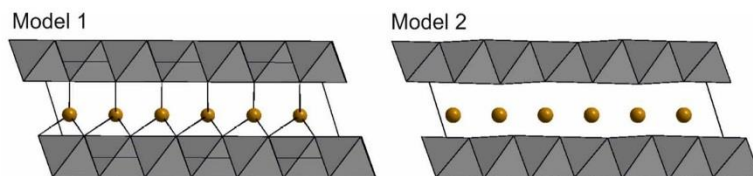


Figure S6: Both model used for HRTEM contrast simulations.

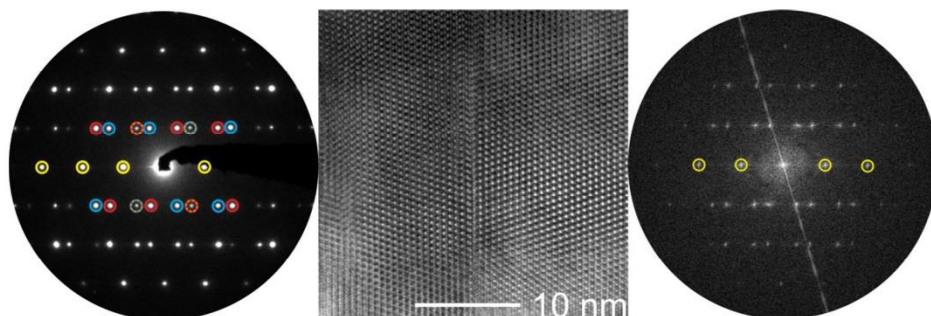


Figure S7: ED pattern, HRTEM micrograph and corresponding FFT of a $\Sigma 3$ twin boundary of CuCr_2S_4 on edge (zone axis $[110]$). Yellow circles in the diffraction pattern and the FFT highlight the (111) twin boundary. Red and blue circles mark the two different domains while the orange striped circles mark intensities due to double diffraction for the respective domain.

Powder diffraction data

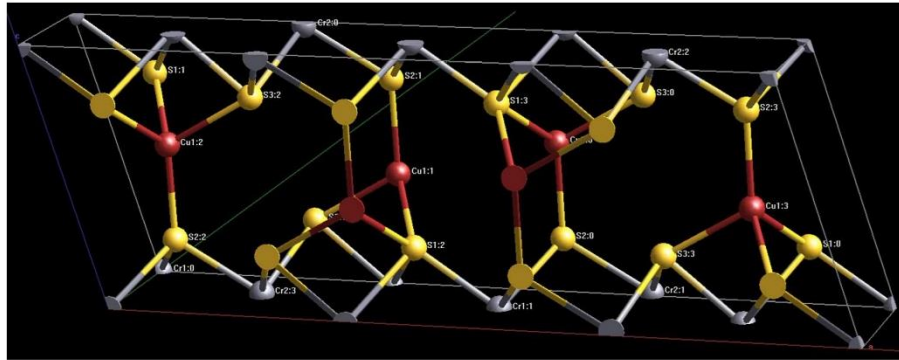
CuCrS_2 , PETRA III, DESY; $\lambda = 0.20722 \text{ \AA}$ Rietveld Refinement, $R_{\text{WP}} = 6.15 \%$, $R_{\text{BRAGG}} = 2.43 \%$,

CuCrS_2		<i>a</i>	<i>b</i>	<i>c</i>	β	
R3m		\AA	\AA	\AA	$^\circ$	
		3.4802(1)	3.4802(1)	18.697(1)		
Atom	Wyckoff position	x	y	z	occ	Biso \AA^2
Cr1	3a	0	0	0	1	0.85(3)
S1	3a	0	0	0.2651(2)	1	0.54(5)
S2	3a	0	0	0.7423(2)	1	0.54(5)
Cu1	3a	0	0	0.1478(1)	1	2.27(5)

Cu_xCrS_2 PETRA III, DESY; $\lambda = 0.20722 \text{ \AA}$ Rietveld Refinement, $R_{\text{WP}} = 6.4 \%$, $R_{\text{BRAGG}} = 4.53 \%$,

Table S2: unit cell parameter, obtained by Rietveld Refinement

Cu_xCrS_2		<i>a</i>	<i>b</i>	<i>c</i>	β	
C2/m		\AA	\AA	\AA	$^\circ$	
		17.6782(9)	3.4266(1)	6.4177(3)	107.203(4)	
Atom	Wyckoff position	x	y	z	occ	Biso \AA^2
Cr1	2a	0	0	0	1	1.03(7)
Cr2	4i	0.3218(2)	0	0.9875(7)	1	1.03(7)
S1	4i	0.9109(3)	0	0.2176(9)	1	0.47(5)
S2	4i	0.5817(3)	0	0.2051(9)	1	0.47(5)
S3	4i	0.7543(3)	0	0.7682(9)	1	0.47(5)
Cu1	4i	0.6163(2)	0	0.5729(5)	1	1.74(5)



List of bond lengths:

Cr1:0	S2:5	2.373(4)	S1:0	Cu1:5	2.315(5)
	S2:4	2.373(4)		Cu1:5	2.315(5)
	S2:5	2.373(4)		Cr1:0	2.393(7)
	S2:4	2.373(4)		Cr2:4	2.494(5)
	S1:0	2.393(7)		Cr2:4	2.494(5)
	S1:1	2.393(7)	S2:0	Cu1:0	2.256(7)
Cr2:0	S3:4	2.313(4)		Cr1:4	2.373(4)
	S3:4	2.313(4)		Cr1:4	2.373(4)
	S3:1	2.349(9)		Cr2:1	2.384(9)
	S2:1	2.384(9)	S3:0	Cr2:4	2.313(4)
	S1:4	2.494(5)		Cr2:4	2.313(4)
	S1:4	2.494(5)		Cr2:1	2.349(9)
	Cu1:1	2.707(6)		Cu1:0	2.390(7)
	Cr2:5	3.107(8)	Cu1:0	S2:0	2.256(7)
	Cr2:5	3.107(8)		S1:5	2.315(5)
				S1:5	2.315(5)
				S3:0	2.390(7)
				Cr2:1	2.707(6)

Total Scattering data – Pair distribution Function Analysis

Cu_xCrS_2 PETRA III, DESY; $\lambda = 0.20722 \text{ \AA}$,

Table S3: Unit cell parameters and atomic positions used for modelling the pair distribution function. Only Debye-Waller factors of copper were refined. For all other atoms the values $u_{11} = u_{22} = u_{33}$ were fixed to 0.0126.

Cu_xCrS_2	a	b	c	β			
C2/m	\AA	\AA	\AA	$^\circ$			
	17.686	3.429	6.423	107.21			
Atom	x	y	z	u_{11}	u_{22}	u_{33}	u_{13}
Cr1	0	0	0	0.0126	0.0126	0.0126	
Cr2	0.3221	0	0.9891	0.0126	0.0126	0.0126	
S1	0.9102	0	0.213	0.0126	0.0126	0.0126	
S3	0.5812	0	0.2122	0.0126	0.0126	0.0126	

S4	0.755	0	0.763	0.0126	0.0126	0.0126	
Cu1	0.6172	0	0.5701	0.023	0.027	0.0049	0.0052

PDF REFINEMENT

Using PDFFIT version : 1.1a

=====

PHASE 1 : AH3014E3_Cu_xCrS₂_C2/m

Scale factor : 0.529382

Particle diameter : not applied

Step cutoff : not applied

Quad. corr. factor : 0

Lin. corr. factor : 1.83707

Low r sigma ratio : 1

R cutoff [Å] : 0

Lattice parameters : 17.6869 (0.014) 3.42985 (0.0024) 6.42319 (0.0038)

& angles : 90 107.219 (0.054) 90

Atom positions & occupancies :

CR	0	0	0	1
CR	0.5	0.5	0	1
CR	0.322202	0	0.989096	1
CR	0.677798	0	0.0109035	1
CR	0.822202	0.5	0.989096	1
CR	0.177798	0.5	0.0109035	1
S	0.910178	0	0.212891	1
S	0.0898221	0	0.787109	1
S	0.410178	0.5	0.212891	1
S	0.589822	0.5	0.787109	1
S	0.58104	0	0.212267	1
S	0.41896	0	0.787733	1
S	0.08104	0.5	0.212267	1
S	0.91896	0.5	0.787733	1
S	0.754908	0	0.762894	1
S	0.245092	0	0.237106	1

S	0.254908	0.5	0.762894	1
S	0.745092	0.5	0.237106	1
CU	0.617184	0	0.570205	1
CU	0.382816	0	0.429795	1
CU	0.117184	0.5	0.570205	1
CU	0.882816	0.5	0.429795	1

Anisotropic temperature factors :

CR	0.0126652	0.0126652	0.0126652
CR	0.0126652	0.0126652	0.0126652
CR	0.0126652	0.0126652	0.0126652
CR	0.0126652	0.0126652	0.0126652
CR	0.0126652	0.0126652	0.0126652
CR	0.0126652	0.0126652	0.0126652
S	0.0126652	0.0126652	0.0126652
S	0.0126652	0.0126652	0.0126652
S	0.0126652	0.0126652	0.0126652
S	0.0126652	0.0126652	0.0126652
S	0.0126652	0.0126652	0.0126652
S	0.0126652	0.0126652	0.0126652
S	0.0126652	0.0126652	0.0126652
S	0.0126652	0.0126652	0.0126652
S	0.0126652	0.0126652	0.0126652
S	0.0126652	0.0126652	0.0126652
S	0.0126652	0.0126652	0.0126652
S	0.0126652	0.0126652	0.0126652
CU	0.0230243 (0.0084)	0.0267392 (0.008)	0.0049829 (0.0038)
0	0.00524545 (0.0049)	0	
CU	0.0230243 (0.0084)	0.0267392 (0.008)	0.0049829 (0.0038)
0	0.00524545 (0.0049)	0	
CU	0.0230243 (0.0084)	0.0267392 (0.008)	0.0049829 (0.0038)
0	0.00524545 (0.0049)	0	
CU	0.0230243 (0.0084)	0.0267392 (0.008)	0.0049829 (0.0038)
0	0.00524545 (0.0049)	0	

DATA SET : 1 (string)

Data range in r [Å] : 1.29 -> 80 Step dr : 0.01
Calculated range : 1.29 -> 81.7691
Refinement r range : 1.29 -> 80 Data pts : 0 -> 7871
Reduced chi squared : 0.00486105
Rw - value : 0.156994
Experimental settings :
Radiation : X-Rays
Termination at Qmax : 21.31 Å⁻¹
DQ dampening Qdamp : 0.02729 Å⁻¹
DQ broadening Qbroad : not applied
Scale factor : 1

PARAMETER INFORMATION :

Number of constraints : 62
Number of refined parameters : 8
Number of fixed parameters : 12

Refinement parameters :

1: 17.6869 (0.014)	2: 3.42985 (0.0024)	3: 6.42319 (0.0038)
4: 107.219 (0.054)	5: 0.529382	6: 1.83707
271: 0.322202	273: 0.989096	311: 0.910178
313: 0.212891	351: 0.58104	353: 0.212267
391: 0.754908	393: 0.762894	431: 0.617184
433: 0.570205	1014: 0.0230243 (0.0084)	1015: 0.0267392 (0.008)
1016: 0.0049829 (0.0038)	1018: 0.00524545 (0.0049)	

REFINEMENT INFORMATION:

Number of iterations : 7
Reduced chi squared : 0.00486105

Rw - value : 0.156994

Correlations greater than 0.8 :

*** none ***

Danksagung

An dieser Stelle möchte ich allen Menschen danken, die an der Entstehung dieser Arbeit beteiligt waren.

An erster Stelle danke ich meinem Doktorvater Prof. Dr. Wolfgang Bensch für die Möglichkeit diese Arbeit in seinem Arbeitskreis anzufertigen, sowie sein Vertrauen mir dieses Thema als Kristallographin mit einem ausgesprochenen Maß an Freiraum zu überlassen. Natürlich will ich es nicht versäumen, mich auch für das stets ausgesprochen gute Essen und die begleitenden Weine bei unseren AK Treffen zu bedanken.

Des Weiteren bedanke ich mich bei Prof. Dr. Christian Näther für die Übernahme des Zweitgutachtens.

Prof. Dave Johnson danke ich für seine Unterstützung, Mitarbeit an Publikationen und seine aufbauenden Worte.

Dr. Lars Peters danke ich für meine Empfehlung, ohne die ich diese Arbeit nicht hätte antreten können, sowie seine stete Bereitschaft mir besonders zu Beginn meiner Arbeit mit Rat und Tat zur Seite zu stehen.

Ich danke meinen Kooperationspartnern für die stets fruchtbare und erkenntnisreiche Zusammenarbeit: Prof. Dr. Lorenz Kienle, Torben Dankwort, Dr. Markus Winkler, Dr. Jan König.

Den zahlreichen Mensch, denen ich auf Tagungen, Kursen und Messzeiten begegnen durfte, danke ich für Diskussionen, Kooperationen oder das ein oder andere Glas Wein. Allen voran Dr. Sebastian Bette, Jonas Sottman, Hanka Becker, Dr. Robert Haberkorn, Christoph Bauer, Marco Esters, Dr. Martin Etter und ganz besonders herzlich Dr. Daniel Woodruff.

Meinem Arbeitskreis danke ich, denn jeder hat auf seine ganz eigene Weise dazu beigetragen diese Arbeit zu ermöglichen. Einige seien hier erwähnt:

Dr. Michael Wendt und Dr. Lydia Gräfenstein danke ich für die herzliche Aufnahme im Arbeitskreis.

Dr. Nicole Pienack für ihre stets offene Tür, ein nie enden wollenden Vorrat an Seelentröstern und eine tolle Zeit in Innsbruck und am DESY.

Christine Koch für ihre ehrlichen Gespräche und ihre Hilfsbereitschaft.

Dr. Jana Timm danke ich tolle Zeiten in London, Oxford und natürlich auch hier in Kiel, sowie das ein oder andere Babysitting.

Joanna Dopta, Lisa Mahnke, Felix Danker, Pia Rönfeld und Niclas Heidenreich danke ich für die Unterstützung und den Spaß während langer Messzeiten.

Und natürlich danke ich meiner Familie, allen voran Julian, Jannes und Mila, die die Auf- und Abs während meiner Doktorandenzeit mit stoischer Ruhe und Durchhaltevermögen durchstanden haben, auch wenn ich oft in der Welt unterwegs war und viel zu viel Zeit an meinem Laptop verbracht habe.

Erklärung

Hiermit erkläre ich, Anna-Lena Hansen, an Eides statt, dass ich die vorliegende Arbeit, abgesehen von der Beratung durch meinen Doktorvater Prof. Dr. W. Bensch, selbstständig und nach den Grundsätzen guter wissenschaftlicher Arbeit der Deutschen Forschungsgemeinschaft in Inhalt und Form angefertigt habe. Weder ganz noch zum Teil wurde diese Arbeit an anderer Stelle im Rahmen eines Prüfungsverfahrens vorgelegt oder zur Veröffentlichung eingereicht.

gez. Anna-Lena Hansen

Wissenschaftlicher Werdegang

Anna-Lena Hansen, geb. Gritzuhn

Staatsangehörigkeit: deutsch

Geboren am 06.04.1983 in Kiel

Verheiratet, 2 Kinder

2002 Abitur Klaus-Groth-Gymnasium, Neumünster

2011 Diplom Christian-Albrechts-Universität

Mineralogie

Hauptfach Kristallographie

2011 – 2012 wissenschaftliche Mitarbeiterin Institut für Geowissenschaften CAU Kiel

Seit 2013 wissenschaftliche Mitarbeiterin Institut für anorganische Chemie CAU
Kiel